

THE LATENT POTENTIAL OF RESTORATION

Biophysical Climate Effects of Land Restoration in Africa

Jessica Ruijsch

Propositions

1. The latent potential of land restoration is controlled by the sensible heat flux.
(this thesis)
2. Cloud impacts should be factored into the design of land restoration projects.
(this thesis)
3. Land restoration-induced changes in brightness bring an ignored uncertainty to carbon credits.
4. Remote sensing is both literally and figuratively a top-down approach.
5. Academic curricula on water science should not artificially separate hydrology and meteorology.
6. Ignoring local trade-offs to obtain benefits amplifies world-wide inequality.
7. To overcome procrastination, one should stop thinking and start writing.

Propositions belonging to the thesis, entitled

The Latent Potential of Restoration: Biophysical Climate Effects of Land Restoration in Africa.

Jessica Ruijsch
Wageningen, 25 September 2025

The Latent Potential of Restoration: Biophysical Climate Effects of Land Restoration in Africa

Jessica Ruijsch

Thesis committee

Promotors

Dr R.W.A. Hutjes

Associate professor in Earth Systems and Global Change
Wageningen University & Research

Dr A.J. Teuling

Associate professor in Hydrology and Environmental Hydraulics
Wageningen University & Research

Other members

Prof. Dr K.M. de Beurs, Wageningen University & Research

Dr G. Lenderink, Royal Netherlands Meteorological Institute (KNMI), De Bilt

Prof. Dr D.G. Miralles, Ghent University, Belgium

Prof. Dr E.L. Davin, University of Bern, Switzerland

This research was conducted under the auspices of the Graduate School for Socio-Economic and Natural Sciences of the Environment (SENSE).

The Latent Potential of Restoration: Biophysical Climate Effects of Land Restoration in Africa

Jessica Ruijsch

Thesis

submitted in fulfilment of the requirements for the degree of doctor
at Wageningen University
by the authority of the Rector Magnificus,
Prof. Dr C. Kroeze,
in the presence of the
Thesis Committee appointed by the Academic Board
to be defended in public
on Thursday 25 September 2025
at 3.30 p.m. in the Omnia Auditorium.

Jessica Ruijsch

The latent potential of restoration: biophysical climate effects of land restoration in Africa,
260 pages.

PhD thesis, Wageningen University, Wageningen, the Netherlands (2025)
With references, with summary in English and Dutch

DOI <https://doi.org/10.18174/681479>

*"In this great chain of causes and effects,
no single fact can be considered in isolation"*

- Alexander von Humboldt (1845) -

Table of Contents

Summary.....	9
Samenvatting	13
Chapter 1 General Introduction	17
Chapter 2 Land Restoration and Greening	39
Chapter 3 Land Restoration and Cooling	55
Chapter 4 Land Restoration and Cloud Formation	81
Chapter 5 Land Restoration Patterns and Cloud Formation	103
Chapter 6 Synthesis and outlook	131
References	151
Appendix.....	180
Code and Data Availability.....	251
Statement of Author Contribution.....	252
List of Publications	253
Acknowledgement	255
Curriculum Vitae	257
Sense diploma	258

Summary

Ongoing land degradation and climate change unequally impact developing regions across the world, affecting biodiversity, food production, water availability and livelihoods in the affected region. Dryland regions in Africa are especially vulnerable to the impacts of land degradation and climate change due to a combination of water scarcity, population growth and high dependence on rainfed agriculture.

Recognising these threats, many organisations increasingly advocate for land restoration, which can encompass a wide range of activities, including tree planting, area protection, natural regeneration and sustainable land management. Under the current United Nations Decade of Ecosystem Restoration (2021-2030), many projects are implemented across Africa, including large-scale initiatives such as the Great Green Wall project and the African Forest Landscape Restoration Initiative. Through land restoration, these projects aim to combat land degradation and increase biodiversity, while providing other benefits such as wood, food, shade and income to local residents.

Land restoration is widely implemented to mitigate global climate change through the sequestration of carbon in biomass. However, on a more local scale, **land restoration may impact the local climate because restoration-induced changes in vegetation cover alter the properties of the Earth's surface, such as albedo, surface roughness and the amount of evaporation**. This changes the exchange of water and energy between the Earth's surface and the atmosphere, impacting temperature, cloud formation and water availability. These changes are referred to as biophysical climate effects.

However, even though the biophysical mechanisms of forests and vegetation changes are generally well understood, the net biophysical climate effect depends on location, scale, background climate and atmospheric conditions. In addition, it is unknown to what extent the relatively small-scale restoration projects are able to impact the climate through biophysical processes. As a result, it is currently not possible to apply the existing knowledge on land-atmosphere interactions in such a way that accurate predictions on the expected biophysical climate effects of land restoration can be made. **This thesis aimed to determine how land restoration affects the local climate through biophysical processes**. I used a combination of remote sensing and atmospheric modelling to sequentially study how land restoration affects vegetation greening (Chapter 2), land surface temperature (Chapter 3) and cloud formation (Chapter 4 and 5).

In Chapter 2, I used satellite observations of vegetation greenness across Africa to determine how land restoration contributes to vegetation greening. Although restoration-induced changes in vegetation greenness are an imperative intermediate step to determine the connection between land restoration and biophysical climate effects, the effect of land restoration on greening in Africa is currently unknown due to the absence of a (public) complete database of land restoration projects. To this end, I used 20 years of satellite observations of vegetation greenness (represented by the Normalized Difference vegetation Index and the Enhanced Vegetation Index derived from MODIS data), to which I applied a spatial-context method to limit the effect of natural climate variability and climate change. This resulted in information on small-scale greening hotspots across Africa. I find that 2.1% of

the continent, roughly 400,000 km², experiences small-scale greening, especially in semi-arid regions. Combining this data with known locations of sustainable land management projects shows that sustainable land management results in a significant local greening compared to reference areas. Comparing different restoration practices reveals that active planting of vegetation results in stronger greening compared to natural regeneration, but over a smaller region.

In Chapter 3, I extended this analysis of vegetation greening with remotely sensed observations of temperature and albedo over a 22-year period to determine the local biophysical cooling potential of land restoration across Africa. I compared vegetation greenness, albedo and land surface temperature to surrounding regions, showing whether greener regions are cooler or warmer than their surroundings. I used a random forest algorithm to extrapolate the results and to determine the local cooling potential that can be achieved with maximum land restoration. Across the continent, land restoration decreases the local land surface temperature by an average of 0.2 K due to the strong evaporative cooling potential in semi-arid regions. However, the driest regions in the study area experience local warming due to land restoration, potentially due to albedo warming and the limited water available for evaporative cooling, highlighting a spatial variation of the local biophysical cooling potential of land restoration across Africa.

In Chapter 4, I zoomed in on West Africa to determine to what extent land restoration can affect cloud development. After all, if land restoration has the ability to impact land surface temperature through changes in vegetation greenness, it may also impact cloud formation through changes in albedo and surface roughness (providing a lifting mechanism) and evapotranspiration (providing moisture). I applied a statistical algorithm to detect cloud occurrence from 20 years of satellite data from the Meteosat Second Generation high-resolution visible channel. The high temporal resolution (15 minutes) and long data range (20 years) of this dataset allowed me to determine the relationship between cloud occurrence and land restoration (represented by vegetation greenness and protected areas). The result highlighted an enhanced cloud formation over greener regions and protected areas larger than 121 km², especially at the start and end of the wet season. Interestingly, the data shows stronger cloud enhancement over larger protected areas, suggesting a scale-dependent, positive relationship between land restoration and cloud formation.

In Chapter 5, I used the WRF atmospheric model to reveal the underlying mechanisms for the relationships found in the previous chapters and to determine how the spatial pattern of land restoration projects impacts cloud formation. First, I ran the model for three case study days with an observed cloud enhancement over the W-Arly-Pendjari national park complex in West Africa. Changing the albedo, soil moisture content and surface roughness over the forested region shows that during these case study days, cloud formation is strongly inhibited under wetter soil moisture conditions, while a decrease in albedo and an increase in surface roughness enhance cloud formation. Next, I ran 27 land restoration scenarios with varying forest cover and spatial clustering of forests to study the effect of the spatial pattern of land restoration on cloud development. This showed that, under conditions where cloud formation is enhanced over forested regions, a higher clustering of forests cause enhanced cloud formation (with an average cloud cover fraction of 21.1%) compared to a more heterogeneous forest cover distributed across the domain (with an average cloud cover

fraction of 6.4%), caused by enhanced mesoscale circulation and convergence at the forest edge.

Lastly, I synthesise these results in Chapter 6 to provide insight into the latent potential of land restoration. Despite uncertainties related to a simplified definition of land restoration throughout this thesis, the used methodology and potential feedbacks that are not included, this thesis shows that land restoration in Africa has the potential to affect the local climate through biophysical processes, depending on the type of projects, aridity and the size and spatial patterns of the projects. I therefore recommended incorporating the biophysical climate effects of land restoration in project planning and decision-making, both to optimise potential benefits and to avoid unwanted trade-offs.

Samenvatting

Aanhoudende landdegradatie en klimaatverandering hebben een onevenredig grote impact op ontwikkelingsregio's over de hele wereld, wat de biodiversiteit, voedselproductie, beschikbaarheid van water en het levensonderhoud negatief beïnvloed in de getroffen gebieden. Droge gebieden in Afrika zijn bijzonder kwetsbaar voor de gevolgen van landdegradatie en klimaatverandering door een combinatie van waterschaarste, bevolkingsgroei en een relatief groot aandeel regenafhankelijke landbouw.

Steeds meer organisaties erkennen deze problemen en pleiten voor landrestoratie. Dit kan een breed aantal activiteiten omvatten, waaronder het planten van bomen, het beschermen van gebieden, natuurlijke regeneratie en duurzaam landbeheer. Onder het huidige 'United Nations Decade of Ecosystem Restoration' (2021–2030) worden in heel Afrika landrestoratieprojecten geïmplementeerd, waaronder grootschalige initiatieven zoals het Great Green Wall-project en het African Forest Landscape Restoration Initiative. Via landrestoratie streven deze projecten ernaar om landdegradatie tegen te gaan en de biodiversiteit te vergroten, terwijl ze ook andere voordelen bieden zoals hout, voedsel, schaduw en inkomen voor de lokale bevolking.

Landrestoratie wordt wereldwijd geïmplementeerd voor de mitigatie van klimaatverandering door middel van het opslaan van CO₂ in biomassa. **Op een lokale schaal kan landrestoratie echter ook het klimaat beïnvloeden doordat veranderingen in vegetatie invloed hebben op de eigenschappen van het aardoppervlak**, waaronder albedo, oppervlakteruwheid en de hoeveelheid verdamping. Deze veranderingen hebben namelijk invloed op de energie- en wateruitwisseling tussen het aardoppervlak en de atmosfeer, wat op zijn beurt invloed heeft op temperatuur, wolkenvorming en waterbeschikbaarheid. Dit worden de biofysische klimaateffecten van land restoratie (of van vegetatie in het algemeen) genoemd.

Hoewel de verschillende biofysische mechanismen relatief goed begrepen worden, hangt het uiteindelijke biofysische klimaateffect van vegetatieveranderingen af van locatie, schaal, achtergrondklimaat en atmosferische omstandigheden. Daarnaast is het onduidelijk in hoeverre kleinschalige landrestoratieprojecten in staat zijn het klimaat te beïnvloeden via deze biofysische processen. Daardoor is het op dit moment moeilijk de bestaande kennis over land-atmosfeerinteracties zodanig toe te passen dat er nauwkeurige voorspellingen over de verwachte biofysische klimaateffecten van landrestoratie gedaan kunnen worden. **Dit proefschrift heeft dan ook als doel te bepalen hoe landrestoratie het lokale klimaat beïnvloedt via biofysische processen**, waarbij ik gebruikmaak van een combinatie van satellietbeelden en atmosferische modellen om in vier hoofdstukken stapsgewijs te onderzoeken hoe landrestoratie invloed heeft op de vergroening van vegetatie (Hoofdstuk 2), de temperatuur van het aardoppervlak (Hoofdstuk 3) en wolkenvorming (Hoofdstuk 4 en 5).

In Hoofdstuk 2 heb ik satellietwaarnemingen van de groenheid van vegetatie gebruikt om te bepalen in hoeverre landrestoratie bijdraagt aan vergroening in Afrika. Hoewel veranderingen in de groenheid van vegetatie, als gevolg van landrestoratie, een cruciale tussenschakel vormen om het verband tussen landrestoratie en biofysische klimaateffecten te begrijpen, is het effect van landrestoratie op vergroening in Afrika momenteel onbekend, mede door het ontbreken van een (publiek toegankelijke) volledige database van

landrestoratieprojecten. Daarom heb ik twintig jaar satellietdata van vegetatiegroenheid (op basis van de Normalized Difference Vegetation Index en Enhanced Vegetation index gebaseerd op MODIS data) geanalyseerd en gecorrigeerd voor natuurlijke klimaatvariabiliteit en klimaatverandering door een 'spatial-context' methode toe te passen. Dit resulteerde in informatie over kleinschalige vergroening-hotspots op continentale schaal. Uit mijn analyse blijkt dat 2,1% van Afrika, ongeveer 400.000 km², kleinschalige vergroening laat zien, met name in semi-aride gebieden. Door deze data te combineren met bekende locaties van landrestoratieprojecten, blijkt dat deze initiatieven leiden tot significante lokale vergroening in vergelijking met omliggende referentiegebieden. Een vergelijking van verschillende landrestoratieprojecten toont aan dat het actief aanplanten van vegetatie tot sterkere vergroening leidt dan natuurlijke regeneratie, maar wel over een kleiner gebied.

In Hoofdstuk 3 heb ik deze analyse uitgebreid met satellietwaarnemingen van oppervlaktetemperatuur en albedo over een periode van 22 jaar om het lokale biofysische koelingspotentieel van landrestoratie in Afrika te bepalen. Ik heb de groenheid van vegetatie, albedo en oppervlaktetemperatuur vergeleken met omliggende gebieden om vast te stellen of groenere regio's kouder of warmer zijn dan hun omgeving. Met behulp van een random forest-algoritme heb ik de resultaten geëxtrapoléerd om het lokale koelingspotentieel bij een maximale landrestoratie te voorspellen. Op een continentale schaal blijkt landrestoratie de oppervlaktetemperatuur gemiddeld met 0,2 K te verlagen, voornamelijk door sterke afkoeling door verdamping in semi-aride gebieden. In de droogste gebieden leidt landrestoratie daarentegen tot een lokale opwarming, mogelijk door albedo-effecten en een gebrek aan water voor afkoeling door verdamping. Dit laat zien dat het lokale biofysische koelingspotentieel van landrestoratie sterk varieert over Afrika.

In Hoofdstuk 4 heb ik ingezoomd op West-Afrika om te bepalen in hoeverre landrestoratie wolkenvorming kan beïnvloeden. Als landrestoratie namelijk invloed heeft op de landoppervlaktetemperatuur via veranderingen in vegetatie, dan kan het ook invloed hebben op wolkenvorming via veranderingen in albedo en oppervlakteruwheid (wat zorgt voor het opstijgen van lucht) en verdamping (wat vocht aanlevert). Ik heb een statistisch algoritme toegepast om wolkenvorming te detecteren op basis van twintig jaar aan data van de high-resolution visible band van Meteosat Second Generation satellieten. De hoge temporele resolutie (elke 15 minuten) en de lange datareeks (20 jaar) maakten het mogelijk om het verband tussen wolkenvorming en landrestoratie (in dit geval groenheid van vegetatie en beschermde gebieden) vast te stellen. De resultaten laten een verhoogde wolkenvorming boven groenere regio's en beschermde gebieden groter dan 121 km² zien, vooral aan het begin en einde van het regenseizoen. Interessant is dat wolkenvorming vaker voorkomt boven grotere beschermde gebieden, wat wijst op een schaalafhankelijke, positieve relatie tussen landrestoratie en wolkenvorming.

In Hoofdstuk 5 heb ik het atmosferisch model WRF gebruikt om de onderliggende mechanismen achter de verbanden uit de vorige hoofdstukken te analyseren en te bepalen hoe het ruimtelijke patroon van landrestoratieprojecten wolkenvorming beïnvloedt. Als eerste heb ik simulaties uitgevoerd voor drie casestudiedagen waarop ik een verhoogde wolkenvorming had waargenomen boven het W-Arly-Pendjari nationaal parkcomplex in West-Afrika. Door het albedo, het bodemvochtgehalte en de oppervlakteruwheid in het beboste gebied aan te passen in het model, blijkt dat wolkenvorming tijdens deze dagen sterk wordt onderdrukt bij nattere

bodemomstandigheden. Een lager albedo en een hogere oppervlakteruwheid bevorderen daarentegen juist de wolkenvorming. Vervolgens heb ik 27 modelscenario's uitgevoerd met variërende hoeveelheid beboste gebieden en ruimtelijke clustering om het effect van de ruimtelijke verdeling van landrestoratie op wolkenvorming te onderzoeken. Hieruit blijkt dat, onder omstandigheden met wolkenvorming boven beboste gebieden, een hogere clustering van bos leidt tot sterkere wolkenvorming (gemiddeld 21,1% bedekt met wolken) dan een verspreiding van bos over het hele gebied (gemiddeld 6,4% bedekt met wolken), als gevolg van versterkte meso-schale circulatie en convergentie aan de rand van het beboste gebied.

In Hoofdstuk 6 heb ik deze hoofdstukken gesynthetiseerd om het mogelijke latente potentieel van landrestoratie te bepalen. Ondanks onzekerheden met betrekking tot de gebruikte (en mogelijk eenvoudige) definitie van landrestoratie, de gebruikte methode en mogelijke terugkoppelingen die niet zijn meegenomen, laat dit proefschrift zien dat landrestoratie in Afrika het lokale klimaat kan beïnvloeden via biofysische processen. Het uiteindelijke effect is wel afhankelijk van het type project, de droogtegraad, de grootte van het project en het ruimtelijke patroon waarin de projecten geïmplementeerd zijn. Ik adviseer daarom om de biofysische klimaateffecten van landrestoratie mee te nemen in projectplanning en besluitvorming, zowel om de potentiële voordelen optimaal te benutten als om ongewenste neveneffecten te voorkomen.



An aerial photograph of a river delta, showing a network of water channels and land. The water is a light greenish-brown color, and the land is a mix of brown and tan. A prominent white rectangular box is positioned at the top of the image, containing the chapter title. The text is in a bold, black, sans-serif font.

Chapter 1 | General Introduction

Abstract | Land degradation is a globally recognised problem, decreasing food production, water availability, biodiversity and human welfare. As a reaction, several restoration initiatives have emerged that aim to reduce or reverse land degradation and its negative consequences. The increase in vegetation cover caused by land restoration projects can affect the regional and global climate, not only through carbon sequestration, but also by changing the biophysical properties of the earth's surface (e.g. albedo, surface roughness or evapotranspiration). Some land restoration initiatives explicitly focus on improving the regional climate through these biophysical processes. However, how these mechanisms apply to the often small-scale restoration projects remains uncertain. As a result, it is unknown how restoration through changes in vegetation can contribute to climate change adaptation. In this thesis, I aim to contribute to closing this gap by determining the biophysical climate effects of land restoration projects, focusing on Africa.

1.1 Motivation

1.1.1 Land degradation and climate change

Land is the basis for life. It provides important resources like food, water and ecosystem services, and has an important role in regulating biodiversity and the climate (IPCC, 2019). Yet, the Earth's surface and its resources are finite. Human societies have been shaping the landscape through burning, hunting, domestication and agriculture for at least 12,000 years (Dotterweich, 2013; Ellis et al., 2021). By 3000 years ago, the largest part of the Earth's landscape was transformed by humans (Stephens et al., 2019), which currently results in degradation at global and regional scales (UNCCD, 2017). Despite the increasing efforts to reverse or halt environmental change (Martin et al., 2021), around 8-45% of the ice-free land surface is in a degraded state, which affects 1.3 to 3.2 billion people worldwide (Gibbs & Salmon, 2015; Le et al., 2016).

The locations as well as the negative impacts of land degradation are unequally distributed across the globe, with 95% of the people affected by land degradation living in developing countries (Barbier & Hochard, 2018). As land degradation hampers food production, water availability and biodiversity (ELD Initiative, 2015), continued degradation may enhance poverty in the affected regions (Barbier & Hochard, 2018). Drylands, consisting of arid, semi-arid and subhumid regions, are regions that are especially vulnerable to land degradation due to a combination of water scarcity and population growth (Closset et al., 2018; UNCCD, 2020).

Next to land degradation, climate change, induced by excessive anthropogenic emissions and land use change, is already showing its consequences. This has not only increased global average temperatures by almost 1.5 °C but also affected weather and climate extremes across the world, threatening ecosystems, food security, agricultural productivity and human livelihoods (IPCC, 2023). In addition, climate change has amplified land degradation over the past years due to increased soil erosion induced by droughts, heavy rainfall, and floods, and it will likely continue to do so when climate change intensifies in the future (IPCC, 2019).

Although the relative impact of climate change and local anthropogenic pressures on land degradation remains uncertain (Rasmussen et al., 2016; IPCC, 2019), it is clear that a combination of socio-economic and physical pressures results in droughts, biodiversity loss, reduced food production and economic growth, and loss of lives in the affected regions (Trisos et al., 2022). Of course, global actions preventing future climate change and further land degradation are crucial in solving these problems. But could there also be a way to recover the already degraded ecosystems while also reducing some of the burdens of climate change for local communities?

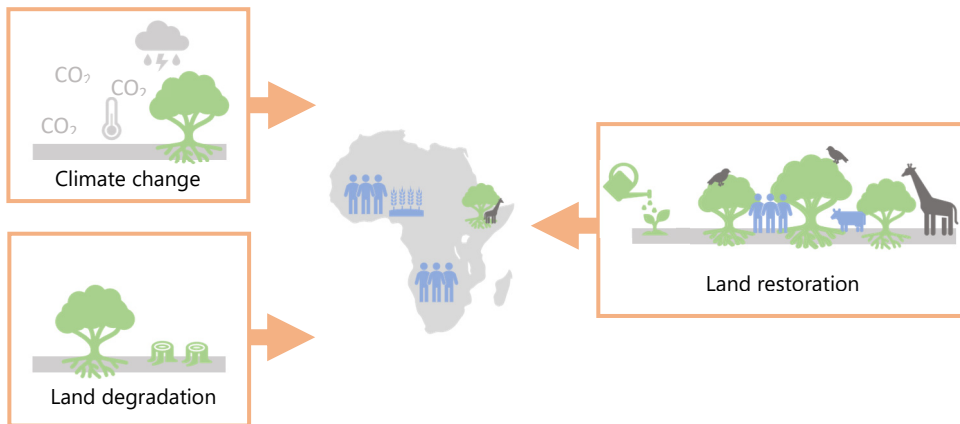


Figure 1.1 | Climate change, land degradation and land restoration. Climate change and land degradation negatively impact biodiversity, food production, economic growth and quality of life. Land restoration is proposed as a solution to combat these negative effects, including in Africa. For visualization purposes, land restoration is often illustrated with trees throughout this thesis. Please note that not all restoration practices include tree planting or result in an increase in tree cover, especially in dryland regions.

1.1.2 Land restoration as a solution?

Several organisations have proposed implementing land restoration as a potential solution to ongoing land degradation and climate change (Figure 1.1). Land (or landscape) restoration is a broad concept and includes activities such as tree planting, area closure and sustainable land management. Although many definitions of land restoration exist, they often include some sort of human intervention to increase biodiversity, prevent or reverse land degradation or desertification and restore ecosystem services and human well-being. The United Nations Convention to Combat Desertification (UNCCD) defines land restoration as:

“The process of avoiding, reducing, and reversing land degradation to recover the biodiversity and ecosystem services that sustain all life on Earth. Land restoration refers to a regenerative process along a continuum of land and water management practices adapted to local conditions and societal choices – applied to conserve natural areas, sustainably manage production landscapes, such as agriculture and forestry, and recover past ecological integrity” (UNCCD, 2020).

Over the years, land restoration has been increasingly advocated for, and more and more land restoration projects are being implemented (Martin et al., 2021). The United Nations even declared the years 2021 to 2030 the Decade of Ecosystem Restoration, aiming to prevent, halt and reverse further loss of nature, through supporting and scaling up projects, as well as raising awareness for successful restoration (UNEP, 2019). Many global and national restoration projects are currently being implemented.

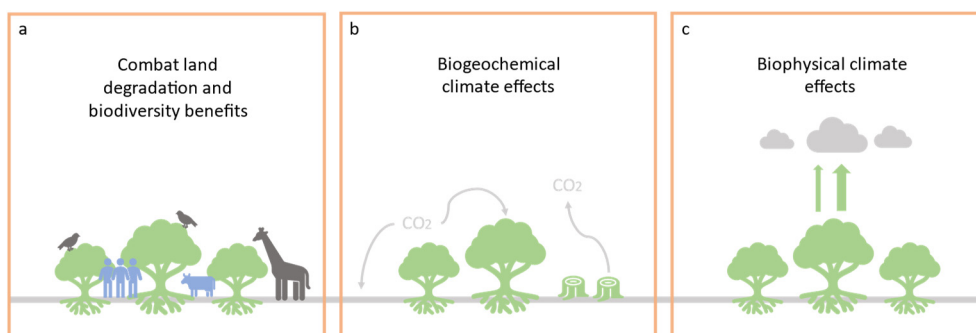


Figure 1.2 | Potential benefits of land restoration. (a) Land restoration provides ecosystem services like biodiversity, food, income or cultural benefits and combats land degradation. (b) In addition, the resulting changes in vegetation cover affect the local climate through biogeochemical and (c) biophysical processes. Adapted from Kirschbaum et al. (2024).

Projects such as the Bonn Challenge (<https://www.bonnchallenge.org/>), the Trillion Tree Campaign (<https://www.trilliontreecampaign.org/>), the Three-North Shelterbelt Forest Program in China and the African Forest Landscape Restoration initiative (AFR100) (<https://afr100.org/>) are all aiming to restore millions of hectares in the coming years.

Although many large-scale projects are aimed at tree planting, they can also contain a wide variety of other restoration practices. The Great Green Wall of Africa, for example, was initiated in 2007 by the African Union to combat desertification in the Sahel. Although the original idea was to create a ‘wall’ of trees along the entire width of the African continent to stop the expansion of the Sahara, it developed into a broader range of land restoration projects over the years, including farmer-managed natural regeneration and area protection (UNCCD, 2020). Through land restoration, these projects not only try to combat land degradation and provide biodiversity benefits but can, if implemented correctly, also increase landscape connectivity and deliver wood, food, shade and income to local communities. In addition, an increase in vegetation cover may help local communities sustain livelihoods during climate anomalies such as droughts or heat waves (Holl & Brancalion, 2020) (Figure 1.2a).

1.1.3 Biogeochemical and biophysical climate effects of land restoration

Besides providing the ecosystem services mentioned above, land restoration is widely implemented to mitigate anthropogenic climate change through carbon sequestration (Shevliakova et al., 2013; IPCC, 2019; Friedlingstein et al., 2020). Because vegetation captures carbon through photosynthesis, increasing the vegetation cover through land restoration can store residual anthropogenic emissions (Bastin et al., 2019; Friedlingstein et al., 2020). It is estimated that, from the 11 GtC per year that is being emitted through fossil fuel emissions and land use change, the biosphere currently

stores roughly 2 GtC per year in biomass and soil organic carbon (Kirschbaum et al., 2019; Kirschbaum et al., 2024). Using the global potential for tree restoration to its maximum, tree planting may store up to an additional 205 GtC (Bastin et al., 2019). This idea has boosted ways for companies or consumers to support land restoration or tree planting for carbon sequestration, and it is now often offered to 'compensate' carbon emissions of a flight or product through voluntary carbon offset programs (Liu et al., 2023), or so-called carbon credits, and carbon accounting systems. Although the actual effectiveness of such projects to store carbon is debated (Probst et al., 2024), land restoration has the potential to change the climate on a global scale by removing carbon from the atmosphere. These interactions are referred to as the biogeochemical climate effects (or impacts) of land restoration (Figure 1.2b).

However, carbon sequestration is not the only way land restoration affects the climate, as vegetation also interacts with the regional and local climate in a very direct way: it changes the properties of the Earth's surface, including the albedo, surface roughness and the amount of evapotranspiration. Through interaction between the land surface and the atmosphere, changes in vegetation can influence cloud development, precipitation and the climate (Bonan, 2008; Piao et al., 2020). These climate effects are referred to as the biophysical climate effects of land restoration (Figure 1.2c). In contrast to biogeochemical effects, which act globally and relatively slowly, biophysical effects are more regional or local, as well as immediate.

Although the biophysical effects of vegetation are generally less known than carbon sequestration, more and more initiatives propose utilising these properties to improve the local climate and human well-being through land restoration. These include, for example, the Dutch NGO Justdiggitt (<https://justdiggitt.org>), the Green Up to Cool Down movement (<https://www.greenuptocooldown.com>) or the WeForest organisation (<https://www.weforest.org>). Even though scientists have been trying to unravel these biophysical climate effects for more than 200 years, they are considerably less understood than the biogeochemical processes (Bonan, 2023). Yet, it is becoming clear that the effect of vegetation on the climate through these biophysical processes may be as large, or even larger, than the biogeochemical processes (Windisch et al., 2021).

In combination with the high environmental pressures of land degradation and climate change in dryland regions, this highlights the need to provide accurate predictions on the expected biophysical climate effects of land restoration. This will not only allow us to identify how land restoration can be used to create a more comfortable climate for local communities, but it will also help to predict and avoid unwanted or unexpected side effects of these projects.

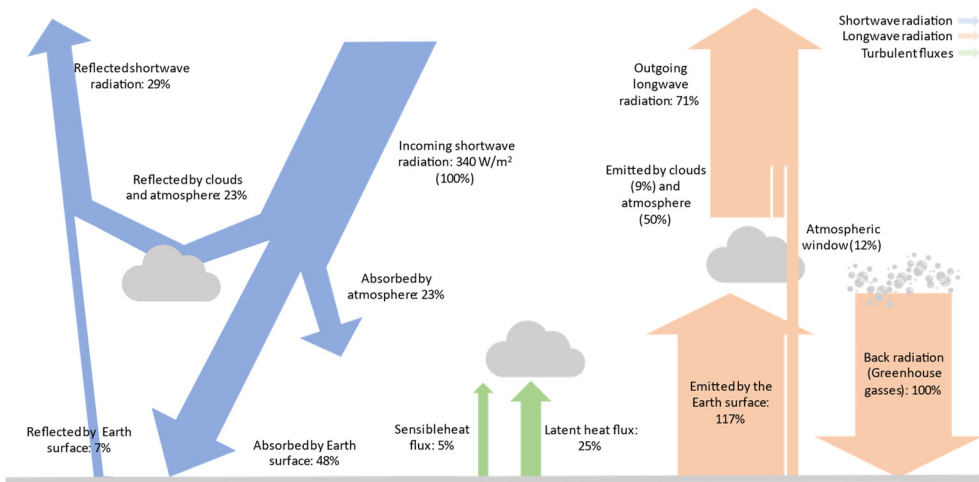


Figure 1.3 | Energy balance of the Earth's surface. Arrows indicate shortwave radiation (blue), longwave radiation (orange) and turbulent fluxes (green). Percentages are relative to the incoming shortwave radiation at the top of the atmosphere (304 W/m^2). Adapted from Ruijsch, Hutjes, et al. (2023), based on Trenberth et al. (2009).

1.2 The scientific basis

1.2.1 Vegetation-atmosphere interactions

Vegetation (or land restoration projects that affect vegetation cover and composition) interacts with the atmosphere through several mechanisms. These include changes in the Earth's energy balance and surface roughness, which in turn have an impact on the surface and air temperature, atmospheric boundary layer development, atmospheric convection and cloud development. If these clouds create precipitation, this affects moisture recycling and water availability in the region. The state-of-the-art scientific knowledge on these land-atmosphere interactions is described below to form the scientific basis on which this thesis builds.

1.2.2 The Earth's energy balance

The climate on Earth is largely driven by the sun. Under optimal conditions, as much as 1000 W/m^2 of solar radiation can reach the surface around noon. On average, however, 340 W/m^2 reaches the top of the atmosphere as shortwave radiation, of which a part is reflected back into space (23%) or absorbed (23%) by clouds and the atmosphere (Kiehl & Trenberth, 1997; Trenberth et al., 2009) (Figure 1.3). The fraction of the remaining shortwave radiation (S) reflected at the Earth's surface is called albedo (α) and heavily depends on the properties of the Earth's surface. The shortwave radiation absorbed by the Earth's surface is, in combination with the net longwave radiation (L), also called net radiation (R_n) and is brought back into the atmosphere or ground

through the latent heat flux (LE) (used for the evapotranspiration of water), the sensible heat flux (H) (results in transport heat) and the ground heat flux (G) as:

$$Rn = S \downarrow (1 - \alpha) + (L \downarrow - L \uparrow) = H + LE + G \quad (1.1)$$

Vegetation can affect the surface energy balance through changes in albedo, as well as changes in the allocation of the net radiation to the latent heat flux, sensible heat flux and ground heat flux. The albedo has a large variation across different land cover types. Values range from 5% for water and asphalt to as high as 95% for fresh snow (Oke, 1987). This also suggests that land cover change may, through changes in albedo and the energy balance, have a considerable impact on the local and global climate (Davin & de Noblet-Ducoudré, 2010; Arora & Montenegro, 2011). Due to the relatively dark surface, vegetation often has a low albedo compared to bare soil, although the value depends on species (Betts & Ball, 1997; Bright et al., 2015), season (Betts, 2000; Kuusinen et al., 2014; Li et al., 2023) and age (Hovi et al., 2019; Alibakhshi et al., 2020). Deciduous forests generally have an albedo between 15% and 20%, while the albedo of grasslands ranges from 16% to 26%. Because albedo has a large effect on the net radiation (Betts, 2000; Pitman, 2003), changes in vegetation cover through, for example, reforestation or deforestation, may have large-scale impacts on temperature.

The net radiation at the surface will be brought back to the atmosphere as sensible and latent heat fluxes or stored in the soil. The distribution of the net radiation over these fluxes depends, amongst others, on land cover and water availability. Evapotranspiration or, in energy terms, the latent heat flux, occurs automatically when a moist surface comes in contact with a dry atmosphere, but is determined by the availability of water and energy, and the efficiency of transport (Jansen et al., 2023). In addition to atmospheric conditions (Nistor et al., 2018), and physiological difference (e.g. C_3 or C_4 plants, stomatal density and control, etc), the amount and type of vegetation are important factors affecting evapotranspiration (Breil et al., 2021). In addition, tropical forests generally have high evapotranspiration due to the high availability of energy and water, while boreal forests often lack the energy to facilitate high evapotranspiration rates (Bonan, 2008). This increased evapotranspiration results in a high allocation of the net radiation to the latent heat flux, which results in a relative decrease in sensible heat flux over regions with a high vegetation cover.

At the same time, the lower albedo over forested regions increases net radiation, increasing both the sensible and latent heat flux (Figure 1.4). In water-limited regions, reforestation may therefore increase the sensible heat flux because not enough water is available to increase the evapotranspiration and the latent heat flux (Laguë & Swann, 2016). In addition, an increase in vegetation often increases surface roughness. A surface with a higher surface roughness enhances turbulence and reduces atmospheric resistance through which the sensible and latent heat flux increase under similar atmospheric conditions (Pitman, 2003). On a larger scale, also the spatial distribution

of land use can increase surface roughness (Khanna & Medvigy, 2014; Spracklen et al., 2018).

1.2.3 Temperature

The changes in albedo, sensible and latent heat flux, and surface roughness due to vegetation changes also impact the surface temperature (or radiative skin temperature of the Earth's surface or canopy) and air temperature (ambient air temperature). A lower albedo can increase the surface temperature due to a higher absorption of incoming solar radiation (Betts, 2000), which is often referred to as the 'albedo warming' effect of vegetation. Some modelling studies even estimate that global deforestation will cause a net cooling effect because the decrease in albedo and resulting cooling effect will be larger than the warming effect due to the release of greenhouse gases (Bala et al., 2007), although the results differ per model (Boysen et al., 2014). At the same time, an increased evapotranspiration over vegetated areas decreases the share of net radiation that is allocated to the sensible heat flux and can therefore decrease the local surface temperature. This is referred to as the 'evaporative cooling' effect of the vegetation (Bonan, 2008). In addition, higher surface roughness will decrease aerodynamic resistance, which decreases the surface temperature (Chen, Li, et al., 2020).

Whether the counteracting effects of evaporative cooling and albedo warming result in a net cooling or warming depends on location (Perugini et al., 2017), scale (Spracklen et al., 2018), background climate (Pitman et al., 2011) and atmospheric conditions (Teuling et al., 2010; Chapman et al., 2020). In general, reforestation in boreal areas will increase the temperature, while tropical reforestation will likely result in cooling (Bonan, 2008; Jackson et al., 2008; Arora & Montenegro, 2011; Li et al., 2016; Forzieri et al., 2017; Boysen et al., 2020; Duveiller et al., 2020; De Hertog et al., 2022). Temperate reforestation often results in a low or unclear effect on the temperature (Boisier et al., 2012; Chacón et al., 2016). It should be kept in mind, however, that the evaporative cooling effect is local and temporary, because the heat is released again once the evaporated water condensates in the atmosphere, while the albedo warming effect impacts the energy balance of the Earth as a whole.

1.2.4 Boundary layer development, convection and cloud formation

Through changes in energy (latent and sensible heat flux) and water transport (evapotranspiration) from the Earth's surface to the atmosphere, vegetation has the ability to impact boundary layer development and cloud formation. Clouds form when water vapour in the atmosphere becomes saturated through cooling, moistening or mixing, which often occurs through vertical movement of air induced by mountains (orographic flows), frontal rise or convection. Surface heating and turbulence through increased turbulent fluxes stimulate growth of the boundary layer (van Heerwaarden

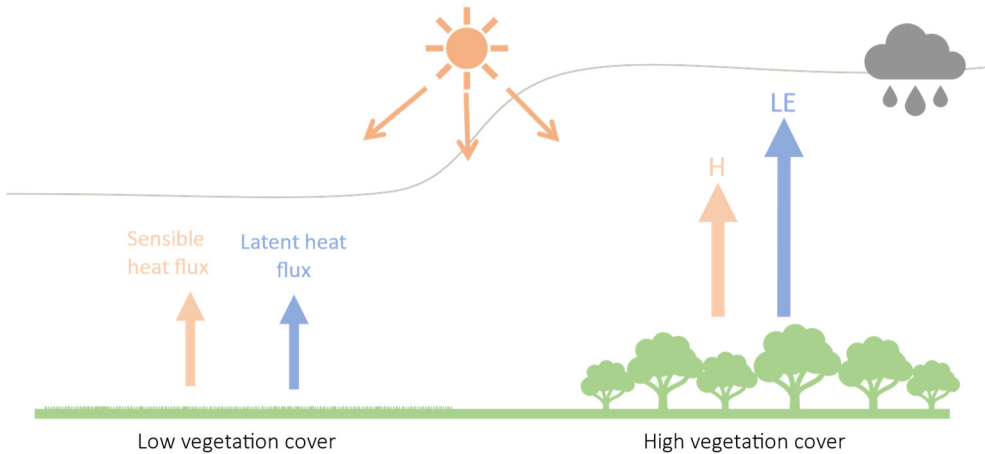


Figure 1.4 | Local effects of an increase in vegetation cover on the energy balance, boundary layer development and cloud formation. The arrows show the sensible heat flux (H) and latent heat flux (LE). The grey line shows the boundary layer height.

& Teuling, 2014), the part of the atmosphere that is influenced by the Earth's surface and is subject to diurnal variations (Vilà-Guerau de Arellano et al., 2015). When the boundary layer growth is sufficient, the atmospheric moisture will rise and cool, reaching saturation at the lifting condensation level, where boundary layer clouds will start to form. Under sufficiently unstable (buoyant) conditions, air may rise up the level of free convection, triggering convective cloud formation or even deep convection.

Whether cloud formation is enhanced over regions with a higher vegetation cover seems to differ from location to location, depending, amongst other factors, on whether the sensible heat flux increases with vegetation cover or not (Bosman et al., 2019). At the same time, vegetation increases atmospheric moisture through evapotranspiration, and therefore lowers the lifting condensation level, which can result in cloud formation over wet soils (Findell & Eltahir, 2003b, 2003a). In Africa, however, enhanced cloud formation is often observed over regions with lower soil moisture (Taylor et al., 2012; Taylor et al., 2013; Taylor, Klein, Parker, et al., 2022), which suggests that the sensible heat flux and boundary layer development are important factors in determining cloud development in this region (Figure 1.4).

1.2.5 Precipitation, atmospheric circulation and water availability

Over the past decades, there has been an increased interest in the question of whether forests and vegetation increase or decrease rainfall and water availability (Bennett & Barton, 2018). However, up to now, a scientific consensus is largely lacking (Sheil, 2018). On the one hand, increased evapotranspiration in forested areas enhances precipitation. Especially in tropical forests, studies show that large-scale deforestation

results in a strong decrease in the amount of precipitation (Bonan, 2008; Boysen et al., 2020; Smith et al., 2023) because a large part of the precipitation in these regions is formed by locally evaporated water (Staal et al., 2018). On smaller scales, however, deforestation can increase precipitation due to changes in moisture recycling (Spracklen et al., 2018). In drylands, where evapotranspiration is strongly limited by water availability, vegetation can increase precipitation (Miralles et al., 2016; Yosef et al., 2018; Branch & Wulfmeyer, 2019; Lal et al., 2021). On the other hand, this increased evapotranspiration reduces water availability in the region if the enhanced precipitation falls outside the forested area (Ellison et al., 2012; Ellison & Speranza, 2020). On a global scale, large-scale tree restoration will result in a redistribution of global water availability, with a considerable decrease in the water-scarce hotspots for tree restoration (Hoek van Dijke et al., 2022).

1.3 Knowledge gaps

Although there is thus a thorough scientific understanding of vegetation-climate interactions in general, critical information is currently missing when applying this knowledge to land restoration. This prevents projects from implementing targeted restoration to obtain maximum climate benefits or to predict unwanted side effects.

1.3.1 Greening potential of land restoration

Despite the increase in restoration projects being implemented over the years (Martin et al., 2021), it is not known in much detail how land restoration projects affect vegetation greenness. The projects cannot automatically be assumed to increase vegetation cover because projects often report a low survival rate of the planted vegetation (Trac et al., 2007; Murekezi et al., 2013; Nunes et al., 2016; Kodikara et al., 2017). In addition, not all projects are implemented to increase vegetation cover per se. Filling this knowledge gap is hindered by the lack of a complete and freely available dataset of land restoration projects, especially in data-scarce regions such as Africa. The large number of organisations working on implementing these projects makes it difficult to acquire such a complete database. Another complication arises from the intertwined signal of restoration and natural climate variability and climate change on the vegetation, especially in water-limited regions. Yet, determining the effect of restoration on vegetation is a crucial first step in determining the local climate effect of these projects because vegetation is a major factor impacting the biophysical properties of the Earth's surface.

1.3.2 Biophysical effects of greening across climate regions

The climate effect of changes in vegetation cover depends on the location (Perugini et al., 2017), scale (Spracklen et al., 2018), background climate (Pitman et al., 2011) and

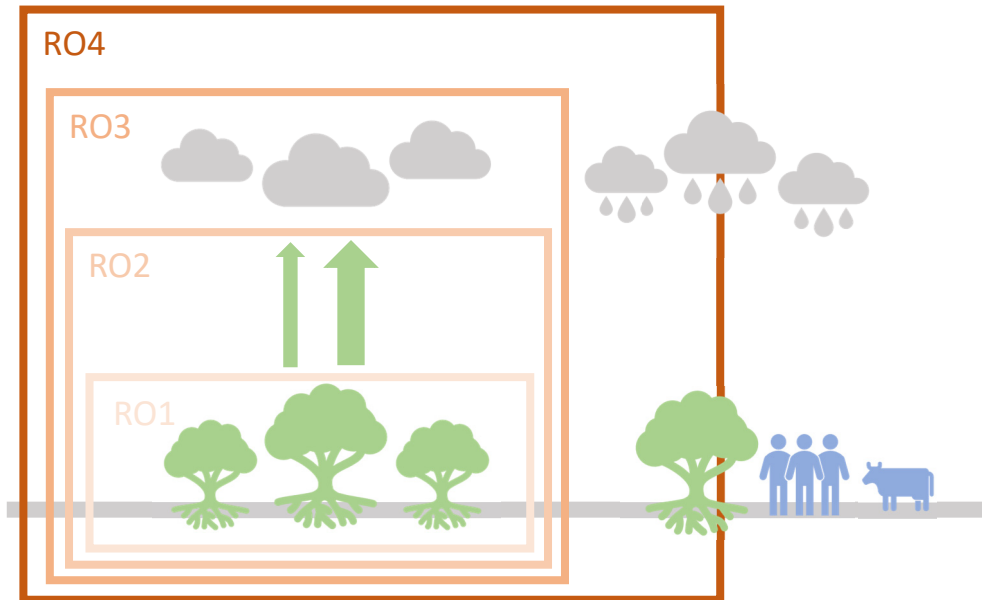


Figure 1.5 | Land-atmosphere feedback studied in the research objectives (RO). The effect of land restoration on vegetation (RO1), surface fluxes and temperature (RO2), cloud formation (RO3) and feedbacks (RO4).

atmospheric conditions (Teuling et al., 2010; Chapman et al., 2020). This means results from one study area are not directly applicable to other regions. Yet, most of the research on vegetation-climate interactions has been done in tropical forests such as the Amazon, temperate and boreal regions in Europe, and China (e.g. Durieux et al., 2003; Negri et al., 2004; Roy, 2009; Wang et al., 2009; Khanna et al., 2017). Many of these studies focus on deforestation rather than restoration, even though an increase in vegetation may have a different biophysical effect than a decrease (Zhang et al., 2024). Most studies that do look at an increasing vegetation cover specifically focus on tree restoration or potential tree cover maps (e.g. Duveiller et al., 2018b; Prevedello et al., 2019; Hoek van Dijke et al., 2022), while restoration in dryland regions could also encompass changes in grassland or shrubland vegetation cover that do not per se result in a change in forest cover. As a result, little is known about the effects of land restoration in data-scarce or non-forest regions such as the drylands in Africa.

1.3.3 Small-scale restoration projects

Although the effects of changes in vegetation on variables like surface temperature are expected to be direct and apparent on even the smallest scales, the changes to boundary layer development and cloud formation are expected to be scale-dependent. In the Amazon, small patches of deforestation enhance cloud formation due to increased

mesoscale circulation (Negri et al., 2004), while deforestation on larger scales reduces cloud formation and rainfall (Knox et al., 2011). In Africa, on the other hand, studies show enhanced cloud formation even over large patches of deforested areas (Taylor, Klein, Parker, et al., 2022). Up to now, it is unknown if the often small-scale land restoration projects are able to impact the atmosphere, what the minimum size is to have an impact, and whether spatial configuration and heterogeneity matter herein (te Wierik et al., 2021).

1.4 Research objectives

To this end, it is currently not possible to apply the existing knowledge on land-atmosphere interactions in such a way that accurate predictions on the expected biophysical climate effects of land restoration can be made. **This thesis, therefore, aims to determine how land restoration affects the local climate through biophysical processes.** More specifically, I use remote sensing and atmospheric modelling to answer the following research questions:

- How does land restoration contribute to vegetation greening? (R01)
- What is the local biophysical cooling potential of land restoration? (R02)
- To what extent can land restoration affect cloud development? (R03)
- How does the spatial pattern of land restoration projects affect cloud development? (R04)

The research questions follow a vertical structure (Figure 1.5), starting near the surface with changes in vegetation cover (R01) and the surface energy balance and temperature (R02), moving to atmospheric effects such as cloud development (R03), and finally exploring feedbacks shaped by the size and configuration of restoration projects (R04). By studying the different land-atmosphere feedbacks step by step, I hope to not only increase our theoretical knowledge on land-atmosphere interactions in the context of vegetation changes and land restoration, but also to provide practical information on the potential positive (and negative) effects of land restoration. This can be used to improve the planning of land restoration projects by optimising potential climate benefits and increasing adaptation benefits.

1.5 Study area

This thesis focuses on Africa. With its 30 million km², 54 countries, 1.5 billion people and more than 2000 languages, the continent is diverse in its culture and its people. Stretching from roughly 37°N in Tunisia to 34°S in South Africa, a wide range of climate and ecological zones can be found across the continent. The Intertropical Convergence Zone results in strong convection and high amounts of precipitation around the

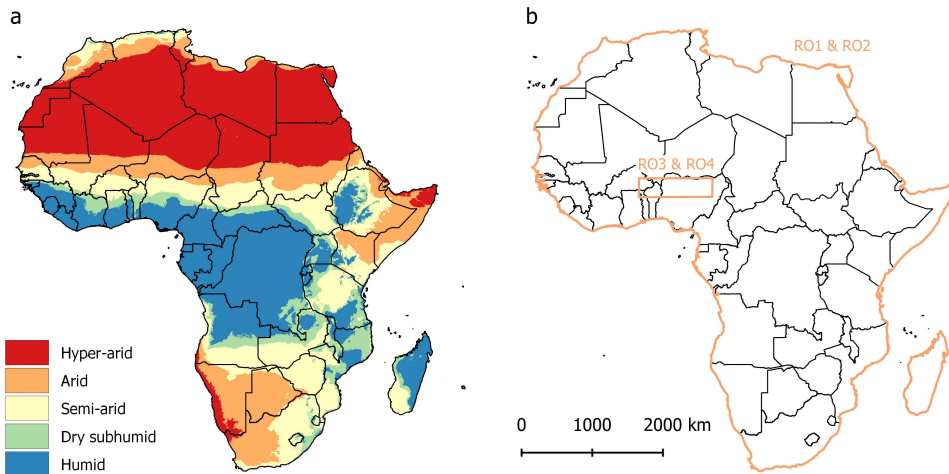


Figure 1.6 | Locations of the study areas and aridity index within Africa. (a) Locations of humid, dry subhumid, semi-arid, arid and hyper-arid regions based on (Zomer et al., 2022). (b) Research Objective (RO) 1 and 2 include the entire African continent, whereas RO3 and RO4 focus on a subregion in West Africa. The orange lines locate the boundaries of the study areas.

equator, while the high-pressure regions around 30°N and 30°S cause sinking air masses and extremely low precipitation. This so-called Hadley Circulation causes strong north-south gradients in aridity (Figure 1.6a), with tropical climates around the equator, and some of the world's largest and hottest deserts towards the southern and northern hemispheres.

Naturally, the vegetation follows the aridity gradients, with (sub)tropical rainforests, savannas, shrublands, steppes, grasslands, semi-arid deserts and desert regions. The northern and southernmost regions in Africa are characterised by Mediterranean vegetation. The drylands in Africa often receive a limited amount of rainfall, and the high temperature results in potential evapotranspiration that is more than twice as large as the rainfall (Mganga, 2023). In addition, the rainfall is often highly variable across both space and time, with considerable variation between the dry and wet seasons and from year to year (Kalele et al., 2021), driven by multiyear patterns in global climate phenomena such as the El Niño-Southern Oscillation and the Indian Ocean Dipole (Palmer et al., 2023).

However, also human-driven global climate change has impacted the African climate. Across the whole continent, both the mean and extreme temperatures have increased compared to the 1850-1900 period. Even though Africa contributes relatively little to greenhouse gas emissions, the continent is already experiencing the consequences of climate change, including increasing temperatures (Ranasinghe et al., 2021) and heatwave frequencies (Engdaw et al., 2022) at a higher rate than the global averages (Dhakal et al., 2022). The temperatures are expected to increase further in the future,

increasing drought frequency and duration, while heavy rainfall events will occur more often. At the same time, land degradation may have contributed to further climate change through a decline in terrestrial carbon stock and changes in dust aerosols (Choobari et al., 2014) and albedo, which alter land-atmosphere interaction through feedback loops (Rotenberg & Yakir, 2010). As a result, declines in soil moisture through land degradation can further exacerbate droughts (Seneviratne et al., 2010).

Climate change poses numerous risks to Africa, including negative effects on ecosystems, reduced food production and increased mortality through heat stress and diseases (Trisos et al., 2022). The high dependence of the African population on rain-fed agriculture, in combination with low adaptive capacity, makes the people in Africa especially vulnerable to these negative impacts (Trisos et al., 2022). In 2024, roughly 1.5 billion people live in Africa, about 18% of the world population, in more than 50 countries. The population is relatively young and the growth rate is high. It is expected that the population will increase to 2.5 billion people in 2050. In 2100, 35% of the world population is expected to live in sub-Saharan Africa (Vollset et al., 2020). In addition, Africa is the least wealthy continent (per capita) in the world, with 37% of the population in Sub-Saharan Africa living on less than \$2.15 per day (World Bank, 2024). About half of the population works in agriculture (FAO, 2023).

Recognising the threats of land degradation and climate change, many organisations are currently implementing restoration projects across Africa, including large projects such as the Great Green Wall and the AFR100 project. These projects may provide different ecosystem services and contribute to mitigating climate change through carbon sequestration. Yet, it remains unknown how these projects impact the local climate through biophysical processes and how this impacts local residents.

This thesis ranges from the continental to the regional (Figure 1.6b). RO1 and RO2 focus on Africa as a whole to identify continental patterns in land-atmosphere interactions, whereas RO3 and RO4 zoom in on West Africa, a dryland region with an especially strong land-atmosphere coupling (Koster et al., 2004; Soares et al., 2019). Detailed information on the regional-scale study regions is provided in the respective chapters.

1.6 Defining and measuring land restoration

Following the definition of the UNCCD (Section 1.1.2), restoration can encompass a wide range of activities, including tree planting, natural regeneration, area closure, farmer-managed natural regeneration and sustainable agriculture. It can also result in a wide range of benefits, such as increased soil quality, food production, biodiversity or income. However, this thesis specifically focuses on the biophysical effects of restoration on the climate. As changes in vegetation cover are expected to be the most important cause of changes in the biophysical properties of the surface, the

combination of the presence of vegetation in combination with the locations of restoration projects is used as a proxy for land restoration.

Although a complete database and openly available dataset of areas under land restoration does not exist for Africa, two alternatives can be used. The World Overview of Conservation Approaches and Technologies (WOCAT) database (WOCAT, 2022) contains sustainable land management (SLM) projects across Africa (Figure 1.7a). Using the description provided, the 628 project locations within the study area are divided into 11 categories of sustainable land management and 55 subcategories. The categories include often-used land restoration practices such as reforestation and natural regeneration, but also sustainable land management in a broader sense, such as sustainable agriculture or water harvesting. The WOCAT database is used in Chapter 2 and Chapter 3. The World Database of Protected Areas (WDPA) (IUCN, 2024), on the other hand, provides polygons rather than point locations of protected areas across the world (Figure 1.7b). Although area protection and land restoration are not strictly the same, the results on vegetation, which is a focal point in this thesis, are expected to be similar. The WDPA database is used to represent land restoration in Chapter 4 and Chapter 5.

1.7 Approaches for studying land-atmosphere interactions

Even if information on the locations of land restoration projects is available, it is not at all straightforward to determine how these projects affect the local climate, especially in Africa. This is one of the reasons why the biophysical effects of vegetation have been unclear for such a long time. Land-atmosphere interactions can be studied using different approaches, including in-situ measurements, remote sensing and modelling. Each of these approaches has distinct strengths and weaknesses, providing different perspectives on land-atmosphere interactions. Most of this thesis is based on remote sensing, with contributions from in-situ measurements and atmospheric modelling.

1.7.1 In-situ measurements

The most direct observations of vegetation and climate can be obtained from in-situ field measurements. Weather stations, for example, provide measurements of air temperature, humidity, rainfall or evapotranspiration. In addition, eddy-covariance measurements make use of high-frequency fluctuations in wind speed and other variables to calculate turbulent fluxes such as the sensible and latent heat fluxes (Baldocchi et al., 2001). However, to determine the biophysical effects of land restoration, a large number of observations within restored and reference areas is needed. Africa is a large continent and field measurements of vegetation and climate variables would be time-intensive, costly or simply impossible in remote areas. In addition, the data scarcity makes it difficult to interpolate the measurements across the

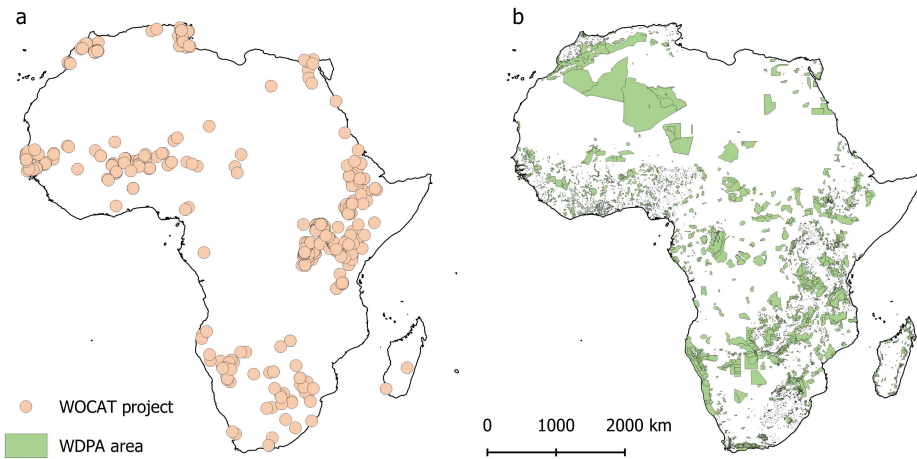


Figure 1.7 | Sustainable land management projects and protected areas in Africa. (a) The World Overview of Conservation Approaches and Technologies (WOCAT) database and (b) the World Database of Protected Areas (WDPA) within the African continent.

continent. Yet, in-situ measurements remain important tools to validate remote sensing and modelling results.

1.7.2 Remote sensing

Remote sensing is a term that often refers to measuring properties of the Earth using satellites, airplanes or drones. Active remote sensing devices emit a signal, such as Radar or Lidar, and measure how it is reflected by the surface, whereas passive remote sensing uses the reflectance of solar radiation to determine characteristics of the land, ocean or atmosphere (Schowengerdt, 2006).

Throughout this thesis, I will use two main sources. The Moderate Resolution Imaging Spectroradiometer (MODIS) consists of two sensors on board two satellites (Terra and Aqua) rotating the Earth. The Terra satellite was launched in 1999 and has a local overpass time of around 10:30 am, whereas the Aqua satellite was launched in 2002 and has a local overpass time of 1:30 pm. Together they create an image covering the whole earth every one or two days. Depending on the spectral bands used, MODIS provides cloud-free composites of different data products on a 250m or 1000m resolution and 16-day time step. Although the spatial resolution of MODIS is lower than for some other satellites (e.g. Landsat), a higher spatial resolution often comes with a lower return period, which makes temporal analysis more challenging.

In contrast to sun-synchronous satellites such as MODIS, the Meteosat Second Generation (MSG) satellites have a geostationary orbit and always observe the same region on Earth. MSG contains the Meteosat-8, Meteosat-9, Meteosat-10 and Meteosat-

11 satellites, and provides data from 2004 onwards, mainly for meteorological purposes. Because they are geostationary, they have much higher temporal resolution (15 minutes) but a lower spatial resolution (1-3 km, depending on the band) and they do not cover the whole Earth. The satellites are used to measure reflectance of the surface and the atmosphere across different wavelengths, providing information properties such as vegetation, temperature, albedo and cloud cover.

Vegetation data, important information when studying land restoration, can be obtained from these satellites in the form of vegetation indices (Didan, 2021) such as the Normalised Difference Vegetation Index (NDVI) and the Enhanced Vegetation Index (EVI). The NDVI uses the distinctive property of vegetation of having a high absorption of red light, but a reflection of Near Infrared (NIR) light. By taking the normalised fraction of the difference between the reflection of NIR and red light, it provides information on the health and density of vegetation, while correcting for differences in illumination. The NDVI can be defined as (Tucker, 1979):

$$NDVI = \frac{NIR-Red}{NIR+Red} \quad (1.2)$$

The NDVI ranges between -1 and 1, where healthy, dense and green vegetation will have a value closer to 1, whereas bare soil can have an NDVI close to 0. Negative values often indicate water bodies. As the NDVI tends to saturate under high biomass values, an alternative vegetation index is provided by the EVI (Huete et al., 1997), which is generally more sensitive to changes in the canopy structure properties, such as the Leaf Area Index, whereas the NDVI provides information on overall vegetation greenness and chlorophyll content. Other vegetation variables, such as leaf area index, fractional vegetation cover, and fraction of absorbed photosynthetically active radiation, provide information on other aspects of vegetation health, productivity and extent. These variables are often derived from more direct indices such as the NDVI and EVI using empirical global-scale models (Knyazikhin et al., 1998).

In addition to vegetation properties, satellites provide information on properties such as temperature, albedo and clouds. Satellite sensors can measure temperature in the form of land surface temperature (LST) at the Earth's surface or top of the canopy (Wan et al., 2021). LST is derived from thermal infrared (TIR) radiation emitted by the Earth's surface (Wan & Dozier, 1996). Although air temperature is an important variable for human comfort (Wolff et al., 2018), LST is more closely linked to the energy balance of the surface and, therefore, easier to link to changes in vegetation greenness. The albedo can be derived from satellite data using the Bidirectional Reflectance Distribution Function (BRDF), which describes how light is reflected by the Earth's surface under different viewing angles. White-sky albedo (WSA) provides a bi-hemispherical albedo (reflection under diffuse illumination) in the shortwave broadband range (containing both visible and near-infrared radiation) (Schaaf & Wang, 2015).

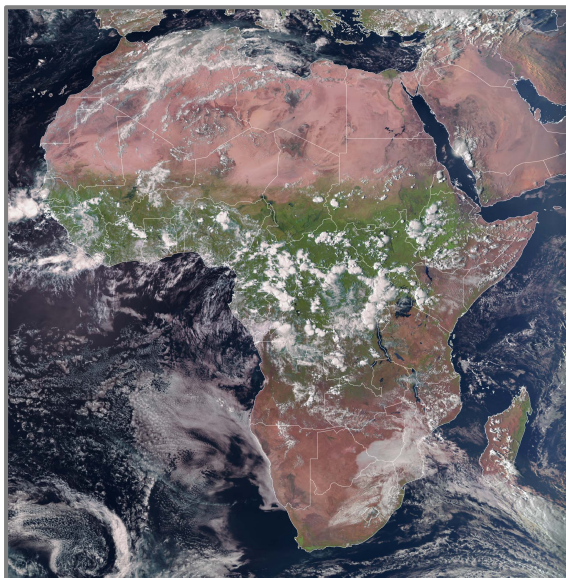


Figure 1.8 | Measuring cloud cover with satellites. Meteosat Second Generation image of Africa in the visible spectrum on 22 September 2024 at 13:45 UTC. Clouds show a high reflectance of visible light, as shown by the white colour in the image.

Although many satellites unavoidably detect clouds, often unwanted, the geostationary orbit and long operational period of MSG allow for cloud cover measurements across diurnal, seasonal and multi-year time scales. Cloud detection often makes use of the strong reflecting properties of clouds in the visible and infrared ranges of the spectrum (Figure 1.8), providing properties such as cloud optical depth, cloud top height and cloud cover (Schmetz et al., 2002).

When using such satellite measurements, a major challenge arises from natural climate variability and climate change. Because dryland vegetation is water-limited, changes in rainfall directly affect vegetation growth (Proud & Rasmussen, 2011). Simply studying the changes in vegetation within the boundary of a restoration project ignores the effect of climate on the vegetation. The environmental impact of human interventions is therefore often assessed using a so-called before/after-control/impact (BACI) design (Underwood, 1991, 1992). By assuming that the climatic effects of vegetation act both inside and outside the project, comparing the differences in vegetation within a project area (impact) with a reference area (control) removes the effect of natural climate variability and climate change from the signal. At the same time, there is a need to compare the amount of vegetation before and after the implementation to account for differences in properties between the control and the impact site. If an increase in vegetation is caused by the project rather than a change in the climate, an increase in vegetation compared to the reference area is thus expected. Similar to a BACI design, a

spatial-context approach (Lhermitte et al., 2010; Hamunyela et al., 2016) can also account for these climate effects. The approach is similar to the BACI design but is applied in an automated way on a larger scale. Rather than studying specific project locations, it is applied in a more automated way without defining specific restoration areas and can therefore be applied on a larger scale. This method can therefore detect small-scale greening or provide information on whether an area that is greener than its surroundings, is also cooler than its surroundings.

1.7.3 Atmospheric modelling

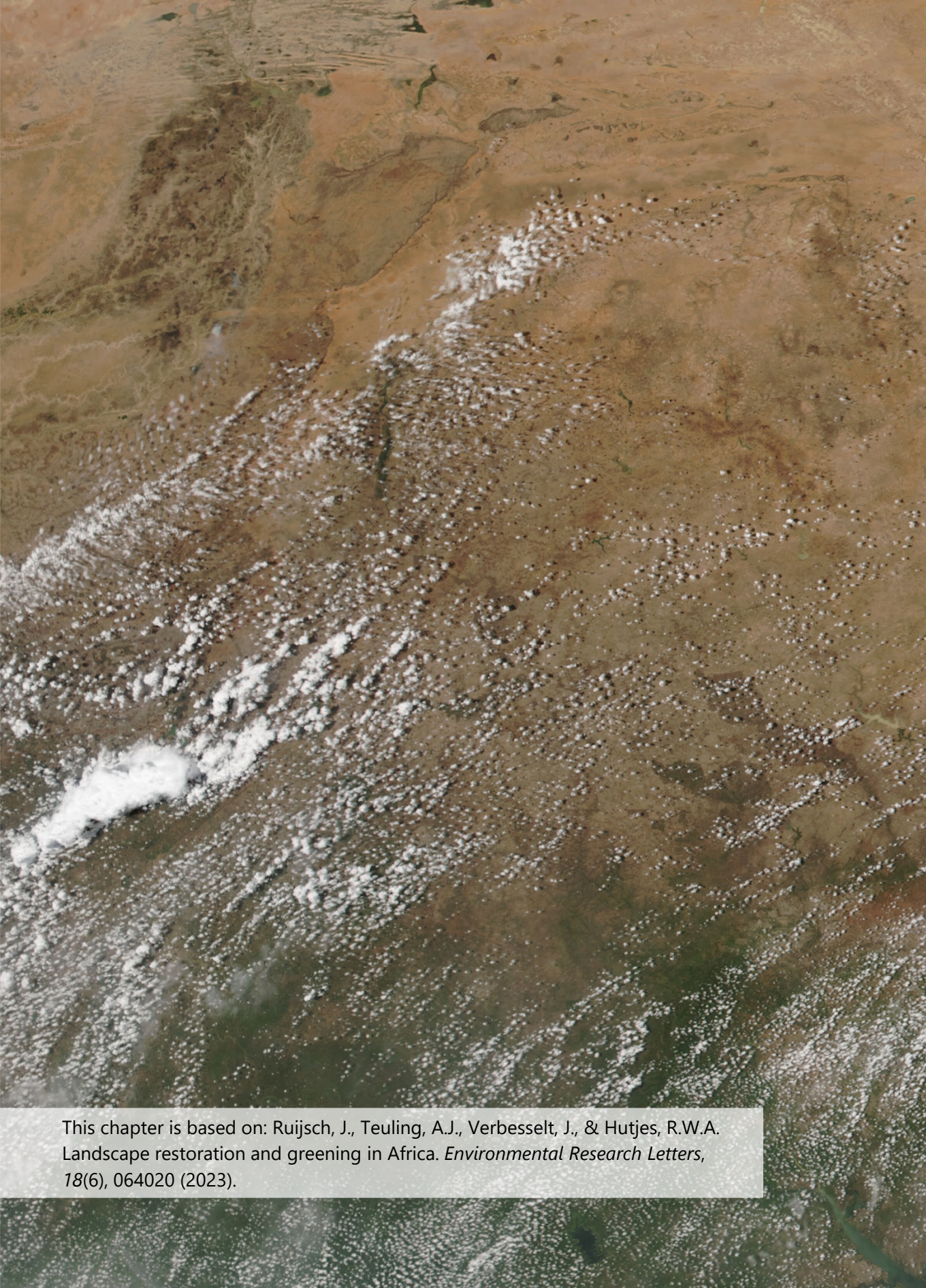
Although more and more datasets are becoming available, some relevant variables, such as evapotranspiration, are less suitable for observation with satellite data because they cannot be measured directly, but rather rely on empirical models (Amani & Shafizadeh-Moghadam, 2023). Information on changes in the energy balance at the Earth's surface either comes from ground measurements, such as eddy covariance data (Baldocchi et al., 2001), or has a coarse resolution compared to the size of restoration projects (e.g. Duveiller et al., 2018b). This means it is not possible to determine all the underlying mechanisms and non-local effects of the biophysical climate effects of restoration with satellite data only. On top of that, satellite data is not as flexible with scenario analysis, as it is only possible to observe what is already there. Atmospheric models may provide a solution to some of these problems.

Many different climate and weather models exist, ranging from global to local scales. General circulation models (GCMs) are typically used for large-scale (global or continental) and long-period (years) purposes, such as climate change projections under different emission scenarios. Large eddy simulations (LES), on the other hand, are used to simulate small-scale atmospheric phenomena such as turbulence, boundary layer growth and convection in the lower atmosphere.

An in-between option is provided by regional climate models or weather forecasting models. As suggested by its name, the Weather Research and Forecasting (WRF) model (Skamarock et al., 2019) is a numerical weather model that can be used for both weather prediction applications and research. The model numerically describes the behaviour of the atmosphere through conservation of momentum, mass, energy and moisture. WRF also includes a land-surface model, which regulates the interactions between the land and the atmosphere, including energy and moisture fluxes. Using such a regional atmospheric model can provide more information on the underlying mechanisms of biophysical effects of land restoration, which are difficult to observe with satellite data only. In addition, the WRF model can be used to simulate different scenarios of land restoration within Africa, providing information on potential biophysical climate effects of future projects that are not (yet) implemented in this region.

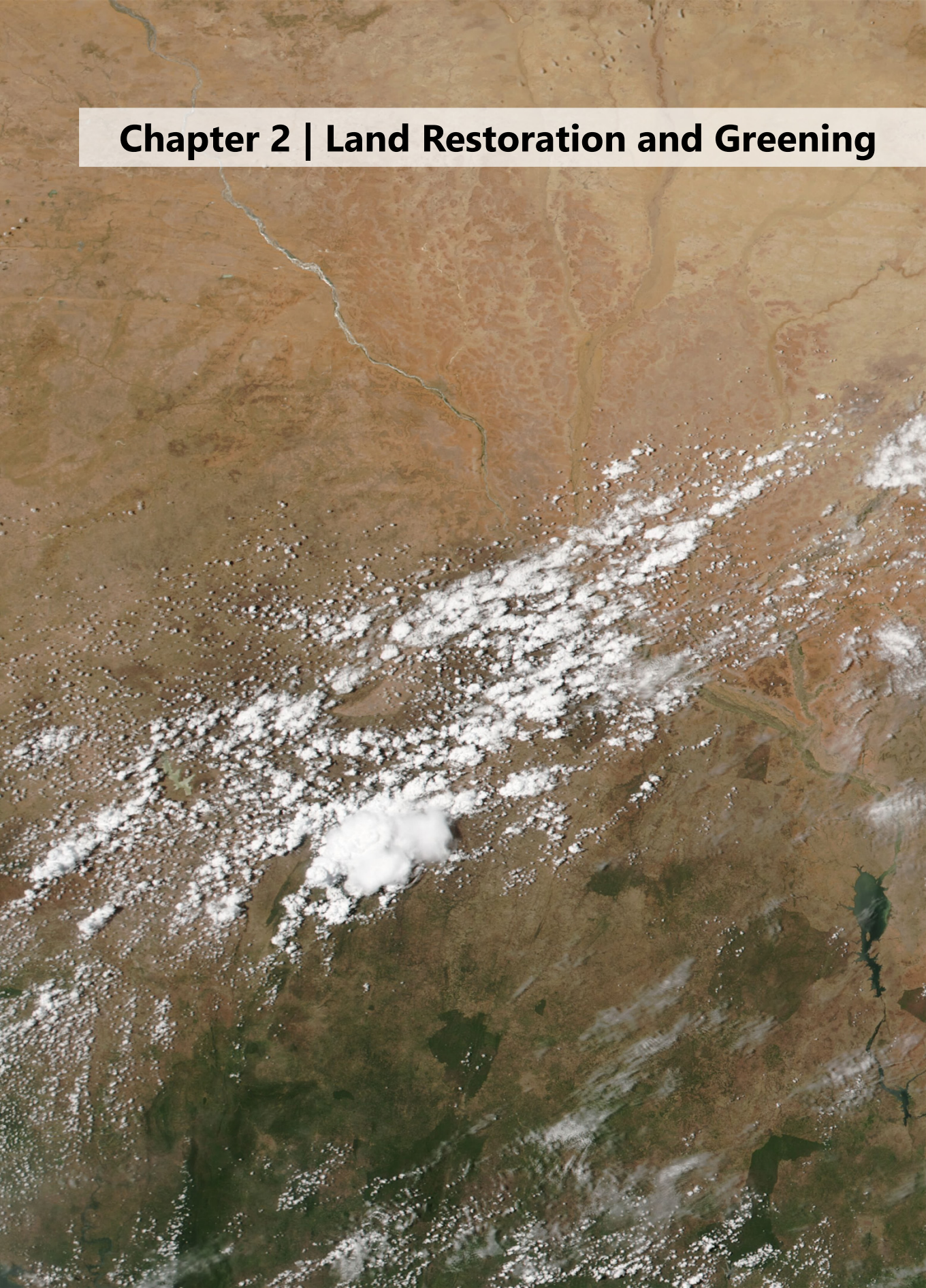
1.8 Thesis outline

After this general introduction (**Chapter 1**), each chapter in this thesis focuses on a specific research objective. In **Chapter 2**, I describe the effect of land restoration on greening in Africa based on remote sensing and the locations of restoration projects, where the spatial-context method is used to correct for climate change and variability. This is a crucial step to be able to determine the connection between land restoration and biophysical climate effects, as changes in vegetation greenness are an imperative intermediate step. In **Chapter 3**, the analysis is extended to observations of temperature and albedo. By studying the relations between vegetation and temperature compared to surrounding regions, the cooling potential of land restoration in Africa can be determined. Eddy-covariance measurements are used to provide in situ information on changes in the energy balance. **Chapter 4** zooms in on West Africa, where the effect of land restoration on cloud development is studied. Using geostationary satellite data, the relationship between vegetation and cloud formation is studied on diurnal, seasonal, and multi-year time scales. In **Chapter 5**, atmospheric modelling is used to provide more insight into the underlying land-atmosphere interactions observed with satellite data in the other chapters. In addition, I use different restoration scenarios to determine how the spatial patterns of land restoration projects impact cloud formation. In **Chapter 6**, the results of these research objectives are synthesised in combination with existing literature to provide recommendations for land restoration projects in order to achieve maximum biophysical climate benefits in the future.



This chapter is based on: Ruijsch, J., Teuling, A.J., Verbesselt, J., & Hutjes, R.W.A. Landscape restoration and greening in Africa. *Environmental Research Letters*, 18(6), 064020 (2023).

Chapter 2 | Land Restoration and Greening



Abstract | As a reaction to ongoing environmental change, many local land restoration projects have emerged that aim to prevent or reverse land degradation, combat climate change through carbon sequestration or improve the local climate. However, the contribution of these projects to the greening of Africa at larger scales is still unknown due to the absence of a (public) complete database of land restoration projects, the lack of monitoring and the low survival rate of planted vegetation. Here, we use climate independent greening time series to detect local greening hotspots in Africa. We find that 2.1% of Africa, an area of roughly 400,000 km², experiences local greening, especially in semi-arid environments. We show that various forms of sustainable land management (SLM) lead to significant local greening and demonstrate that some forms, e.g. active revegetation, are more effective than others, e.g. natural regeneration. This study, therefore, provides a first continental-scale insight in the greening potential of land restoration, which is needed for a thorough understanding of the effectiveness of SLM.

2.1 Introduction

Despite the increasing efforts to halt environmental change (Martin et al., 2021), land degradation continues to affect an estimated 1.3 to 3.2 billion people worldwide (Gibbs & Salmon, 2015; Le et al., 2016), of which the majority lives in developing countries (Barbier & Hochard, 2018). African drylands such as the Sahel are particularly vulnerable to the effects of land degradation and climate change due to water scarcity and population growth (UNCCD, 2017; Closset et al., 2018; UNCCD, 2020). Recognising these pressures we put on key ecosystems, the United Nations declared 2021 to 2030 to be the Decade of Ecosystem Restoration to support efforts in preventing global ecosystem degradation and increase awareness of the importance of restoration (UNEP, 2019). In addition, several organisations have taken the ambitious plan to restore millions of hectares of land in the coming decades by planting billions of trees in African drylands as well as other parts of the world (e.g. the Bonn Challenge, the African Forest Landscape Restoration initiative (AFR100) or the African Great Green Wall initiative (UNCCD, 2020)). Furthermore, land restoration and tree planting projects have also become a widely recognised approach to combat climate change through carbon sequestration (Shevliakova et al., 2013; IPCC, 2019; Friedlingstein et al., 2020) or by changing the biophysical properties of the land surface (Mahmood et al., 2014; Perugini et al., 2017; Spracklen et al., 2018; Piao et al., 2020). Some researchers even argue that land restoration may be one of the most effective methods for climate change mitigation (Bastin et al., 2019).

As a result, the number of land restoration projects in Africa has rapidly increased over the years (Martin et al., 2021). Monitoring these projects is often done with remote sensing products such as the Normalized Difference Vegetation Index (NDVI) (Tucker, 1979) or the Enhanced Vegetation Index (EVI), as field measurements are often time-intensive, costly and, in case of remote or large areas, practically impossible. Using these vegetation indices in combination with, for example, a before/after-control/impact type of design (Underwood, 1992; Meroni et al., 2017) has been used to estimate the changes in greenness and vegetation productivity of projects with a known location. However, the lack of a complete and publicly accessible database of land restoration projects in Africa, the considerable number of organisations that work on this (Martin et al., 2021) and the reported low survival rates of planted vegetation (Trac et al., 2007; Murekezi et al., 2013; Nunes et al., 2016; Kodikara et al., 2017), make these methods less suitable to evaluate the greening of land restoration projects and their climate change mitigation and adaptation potential on a continental scale.

On top of that, the African continent is not only affected by greening due to small-scale processes such as land restoration, but also by large-scale and long-term greening and browning trends. In the 1970s and 1980s Africa has experienced severe large-scale droughts, which are now attributed to the El Niño-Southern Oscillation (ENSO) and changes in sea surface temperature (Giannini et al., 2008; Masih et al., 2014). Contrarily,

observations over the last decades have shown an overall increasing trend in vegetation cover across Africa (Zhu et al., 2016; Piao et al., 2020), which is likely caused by an increase in global CO₂ concentration (Zhu et al., 2016), and an increase in precipitation due to changes in sea surface temperature (Giannini et al., 2003; Ouedraogo et al., 2014; Giannini, 2015; Biasutti, 2019).

Due to the co-existence of small-scale greening caused by land restoration, and this large-scale 'background' greening, simply monitoring changes in vegetation indices does not tell us the effectiveness of land restoration projects or its contribution to the greening of Africa, but rather shows the combined effect of land management and climate variability. To compensate for this effect, previous studies have used vegetation-rainfall relations (Le Hou  rou, 1984), which can partly account for background trends because it provides an indicator of vegetation or ecosystem functioning. Yet, vegetation-rainfall relationships are complex and often differ over biomes, making it less suitable to study vegetation productivity over large scales (Huxman et al., 2004; Horion et al., 2013). In addition, vegetation-rainfall relations do not consider background trends other than rainfall variability, while literature suggests that CO₂ fertilization causes roughly 70% of the observed greening (Zhu et al., 2016).

Alternatively, we can use spatial-context to separate the small-scale or 'local' greening from large-scale background trends. In this approach, it is assumed that background trends due to climate variability act on a much larger scale than a land restoration project (Hamunyela et al., 2016). For example, if the greening at a land restoration project is the result of climate variability rather than the project itself, surrounding areas will likely show a similar amount of greening as the project area. Contrastingly, if the greening is caused by the project, it is expected that the project area shows a larger amount of greening than surrounding areas. For this reason, the background trends can be removed from vegetation index time series by comparing observed greening trends with surrounding areas.

Here, we apply this spatial-context method to NDVI and EVI time series in Google Earth Engine (Gorelick et al., 2017) to: (1) create a map of local greening hotspots for Africa; (2) compare the spatial distribution of local greening to background greening and (3) compare local greening to a publicly available database of sustainable land management projects to determine the effectiveness of land restoration. Although spatial-context methods have been used before to detect deforestation (Lhermitte et al., 2011; Hamunyela et al., 2016), land degradation (Abel et al., 2019; Abel et al., 2020) or burned areas (Lhermitte et al., 2010) in forested as well as grassland areas, this is, to our knowledge, the first time that such a spatial-context method is used to detect local greening hotspots on a continental scale in Africa.

2.2 Methodology

2.2.1 Input data and study area

We used four different input variables (Table 2.1). The main input data consists of NDVI (Didan, 2021) and EVI (Huete et al., 1997) time series data (Supplementary Figure 2.1), which we used as an indicator for vegetation productivity. The main analysis is performed using NDVI and EVI data from MODIS (Didan, 2021) because it is a good compromise between spatial and temporal resolution and the readily availability of quality-controlled vegetation index composite. We used Landsat-7 data on a small sample area to explore the effects of a higher spatial resolution on our results (Supplementary Figure 2.2). Furthermore, we used a land cover (Sulla-Menashe et al., 2019) and aridity index data to provide some insight into potential causes of local greening. The aridity index (AI) is a measure of dryness and can be defined as a 30-year average fraction between precipitation and potential evapotranspiration (Cherlet et al., 2018), which we used to divide the study area into hyper-arid, semi-arid, dry subhumid and humid regions (Middleton & Thomas, 1997).

To evaluate the effect of land restoration practices on the amount of local greening, we used 434 Sustainable Land Management (SLM) projects from the WOCAT database (WOCAT, 2022) within the study area. This database contains often-used land restoration techniques, such as tree planting or assisted natural regeneration, but also techniques like sustainable agriculture and water harvesting. Here, the whole database of SLM projects is used to study the process of land restoration, meaning we used a broader definition of the term land restoration than other studies (e.g. UNCCD (UNCCD, 2017) or IUCN (IUCN, 2019)). If a single SLM project contained multiple locations, we considered it as multiple projects, resulting in 628 project locations. We categorized these projects into 11 categories and 55 subcategories based on their description, where the categories of 'revegetation' and 'natural regeneration' are highlighted in the results. We refer to the combination of all categories simply as 'sustainable land management' (SLM) (Table 2.2).

The study area consists of areas on the African continent with a median NDVI higher than 0.15 or EVI higher than 0.11, which results in similar case study boundaries for the NDVI and EVI. This way, areas with a too low vegetation cover are not considered in the calculations to prevent noisy results. The masked areas mainly consist of the Sahara Desert and constitute 36% of the African continent (Supplementary Figure 2.1).

2.2.2 Spatial-context approach

To separate background trends from the NDVI and EVI time series, we used a spatial-context approach. For each pixel, we determined the vegetation index time series over the 2001-2021 period, after which we calculated neighbourhood-averaged time series

Table 2.1 | Overview of input data.

Name	Source	Spatial resolution	Temporal resolution	Time period	Reference
NDVI	Terra MODIS Vegetation Indices (MOD13Q1.006)	250 m	16-day composites	2001-01-01 to 2022-01-01	(Didan, 2021)
	USGS Landsat-7 ETM+ Level2, Collection 2, Tier 1	30 m	16-day land surface reflectance images	2001-01-01 to 2022-01-01	USGS
EVI	Terra MODIS Vegetation Indices (MOD13Q1.006)	250 m	16-day composites	2001-01-01 to 2022-01-01	(Didan, 2021)
Land Cover	MODIS Land Cover Type (MCD12Q1)	1 km	Yearly	2001	(Sulla-Menashe et al., 2019)
Aridity Index	CRU TS4.04	0.5°	Yearly	1991 to 2029	(Spinoni et al., 2015; Harris et al., 2020)
SLM projects	WOCAT technologies	SLM Point coordinates	-	-	(WOCAT, 2022)

Table 2.2 | Description of categories of WOCAT sustainable land management projects highlighted in this study. An overview of all categories is given in Supplementary Figure 2.11.

Category	Description	Project categories included
Sustainable land management	“The use of land resources, including soils, water, animals and plants, for the production of goods to meet changing human needs, while simultaneously ensuring the long-term productive potential of these resources and the maintenance of their environmental functions” (WOCAT, 2022). WOCAT mainly focusses on preventing and reducing land degradation	All WOCAT SLM projects, e.g. runoff harvesting, alternative cooking methods, riverbank restoration, planting trees, area closure, fire management, cover crops, agroforestry and conservation agriculture.
Revegetation	Active planting of vegetation species to accelerate vegetation regrowth.	Planting (fruit) trees, shrubs and grasses, implementing vegetation strips, and projects described as restoration.
Natural regeneration	A passive method of greening, where vegetation cover is increased through natural regrowth by using, for example, area closure, grazing management or management of invasive species.	Assisted natural regeneration, combating invaders, farmer managed natural regeneration, area closure, grazing management and bush thinning.

over a square-shaped neighbourhood around the pixel. A square centre with a radius of 1000 m, corresponding to a square of 2x2 km, was not included in the mean, to reduce the influence of the original time series on the mean neighbourhood time series. Next, we subtracted the neighbourhood time series from the centre pixel time series to create 'spatially corrected' time series. Creating this spatially corrected time series for the NDVI and EVI allows us to evaluate the changes in greenness compared to surrounding areas, thus separating greening trends resulting from small-scale processes and land management from those caused by natural climate variability. In this study, we applied the spatial-context method to three neighbourhood radii of 25 km, 10 km and 5 km, corresponding to squares of 50x50 km, 20x20 km and 10x10 km, respectively. We highlight the results of the 25 km radius, which captures the effect of large land restoration efforts without crossing multiple AI classes. The results for 10 km and 5 km radii are included in the supplementary data.

2.2.3 Definition of local greening

We applied the Breaks For Additive Seasonal and Trend (BFAST) algorithm (Verbesselt, Hyndman, Newnham, et al., 2010; Verbesselt, Hyndman, Zeileis, et al., 2010; Verbesselt et al., 2012) for Google Earth Engine (Hamunyela et al., 2020) to the spatially corrected NDVI and EVI time series. BFAST decomposes the timeseries into a trend, seasonal and remainder component, by fitting a linear harmonic model to the time series. Unlike other decomposition algorithms, BFAST can detect significant changes, called breakpoints, in the components, resulting in a piecewise linear harmonic model. We applied BFAST using a seasonal harmonic model order of 3, a minimum spacing between two breakpoints of 0.15 (fraction of total time series length, i.e. 3 years) and a maximum of one breakpoint. Here, we use BFAST instead of linear regression because we expect land restoration to show a sudden change in greenness compared to surrounding areas rather than a gradual change, which BFAST can capture in the form of a breakpoint. We therefore expect the breakpoint to represent the moment a project, or another process, will start to affect vegetation cover.

We defined local NDVI/EVI greening as pixels where: (1) the BFAST algorithm detects a breakpoint in the trend of the spatially corrected NDVI/EVI time series; (2) the computed BFAST trend after the breakpoint is positive, significantly different from zero ($p=0.05$) and larger than before the breakpoint and (3) the original (centre pixel) NDVI/EVI time series shows a positive linear trend after the breakpoint (Figure 2.1a). We included this last condition, as pixels could theoretically show a greening trend compared to its surroundings, even though the pixel itself is browning. Next, we defined local greening hotspots in Africa as areas that simultaneously experience local NDVI greening and local EVI greening. By combining the NDVI and EVI, we aim to reduce noise and therefore improve the accuracy of this spatial context method.

2.2.4 Calculation of background trends

To calculate the background trends, we applied linear least squares regression to the original NDVI and EVI data between 2001 and 2021 within the study area (Figure 2.1b). We then assigned background greening to pixels that show a significant positive trend for both the NDVI and EVI ($p = 0.05$). Similarly, browning trends show a significant negative trend. Areas that have a positive NDVI trend and a negative EVI trend or vice versa, and areas without a significant trend are considered not to have a background trend.

2.2.5 Local greening of sustainable land management

Next, we used the WOCAT project database to evaluate the regreening effects of sustainable land management projects. Therefore, we used local greening instead of the often-used background greening, to reduce the effects of large-scale processes such as natural climate variability, which makes it more likely that observed greening is due to the changes in land management. Because WOCAT only contains point coordinates of projects instead of boundaries, we cannot directly calculate the amount of local greening inside the project. Instead, we computed the percentage of local greening pixels in a circle around the project's geo-tag multiple times, using a radius of 5000, 4000, 3000, 2000, 1000 and 500 m. Next, we computed for each project the percentage of greening pixels over the locations in the study area within the same country, aridity index class and land cover class as the project (Supplementary Figure 2.3). We then determined whether SLM projects cause a significant increase in local greening using the two-sided t-test for independent samples, assuming unequal variances and a significance level of 5%.

2.3 Results

2.3.1 Spatial distribution of local greening in Africa

Applying the spatial-context method (Figure 2.1a) to the African continent with a neighbourhood radius of 25 km, 2.1% of the study area (roughly 400,000 km²) shows local greening over the last two decades (Figure 2.1c). Most of these areas have a breakpoint towards the end of the study period, with peaks around 2015 and 2018, suggesting that many areas start to show an increase in greenness compared to its surroundings around these years (Figure 2.1e), although it should be noted that the used settings of the BFAST algorithm do not allow for the detection of breakpoints after 2018. We can also observe that the local greening is not evenly distributed across the continent, as a large part of the local greening can be found in the Sahel, Kenya, Tanzania, and regions in southern Africa (Supplementary Figure 2.3). Similar spatial distributions can be found for a neighbourhood radius of 10 km and 5 km and, although

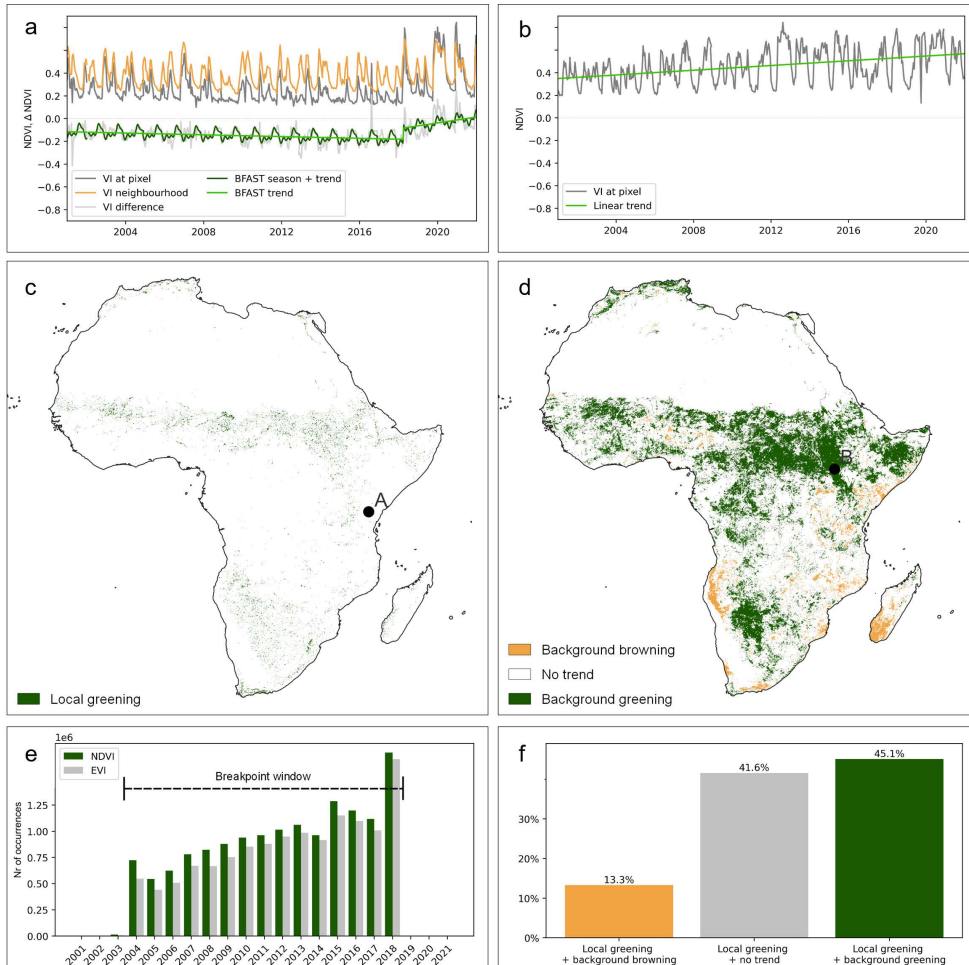


Figure 2.1 | Spatial distribution of local greening and background trends. (a) Illustration of the spatial-context method and (b) the background trends with NDVI time series (a more detailed description of these methods can be found in the methodology section and Supplementary Figure 2.7). (c) Spatial distribution of the combined NDVI and EVI local greening pixels. Point A shows the location of the timeseries in figure (a). A larger map of the spatial distribution of local greening of NDVI, EVI and combined pixels is included in Supplementary Figure 2.8-2.10. (d) Spatial distribution of the combined NDVI and EVI background trends, calculated with a linear least squares regression. Negative trends are shown as browning, positive trends as greening and non-significant trends as no trend ($p = 0.05$). Point B shows the location of the timeseries in figure (b). A larger map of the spatial distribution of EVI and NDVI background greening is included in Supplementary Figure 2.5. (e) Histogram of breakpoint year of the EVI and NDVI local greening pixels. The breakpoint window indicates the years where a breakpoint can be detected by the BFAST algorithm. (f) Distribution of background trends at the location of the combined local greening pixels.

the total area classified as local greening as well as the number of adjacent local greening pixels is smaller (Supplementary Figure 2.4). For a 10 km and 5 km radius, respectively 1.9% and 1.8% of the study area shows local greening, compared to 2.1% for a 25 km radius.

We also compared the local greening hotspots to NDVI and EVI background trends (Figure 2.1b), to provide more insight into the contributions of local greening to the greening of the African continent. Overall, a larger area shows background greening (32.4 % of the study area) than local greening (2.1% of the study area), especially in more humid areas such as the Congo Basin in central Africa (Figure 2.1d; Supplementary Figure 2.5). These areas do usually not show a breakpoint when BFAST is applied to the spatially corrected NDVI time series, suggesting that a large part of the background trends, especially in humid areas, is not caused by small-scale or abrupt processes, but by longer large-scale processes. In other, drier areas such as in Botswana and Namibia, we observe strong background greening combined with a large amount of local greening pixels, suggesting a combination of large-scale and small-scale processes. Although most local greening in the study area is located in areas that also show a background greening trend (45.1%) or no background trend (41.6%), also a considerable amount of local greening is present in areas that show a long-term browning trend (13.3%) (Figure 2.1f). The combination of local greening and background browning suggests a long-term linear browning trend, with a sudden increase in greenness, compared to surrounding areas, at the end of the time series. A similar spatial-context method can, of course, be used to detect local browning, which occurs at 1.9% of the study area (Supplementary Figure 2.6).

2.3.2 Drivers and properties of local greening hotspots

We compared local greening to an aridity and land cover classification and find that 39.1% of the local greening can be found in semi-arid regions, while these regions only cover 26% of the study area (Figure 2.2h; Supplementary Table 2.1). Here, 3.0% of the area is found to be greening compared to its neighbourhood. Humid areas, on the other hand, account for only 32.0% of the local greening, while covering more than half of the study area. This pattern is also visible in the distribution of the local greening over the land cover types, as most local greening occurs in shrublands, grasslands and savannas, but also areas classified as cropland sometimes show local greening (Figure 2.2h; Supplementary Table 2.1).

By visually interpreting high-resolution satellite imagery, we also aim to provide some more insight into potential drivers of local greening. Land restoration practices such as in Kenya, show greening between 2014 (Figure 2.2a) and 2019 (Figure 2.2b), while surrounding areas are untreated. Similar results can be found in South Africa, where local greening pixels are located roughly inside protected areas (UNEP-WCMC, 2022) (Figure 2.2f). However, also reduction in open-water surface area, such as in Lake Chad,

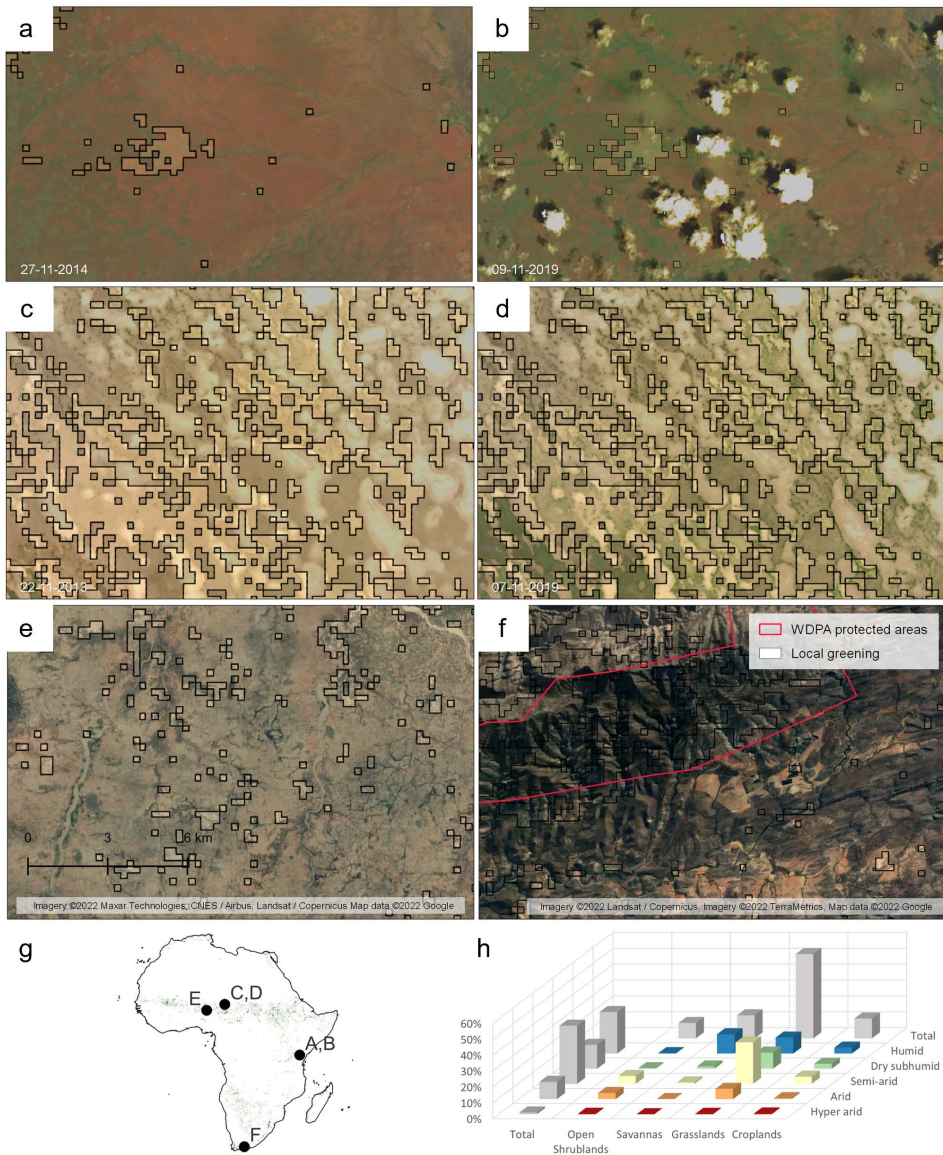


Figure 2.2 | Examples and surface properties of local greening pixels. (a, b) Local greening pixels in Kenya where land restoration is implemented. The background contains Landsat 8 imagery (Irons et al., 2012) from November 2014 (a) and November 2019 (b), which visually shows greening over time. For visualization purposes, the local greening pixels are made lighter compared to the background. (c, d) Local greening pixels in Chad along the borders of Lake Chad, showing greening due to changes in water level between 2013 (c) and 2019 (d). (e) Agriculture along riverbanks in Nigeria. (f) Local greening pixels in South-Africa, located in WDPAs protected areas (UNEP-WCMC, 2022). (g) Locations of above examples. The background shows the local greening pixels. (h) Percentage of greening pixels per land use class, aridity class and the combined land use and aridity classes (Supplementary Figure 2.3). For readability, we did not include the land use and aridity classes that contained less than 5% of the greening pixels. The complete histogram is attached in Supplementary Table 2.1.

can cause unwanted classification of local greening (Figure 2.2c,d). This is caused by the low NDVI value of water and, consequently, a local increase in NDVI when the water retreats. In addition, we observed a reasonably large amount of local greening in agricultural areas such as in the north of Nigeria (Figure 2.2c), which is also visible in the histogram (Figure 2.2h) and may result from intentional greening efforts.

2.3.3 Sustainable land management as driver of local greening

As most of the local greening can be found in semi-arid environments, most SLM projects in these regions also show generally a high percentage of local greening (Figure 2.3a). Furthermore, even though projects in more hyper-arid or humid regions show less local greening, sustainable land management projects show an overall significant increase in local greening compared to the areas with similar aridity and land cover for all distances around the project we included in this study (Figure 2.3b). Revegetation projects, including the planting of (fruit) trees, shrubs and grasses, have a significantly higher percentage of local greening in an area of 500 and 1000 m around the project's geo-tag, while the other radii show an increased, yet not significant, local greening. Especially planting trees and fruit trees seems to have a large effect (Supplementary Figure 2.11). Natural regeneration projects, such as farmer-managed natural regeneration, assisted natural regeneration or area closure, appear to have a lower effect on the amount of local greening than revegetation projects for all area sizes around the project. Yet, there is a significant increase in local greening around 5000, 4000 and 3000 m around the project. Other categories of SLM, such as water harvesting, erosion prevention or agriculture management have a more mixed effect on local greening (Supplementary Figure 2.11).

2.4 Discussion and conclusions

In this study, we used a spatial-context approach in Google Earth Engine, to separate small-scale greening caused by land restoration and sustainable land management (SLM), from background trends due to natural climate variability. With this method, we showed that 2.1% of the African continent experienced local greening over the 2001-2021 period, especially in semi-arid environments. In more humid regions, we saw less local greening, even though these regions showed significant background greening. This matches with our expectations from the spatial-context method, because changes in land management may result in a larger vegetation cover increase in sparsely vegetated semi-arid regions than in regions that are already densely vegetated. In humid areas, it is less likely that small-scale processes result in such a large increase in vegetation cover that it would be detected as a breakpoint in the NDVI time series.

In addition, our results also suggest that even though SLM as a whole has a positive effect on the amount of local greening, revegetation and tree planting appear to be more

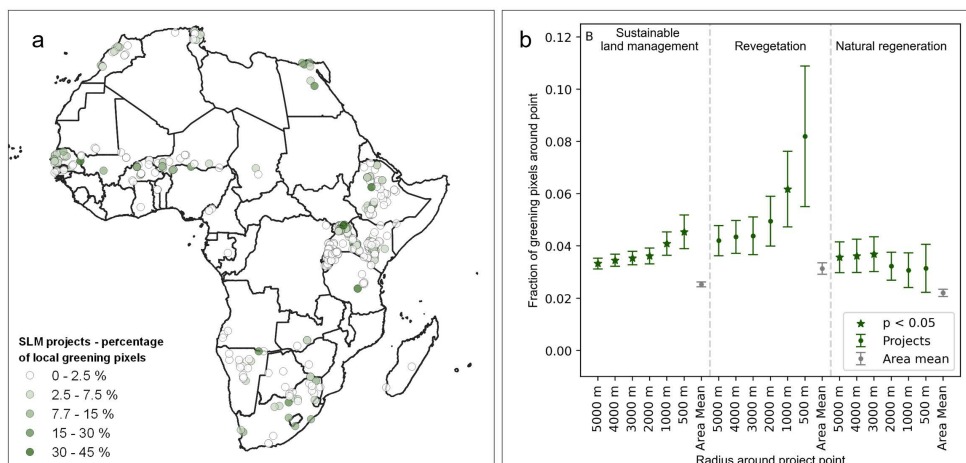


Figure 2.3 | Evaluation of local greening due to sustainable land management (SLM). (a) Location of WOCAT Sustainable Land Management projects. The shade of the colour indicates the percentage of greening pixels inside an area of 2000 m around the point and (b) mean and standard error of the percentage of local greening pixels in areas with different sizes around all sustainable land management projects, revegetation projects and natural regeneration projects. Significant differences with areas with the same land use type, aridity class and countries are marked with a star ($p = 0.05$). The Sustainable Land Management column consists of all projects in the database. The Revegetation and Natural Regeneration columns contain a subset. Projects in Cape Verde and areas with a median NDVI lower than 0.15 are not shown, because they fall outside the study area of the NDVI spatial-context method. Local greening effects of the other subcategories of sustainable land management are visualized in Supplementary Figure 2.11.

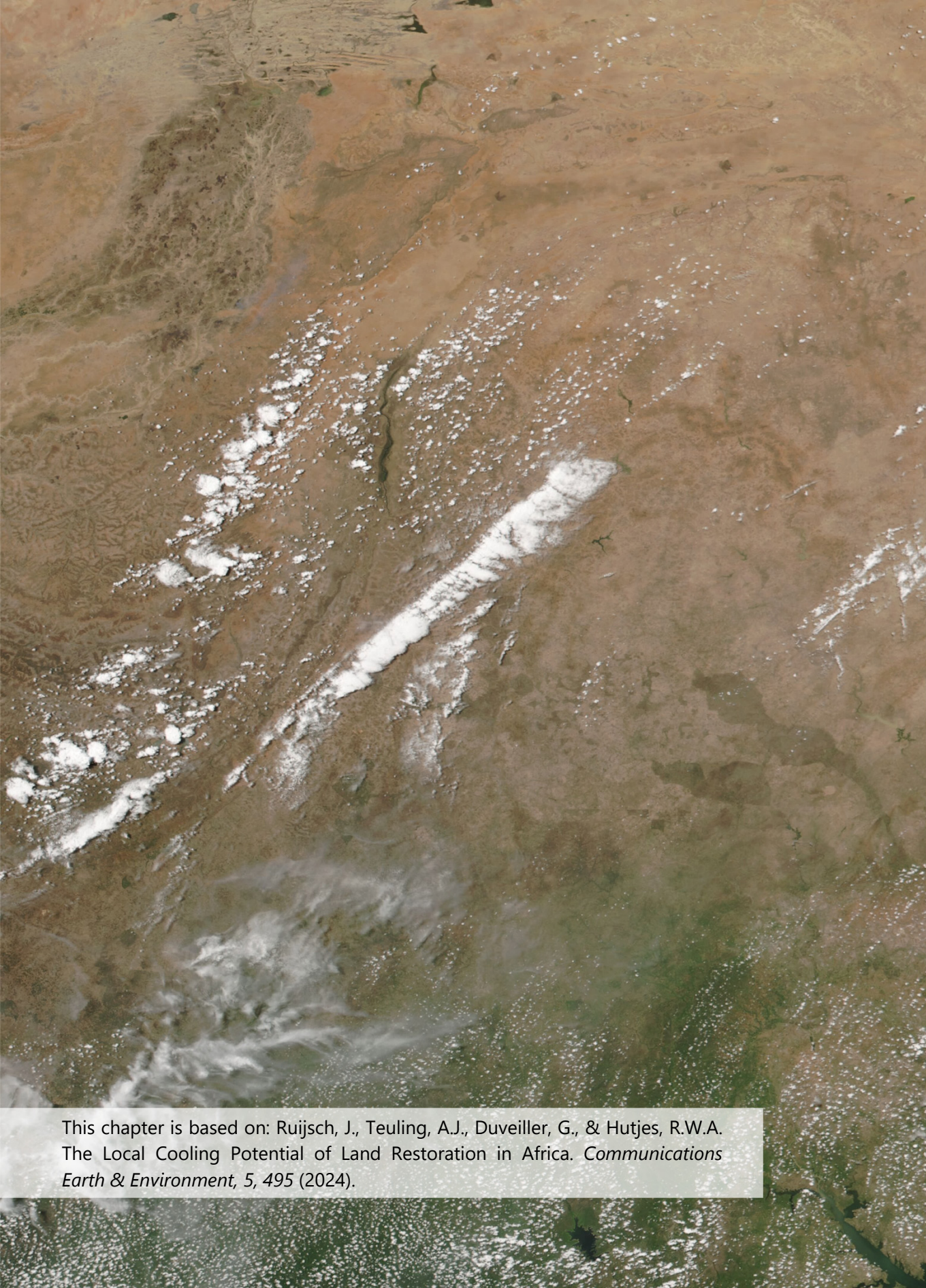
effective than natural regeneration over smaller areas. Natural regeneration does, however, show a significant increase in local greening pixels around a larger area than active revegetation. This coincides with other studies, that found a faster recovery of highly degraded land due to active restoration practices such as tree planting compared to more passive methods (Zahawi et al., 2014; Toledo-Aceves et al., 2021). On the other hand, natural regeneration is, although slower, often much cheaper (Prach & del Moral, 2015) and can therefore result in the restoration of much larger areas, with a more natural species composition (Bechara et al., 2016) if enough time is available. Therefore, natural regeneration projects may prove to be more effective once a longer study period is available. In addition, we want to emphasise that greening is often not the only goal of SLM and land restoration projects (Martin et al., 2021), as people also implement land restoration for biodiversity conservation, income generation, legislation or cultural reasons (Brancalion & Holl, 2020). A lack of local greening found for some projects in this study does, therefore, not necessarily mean that the SLM project is not at all effective or failed, as greening may not have been the main goal of the project.

Yet, several uncertainties should be kept in mind when interpreting the spatial-context approach. As we defined local greening as a sudden increase greenness compared to

surrounding areas, it does not only show changes in land restoration, but every type of small-scale greening, including changes in water level or agriculture. This calls for further development of the spatial-context method such that these different causes can be split, allowing for the evaluation of land restoration only. In addition, we evaluated the SLM projects based on a circle around a point coordinate. An exact size and boundary of each project would result in a more accurate evaluation. Furthermore, the moderate spatial resolution (250m) of MODIS limits the detection of small SLM projects and spatial heterogeneity within these projects. Because 7% of the projects within the WOCAT database reported a size smaller than the spatial resolution of MODIS, there lies great potential in high-resolution satellite imagery or microwave and LiDAR observations, which can detect vegetation optical depth, forest structure or even individual trees and shrubs outside forested areas (Brandt et al., 2017; Tang et al., 2019; Brandt et al., 2020). Unfortunately, higher-resolution imagery usually comes with a lower temporal resolution or shorter data range, which limited their use in this study. In addition, applying the spatial-context method to higher-resolution Landsat-7 data showed a similar pattern of local greening and smaller areas of local greening were detected, probably caused by the lower temporal resolution of Landsat-7, suggesting that this data will not result in a more sensitive detection of local greening. Similarly, the spatial-context method is unable to detect greening over areas larger than the used neighbourhood (approximately 2500 km²), due to uniform greening of the neighbourhood. Fortunately, only 4% of the SLM projects reported to have a size larger than 2500 km², although it should be noted that 38% of the projects did not report any project size and oftentimes it is not clear whether this is the actual size of the project or of the region in which it is implemented. Finally, studying seasonal changes of greenness due to land restoration more in depth may provide useful information for policymakers when implementing land restoration projects.

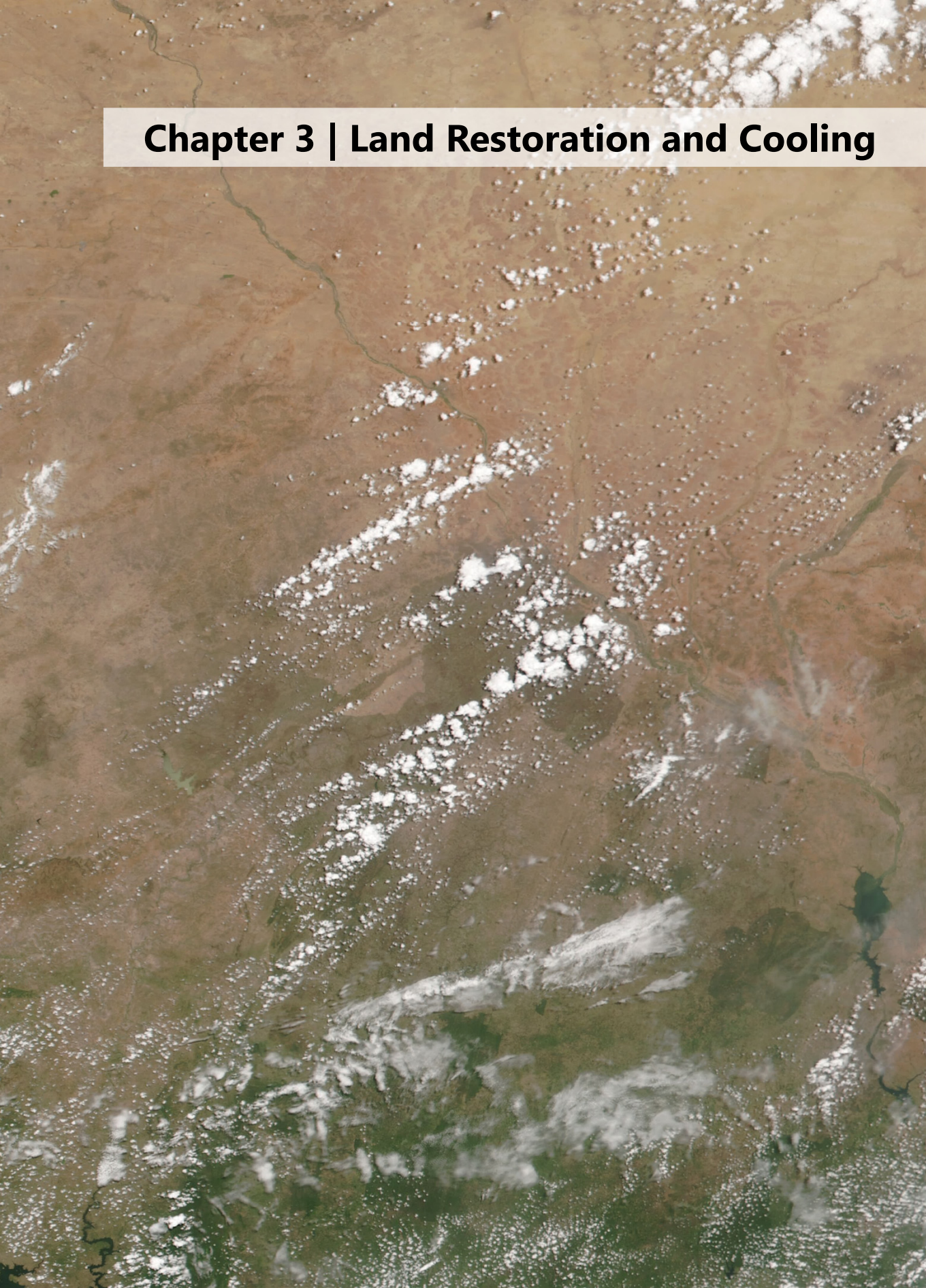
These days, tree planting and land restoration projects are seen as an effective method for climate change mitigation, and are therefore widely included in climate change policy proposals, resulting in ambitious tree planting projects across the world (Bastin et al., 2019; Fagan et al., 2020). However, if not implemented correctly, land restoration can also have severe negative consequences on the environment (Holl & Brancalion, 2020), such as a decrease in biodiversity through monocultures or non-native vegetation (Veldman et al., 2015; Veldman et al., 2019), changes in water availability through increased evapotranspiration (Feng et al., 2016; Filoso et al., 2017; Hoek van Dijke et al., 2022), or the destruction of native ecosystems through displacement of land use (Meyfroidt et al., 2010). The increasing interest in land restoration thus asks for more research on the cost and benefits of land restoration (Cooke et al., 2019; Dudley et al., 2020). However, due to the co-existence of small-scale greening and background trends, in combination with the lack of an available dataset of land restoration projects, it is not known to what extent land restoration actually causes greening. In this study, we provided insight into the hotspots of local greening, as well as an objective meta-

evaluation of different types of SLM. We show that implementing SLM projects in semi-arid areas can indeed result in local greening. If the goal of projects is to increase vegetation cover, active revegetation may provide good results on smaller scales, while natural regeneration has the potential to regreen larger areas. Policymakers should therefore carefully match the project approach to its goals, keeping all positive as well as negative consequences of vegetation changes in mind. Yet, even though this research provided a useful monitoring and evaluation tool for land restoration projects, we want to stress the importance of documenting and monitoring the project's implementation, which would improve the accuracy of the evaluation. We therefore argue that more research should focus on the creation of a complete and open-access database of land restoration projects, before large-scale implementation does more harm than good.



This chapter is based on: Ruijsch, J., Teuling, A.J., Duveiller, G., & Hutjes, R.W.A. The Local Cooling Potential of Land Restoration in Africa. *Communications Earth & Environment*, 5, 495 (2024).

Chapter 3 | Land Restoration and Cooling



Abstract | Land restoration is becoming increasingly popular as a climate change mitigation and adaptation measure. It is suggested that resulting vegetation changes can impact the local surface temperature through biophysical processes such as albedo warming and evaporative cooling. Yet, the potential effect of land restoration on the local surface temperature in Africa remains uncertain. In this study, we use Terra MODIS time series of vegetation, albedo, and land surface temperature to determine vegetation-temperature relationships at a continental scale. We show that vegetation-albedo and vegetation-temperature relationships do not only vary spatially across Africa but also temporally over different time scales, with strong cooling effects in semi-arid environments. Furthermore, we predict that land restoration can decrease local land surface temperature by around 0.2 Kelvin on average. This study gives a more detailed insight into where future land restoration provides additional positive climate impacts, and where land restoration may instead warm the local environment.

3.1 Introduction

Land restoration practices, such as active reforestation, natural regeneration, and water harvesting, have been proposed as a solution to a wide range of environmental problems across the world (Brancalion & Holl, 2020). They have the potential to decrease and reverse land degradation, conserve biodiversity, and increase the livelihood of the local population through ecosystem services and income provision (Holl, 2020). On top of that, planting trees is currently seen as one of the more realistic ways to sequester carbon, thereby compensating partly for the residual emissions that are hardest to decarbonize (Shevliakova et al., 2013; Mahmood et al., 2014; Bastin et al., 2019; Friedlingstein et al., 2020). Consequently, land restoration efforts are becoming increasingly popular (Martin et al., 2021), including ambitious initiatives to plant millions of trees across the globe (e.g., the Bonn Challenge, the AFR100 project, and the Trillion Trees initiative). The African continent, even though having one of the lowest per-capita contributions to greenhouse gas emissions (Dhakai et al., 2022), is already experiencing an increase in temperature (Ranasinghe et al., 2021) and heatwave frequency (Engdaw et al., 2022) that is higher than the global average. This has resulted in biodiversity loss, droughts, reduced food production and economic growth, and loss of lives (Trisos et al., 2022).

Land restoration may, in addition to global mitigation strategies, reduce the climate change impact in Africa (Williams et al., 2021). Although it can encompass a wide range of measures and is implemented with different goals, land restoration often entails an increase in the greening of the surface (Ruijsch, Teuling, et al., 2023) and can, therefore, directly affect the local climate through changes in the biophysical properties of the Earth's surface (e.g. albedo, evapotranspiration, and surface roughness). This way, land restoration projects have the potential to change the local and regional temperature (Castelli et al., 2019; Piao et al., 2020) and create a more comfortable living environment for the local population (Wolff et al., 2018). Yet even though the scientific debate on how vegetation affects the regional climate started over two hundred years ago (Bennett & Barton, 2018), and that the biogeophysical processes may sometimes be stronger than the biogeochemical ones (Breil et al., 2023), the biogeophysical processes and their related feedbacks have received much less attention.

When studying these vegetation-temperature relationships, it is, however, important to make a distinction between air temperature, which describes the ambient temperature of the air, usually measured at 2 m above a standard grass cover by weather stations; and land surface temperature, which is the radiative skin temperature of the Earth's surface as often measured by satellites. Although air temperature is an important variable because it can be directly felt by humans (Wolff et al., 2018), mixing effects of surface fluxes in the boundary layer, in combination with limited data availability, make a continental analysis of vegetation-temperature interactions in Africa challenging. Land surface temperature, on the other hand, is available on a continuous grid

throughout Africa by remote sensing data (e.g. MODIS land surface temperature (Wan et al., 2021)). In addition, although having a larger variation than the air temperature, the surface temperature is closely coupled to the Earth's energy balance and biophysical effects of vegetation changes, which makes it an ideal variable to study vegetation-temperature interactions.

Vegetation can directly affect the local surface temperature through multiple biophysical processes that amplify or counteract each other. For example, since highly vegetated areas are usually less reflective than bare land, the surface albedo in the visible range of the spectrum decreases with increasing vegetation cover. This results in a lower surface reflectance and a higher amount of net available energy, which therefore contributes towards the warming of the surface and an increase in surface temperature (Betts, 2000; Bonan, 2008). This effect is often referred to as albedo warming. At the same time, an increased vegetation cover will result in a higher latent heat flux through evapotranspiration, contributing to the cooling of the Earth's surface by a decrease in sensible heat flux (Bonan, 2016; Zeng et al., 2017). This process is often called evaporative cooling. Unlike albedo warming, which warms the Earth as a system, the cooling due to evapotranspiration is local, and the heat is released upon condensation elsewhere. In addition, an increased surface roughness reduces aerodynamic resistance and therefore increases turbulent energy flux dissipation, which also contributes to surface cooling (Chen, Li, et al., 2020; Feldman et al., 2022).

Next to albedo warming and evaporative cooling, vegetation can also have more indirect effects on the surface temperature. The increased evapotranspiration in combination with higher surface roughness can increase atmospheric water vapour, causing an increased cloud cover and planetary albedo. This reduces incoming shortwave radiation and surface temperature (Teuling et al., 2017a; Spracklen et al., 2018). At the same time, clouds can increase longwave radiation entrapment and, therefore, the surface temperature. Whether increases in vegetation cover, and thus land restoration, result in a net surface warming or cooling depends on the relative importance of these direct and indirect processes (Zeng et al., 2017; Piao et al., 2020), which appear to depend strongly on latitude (Li et al., 2015b; Perugini et al., 2017), background climate (Pitman et al., 2011), scale (Spracklen et al., 2018) and atmospheric conditions (Teuling et al., 2010). This makes it difficult to transfer results found in specific case studies to other areas. In addition, modelling studies also suggest non-local effects of vegetation cover on the surface temperature due to changes in large-scale circulation and atmospheric feedbacks that are difficult to capture with observational data (Winckler et al., 2019; Chen, Ge, et al., 2022).

As a result, it is largely unknown if land restoration, by increasing vegetation, can be used to reduce local surface temperatures in Africa through biophysical processes, and how large this temperature reduction is. To reduce this knowledge gap, previous studies have investigated the relationships between vegetation cover change and

temperature on continental or global scales using modelling as well as remote sensing data (Perugini et al., 2017). However, many of these studies specifically focus on forests using idealized afforestation scenarios or potential tree cover maps (Duveiller et al., 2018b; Bastin et al., 2019; Prevedello et al., 2019; Hoek van Dijke et al., 2022), while large parts of dryland Africa consist of savannas and grasslands. In these regions, land restoration-induced vegetation changes do not, and should not (Parr et al., 2024), necessarily result in a change in forest cover but rather increase the vegetation greenness by converting, for example, bare land to grasslands (Ruijsch, Teuling, et al., 2023). As these dryland areas may experience lower evaporative cooling due to their aridity, there is a need to include changes in dryland vegetation cover in these analyses. On top of that, little research has been done to predict the amount of local surface cooling that can be achieved through potential future land restoration practices of non-forested areas.

In this study, we aim to determine the direct local biophysical surface cooling effects of land restoration across Africa. Although land restoration is a broad concept and not all projects aim to increase vegetation cover, we follow the definition of the UNCCD (UNCCD, 2022), which includes both natural area conservation and sustainable land management of agricultural areas. For this reason, we expect restored areas generally to be associated with more natural ecosystems and a greener surface, including increases in grasslands or shrublands. In addition, we expect restoration-induced surface temperature changes mainly to be caused by changes in vegetation cover. To this end, we study the effect of increased vegetation greenness on the local surface temperature across the African continent. We apply a spatial-context method (Lhermitte et al., 2010; Hamunyela et al., 2016; Ruijsch, Teuling, et al., 2023) to time series of Normalized Difference Vegetation Index (NDVI) and Land Surface Temperature (LST) obtained from the Moderate-resolution Imaging Spectroradiometer (MODIS) on board the Terra platform, resulting in spatially-corrected time series of these variables. In this method, we compare the time series at a given point with the average values of its surroundings. By doing so, we limit the effect of the natural climate variability, and we can thus demonstrate whether a pixel that is greener than its surroundings is also cooler. We also study the relationship between NDVI and white-sky albedo (WSA), as the albedo is an emergent property of the underlying vegetation, and it is also a driver of surface temperature. Combined with eddy-covariance data from six measurement sites, this allows us to explore relationships amongst the variables (NDVI-LST and NDVI-WSA) at both continental and case study scales for different aridity zones and land cover types. In addition, we use a data-driven approach to predict the direct local biophysical surface cooling or warming that could be achieved following greening due to large-scale land restoration in Africa. We recognize that not all small-scale greening is induced by land restoration (Ruijsch, Teuling, et al., 2023), but we believe that by studying these vegetation-temperature relationships, we provide high-resolution information across multiple aridity zones on where land restoration projects

can expect local biophysical surface cooling, and where they instead result in warming. This can guide policymakers in the design of future land restoration projects across Africa.

3.2 Methodology

3.2.1 Input data and pre-processing

In this study, we used five main datasets. The calculations were mostly done in Google Earth Engine (Gorelick et al., 2017). To detect changes in vegetation cover, we used Normalized Difference Vegetation Index (NDVI) data from the Terra Moderate Resolution Imaging Spectroradiometer (MODIS) Vegetation Indices Collection 6 dataset (MOD13Q1.061) (Didan, 2021) (Supplementary Figure 3.1a). This dataset contains 16-day maximum value composites of NDVI at a 250 m resolution. The images were atmospherically corrected and masked for water, clouds, aerosols, and cloud shadows, using the provided quality indicators. For this analysis, images between 2001/01/01 and 2023/01/01 on the African continent were used. Although the NDVI dataset has a 250 m resolution, we performed the analysis on a 1 km spatial resolution to match the land surface temperature data (using nearest-neighbour resampling to ensure fast computation). In addition, we masked areas with a median NDVI lower than 0.15, because of their low or absent vegetation cover. The masked areas are mostly located in the Sahara Desert and account for 36% of the African continent. It should be noted that this threshold is calculated on a 1 km spatial resolution, including small regions of high vegetation cover in the desert areas.

We studied the land surface albedo from the Terra and Aqua MODIS Albedo dataset (MCD43A3.006) (Schaaf & Wang, 2015), using white-sky (bi-hemispherical) albedo (WSA) (Supplementary Figure 3.1c). The data is available on a daily time scale representing the 16 days around the central daily value. To match the NDVI data, we sampled the WSA data at the centre day of the NDVI 16-day periods generating 16-day WSA data. The main analysis was performed using the shortwave broadband range albedo (0.3-5.0 μm), containing both visible and near-infrared radiation, but a comparison to the visible broadband albedo (0.3-0.7 μm) and near-infrared broadband albedo (0.7-5.0 μm) is included in Supplementary Figure 3.2. Note that the near-infrared spectral range of 0.7-5.0 μm is larger than the commonly used range and technically also contains shortwave-infrared. Although the WSA has a 500 m spatial resolution, calculations were done at a 1000 m resolution to match the LST data (using nearest-neighbour resampling). Again, areas with a median NDVI lower than 0.15 were masked.

Changes in surface temperature were detected using Land Surface Temperature (LST) data from the Terra MODIS Land Surface Temperature and Emissivity dataset

(MOD11A1.061) (Wan et al., 2021) (Supplementary Figure 3.1b), containing average LST data on a daily time step and a 1 km spatial resolution at an overpass time of 10:30 a.m. We used daytime land surface temperature values because we expected the effects of vegetation changes to be higher during the daytime. Although Aqua MODIS data (MYD11A1.061) has an overpass time of 1:30 p.m., which is closer to the expected highest daily temperature, we used Terra MODIS in this study due to the longer data availability. However, we explored the results of the different overpass times of the sensors in Supplementary Figure 3.3. In addition, we included a sensitivity analysis of the results in the used LST algorithm (i.e., MOD11A1.061 vs. MOD21A1.061) in Supplementary Figure 3.4. Both datasets showed similar spatial patterns on the continental scale. To match the temporal resolution of the NDVI data, the LST was downsampled to a 16-day temporal resolution by taking the median LST value over the 16-day period of the NDVI data, to represent the whole 16-day period. Supplementary Figure 3.5 and 3.6 investigate different LST downscaling methods, showing variation in correlation strength but similar spatial patterns. Again, the areas with a median NDVI lower than 0.15 were masked.

Land cover data was retrieved from the MODIS Land Cover Type Collection 6 dataset (MCD12Q1), created using a supervised classification of the Terra MODIS and Aqua reflectance data (Sulla-Menashe et al., 2019) (Supplementary Figure 3.1f). For this study, we used data from 2001 at a 500 m spatial resolution, representing the original land use at the start of the study period.

The aridity index (*AI*) (Cherlet et al., 2018) can be defined as the thirty-year average fraction of precipitation and potential evapotranspiration. We used Aridity Index data from Zomer et al. (2022), calculated over the 1970-2000 period on a 30-arcsecond resolution (Supplementary Figure 3.1e). We then defined hyper-arid, arid, semi-arid, dry subhumid and humid areas as having aridity index values of: $AI < 0.05$, $0.05 \leq AI \leq 0.2$, $0.2 \leq AI \leq 0.5$, $0.5 \leq AI \leq 0.65$ and $AI > 0.65$, respectively (Middleton & Thomas, 1997).

3.2.2 Spatial-context approach

Changes in WSA and LST are not only caused by changes in NDVI but also by large-scale background trends such as natural climate variability and global climate change. We corrected for these background trends using a spatial-context approach (Lhermitte et al., 2010; Hamunyela et al., 2016; Ruijsch, Teuling, et al., 2023). In this approach, we assumed that natural climate variability acts on a larger scale than land restoration processes. Therefore, we could remove the background trend from a time series by subtracting the time series average over a neighbourhood around a pixel, from the original time series. We called the resulting time series the spatially corrected time series (Supplementary Figure 3.7). The neighbourhood is square-shaped with a radius of 25 km, corresponding to an area of 50 by 50 km. The centre of the neighbourhood

with a radius of 1 km was not included in the neighbourhood average. We applied this method to each pixel in the study area, resulting in spatially-corrected NDVI, WSA and LST time series. Using this approach, we could thus determine to what extent areas that are greener than surrounding areas are also cooler or warmer than surrounding areas. The size was based on Ruijsch, Teuling, et al. (2023) and is a compromise between a large area and remaining within similar aridity areas. A sensitivity analysis of the used neighbourhood size is included in Supplementary Figure 3.8, showing lower correlations for smaller neighbourhood areas. A comparison of the corrected and uncorrected time series, which include large-scale natural variability, is included in Supplementary Figure 3.9 and 3.10.

3.2.3 BFAST algorithm and breakpoints

Sometimes, land restoration can cause a detectable change in the ongoing trend of NDVI, WSA and LST time series. In addition, spatially corrected time series contain changes due to both seasonality and trend components. Simple linear regression does, therefore, not provide sufficient information. To this end, we applied the Breaks for Additive Seasonal and Trends (BFAST) algorithm (Verbesselt, Hyndman, Newnham, et al., 2010; Verbesselt, Hyndman, Zeileis, et al., 2010; Verbesselt et al., 2012) in Google Earth Engine (Hamunyela et al., 2020) (Supplementary Figure 3.7). This algorithm separates a time series into a seasonality, trend and remainder component and can detect significant changes in the trend and seasonal component (i.e., breakpoints). We applied the BFAST algorithm to the spatially corrected NDVI, WSA and LST time series. We used the BFAST algorithm on each pixel in the study area with a seasonal harmonic model order of 3, the maximum number of breakpoints to 1 and a minimum spacing between two breakpoints to 0.15, which is the fraction of the total time series length (i.e., 3 years). These settings were chosen to match the vegetation changes after land restoration (by including breakpoints) while limiting computation time (by limiting the number of breakpoints and seasonal harmonic model order) (Ruijsch, Teuling, et al., 2023).

3.2.4 Correlations between NDVI, Albedo and LST

To provide insight into the relationships between NDVI, WSA and LST, we calculated the Pearson correlation coefficient between spatially-corrected NDVI and spatially-corrected WSA, as well as between spatially-corrected NDVI and spatially-corrected LST (results for the Spearman's Rank Correlation are included in Supplementary Figure 3.11 to study nonlinear relations). We defined statistically significant values as having a p-value lower than 0.05. First, we compared for each pixel the 16-day average spatially corrected NDVI, WSA and LST, resulting in two correlation values over time for each pixel in the study area. This way, we can visualize spatial patterns in correlations. To distinguish how different time scales contribute to this correlation, we

also calculated the correlation values for the seasonal and trend components of these 16-day time series. Next, we calculated the 20-year average spatially corrected NDVI, WSA and LST, after which we calculated the correlations over the whole study area. In addition, we compared the timing of breakpoints in the trend component as calculated by the BFAST algorithm. This allowed us to determine whether changes in NDVI directly result in changes in WSA and LST, or if there is a delay. Finally, we compared the found correlations with aridity index and land cover values to gain more insight into what causes spatial variations.

3.2.5 Eddy-covariance measurements

We used eddy-covariance measurements across Africa to provide more field-measured insights into the underlying relations of the remotely sensed data. The measurements are obtained from six stations in different aridity zones from the FLUXNET database in Sudan (Ardö et al., 2008), Senegal (Tagesson et al., 2015), South-Africa (Archibald et al., 2009), Zambia (Merbold et al., 2009), Congo-Brazzaville (Merbold et al., 2009) and Ghana (Chiti et al., 2010). Detailed information on each station is available in Supplementary Table 3.1. The hourly sensible heat flux (H), latent heat flux (LE) and incoming shortwave radiation (SW_{in}) are matched to the MODIS data by taking the average value over each 16-day period. Only daytime values are used. In addition, because a comparison to surrounding areas is not possible with the EC measurements, we compare H , LE and SW_{in} to uncorrected (i.e., not spatially-corrected) MODIS data. Due to limited data availability, we used the mean NDVI, LST and WSA of an area of 10 km around the stations Congo-Brazzaville and Ghana. For the other stations, we used the data from the specific grid cell corresponding to the station location.

3.2.6 Sustainable land management projects

Next, we compared the results to existing land restoration projects to determine how land restoration affects local surface temperatures. To this end, we used 434 Sustainable Land Management (SLM) projects in Africa from the World Overview of Conservation Approaches and Technologies (WOCAT) (WOCAT, 2022), downloaded from the Food and Agricultural Organisation of the United Nations (FAO) database. This dataset contains point locations with the locations of sustainable land management projects, ranging from tree planting to area closure and sustainable agriculture. As with the NDVI, we removed projects in areas with an NDVI lower than 0.15. Furthermore, as some projects consist of multiple locations, we split the projects into individual points, resulting in 628 project locations (Supplementary Figure 3.1d). In addition, since the projects only contain point coordinates, we created a buffer area around each project point with a radius of 2000 m. For each of these buffer areas, we calculated the mean NDVI, WSA and LST to determine the NDVI-WSA and NDVI-LST relationship at sustainable land management projects in Africa. In addition, we calculated the actual

changes in LST and WSA at the project locations, defined as the difference in trend component between the end and the beginning of the study period.

3.2.7 Predicting local biophysical cooling/warming due to land restoration

As a final step, we predicted the amount of local biophysical cooling or warming that can be achieved due to large-scale land restoration in Africa in two steps: (1) we calculated the potential NDVI that can be achieved due to land restoration and (2) we predicted the local surface temperature change of the NDVI increase using the relationships between NDVI and LST determined with the methods above.

As the maximum NDVI obtainable by land restoration depends on environmental conditions, we first predicted the NDVI that can potentially be achieved from land restoration in Africa, where we assumed that the potential NDVI is limited by the aridity index (Zomer et al., 2022), land surface temperature (MOD11A1.061) (Wan et al., 2021), elevation, slope, aspect (SRTM90_V4) (Reuter et al., 2007), soil fertility (Hengl et al., 2021) and water table depth (Fan et al., 2013; Fan et al., 2017). We thus considered only environmental and climatological constraints to vegetation rather than socio-economic constraints. We determined the relationship between NDVI and these variables based on 5000 random samples in the study area. After filtering for areas that are irrigated (Meier et al., 2018) or have a median NDVI lower than 0.15 (as the NDVI may be higher than can be expected based on natural conditions, or the points lay outside the study area), we divided the samples randomly into a training set (1840 samples) and a validation set (1839 samples). We used the training set to train a quantile regression forest (Meinshausen & Ridgeway, 2006) with 50 trees and 3 variables per tree. This was decided based on performance (visual inspection of the created map) and computation time. Quantile random forest fits the data to a percentile, in this case the 100-percentile, rather than the mean, representing the potential NDVI under the given environmental conditions (Roebroek et al., 2023). We subtracted this median NDVI from the potential NDVI to create a map of potential NDVI increase (Δ NDVI) due to land restoration. If the predicted potential NDVI is lower than the current NDVI, the value was not changed. An evaluation of the random forest model is included in Supplementary Figure 3.12, suggesting aridity to be the most important variable in predicting maximum NDVI.

To calculate the potential LST changes (Δ LST) from this Δ NDVI, we predicted the Δ LST across Africa using observed values of Δ LST and Δ NDVI and a random forest regression (Breiman, 2001). To this end, we sampled the observed maximum change in the NDVI trend component over the study period of the spatially corrected time series, as well as the related change in the LST trend component, at 3000 random points in each land cover class in the study area. We used the trend component instead of the 16-day component because we were interested in long-term changes in NDVI instead of the seasonal variability. Next, we filtered out random points with a median NDVI lower than

0.15. Using these methods, we created a training set (37518 samples) and a validation set (5000 samples). The training set was used to train a random forest regression with 100 trees and 5 variables per tree, based on performance (highest correlation between observations and predicted values of the validation data set) and computation time. As predicting variables, we used the aridity index, land cover, median NDVI, median LST, median WSA (shortwave, visible and near-infrared), the NDVI-LST correlation of the trend component, latitude, longitude and altitude (Reuter et al., 2007) as described in the input data. To then predict the potential LST change (Δ LST) related to land restoration, we ran the trained random forest model with the potential NDVI change (Δ NDVI) as input instead of the observed NDVI change. An evaluation of the random forest model is included in Supplementary Figure 3.13, showing an r^2 value of 0.83 and 0.53 for the training and validation data, respectively. The most important variables are the change in NDVI and the NDVI-LST correlation.

3.3 Results

3.3.1 Vegetation, albedo and surface temperature relationships across time scales

In order to reconcile previous studies, we analyse the vegetation-temperature relationships at three different time scales. On a 16-day time scale (i.e., the original time scale of the input data), 31% of the study area shows a significantly negative correlation between the spatially-corrected Normalized Difference Vegetation Index (NDVI) and spatially-corrected shortwave white-sky albedo (WSA). Even though there is small-scale variability in correlations, we see clear large-scale patterns, with negative NDVI-WSA correlations mainly in southern Africa and the Sahel area (Figure 3.1a). This suggests that these areas experience a decrease in WSA (darker surface) compared to surrounding areas if the NDVI increases (more vegetation) compared to surrounding areas. Positive correlations between the NDVI and shortwave WSA cover 29% of the study area. As vegetation is usually considered less reflective (lower albedo) than bare land, positive NDVI-WSA correlations may appear counterintuitive. However, denser vegetation will also reflect more near-infrared light, thereby contributing to a positive relationship in that part of the spectrum. To elaborate on this effect, we applied a similar analysis separately to the visible broadband (0.3-0.7 μ m) and near-infrared broadband (0.7-5.0 μ m) WSA, which are both provided by the MODIS albedo products. This shows that the positive correlations in the shortwave broadband (0.3-5.0 μ m) are mainly caused by the NIR broadband, as the visible broadband WSA is negatively correlated with NDVI across the study area as could be expected (Figure 3.1a, Supplementary Figure 3.2).

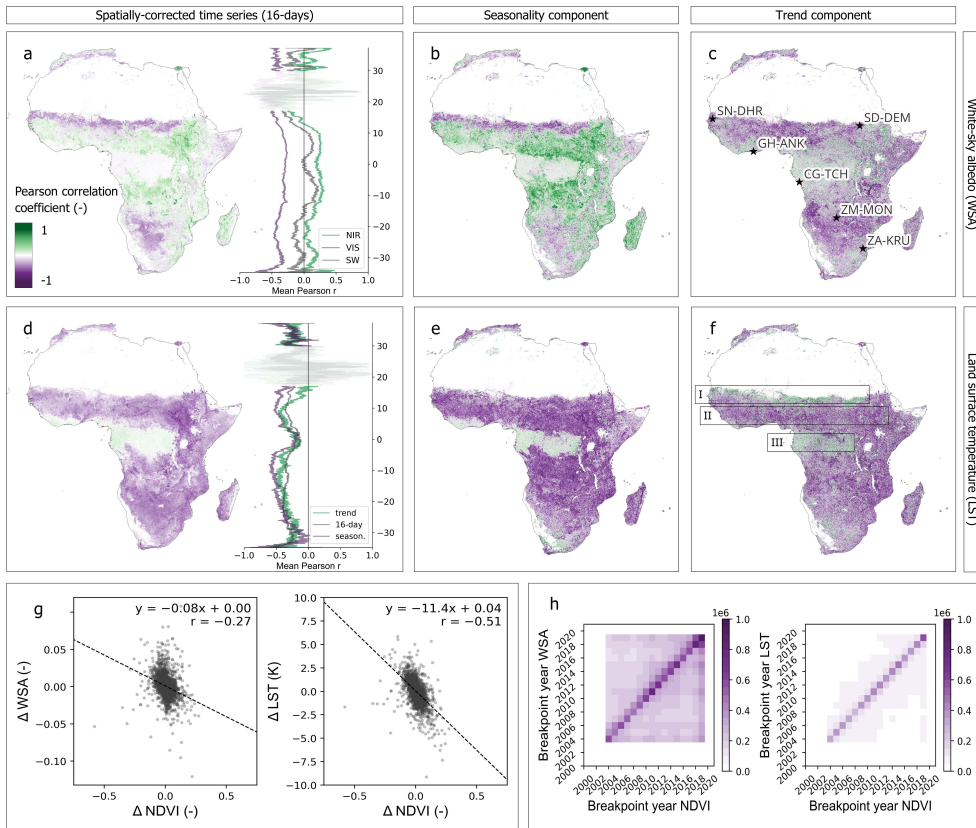


Figure 3.1 | Sensitivity of white-sky albedo and land surface temperature to vegetation. Spatial distribution of the correlation between spatially corrected NDVI and spatially corrected shortwave broadband white-sky albedo (WSA) on either (a) the standard 16-day times series, (b) the seasonal component only or (c) the trend component. The line graph in (a) shows the mean 16-day correlation coefficient per degrees latitude for the shortwave (SW), visible (VIS) and near-infrared (NIR) WSA. Due to the limited data availability, the graph is masked between 17°N and 30°N. (d-f) Similar for the land surface temperature (LST), but the line graph in (d) shows the mean correlation coefficient per degrees latitude for the 16-day, seasonality, and trend component. (g) Median spatially corrected NDVI, shortwave WSA and LST over the study period at 3183 randomly selected points. The line shows the linear fit of the points. (h) Distribution of year of breakpoint for 16-day NDVI, WSA and LST in the study area. Only pixels where both variables show a breakpoint are included, containing 22% and 7% of the pixels for the WSA and LST, respectively. In the figures, areas with a median NDVI lower than 0.15 or a non-significant correlation ($p > 0.05$) are not included. The boxes I, II, and III in (f) represent three exemplary regions in Africa with distinctive albedo-temperature-vegetation relations. The stars in (c) represent the locations of the EC-measurements in Figure 3.3.

Because previous studies have found contrasting biophysical vegetation-surface temperature relationships across time scales (Feldman et al., 2022), we separate the 16-day time series into seasonal and long-term effects of vegetation cover changes using time series decomposition. This is especially relevant when determining the biophysical effects of land restoration, as these projects can affect the long-term greenness trends. Interestingly, contrasting spatial patterns in WSA-NDVI correlation appear for different time scales (Figure 3.1b, 3.1c). Areas in subtropical Africa (delineated as box II in Figure 3.1f) show, for example, a positive correlation on a seasonal scale, but a negative correlation across years (i.e., the trend component). Over the whole study period, the median spatially-corrected NDVI and WSA values show a weak negative correlation with a correlation coefficient of -0.27 (Figure 3.1g). To further explore the relationship between vegetation and albedo, we compare the timing of breakpoints (i.e., significant and sudden changes in the trend component) and find that these moments often coincide, although sometimes the breakpoint in WSA is one year delayed (Figure 3.1h). This suggests that sudden changes in NDVI trends are often followed by sudden changes in the WSA trend. Yet, in only 22% of the study area, a breakpoint is detected for both the NDVI and WSA. In 41% of the study area, no breakpoint is detected for both variables.

Similarly, on a 16-day time scale, NDVI and land surface temperature (LST) are significantly negatively related for 79% of the study area, suggesting an increase in NDVI (more vegetation) corresponds to a lower LST (cooler surface) compared to surrounding areas (Figure 3.1d). In central Africa (box III in Figure 3.1f), on the other hand, positive correlations occur. Similar patterns appear for the season and trend components of the time series (Figure 3.1e, 3.1f). Only in the Sahel area (box I in Figure 3.1f), do the trend components show a different result, with positive correlations between NDVI and LST, while the seasonal component shows negative correlations. Over the whole study period, the correlation between spatially-corrected NDVI and LST is negative, with a slope of -11.4 K (or -11.4 °C) and a correlation coefficient of -0.51 (Figure 3.1g). In addition, the breakpoint year of the NDVI and LST seem to coincide (Figure 3.1h), suggesting that sudden trend changes in NDVI and LST occur simultaneously, although in 7% of the study area shows a breakpoint for both NDVI and LST and 58% does not show a breakpoint for both the NDVI and LST. Interestingly, in 33% of the study area, there is a breakpoint detected in the NDVI time series, but not in the LST time series. This suggests that the LST often changes more gradually, or other processes affect the LST from changing with the NDVI.

3.3.2 Effects of aridity and land cover

The biophysical effects of vegetation show clear spatial patterns related to both aridity and land cover. The negative 16-day correlations between NDVI and WSA often coincide with lower aridity index values (i.e., more arid environments), with increasing

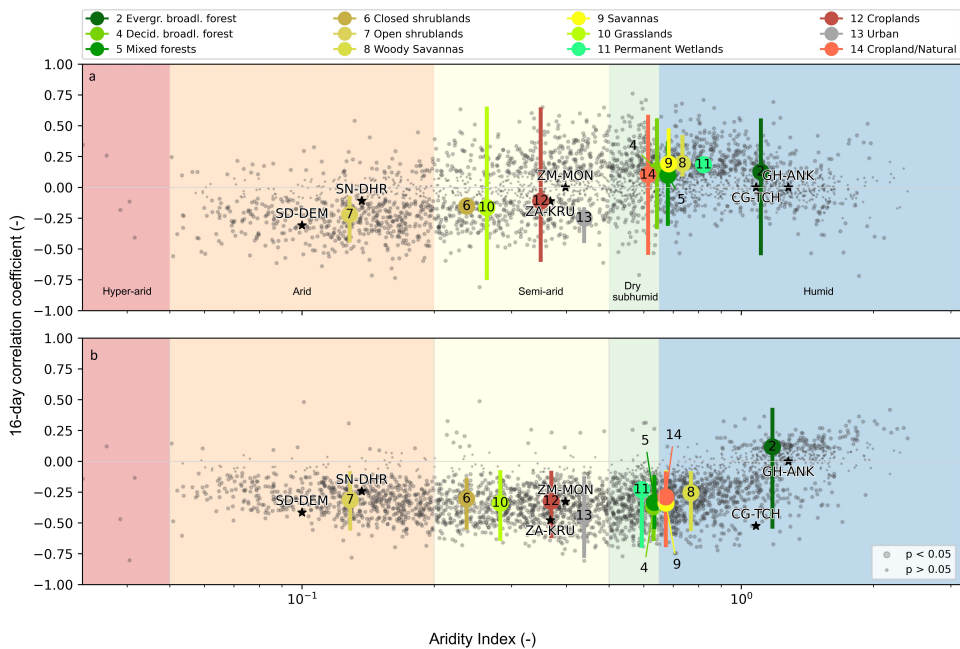


Figure 3.2 | Land cover and aridity controls on vegetation-climate relationships. (a) Correlation coefficient of spatially corrected NDVI and shortwave White Sky Albedo (WSA) and (b) spatially corrected NDVI and land surface temperature (LST) over aridity index (scatter) and land cover classes (bars) based on 3183 random points inside the study area, with a median NDVI higher than 0.15. The points and vertical lines indicate, respectively, the median and interquartile range of the correlation coefficient per land cover class overall data. The horizontal position is determined by the median aridity index value of the respective land cover class. Only land cover classes that occur in the study area are included in this graph. In the scatter plot, non-significant correlations are marked with a smaller point ($p > 0.05$). In the land cover classes, non-significant correlations are not included. The stars represent the locations of the EC-measurements in Figure 3.3.

correlations over higher aridity index values (Figure 3.2a). The highest (i.e., most positive) correlation coefficient values are found with an aridity index around 0.5, corresponding to semi-arid to dry subhumid environments. Towards more humid environments, the correlations between NDVI and WSA are low. A similar, but opposite pattern appears for the correlation value between NDVI and LST, as the correlation values decrease with the aridity index until an aridity index value of 0.5, and then increase again (Figure 3.2b). However, for the most humid areas in Africa, the correlation between NDVI and LST is not zero, but slightly positive.

Besides aridity, land cover also affects the correlation values between NDVI and WSA, even though land cover and aridity are certainly related. Positive correlation can mostly be found in forested areas and savannas, while negative relationships are present in grasslands, shrublands and barren lands (Figure 3.2a). Most land cover classes show negative correlations between NDVI and LST (Figure 3.2b), except for evergreen

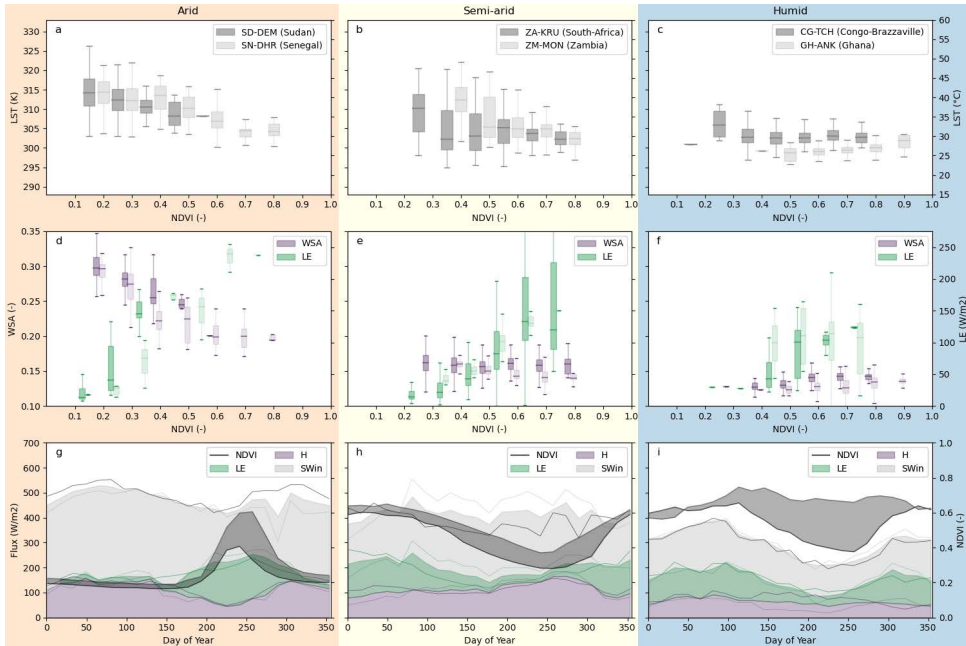


Figure 3.3 | Aridity controls on vegetation-climate relationships from MODIS and eddy-covariance (EC) data. Relationships between NDVI and (a-c) LST, (d-f) WSA and (d-f) latent heat flux (LE) at six EC measurement sites (two per plot) across aridity classes. Plots show median (line), interquartile range (box) and data range with a maximum of 1.5 times interquartile range (whiskers). (g–i) Seasonality of the NDVI, latent heat flux (LE) (green area), sensible heat flux (H) (purple area) and difference between incoming shortwave radiation and sum of latent and sensible heat (SWin) at the same sites. The thin coloured lines (fluxes) and black shaded areas (NDVI) show the two sites separately. The locations of the sites are shown in Supplementary Fig. 1d. Measurements of NDVI, LST and WSA are obtained from not spatially corrected MODIS data, the net radiation, sensible heat flux and latent heat flux are obtained from EC measurements. Seasonality of the other variables at the six stations is included in Supplementary Fig. 14, showing a distinct seasonal variation in NDVI–WSA, NDVI–LST, NDVI–air temperature and NDVI–LE relations and a changing negative to positive correlations from arid to humid stations.

broadleaf forest. Although land cover thus seems to influence the direction of the correlations, both positive and negative correlations can often be found within single land cover classes.

To provide a more mechanistic insight into the vegetation-climate relationships, we extend our analysis with eddy-covariance (EC) data from six measurement sites across aridity zones in Africa. At these sites, the transport of heat, mass and momentum is measured at high frequency, providing data for incoming shortwave radiation (SW_{in}), latent heat flux (LE) and sensible heat flux (H). Although measuring only at a single location and long-time series are often not available, these EC-measurement sites provide more detailed information on the effect of vegetation on the energy balance at a seasonal scale.

These site measurements show that LE is positively correlated to NDVI in arid regions in Sudan and Senegal, suggesting higher evaporation during greener periods (Figure 3.3d). At the same time, the NDVI and WSA are negatively correlated (Figure 3.3d), resulting in a lower reflection of incoming solar radiation, and a higher available radiation (represented by the sum of LE and H compared to SW_{in}) during periods of high NDVI (Figure 3.3g). However, during these periods, the LE increases to such an extent, that we see a decrease in H during periods of the year with higher NDVI. This is consistent with the decreasing surface temperature during periods of high vegetation greenness measured with MODIS (Figure 3.3a). In semi-arid regions, as represented by the sites in Zambia and South Africa, similar relationships to those in arid regions are observed (Figure 3.3b, 3.3e, 3.3h), also suggesting a surface cooling effect of vegetation greening. However, NDVI-WSA relationships seem to be particularly weaker compared to arid regions. In addition, some other regions in northern Africa show positive NDVI-WSA correlations (Figure 3.1b). Yet, the negative NDVI-H and NDVI-LST relationships suggest that also in these semi-arid regions, the increase in latent heat dominates the temperature signal of vegetation. In humid regions in Ghana and Congo-Brazzaville, on the other hand, an increasing NDVI does not have a large effect on LST (Figure 3.3c) or H (Figure 3.3i), even though the available radiation has a defined seasonality. In addition, the NDVI-WSA relationships seem to have a limited effect on the energy balance, represented by a constant sum of LE and H compared to SW_{in} throughout the year. The limited data availability of the MODIS data due to high cloud cover makes it, however, more difficult to interpret the energy balance.

3.3.3 Surface cooling effects of land restoration projects

To determine what the effect of implementing land restoration projects has been on the surface temperature, we compare the WSA and LST at project locations of 434 Sustainable land management (SLM) projects in Africa. The median change in the trend component of WSA and LST over the study period (i.e., $T_{2023-01-01} - T_{2001-01-01}$) shows mixed results across the project locations, with both decreases and increases in WSA and LST without a clear spatial pattern (Figure 3.4a, 3.4b). Yet, comparing the results to changes in NDVI, general negative NDVI-WSA and NDVI-LST relationships can be found for the SLM projects (Figure 3.4c, 3.4d), although it should be mentioned that projects larger than the resolution of the data (1 km²) show stronger NDVI-LST relationships. This suggests that both WSA and LST decrease with increasing NDVI and the spatial pattern in Figure 3.4a, 3.4b results from variations in changing NDVI, or the effectiveness of greening, at the project sites. Across Africa, greening at SLM projects thus generally seems to have a cooling effect on the land surface temperature, with the limited impact of albedo warming represented by the negative NDVI-WSA relationships. No particularly different relationships were found for different aridity zones. It should be noted that the concept of sustainable land management could be considered broader than the definition of land restoration provided by UNCCD (2022).

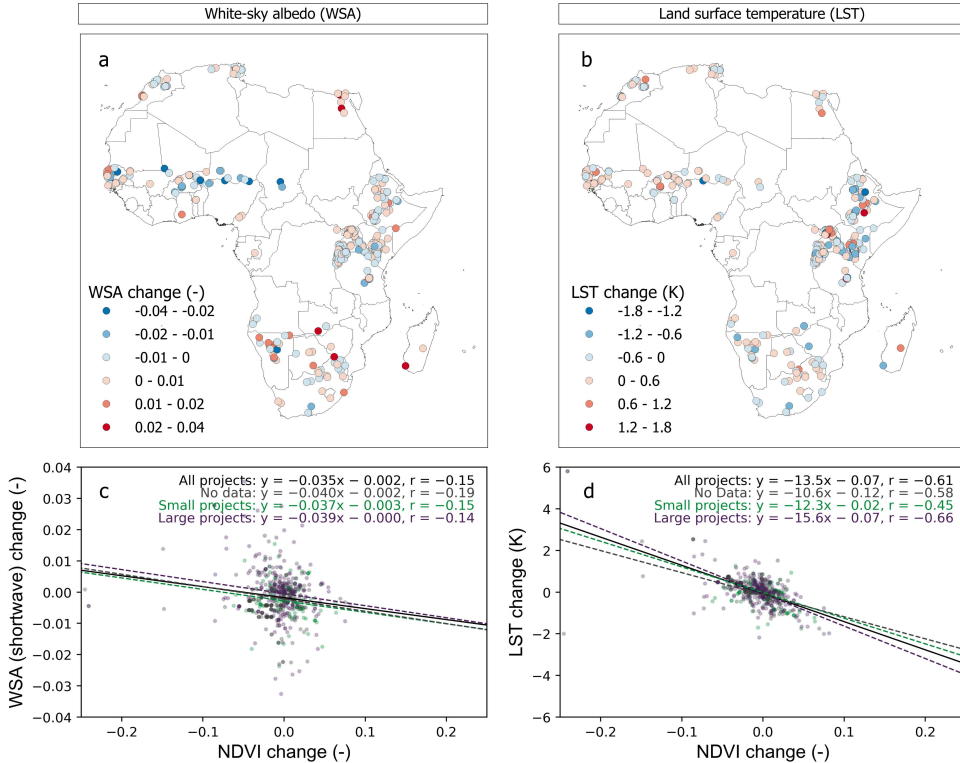


Figure 3.4 | Observed climate impacts of local land restoration. Median change in the trend component of (a) the spatially-corrected WSA and (b) LST in a 2000 m buffer around the WOCAT sustainable land management projects. The change is calculated as the last trend value of the study period minus the first trend value of the study period (i.e. $T_{2023-01-01} - T_{2001-01-01}$). Relationship between median change in trend component of (c) the NDVI and WSA and (d) the NDVI and LST for all projects (black), projects smaller than 1 km² (green; 24%), projects larger or equal to 1 km² (green; 37%) and projects that do not report a size (grey; 39%). The relationships for different types of sustainable land management project is shown in Supplementary Figure 3.15.

Therefore, we included a similar analysis for separate SLM types in Supplementary Figure 3.15, where the strongest NDVI-WSA correlations are found for revegetation and the strongest NDVI-LST correlations are found for agroforestry.

3.3.4 Local surface cooling potential of large-scale land restoration

By extrapolating on the relations found in this study, we can predict the local cooling effect of large-scale land restoration in Africa using a data-driven approach. As a first step, we determined the maximum potential NDVI constrained by aridity, surface temperature, elevation, slope, aspect, soil fertility and water table depth through maximum random forest regression (Figure 3.5a). The difference between this potential NDVI and the current NDVI (ΔNDVI_p) represents the NDVI increase obtainable by large-scale land restoration initiatives. We can observe that the largest NDVI

increases can be achieved in semi-arid regions. In the more humid areas in central Africa, as well as very dry areas, there is little potential for greening (Figure 3.5b). It is important to note, however, that the potential NDVI increase is only constrained by climatological and environmental variables. Socio-economic constraints, which play less of a role in explaining vegetation potential than climatic variables (Hackländer et al., 2023), as well as the need for agricultural land or urban areas, are not considered.

To predict the potential LST change (ΔLST) corresponding to $\Delta NDVI_p$, we used a random forest regressor at each location based on observed values of ΔLST and $\Delta NDVI$, and the aridity index, land cover class, median NDVI, median LST, median WSA, longitude, latitude, and elevation sampled at random locations. These observed values of ΔLST and $\Delta NDVI$ are obtained from the trend component rather than the seasonal changes to match the gradual increase in NDVI from land restoration. Using this regression model, large parts of Africa show cooling as a result of large-scale land restoration, with LST changes up to -4 K (Figure 3.5c), although 98% of the study area shows a change between -1.5 K and 1.5 K. In these areas, large-scale land restoration projects can result in a potential surface temperature decrease. However, the driest regions in the study area, such as in the Sahel and southern Africa, as well as humid areas such as the rainforests of Congo, show a slight warming potential (Figure 3.5d). The mean LST change over the whole study area, including regions with little potential for NDVI increases, is -0.2 K, suggesting an overall local cooling potential of large-scale land restoration in Africa (Figure 3.5d). Yet, as we extrapolate measured relationships between the NDVI and LST, it should be noted that we can only predict the direct local effects of large-scale land restoration across Africa, while non-local or indirect climate effect through changes in atmospheric circulation are not included in this prediction. If all the suggested areas are restored at once on a large scale, different patterns may appear. These results can, however, be used to see where land restoration in Africa can cause local cooling, and where it instead may result in warming.

3.4 Discussion and conclusions

In this study, we observed variations in vegetation-albedo and vegetation-surface temperature relationships across both spatial and temporal scales. However, before we discuss these in more detail, several uncertainties should be kept in mind when interpreting these results. Firstly, the use of image composites for land surface temperature results in a bias for clear-sky conditions, suggesting that the relationships we found related to LST are representative only for days without cloud cover. Clouds can have a considerable impact on the surface energy balance due to changes in incoming longwave and shortwave radiation (Chen, Ge, et al., 2022). Therefore, the year-round relationships between vegetation and surface temperature may deviate from the results found in this study. In addition, the land surface temperature values

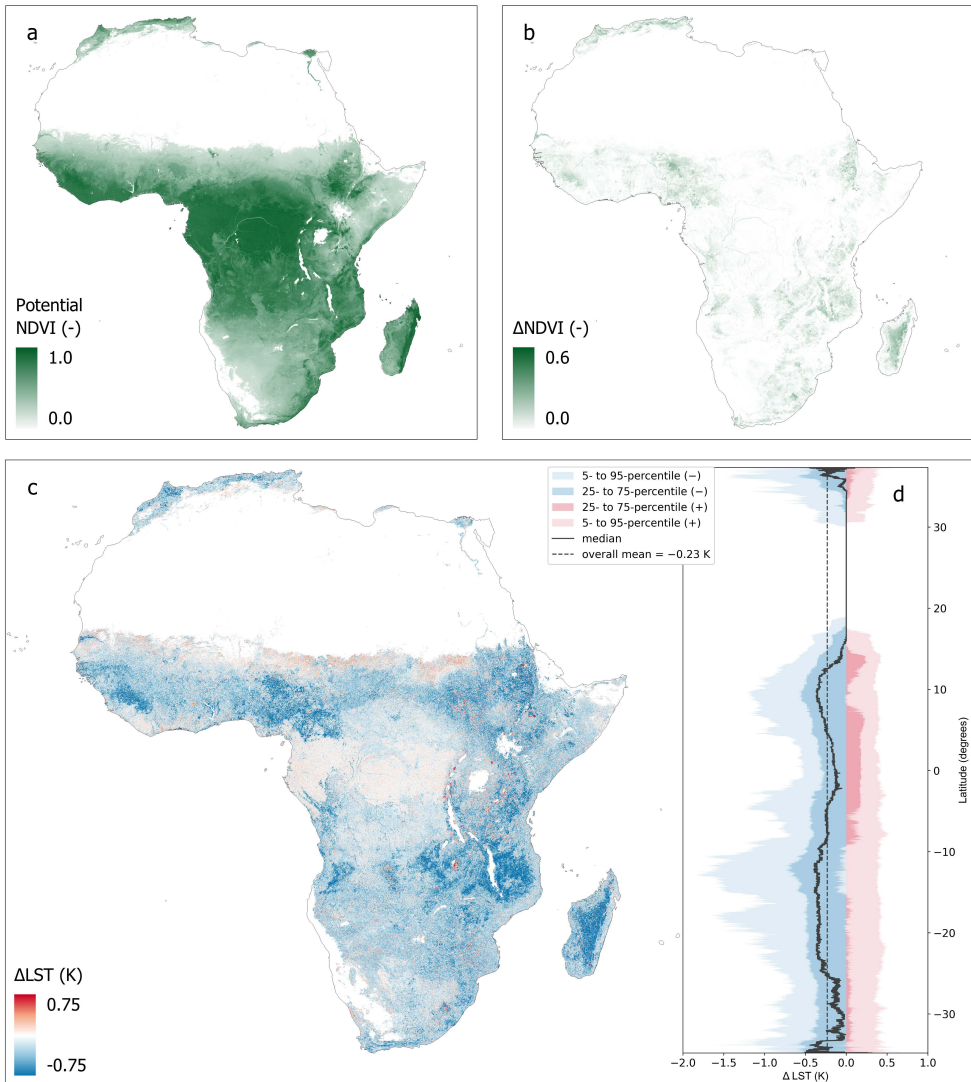


Figure 3.5 | Potential local land surface temperature changes due to land restoration. (a) The potential NDVI obtainable by land restoration, predicted using maximum random forest regression and (b) the NDVI increase compared to the original median NDVI. (c) The potential local LST change obtainable by land restoration, predicted using random forest regression. For visualization purposes, the colour scale ranges from -0.75 to 0.75 K, containing 91% of the values. (d) The median and percentiles in Δ LST grouped by latitude. The overall mean indicates the mean potential change in surface area across the study area (excluding non-vegetated areas) of -0.23 K.

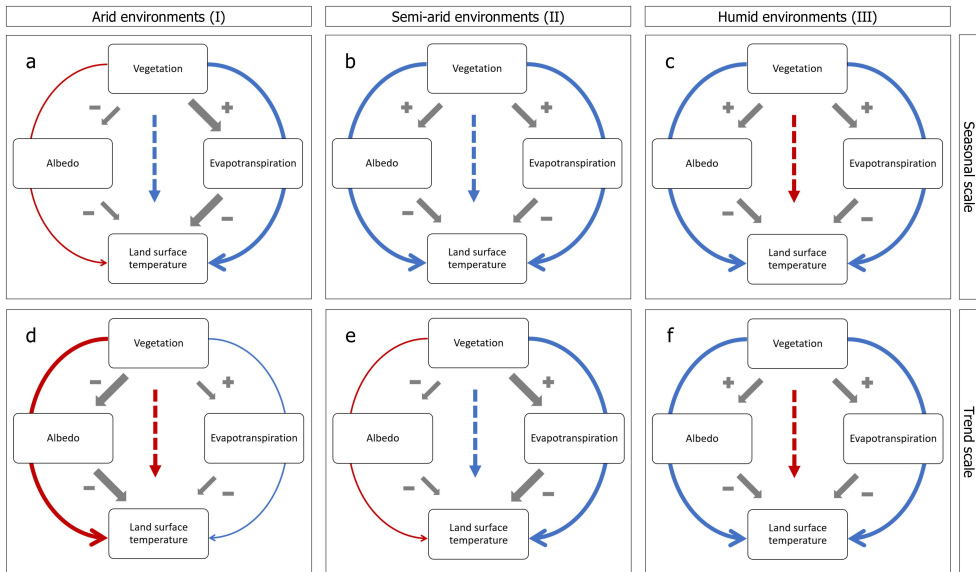


Figure 3.6 | Perceptual model of vegetation-climate relationships. (a, d) Vegetation-albedo and vegetation-temperature relationships in arid, (b, e) semi-arid and (c, f) humid environments in northern Africa on (a-c) seasonal and (d-f) trend time scales. The locations of arid, semi-arid and humid environments correspond to the boxes in Figure 3.1f, annotated with respectively I, II and III. Positive relationships are indicated with a plus sign, negative relationships with a minus sign. The overall net albedo/evapotranspiration warming of potential vegetation increase is indicated with a red arrow, cooling with a blue arrow. The dotted arrows indicate the observed vegetation-temperature relationship, where a red arrow again suggests warming due to a vegetation increase and a blue arrow cooling. For all arrows, large arrows show the assumed dominant processes.

used in this study may be different from the air temperature measured by weather stations and often felt by humans, especially during dry seasons (Vancutsem et al., 2010). It is estimated that the effect of vegetation on land surface temperature is stronger than on air temperature, partly caused by the clear-sky bias of remotely sensed land surface temperature (Alkama & Cescatti, 2016), which is also observed at the EC measurement locations (Supplementary Figure 3.14). Also, the mixing of the boundary layer causes surface temperature effects to be more local than air temperature effects. We therefore expect the air-cooling effect of land restoration projects to be smaller than the surface cooling as observed in this study, which should be taken into consideration while planning future land restoration projects. On the other hand, because satellite-derived surface temperature values are detected at the top of the canopy layer, the additional shade effects that vegetation can provide are not considered. In addition, also radiative heat emitted by the surface can be felt by humans. Similarly, the albedo is not only affected by changes in vegetation but also by soil background signals. This is especially relevant in arid regions with large fractions of bare ground. Furthermore, because wet soils have a lower albedo than dry soils, soil moisture content has a considerable impact on albedo in these areas (Allen et al., 1994;

Yang et al., 2020). In addition, the white-sky albedo only represents the bihemispheric reflectance, while the actual albedo value as measured on the ground (i.e., blue-sky albedo) also contains a directional hemispherical reflectance component (i.e., black-sky albedo). We are convinced that changing white-sky albedo to blue- or black-sky albedo would likely only have a very limited effect on the results. Furthermore, the overall accuracy of MODIS albedo is generally high and does not appear to depend on illumination and viewing angles (Liu et al., 2009; Cordero et al., 2021), which is important when studying larger areas. In addition, as the land surface temperature is affected by both albedo warming and evaporative cooling, as shown by the eddy-covariance data, a continental-scale analysis of evaporation would be informative. However, remotely sensed evaporation is often computed using empirical relations between NDVI and evaporation, making it difficult to study changes in NDVI and evaporation independently. Although also NDVI and WSA cannot be studied completely independently, because the variables are based on the same spectral bands, we believe that using these variables is more appropriate than computed evapotranspiration values. Therefore, combining observed values from remotely sensed data with modelling studies incorporating air temperature, evapotranspiration, blue-sky albedo and cloudy days may provide a more complete picture of the cooling potential of land restoration in Africa.

As vegetation-surface temperature relationships vary across Africa, we discuss three zones with distinctive characteristics in more detail: arid environments in the Sahel (Figure 3.1f, box I), semi-arid and dry subhumid environments in northern Africa (Figure 3.1f, box II) and humid environments in central Africa (Figure 3.1f, box III), creating a perceptual model of vegetation-climate relationships across Africa. The perceptual model can also be applied to regions in southern Africa, although the boundaries between positive and negative relationships are less sharp.

In arid environments such as the Sahel, the results showed negative vegetation-albedo correlations on a seasonal scale, increasing net radiation and energy available for heat generation. Yet, the positive vegetation-evaporation relationships cause an increasing latent heat flux that compensates for this increase in available energy. This leads to a decrease in sensible heat flux and evaporative cooling during periods in the year with high vegetation cover (Figure 3.6a). Although the EC measurements are too short to accurately analyse changes in long-term changes in the energy balance, we can extend the same reasoning to the trend scale (Figure 3.6d), where we observe positive vegetation-surface temperature relationships. Warming due to a decrease in albedo thus seems to outweigh the decrease in sensible heat flux due to evaporation. This suggests that enough water is available for evaporative cooling during the wetter periods in the year when vegetation cover is high, but there is insufficient water to sustain this evaporative cooling effect during an overall increase in vegetation cover, resulting in a dominant albedo warming on the trend scale. Similar results were found

by Chen, Li, et al. (2020) and Feldman et al. (2022), who showed that the long-term relationship between leaf area index and land surface temperature is dominated by the albedo in this area, causing a warming effect of vegetation increases.

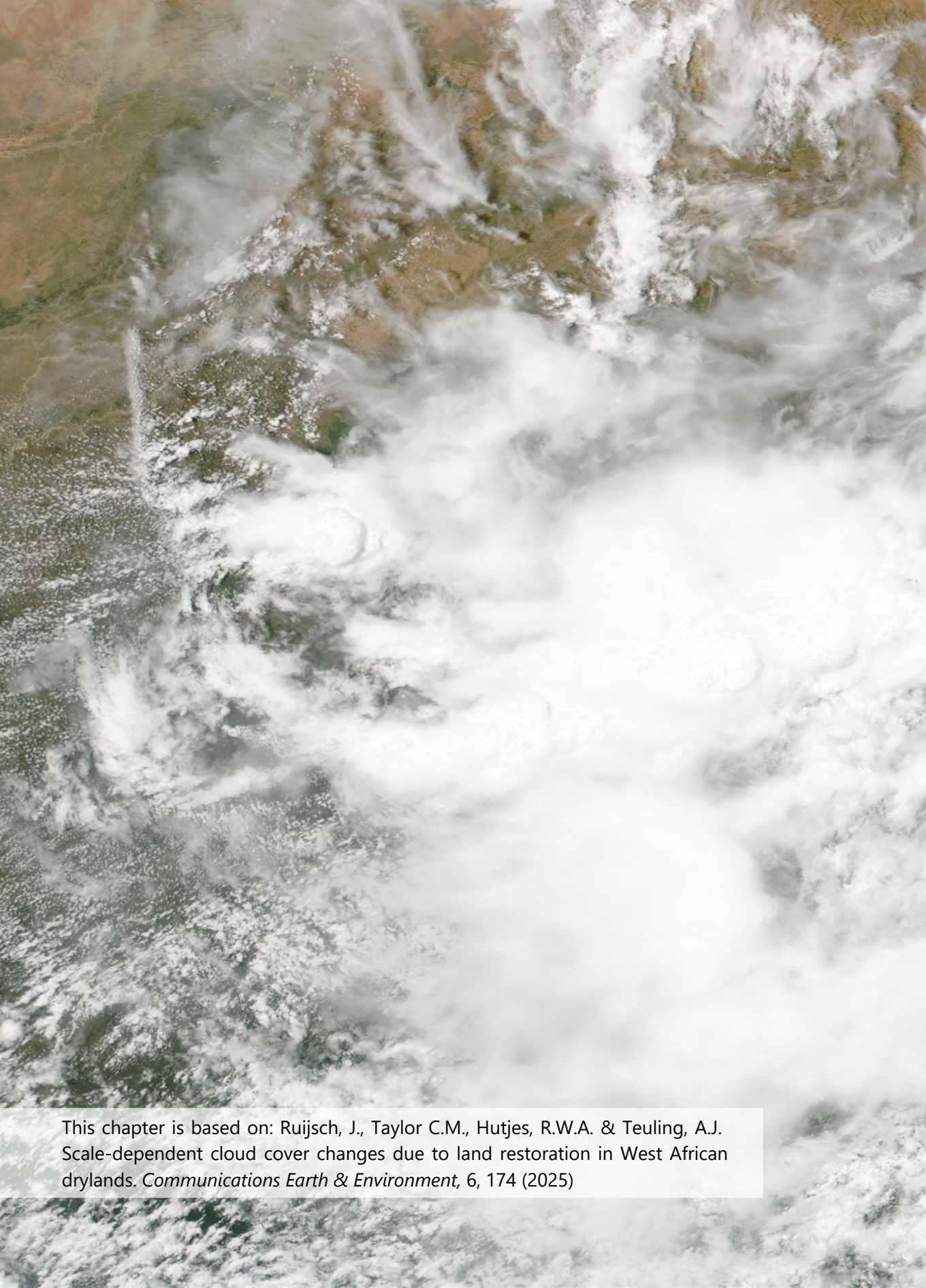
In semi-arid and dry subhumid environments in northern Africa, vegetation variations are positively correlated to the albedo on seasonal time scales, indicating more reflectance with higher vegetation cover (Figure 3.6b). Although this may seem counterintuitive as vegetated surfaces are usually considered darker due to the absorption of visible (VIS) radiation, a distinctive property of vegetation is the high reflectivity of radiation in the near-infrared (NIR) range (Li et al., 2023) (Supplementary Figure 3.2). Since both the NIR and VIS range are included in the white-sky albedo (Liang et al., 1999), a dominant increase in the reflection in the NIR range over a decrease in the reflection in the VIS range can explain the positive vegetation-albedo correlation. Previous research estimated the vegetation-albedo relationship to be highly variable and depending on location (Alibakhshi et al., 2020), where positive relationships between vegetation and NIR albedo were found especially in the growing season (Hammerle et al., 2008; Williamson et al., 2016; Zheng et al., 2019). Together with the fact that albedo can be positively related to leaf area index, but negatively to forest cover (Alibakhshi et al., 2020), this can explain the difference between the seasonal and trend vegetation-albedo correlations found in this study (Figure 3.6e). In addition, dryland Africa is a hotspot for fires, where some regions burn almost every year (Roy et al., 2008). The coincidence of the resulting decrease in albedo (Gatebe et al., 2014; Dintwe et al., 2017) and vegetation cover caused by the fires can explain the positive seasonal-scale albedo-vegetation relationships in these areas. In some semi-arid regions in southern Africa, on the other hand, vegetation and albedo are negatively correlated and EC measurements behave more like arid regions in northern Africa. Yet overall, we see a net cooling effect of vegetation on both the seasonal and trend scales in these semi-arid and dry subhumid areas, represented by the negative vegetation-surface temperature relationships, which may be caused by both a higher reflectance of near-infrared radiation on the seasonal scale, and evaporative cooling on the seasonal and trend scales.

Tropical forests and humid areas in central Africa, on the other hand, showed low, yet positive vegetation-surface temperature relationships on both the seasonal and trend scale, suggesting that an increase in forest cover would cause warming of the Earth's surface (Figure 3.6c, f). This contradicts expectations, as tropical forests have a high evapotranspiration potential throughout the year and vegetation and latent heat flux are positively correlated. Combined with generally low vegetation-albedo correlation, a cooling effect would be expected (Bonan, 2008), as predicted by many modelling and observational studies (Davin & de Noblet-Ducoudré, 2010; Abiodun et al., 2012; Akkermans et al., 2014). Yet, several studies using satellite-based vegetation and temperature data show a similar weak or slightly positive vegetation-albedo

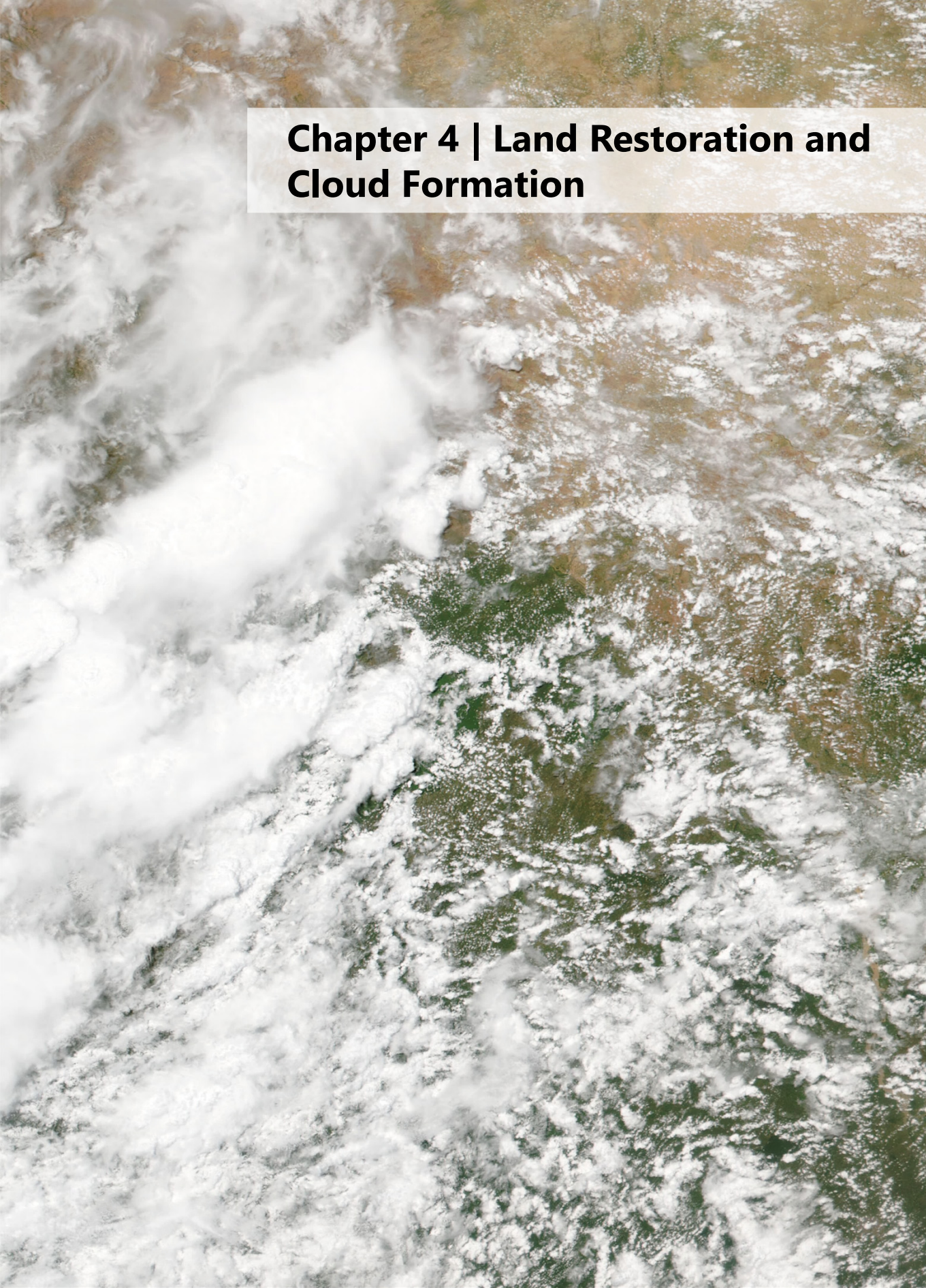
relationship in the tropical forests of central Africa (Alkama & Cescatti, 2016; Chen, Li, et al., 2020; Feldman et al., 2022). In addition, satellite data estimations that deforestation in the Congo basin (i.e., a change from forests to grasslands) may potentially result in an increase in latent heat flux and a decrease in sensible heat flux. This would then cause a decrease in surface temperature and positive vegetation-surface temperature relationships (Duveiller et al., 2018b; Duveiller et al., 2020). Literature addressing this difference between different observational datasets and model results in tropical areas like Central Africa suggests the high cloud cover and the saturation of NDVI under high vegetation cover as potential causes (Feldman et al., 2022). Indeed, visual inspection of the NDVI time series reveals a large amount of noise (Supplementary Figure 3.16), although using the Enhanced Vegetation Index (EVI) or Leaf Area Index (LAI), which are less sensitive to this saturation effect (Huete et al., 1997), does not result in substantial different spatial patterns (Supplementary Figure 3.17-3.18). In addition, it should be noted that these humid regions are often energy-limited, rather than water-limited. This effect is distinctly visible in the EC measurements, as an increase in incoming shortwave radiation directly leads to increased evapotranspiration while the sensible heat remains constant. This could explain the weak correlations between vegetation and surface temperature in this study. However, considering the clear-sky bias and the overall low correlations found in these areas, we argue that the warming effect of reforestation in humid areas should be handled with care and more observational data is needed to provide a complete explanation.

If we look in more detail at sustainable land management projects, no clear patterns in white-sky albedo and land surface temperature changes could be observed. This indicates that sustainable land management in general does not directly cause a cooling effect in Africa. This may partly be caused by the uncertainty related to the location and size of the WOCAT projects used in this study, as 27% of the projects is reported to be smaller than 1 km² and 38% did not report a size, and the absence of greening at some locations. In addition, it should be noted that the use of our spatial context method results in the detection of small-scale deviations in vegetation, albedo and temperature. In addition to land management, other small-scale processes such as changes in the extent of surface water, irrigation and especially the distribution of water can cause variations in vegetation-surface temperature relationships (Ruijsch, Teuling, et al., 2023). Yet, comparing the changes in surface temperature with changes in NDVI, a clear negative relationship suggests that warming at the project locations is often due to a decrease in vegetation over time rather than the absence of a cooling effect of greening. Some projects that showed considerable greening resulted in a cooling of almost 2 K, suggesting that if the SLM projects result in greening, a cooling effect can often be expected.

Extrapolating the relationships found in this study to a large-scale restoration scenario, large parts of Africa, especially semi-arid environments, may experience local cooling under future land restoration, assuming enough water is available to sustain the increased evapotranspiration. Across Africa, we estimate that the potential land restoration can decrease the local surface temperature on average by 0.2 K, which is considerable in comparison to the projected mid-century temperature change between 0.5 and 2.5 K (Ranasinghe et al., 2021). From a temperature perspective, a widespread increase in vegetation cover may therefore be beneficial in these areas. In addition, comparing the results of this study with the locations of existing land restoration projects, we expect a cooling effect of vegetation increases in large parts of projects such as the participating countries of the Great Green Wall of Africa (UNCCD, 2020). However, some of these projects implemented in the driest regions, including parts of the Great Green Wall project, may experience biophysical warming due to a lack of moisture available for the increased evaporation. The contradicting vegetation-surface temperature relationships across time scales highlight the need to include both interannual as well as seasonal analyses before implementing land restoration projects. Furthermore, it should be kept in mind that we only determined the effect on land surface temperature in this study, while large-scale land restoration may have many other benefits as well as potential disadvantages related to biodiversity, socio-economic aspects and land use change (Holl & Brancalion, 2020). In addition, land restoration does not only alter the energy balance through biophysical processes but can also affect the water cycle through changes in evapotranspiration, soil moisture and even precipitation (Hoek van Dijke et al., 2022). On top of that, unexpected climate effects may appear outside the restored area, even if the restored area itself is cooling (Abiodun et al., 2012; Chen, Ge, et al., 2022). These effects are not included in this study. We therefore argue that a more complete picture of these different potential climate effects of land restoration is needed before large-scale land restoration is implemented. In this research, we do, however, provide some first guidance on where future land restoration could result in cooling, and where it instead shows warming.



This chapter is based on: Ruijsch, J., Taylor C.M., Hutjes, R.W.A. & Teuling, A.J. Scale-dependent cloud cover changes due to land restoration in West African drylands. *Communications Earth & Environment*, 6, 174 (2025)

An aerial photograph of a river with white water rapids. The water is turbulent and white with foam, contrasting with the green vegetation on the banks. The text 'Chapter 4 | Land Restoration and Cloud Formation' is overlaid on a semi-transparent white box in the upper left corner.

Chapter 4 | Land Restoration and Cloud Formation

Abstract | Land restoration projects, including reforestation and area protection, are being implemented across African drylands such as the Sahel. In addition to biodiversity, livelihood and carbon sequestration benefits, restoration can also affect the local climate through land-atmosphere interaction. Yet, it remains unknown to what extent dryland restoration can affect cloud cover development and, ultimately, precipitation. Here, we use twenty years of high-resolution data from the Meteosat Second Generation satellite to study the impact of land restoration on cloud development in West African drylands. Results show that cloud cover frequency and convective initiation are higher above vegetated areas, particularly during the start and end of the wet seasons. Furthermore, we find a more pronounced cloud cover enhancement over protected areas larger than 121 km², suggesting a scale-dependent relationship between project size and cloud cover development.

4.1 Introduction

Similar to other drylands, the Sahel and West Sudanian savanna regions in West Africa are particularly vulnerable to the effects of land degradation and climate change. Although the main cause remains debated, high rainfall variability, water scarcity and anthropogenic pressures can drive further degradation in the region (Closset et al., 2018). Ambitious restoration projects like the Great Green Wall initiative (UNCCD, 2020) or the African Forest Landscape Restoration Initiative (AFR100) try to combat degradation, increase biodiversity or enhance carbon sequestration, while improving the livelihood of the local population (Holl, 2020). Such restoration practices can include, for example, active tree planting, natural regeneration, farmer-managed natural regeneration and area protection (UNCCD, 2022).

Because land restoration may cause changes in vegetation cover, it affects not only biogeochemical processes but also the biophysical properties of the Earth's surface (e.g. albedo and surface roughness) (Windisch et al., 2021; Hasler et al., 2024), especially in regions of strong land-atmosphere coupling such as West Africa (Koster et al., 2004; Soares et al., 2019). As a result, restoration has the potential to alter both the surface energy balance, land-atmosphere interactions and water availability (Ellison & Speranza, 2020). Several projects have proposed to utilise these so-called biophysical climate effects to regulate the microclimate by decreasing temperature or enhancing soil moisture (Syktus & McAlpine, 2016; Castelli et al., 2019; Villani et al., 2020; Villani et al., 2021; Constenla-Villoslada et al., 2022), to improve human well-being (Wolff et al., 2018) or to provide adaptation benefits (Saley et al., 2019). Yet, projects may alter properties such as turbulent fluxes and evapotranspiration through vegetation changes, which gives rise to the question of whether they can also change boundary layer properties and cloud development in the restored area or elsewhere. This is especially relevant in the context of land restoration in dryland regions, as increased cloud development may also affect precipitation and water availability. Combined with the uncertainty about the ecological and socioeconomic benefits of land restoration in dryland regions (Holl & Brancalion, 2020; Parr et al., 2024) and the increased project implementation over the years (Martin et al., 2021), this highlights the need to make accurate predictions on the expected changes in cloud development (as a first step towards precipitation) due to land restoration.

Predicting the net effect of changes in vegetation on cloud development in a certain area is not trivial due to the different mechanisms at play. Clouds can form when the boundary layer grows and the moisture in the atmosphere is lifted to the lifting condensation level. Vegetation affects this process by increasing atmospheric moisture through enhanced evapotranspiration, and by altering boundary layer growth through changes in albedo and available radiation, surface roughness and allocation of the available radiation to the latent and sensible heat flux. In addition, certain degrees of vegetation cover may increase water availability by increasing soil infiltration and

reducing overland flow (Ilstedt et al., 2016; Ellison et al., 2017; Ellison et al., 2024). Previous research suggests that it is more likely that clouds are enhanced over forests when the sensible heat flux is larger than surrounding regions (Xu et al., 2022), caused by a growing boundary layer. This mechanism has been observed in, for example, case studies in France (Teuling et al., 2017b) and the United States (Tian et al., 2022). In the Amazon, deforestation is suggested to increase shallow cloud formation, although this is likely to be driven by mesoscale circulation (the so-called forest breeze) rather than by increased convection (Wang et al., 2009; Spracklen et al., 2018). This effect is especially strong with large vegetation heterogeneities, with increased precipitation on the non-forested side of sharp vegetation boundaries (Negri et al., 2004). Unlike in the Amazon, where it is observed that extensive deforestation can again inhibit cloud formation (Knox et al., 2011), studies in moist tropical West Africa have shown enhanced convective initiation over larger patches of deforestation caused by mesoscale circulation (Taylor, Klein, Parker, et al., 2022). In addition, precipitation is enhanced over negative (dry) soil moisture anomalies in the Sahel (Taylor et al., 2012), especially on the boundaries of dry and wet patches (Taylor et al., 2011).

Due to the different mechanisms proposed in previous research, it remains unclear how vegetation cover, and heterogeneities therein, affect cloud formation in dryland West Africa, despite these numerous studies on vegetation-cloud interactions. In addition, it is currently unknown how large a restoration project must be to affect cloud cover and precipitation, both in general and in West Africa (te Wierik et al., 2021). Although recent developments in convection-permitting models now allow studying the land-atmosphere interactions at a higher resolution (Crook et al., 2023; Semeena et al., 2023), observational evidence for these interactions is needed to validate model results. These observations usually come from satellite data, providing several decades of cloud cover and vegetation data. Instruments such as the Moderate Resolution Imaging Spectroradiometer (MODIS) can be used for global vegetation-cloud interaction studies at a high spatial resolution (Duveiller et al., 2021; Xu et al., 2022). However, the daily time scale of these higher-resolution datasets provides limited information on cloud development throughout the day.

An alternative, at least over Africa, is provided by the Spinning Enhanced Visible and InfraRed Imager (SEVIRI) on board the Meteosat Second Generation (MSG) satellites (Schmetz et al., 2002). Due to its geostationary orbit, MSG provides data on a 15-minute temporal resolution, allowing for the analysis of vegetation-cloud relationships on diurnal, seasonal and multiyear time scales. As the 3 km spatial resolution of the conventional MSG cloud products is relatively coarse compared to the size of most restoration projects, we apply a data-driven cloud detection algorithm, originally developed for a case study in France (Teuling et al., 2017b), and similar to Bley and Deneke (2013), to detect cloud cover from the High-Resolution Visible (HRV) broadband channel with a 1 km resolution. This methodology is applied to a case study

region in West Africa of approximately 300 x 1300 km (10-13°N,0-12°E), containing regions within Nigeria, Niger, Benin, Burkina Faso, Togo and Ghana (Supplementary Figure 4.1). This area is selected to meet computational limitations of processing the 321,200 HRV images available between 2004 and 2024, as well as to fall within the shifting scan modes of HRV SEVIRI for most of the day (07:00-15:45 UTC). This high number of images allows the detection of vegetation-cloud relationships, even if only a limited number of days of land-atmosphere coupling appear to exist.

We compare the high-resolution (1 km) cloud cover fraction to (1) spatiotemporal patterns in vegetation greenness and (2) areas within the World Database on Protected Areas (WDPA) (IUCN, 2024). As a complete database of the extent of land restoration projects is lacking, we combine the analysis of vegetation greenness with area protection, to provide a proxy for the expected effects of land restoration. In addition, the size of the WDPA regions and two subregions with different spatial patterns in vegetation greenness are used to determine the scale-dependence of the vegetation-cloud relationships. As a last step, locations of convective initiations based on MSG cloud-top temperature data (following Taylor (2015)) are used to study the relationship between land restoration and the initiation of deep convection. Hereby, we aim to determine to what extent land restoration can enhance cloud cover in West Africa, offering relevant insights into the biophysical benefits of land restoration in West Africa, as well as providing observational support for policymaking and planning of land restoration projects across dryland regions.

4.2 Methodology

4.2.1 Input data

In this study, several datasets are used (Table 4.1). The main analysis is based on the Spinning Enhanced Visible and Infrared Imager (SEVIRI) instrument on board the Meteosat Second Generation (MSG) satellites. Due to MSG's geostationary position, it has a relatively high temporal resolution of 15 minutes, allowing for both a diurnal and seasonal analysis of cloud development. The cloud detection algorithm is based on the broadband high-resolution visible (HRV) channel, providing a single reflectance value for 0.4–1.1 μm on 1 km spatial resolution and 15-minute temporal resolution. Daytime images between 2004/01/19 and 2024/01/01, 06:00 UTC to 16:45 UTC (07:00 to 17:45 in local time Nigeria, Niger and Benin), were selected, resulting in roughly 321,200 images.

Two cloud products are used for validation. The first product is the standard MSG Cloud Mask (EUMETSAT, 2015) with the same temporal resolution and period as the HRV product, but with a 3 km spatial resolution. Each pixel is classified as either clear sky over water, clear sky over land, cloud, or no data, based on a threshold algorithm using

Table 4.1 | Overview of input data. Name, spatial resolution, temporal resolution, used study period and source of main input datasets.

	Name	Spatial resolution	Temporal resolution	Study Period	Source
HRV	MSG High Rate SEVIRI level 1.5 – 0 degree, HRV channel	1 km	15 minute	2004/01/19 – 2024/01/01	(Schmetz et al., 2002)
CLM	Cloud Mask – MSG – 0 degree	3 km	15 minute	2004/01/19 – 2024/01/01	(EUMETSAT, 2015)
CI	Convective Initiation	3 km	15 minute	2004/01/19 – 2024/01/01	(Taylor, 2015)
VFM	CALIPSO Lidar Level 2 Vertical Feature Mask (VFM) V4-51	1 km	16 days	2006/06/11 – 2023/06/30	(Winker et al., 2003; Vaughan et al., 2005; Winker et al., 2009)
NDVI	MODIS/Terra Vegetation Indices 16-Day L3 Global 1km SIN Grid (MOD13A2)	1 km	16 days	2004/01/01 – 2024/01/01	(Didan, 2021)
SRTM	Shuttle Radar Topography Mission (SRTM) digital elevation V4	90 m	n.a.	2000/02/11	(Jarvis et al., 2008)
WDPA	World Database on Protected Areas (polygons)	n.a.	n.a.	2017/07/01	(IUCN, 2024)

the visible, near-infrared and infrared channels. The other cloud product is derived from the Vertical Feature Mask (VFM) data product (Vaughan et al., 2005) produced from Cloud-Aerosol Lidar with Orthogonal Polarization (CALIOP) instrument onboard the Cloud-Aerosol Lidar and Infrared Pathfinder Satellite Observations (CALIPSO) satellite (Winker et al., 2003; Winker et al., 2009).

Vegetation data is obtained from the Moderate Resolution Imaging Spectroradiometer (MODIS) Normalized Difference Vegetation Index (NDVI) product (Didan, 2021), providing information on vegetation greenness. Although MODIS has a 250 m spatial resolution, we used the 1 km product here to match the spatial resolution of the HRV data. Shuttle Radar Topography Mission (SRTM) data (Jarvis et al., 2008) is used as elevation data. Lastly, the World Database on Protected Areas polygons provide information on the location of protected areas within the study area (IUCN, 2024)

4.2.2 HRV cloud detection algorithm

For each 15-minute time step, the HRV image is converted to a cloud mask using an algorithm based on Teuling et al. (2017b). The basic principle of the algorithm is that clouds have a higher HRV reflectance (brighter) than the Earth's surface and reflectance values above a certain threshold are classified as cloud and below the threshold as clear sky. However, to correct for temporal variations in illumination across the study area, as well as mixed pixels and transparent clouds, the difference between the HRV

reflectance and the clear-sky surface reflectance is compared to a threshold rather than the HRV reflectance itself. Thus, clouds are detected if:

$$r_{HRV}(x, t) - r_{cs}(x, m, h) \geq T(h) \quad (4.1)$$

where r_{HRV} is the reflectance of the HRV image at each location x and 15-minute timestep t , r_{cs} is the clear-sky reflectance of the surface at a specific location (x), month (m) and hour of the day (h), and T is the threshold.

The clear-sky surface reflectance is computed separately for each hour of the day and time of the year. Each month is therefore divided into three 10-day periods, where the last period is 8-11 days, depending on the month. This results in 396 time slices (12 months, 3 slices per month, 11 hours per day) for which the clear-sky reflectance is computed. Within this period, all images over the years are retrieved (~800 images), after which the smoothed empirical cumulative distribution function of each pixel is computed. The clear-sky surface reflectance corresponds to the reflectance value with the steepest slope (or most common/typical reflectance value). This method assumes that the clear sky reflectance corresponds to the most common or typical reflectance value rather than the lowest reflectance value to account for cloud shadows and variations in land cover. Because some areas in the south of the study region are mostly clouded between June and September, the typical reflectance maps are smoothed by taking the moving minimum value of five periods before and after each time step. The result is 396 images of typical HRV reflectance values, which are similar to the surface albedo (Supplementary Figure 4.2).

Next, the threshold value is determined. As the overall reflectance of the image depends on the hour of the day, it is expected that the difference between cloud reflectance and clear-sky reflectance varies over the day. Therefore, the threshold $T(h)$ depends on the average clear-sky reflectance at a certain hour of the day (h):

$$T(h) = \overline{r_{cs}(x, m, h)} * s \quad (4.2)$$

where s is a scaling parameter that can be calibrated. Higher values of s result in a lower number of clouds detected. To calibrate s , 264 random HRV images are selected (with 2 images for each month and hour of the day), for which the cloud masks with different values of s are computed. Visual comparison to the original HRV image is used to choose s in such a way that thick (e.g. cumulus) clouds are detected as clouds, but thin or transparent (e.g. cirrus) clouds are detected as clear. The selected value is validated to another 264 random HRV images. A s -value of 0.7 is used throughout this manuscript, but a comparison to values of 0.5 and 0.9 is included in Supplementary Figure 4.3. Although using these values results in, respectively, higher and lower overall cloud cover frequencies, the spatial patterns remain fairly similar.

After determining the cloud threshold values, all 321,200 HRV images are converted to an HRV cloud mask, where each location is classified as either cloud or clear sky.

Although images from 06:00 UTC to 16:45 UTC were initially obtained, visual inspection determined that the images between 06:00 and 06:45 and between 16:00 and 16:45 are too dark, with too little contrast between clouds and clear-sky reflectance, to accurately determine the cloud mask with this algorithm (Supplementary Figure 4.4). For this reason, these images are not included in further analysis. The remaining cloud masks are used to calculate the cloud cover frequency (CCF), which can be defined as the fraction of cloud occurrence over time, at a certain location. Fractional cloud cover (FCC) is used for the cloud occurrence at a certain time step, averaged over space.

4.2.3 Validation of the HRV cloud mask

The algorithm is validated in two ways. To validate large-scale patterns and seasonal variations in cloud cover frequency, the HRV cloud mask is compared to the standard MSG cloud mask (EUMETSAT, 2015). This cloud mask is readily available for the same temporal resolutions, study period and study area as the HRV cloud mask created in this study, but on a 3 km resolution. The MSG cloud mask is computed using a threshold method based on most of the MSG channels, including thermal infrared data. The MSG cloud mask is visually compared to both separate scenes as well as the overall cloud cover frequency across the study area.

In addition, the created HRV cloud mask is compared to The Vertical Feature Mask from the Cloud-Aerosol Lidar and Infrared Pathfinder Observations (CALIPSO) instrument (Winker et al., 2003; Vaughan et al., 2005; Winker et al., 2009) which uses active lidar to provide vertical transects of cloud types. The VFM data describes vertical distributions of cloud and aerosol types along a scanning line. The scanning lines are located roughly between 1.5 and 2.5 °E from South to North of the study area. The scanning lines have a return period of 16 days at around 13:30 UTC and are available from 2006 to 2023, resulting in 272 time steps. The cloud types at each scanning line are compared to the HRV cloud mask at 13:30 by calculating the cloud fraction of 20 grid cells around the scan line, accounting for potential differences between the observation times of CALIPSO and HRV.

4.2.4 Relationships to vegetation and protected areas

To evaluate the effect of land restoration on cloud formation, we compare the computed cloud masks to spatial and seasonal changes in vegetation. The study area is separated into green areas (with a mean annual NDVI higher than 0.38), and less green areas (with a mean annual NDVI lower than 0.38). This value is chosen to roughly correspond to land cover boundaries in the study area. In addition, we compare cloud cover frequency to locations of protected areas from WDPA. Before calculating the size of the protected areas, adjacent areas are merged. A reference area is created for each merged protected area by creating a 10 km buffer around the boundary of the protected areas. If the buffer

overlaps with another protected area, this region is removed from the reference area. Next, the mean cloud cover frequency within each protected area and reference area is calculated, to determine the effect of area protection on cloud occurrence.

4.2.5 Relationships to convective initiation

Lastly, the vegetated areas are compared to the location of convective initiations, to determine if convection is more likely to occur over vegetated areas. Locations of convective initiation are obtained following the approach from Taylor (2015), with some minor adjustments. The MSG 10.8 μ m channel is used to identify the emergence of pixels with a brightness temperature of -40 °C or less every 15 minutes. A minimum cooling rate for the coldest nearby pixel within a radius of 30 km is applied to images over the preceding hour to ensure that the initiation is due to a rapidly deepening cloud, and to remove cases where cold clouds propagate into an area. A cooling rate of 10°C per hour is applied to pixels within 30 km of the initiation is sufficient to create a large dataset of independent initiations. Regions with strong topography are determined as having an elevation difference larger than 250 m within a circle with a diameter of 50 km (Taylor, 2015) (a sensitivity analysis with elevation differences larger than 100m is shown in Supplementary Figure 4.5). No filtering is applied for large water bodies as they are not largely present in the studied region. This results in a list of points representing the location of convective initiation. For each point, the distance to the contour line, where the NDVI is equal to 0.38, is calculated. Because a larger area is in principle more likely to have a higher number of convective initiations than a smaller area, the total number of points within a certain 5 km bin is divided by the total area that is located within this distance bin. This accounts for potential differences in surface area between the distance bins. This way, it can be determined if convection is more or less likely to initiate over greener areas, or at the boundary.

4.3 Results

4.3.1 Robustness of HRV cloud detection

Comparing the CALIPSO VFM cloud types with the HRV cloud mask at the corresponding scanning lines shows a high similarity of the cloud mask to the location of opaque or thick clouds such as cumulus and altostratus (Figure 4.1a-4.1c), with an overall accuracy (i.e. the fraction of correct classifications) of 80.0%. HRV clouds are classified as opaque cloud by CALIPSO with a success ratio of 89.2% and a false alarm ratio of 10.8%. Thin or transparent cloud layers like cirrus and altocumulus are often not detected in the HRV cloud mask (Supplementary Table 4.1-4.2). This is mainly a result of the threshold set in the HRV algorithm, where transparent clouds were preferably ignored, as they are not assumed to be affected by vegetation but rather by

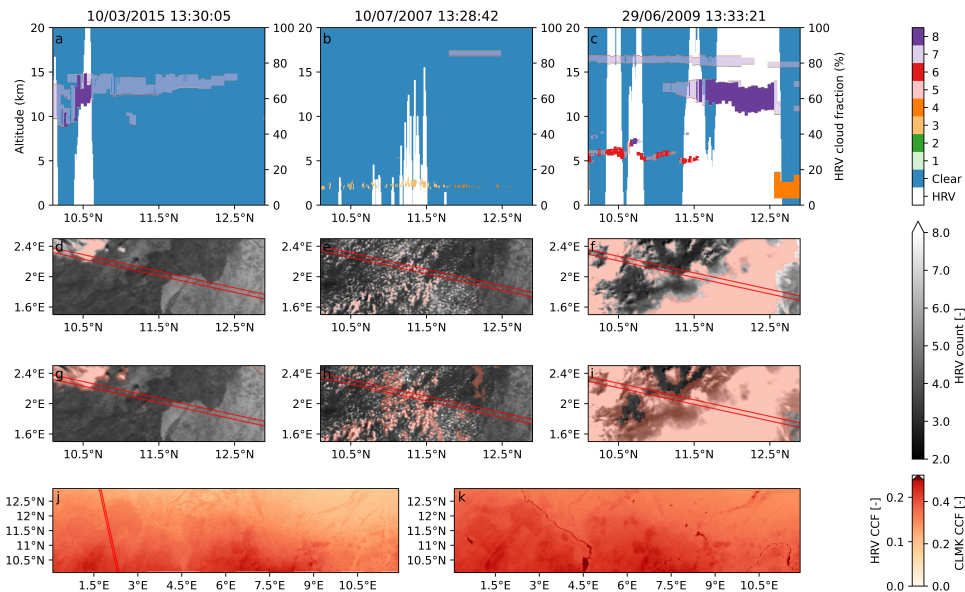


Figure 4.1 | Validation of the HRV cloud mask. (a-c) The validation is based on three CALIPSO Vertical Feature Mask (VFM) cloud type profiles on 10/03/2015, 10/07/2007 and 29/06/2009. The colours indicate different cloud types, where 1=low overcast (transparent), 2=low overcast (opaque), 3=transition stratocumulus, 4=low, broken cumulus, 5=altocumulus (transparent), 6=altostratus (opaque), 7=cirrus (transparent) and 8=deep convective (opaque). The white feature in the background indicates the cloud fraction according to the High Resolution Visible (HRV) algorithm within the scanning line on the same days at 13:30. The corresponding scanning line (red lines), HRV cloud mask (red shading) and HRV image are shown in (d-f). The standard 3km MSG cloud mask (CLMK) (red shading) and HRV image are shown in (g-i). The overall cloud cover frequency (CCF) is computed with the HRV cloud mask (j) and MSG cloud mask (k), based on roughly 321,200 images. Note that the longitude and latitude are switched in (d-i) to allow comparison to (a-c).

atmospheric conditions. In addition, only 34.0% of the CALIPSO opaque clouds are classified as clouded by HRV, often when the clouds are classified as opaque but visually appear relatively thin (Supplementary Figure 4.6). Combined with the high success ratio, this suggests that HRV generally has a higher threshold for cloud detection than CALIPSO.

The MSG cloud mask generally shows clouds at a similar location as the HRV cloud mask, although it often includes more transparent clouds (Figure 4.1d-4.1i). The overall cloud cover frequency (CCF), defined as the frequency of cloud cover occurrence at a certain location, calculated with the HRV cloud mask shows similar spatial patterns as the cloud cover frequency obtained from the MSG cloud mask (Figure 4.1j, 4.1k). Both show a clear north-south gradient in cloud cover corresponding to the increasing aridity in the northern part of the study area. In addition, both products show enhanced cloud occurrence at orographic regions such as the Atakora Mountains (Benin) and the Jos Plateau (Nigeria). Although the overall cloud cover frequency computed with the

HRV cloud mask is generally lower (typically 67%) than if the frequency is calculated with the MSG cloud mask, the spatial pattern is similar, with a coefficient of determination (r^2) of 0.87 (Supplementary Figure 4.7). This is possibly not only due to the lower threshold for cloud detection of the MSG cloud mask, as the MSG cloud mask detects both transparent and opaque clouds, but also caused by the lower spatial resolution, as mixed pixels result in a higher detection with a lower resolution.

4.3.2 Spatial and diurnal variations of vegetation-cloud relationships

Because we expect that land restoration will result in an increased amount of green vegetation (Ruijsch, Teuling, et al., 2023), we first study the relationship between vegetation greenness, represented by the Normalized Difference Vegetation Index (NDVI) (Didan, 2021), and cloud occurrence, obtained from the HRV images. We focus on two subregions within the study area to study vegetation-cloud relationships in more detail. Selecting smaller subregions reduces the influence of variations in aridity and elevation within the study area (Supplementary Figure 4.1). Subregion I is located on the border of Benin, Niger and Burkina Faso, on the northern edge of the transnational W-Arly-Pendjari Complex (12.2-12.7°N, 1.8-3.3°E), one of the largest protected areas in West Africa. The vegetation inside the protected area mainly consists of natural vegetation such as grasslands, savannah shrublands and gallery forests, while the regions outside the protected areas contain an increasing amount of cropland. The climate is dry, with a wet season from July to September (Schulte to Bühne et al., 2017). The total annual precipitation ranges between 654 mm in the north to 792 mm in the south, with an average of 728 mm, based on CHIRPS data (Funk et al., 2015). Previous research has shown that vegetation heterogeneities can affect boundary layer dynamics and cloud formation in this region (Garcia-Carreras et al., 2010). Subregion II is located in Nigeria and contains several small protected areas (10.8-11.3°N, 10.0-11.5°E). This region mainly consists of Sudanian savanna vegetation and cropland. Subregion II receives slightly more precipitation than Subregion I (between 767 and 1073 mm per year, with an average of 848 mm). Both subregions are roughly 55 x 160 km in size and contain sharp vegetation boundaries. However, the areas differ in the scale and heterogeneity of the vegetated areas (Figure 4.2a), providing information on the scale-dependence of vegetation-cloud relationships.

Starting with a visual inspection of the original HRV images in Subregion I, multiple days exist that illustrate an apparent connection between cloud occurrence and vegetation greenness, with pronounced cloud development over the green area of the W-Arly-Pendjari Complex (Figure 4.2b-4.2e). Similar, but less pronounced results can be seen in Subregion II (Figure 4.2f-4.2i). During these days, the clouds often develop at the beginning of the afternoon around the edge of the green region, and quickly move to the less green areas (Supplementary Animation 4.1-8). Later in the afternoon, clouds

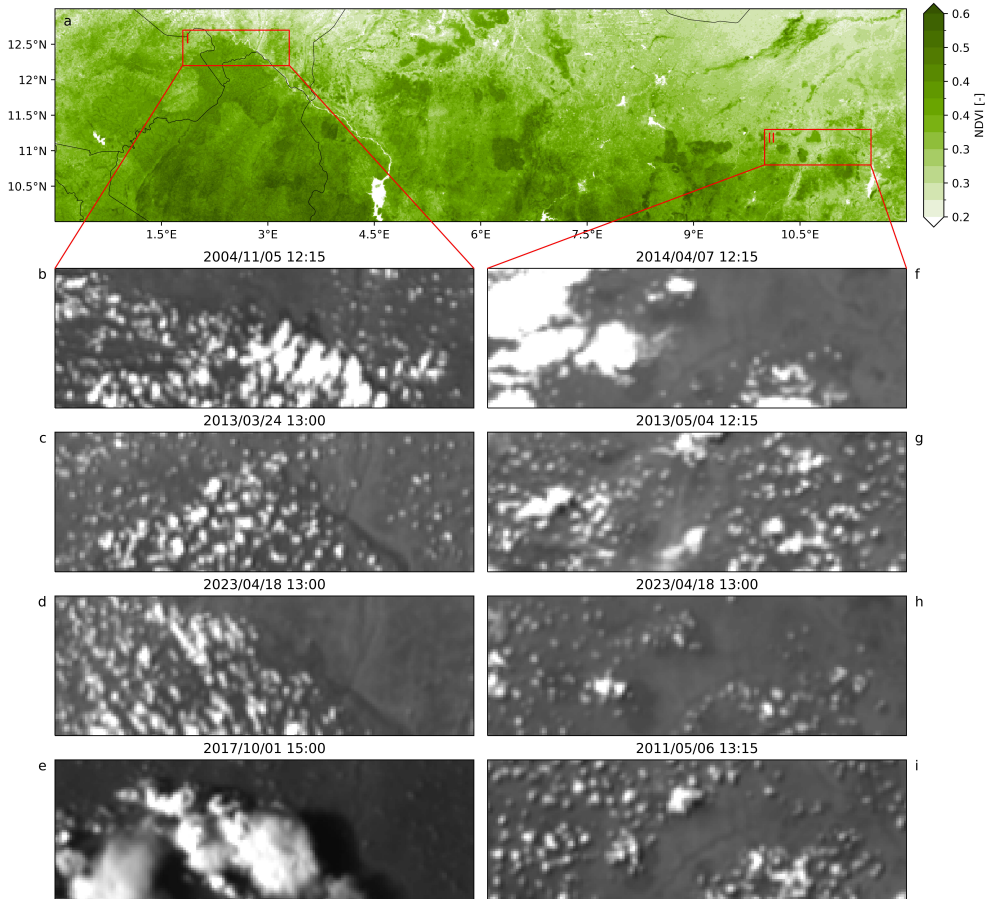


Figure 4.2 | Vegetation and cloud development. (a) Yearly mean Normalized Difference Vegetation Index (NDVI) between 2004/01/01 and 2024/01/01 in the study region. MSG HRV snapshots for (b-e) subregion I and (f-i) subregion II as indicated by the red boxes in (a). Animations of cloud development for the corresponding days are included in Supplementary Movie 4.1-4.8. The images are selected based on time steps that show a high difference in cloud cover fraction between regions with a high and low vegetation. They serve as illustration of days with a high connection between vegetation and cloud cover.

are also present above the less green regions, lowering the clear difference in cloud cover between the areas with low and high vegetation greenness. Days with higher cloud cover over the less green areas are also observed (Supplementary Figure 4.8).

Considering the whole 20-year period, the difference in fractional cloud cover between the green and less green regions (ΔFCC) is often small and positive, suggesting there is a tendency for more clouds above the green area. In Subregion I, ΔFCC is positive for 30.1% of the time, and negative for 20.1% of the time. For 49.7% of the time, there is no difference in cloud cover between the green and less green areas, which usually occurs during times when clouds are absent. In Subregion II, the results are similar to Subregion I, with a positive and negative ΔFCC for, respectively, 31.3% and 21.4% of

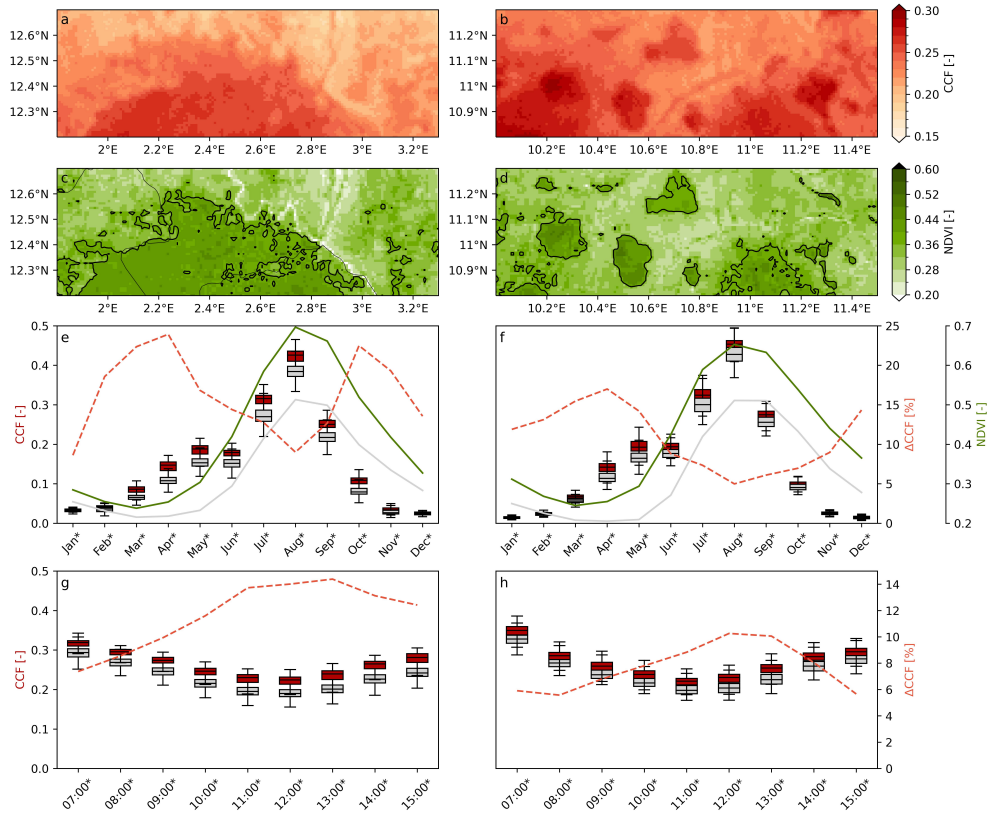


Figure 4.3 | Seasonal and diurnal evolution of vegetation-cloud cover relationships over two subregions. April-September 12:00-15:45 UTC cloud cover frequency (CCF) in (a) subregion I and (b) subregion II, based on ~58,560 individual HRV images. The subregions differ in the spatial scale of the green areas. (e-f) The seasonal and (g-h) diurnal evolution in CCF (boxes) and Normalized Difference Vegetation Index (NDVI) (lines) between areas with a high NDVI (green line, red boxes) and low NDVI (grey line and boxes) are shown for (c) subregion I and (d) subregion II. The high NDVI regions are defined as having a yearly mean NDVI higher than 0.38. The dashed line shows the mean relative difference in CCF (Δ CCF). Seasonal CCF variations are calculated for 12:00-15:45 UTC, the diurnal variations for April-September. Boxes show the median (line), interquartile range (box) and 1.5 times the interquartile range (whiskers) of the data. Note that one map of CCF is calculated for each month (based on ~12,200 images) (e, f) or hour (based on ~14,640 images) (g, h) first and that the boxes only represent the spatial variation. Stars (*) on the x-axis in e-h indicate a significant difference in mean CCF between the high NDVI and low NDVI areas ($p < 0.05$, using the Mann-Whitney U test). All hours and seasons show a significant difference.

the time (Supplementary Figure 4.9). High positive values of Δ FCC, when the clouds are mostly present over the green area, appear mainly between July and September, in the afternoon and early morning (Supplementary Figure 4.10). Interestingly, in Subregion II, the number of positive values of Δ FCC decreases in the late afternoon, while the occurrence of negative values of Δ FCC increases.

Over the whole study period (2004-2024) the cloud cover frequency (CCF) is higher over the green areas, with a positive spatial correlation (r^2) between NDVI and CCF for both Subregion I (0.69) and Subregion II (0.46). Including all months and hours of the day, the absolute (relative) difference between the green and less green areas is 0.01 (8%) in Subregion I and 0.01 (5%) in Subregion II. The difference in CCF is significant ($p < 0.05$) over all months, but is largest (in absolute terms) during the wetter and cloudier months (April-September) (Figure 4.3a-f). The small lower difference in cloud cover in the dry months is enhanced by the large number of cloud-free days.

The relative difference in CCF, however, is highest in April and October. Between April and September, the overall mean CCF in the green area of Subregion I is 0.03 higher than outside the green area, a relative difference of 16%. Both Subregions show this enhanced CCF over green areas during these months, although the difference is higher in Subregion I (0.03, 16%) than in Subregion II (0.02, 9%), even though the difference in mean NDVI is similar (0.09 in Subregion I and 0.10 in Subregion II). The higher CCF is consistent (and statistically significant) over the day, but generally more pronounced in the early afternoon (Figure 4.3g, 4.3h). Interestingly, the CCF is especially high in the early morning and decreases towards noon. A similar diurnal trend is seen in the CCF calculated with the 3 km MSG cloud mask (Supplementary Figure 4.11) and has been identified as nocturnal low-level stratus clouds that persist throughout the following day (Schuster et al., 2013; Adler et al., 2017; Aryee et al., 2021).

4.3.3 Scale-dependent cloud cover enhancement over protected areas

As a complete database of regions that have experienced land restoration is lacking for this region, we use the World Database of Protected Areas (WDPA) (Figure 4.4a) as a substitute to study cloud enhancement from land restoration. Although we acknowledge that land restoration does include a wider range of practices than area protection alone, the protected areas show a consistent increase in NDVI over the past years that is higher than the areas that are not under protection (Supplementary Figure 4.12). This is a result that is also expected under land restoration, which justifies the use of the WDPA data in this study. However, it should be noted that this does not necessarily imply that all the increases in NDVI are directly caused by land restoration or area protection, but also processes such as woody encroachment may contribute (Brandt et al., 2017).

Across the study region, the protected areas have a generally higher NDVI than surrounding regions (Figure 4.4b) and a slightly lower elevation (Figure 4.4c). The April-September cloud cover frequency is enhanced over protected areas, although some of the smaller projects show a lower cloud cover frequency inside the protected areas than outside. On average, the April-September cloud cover frequency inside the protected areas is 0.02 (10.8%) higher than in surrounding areas. Interestingly, there is a significantly positive relationship ($p = 0.002$) between the project size and the

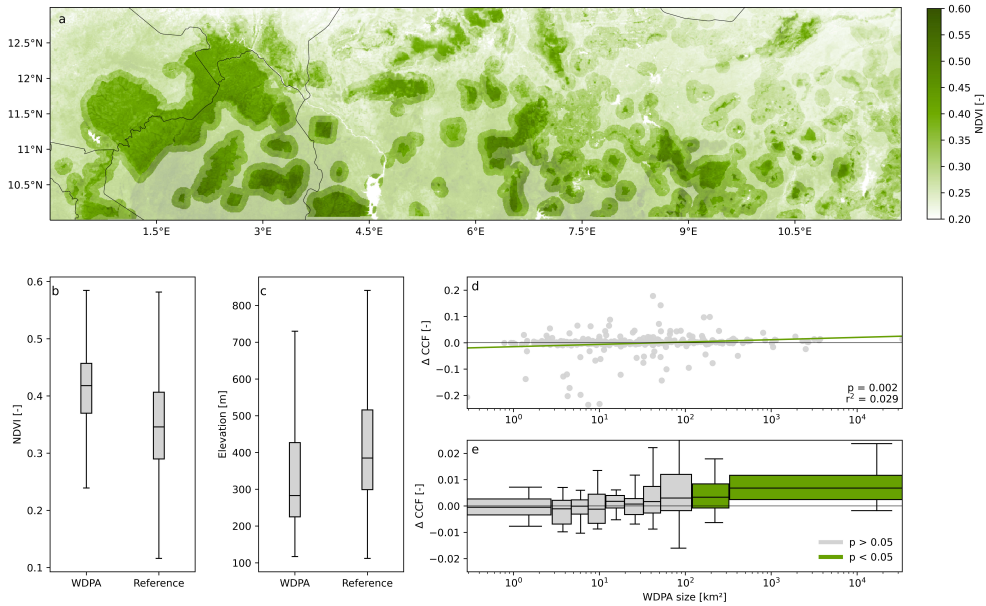


Figure 4.4 | Scale dependent effects of area protection on cloud cover. (a) Location of World Database of Protected Areas (WDPA) (opaque) and reference areas (semi-transparent) in the study region (transparent). (b) Difference in mean annual Normalized Difference Vegetation Index (NDVI) and (c) elevation between the WDPA and reference areas. (d, e) The difference in average April-September 07:00-15:45 cloud cover frequency (Δ CCF) between the WDPA and the corresponding reference area, per size of the WDPA area. The reference area consists of a 10 km buffer around the WDPA area, where overlapping WDPA areas are not considered. Points in d show Δ CCF for the individual areas. The line shows a linear regression between Δ CCF and $\log(\text{WDPA size})$. The green line in (d) shows a linear least-squares regression, including the Pearson's correlation coefficient (r^2) and statistical significance (p) calculated with the Wald test. Boxes in e show the median (line/point), the interquartile range (box) and 1.5 times the interquartile range (whiskers) of the data grouped per 10-percentile of WDPA size. Each box contains 32 WDPA areas. The width of the boxes represents the range of WDPA sizes within the 10-percentile. Note that CCF is first averaged over time (based on ~131,760 individual images) and within the WDPA area and the reference areas, after which the Δ CCF is calculated. The boxes represent the variation in Δ CCF across WDPA areas only. Green boxes indicate that the median is significantly different to zero ($p < 0.05$, using the Wilcoxon signed-rank test). Results for a 5 km and 15 km buffer are respectively shown in Supplementary Figure 4.13 and 4.14, illustrating a larger variation in Δ CCF with a larger buffer.

degree of cloud cover enhancement (Figure 4.4d), although the spread is large. The strongest enhancement of clouds is observed over larger protected areas, and the difference in cloud cover between the protected area and the surrounding area is significant for the 20% largest projects, with an area larger than 121 km² (Figure 4.4e). Although the level of spatial heterogeneity in itself affects cloud formation through mesoscale circulations, it should be noted that also the NDVI difference between the protected and reference areas increases with size (Supplementary Figure 4.15), which may contribute to this size-dependent relationship.

4.3.4 Convective initiation

To further explore the potential of green areas to create these mesoscale circulations, we extend the analysis to consider the climatology of where deep convection is initiated. Triggering deep convection is an important component of land restoration in enhancing rainfall, as precipitation totals in this region are dominated by deep convective systems (Maranan et al., 2018). The locations of convective initiations are identified as rapidly cooling MSG pixels which reach a temperature threshold of -40°C (Taylor, 2015). This results in 40,169 point locations of convective initiations between 10:00 and 16:30 UTC over the whole study area, corresponding to 11:00 and 17:30 in local time Nigeria, Niger and Benin. In Subregion I, there is a pronounced difference in the total number of convective initiations above green areas (with an NDVI higher than 0.38) and above less green areas (Figure 4.5a, 4.5c, 4.5e). In Subregion II, convection is initiated above the larger green areas as well, although a considerable number of convective initiations occur at the boundaries of the smaller green areas at the centre of the subregion (Figure 5b, 5d, 5f). To reconcile with previous research, we studied the distance of the convective initiation to the boundaries in vegetation greenness (where NDVI = 0.38). Both in Subregion I and Subregion II, the relative number of convective initiations in this dataset does decrease further from the boundary, at least on the less green side (Figure 4.5g, 4.5h).

On the green side of the boundary, the relative number of initiations is highest around 10 km from the boundary, but decreases towards the boundary and further inside the green area. It should be noted, however, that vegetation often co-varies with topography (Sandel & Svenning, 2013). In Subregion II, for example, a number of convective initiations are located over regions that have both a high vegetation greenness and elevational differences, making it difficult to separate the effect of these variables on convective initiation. In Subregion I, topography is expected to have a limited effect on convective initiation due to the lower variations in elevation (Supplementary Figure 4.16).

4.4 Discussion and conclusions

In this study, data from the MSG High-Resolution Visible broadband channel is used to study the effect of land restoration on cloud formation in West Africa on a 1 km spatial resolution. Although the applied algorithm only uses information from the visible range of the spectrum, the results show a high similarity to both the standard MSG cloud product and opaque and thick cloud types derived from CALIPSO scanning lines. Zooming in to two subregions in the protected W-Arly-Pendjari Complex (Subregion I) and smaller protected areas in northern Nigeria (Subregion II), we observe enhanced cloud formation above green areas with a high NDVI, especially between April and September. Although the absolute difference is highest in August, the relative difference

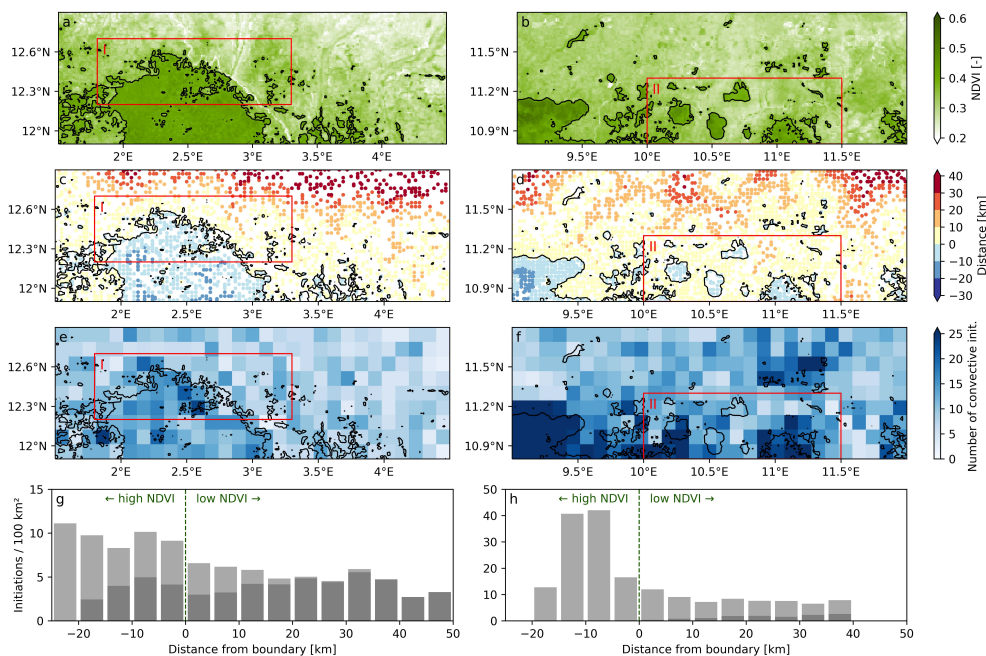


Figure 4.5 | Convective Initiation and vegetation. (a, b) Mean annual Normalized Difference Vegetation Index (NDVI), (c, d) locations of individual convective initiations and (e, f) total number of convective initiations gridded with a resolution of 0.11 degree (~ 12.3 km) between 2004 and 2023 in Subregion I (left) and Subregion II (right). Black lines indicate the contours where the mean NDVI is 0.38, to distinguish between high and low vegetation areas. The colours in (c, d) show the distance to this contour. (g) and (h) show the number of convective initiations per distance to the NDVI contour boundary, relative to the total area with the same distance to the boundary. The lighter shades of grey in (h) include points of convective initiation over regions with topographical differences higher than 250 m over a distance of 25 km in all directions. The histograms in (g) and (h) are based on 2,389 and 3,952 moments of convective initiation, respectively. Negative (positive) distances indicate that the NDVI is higher (lower) than 0.38. The data includes convective initiations between 10:00 and 16:30 UTC over all months of the year.

is especially high, up to 25%, in April and October, just before and after the wet season. This is confirmed by visual evidence of days where the cloud cover shows a high spatial resemblance to the vegetation greenness. The increased influence of the surface properties on cloud formation at the beginning and end of the wet season has also been observed in previous studies (Taylor et al., 2011; Tuinenburg et al., 2011). During the dry season, the atmosphere is too dry for clouds to form, independent of surface conditions, while during the wet season, clouds form relatively easily over both green and less green areas (Findell & Eltahir, 2003a). In addition, during the core of the wet period in July and August, the connection between the surface and the atmosphere is expected to be slightly weaker compared to the other months in the wet season because evaporation is less limited by water availability (Lohou et al., 2014; Taylor, Klein, Dione, et al., 2022).

Several mechanisms could contribute to cloud enhancement or inhibition over green areas. A relatively low albedo and high surface roughness in the green area (Supplementary Figure 4.17c, 4.17d) will increase the net radiation and the sensible and latent heat fluxes, consistent with estimated long-term averages of these fluxes provided by Land Surface Analysis data based on MSG SEVIRI (Ghilain, Arboleda, & Gellens-Meulenberghs, 2011; Ghilain, Arboleda, Sepulcre-Cantò, et al., 2011) (Supplementary Figure 4.17e-j), which promotes boundary layer growth and cloud formation (Teuling et al., 2017b; Bosman et al., 2019; Branch & Wulfmeyer, 2019). At the same time, the expected higher evapotranspiration within the green area (Spracklen et al., 2018) can provide an extra input of atmospheric moisture and lower the lifting condensation level, favouring cloud formation over regions with high evaporation (Findell & Eltahir, 2003a; Garcia-Carreras et al., 2017) on the condition that the planetary boundary layer growth driven by the sensible heat flux is sufficiently large. On shorter time scales, variations in soil moisture also contribute to conditions with strong land-atmosphere coupling, both by providing a source for atmospheric moisture and affecting the height of the sensible heat flux. In West Africa, we often observe an enhanced cloud formation over regions with a negative soil moisture anomaly due to the enhanced sensible heat flux (Taylor et al., 2012; Ellison & Speranza, 2020).

Inhibition of clouds over green areas through heterogeneities in vegetation has been observed in other areas, when differences in turbulent fluxes and surface roughness between the green areas and their surroundings trigger convection through mesoscale circulation and convergence (Birch et al., 2014). If the sensible heat flux is lower over green areas than the neighbouring less green areas (due to a higher share of net radiation going to the latent heat flux), a forest breeze develops where moist air from the green areas is lifted by the higher sensible heat flux above the less green areas (Spracklen et al., 2018). Combined with convergence due to differences in surface roughness, these thermally driven mesoscale circulations have been shown to enhance convective initiation above deforested patches in closed-canopy tropical forests where the sensible heat flux is higher over deforested patches (Garcia-Carreras et al., 2010; Taylor, Klein, Parker, et al., 2022). The strength and occurrence of these circulations depend on atmospheric conditions and the scale of the deforested patches (Khanna et al., 2017). Also in the Sahel, thermally-driven circulations have been shown to have a pronounced impact on convective initiation, with enhanced cloud development over areas with high sensible heat flux (Taylor et al., 2011). Whether clouds are enhanced over green or less green areas depends on the relative contribution of the above processes. On a global scale, cloud enhancement over green areas is most likely when the green area has a higher sensible heat flux than neighbouring areas, and vice versa (Xu et al., 2022). Also in this study, we observe a significant cloud cover enhancement over the largest protected areas, which could be caused by differences in sensible heat flux and spatial heterogeneity.

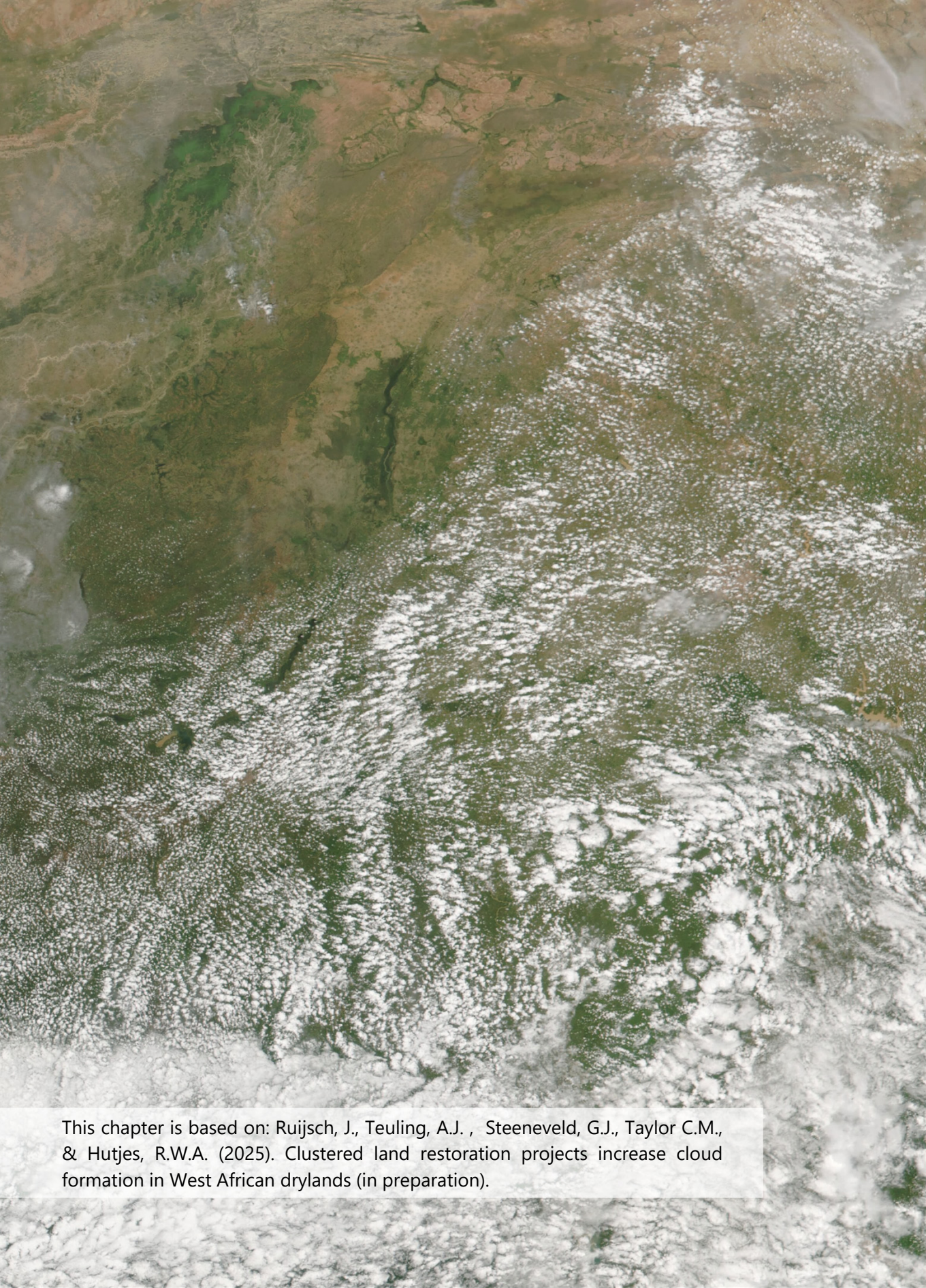
In contrast to previous research, however, we find convective initiation mainly on the green edge of the boundary. Garcia-Carreras et al. (2010), for example, showed through aircraft measurements over the southern edge of the W-Arly-Pendjari Complex, a tendency for convection on the non-forested and warmer side of vegetation heterogeneity. Yet, as many studies suggest enhanced convection over the warm side of the boundary, conditions with a higher sensible heat flux over the greener area, either due to the low albedo or high surface roughness, could explain our results (Xu et al., 2022) and the apparent discrepancies with previous research. Global data suggest that the average sensible heat flux is indeed higher over woody savanna and savanna regions than over grasslands and croplands (Lin et al., 2022), although comparative measurements of surface fluxes between vegetation types in West Africa are limited. Regarding circulations induced by differences in surface roughness, convergence is expected to be largest on the upwind side of the green area (Taylor et al., 2011; Sührling et al., 2014) on the south side of the W-Arly-Pendjari Complex (Supplementary Figure 4.17m, 4.17n). However, topography complicates the analysis of the link between vegetation and convective initiation in that region.

Although all the above mechanisms likely contribute to cloud formation to some degree, we are unable to quantify the relative contribution of these mechanisms from observations, due to a lack of reliable information on the effect of vegetation types and greenness on the sensible and latent heat fluxes in West Africa. More in-depth modelling studies or field measurements are needed to provide more insight into the precise mechanism of cloud enhancement in this study region during these specific days of cloud development because it remains uncertain how the sensible heat flux responds to changes in vegetation cover in West Africa or similar climate zones. Yet, also modelling may come with uncertainty in data-scarce regions.

Although this study is mainly a spatial comparison between regions with low and high vegetation greenness, the results suggest that land restoration can affect cloud formation in West Africa if the vegetation cover, or heterogeneity therein, is increased. However, as the differences in NDVI over space may be larger than the attainable increase in NDVI over time due to restoration, we expect the cloud cover effect of land restoration (i.e. a change in vegetation over time) to be smaller than the effects of spatial differences found in this study. Unfortunately, climate change and variability between years make analysing trends in cloud cover challenging. Running land restoration scenarios with weather or climate models is therefore needed to address these uncertainties.

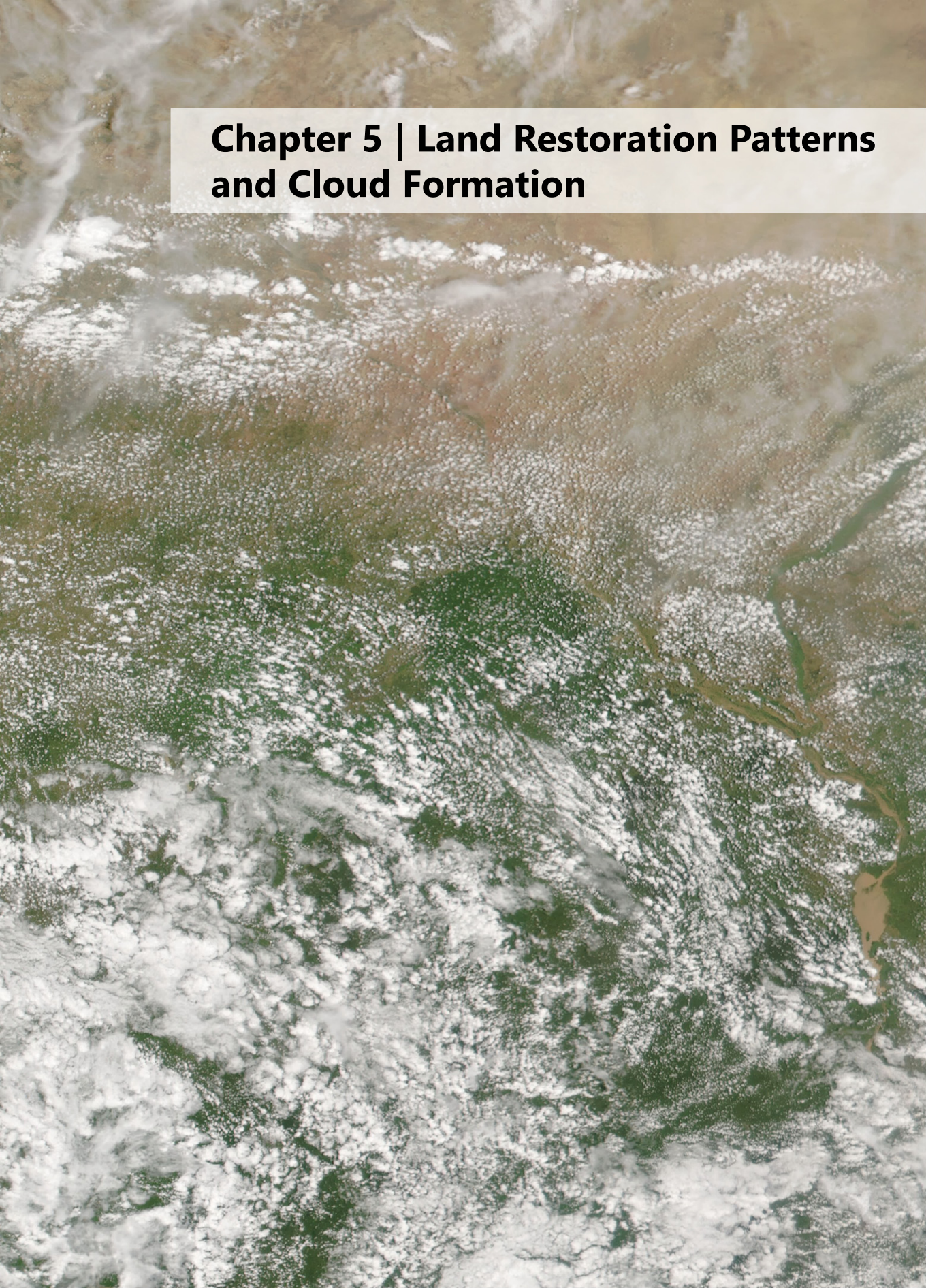
It is estimated that mesoscale convective systems provide as much as 90% of the rainfall in the Sahel (Mathon et al., 2002). In addition, a considerable amount of rainfall in the Sahel (10-40%) (Keys et al., 2016) and Africa (50%) (Te Wierik et al., 2022) originates from vegetation-based evaporation. Yet, more research is needed to determine to what extent the enhanced cloud formation results in deep convection and

rainfall, within a region or elsewhere, and to what extent protected areas may have an effect on the total rainfall and water availability in a larger region (Ellison & Speranza, 2020). On top of that, it remains unclear how the changing climate will affect the land-atmosphere feedbacks in West Africa in the future (de Arellano et al., 2012; Soares et al., 2019; Chen, Dai, et al., 2020; Fitzpatrick et al., 2020). Yet, this research provides observational evidence that land restoration, especially larger projects, can impact cloud formation in dryland regions in West Africa, which is especially relevant given the current implementation of projects within this region and worldwide.



This chapter is based on: Ruijsch, J., Teuling, A.J. , Steeneveld, G.J., Taylor C.M., & Hutjes, R.W.A. (2025). Clustered land restoration projects increase cloud formation in West African drylands (in preparation).

Chapter 5 | Land Restoration Patterns and Cloud Formation



Abstract | Land restoration projects are implemented across Africa to combat land degradation and climate change. By changing the vegetation cover, these projects can potentially impact cloud formation through changes in energy and water partitioning between the Earth's surface and the atmosphere. In West Africa, satellite observations have shown an increase in cloud formation over restored areas. However, even though the topology of restored areas differs between greening approaches (such as farmer-managed natural regeneration, area protection or reforestation), it is unknown how the spatial pattern of restoration projects impacts cloud formation. In this study, we use the WRF mesoscale atmospheric model to determine how land restoration affects cloud formation for a case study at the border of the transnational W-Arly-Pendjari national park complex, with a sharp boundary between forest and grassland. First, we carry out a sensitivity analysis to determine the underlying mechanisms of cloud formation over forest regions, after which we run 27 land restoration scenarios with varying forest cover and spatial clustering to assess the impact of land restoration patterns on cloud formation. The results highlight that a higher clustering of intermediate forest cover (21% and 42%) increases cloud formation due to stronger mesoscale circulation, while smaller-scale heterogeneity or high forest cover (85%) inhibits cloud formation. Because clouds play an important role in the Earth's water and energy balance, these results provide important insight into how projects can be designed to increase their climate benefits.

5.1 Introduction

Land restoration is seen as a promising solution to combat land degradation and climate change through carbon sequestration (Roe et al., 2019; Cook-Patton et al., 2020), while it simultaneously provides ecosystem services such as wood, food, shade and income when implemented in the right way (Holl & Brancalion, 2020). In West African drylands, which are especially vulnerable to land degradation and climate change (Prävälíe, 2021), many countries have pledged to restore land (PBL, 2020) or implemented restoration projects under the current United Nations Decade of Ecosystem Restoration (UNEP, 2021). These projects aim to restore vast areas of land to mitigate climate change, enhance biodiversity and combat land degradation (Martin et al., 2021) and include, for example, natural regeneration, area protection, farmer-managed natural regeneration, or active reforestation (tree planting).

In addition to climate change mitigation through carbon sequestration, land restoration also directly impacts the local climate through biophysical processes. Regions with a high vegetation cover often have a higher aerodynamic roughness, lower albedo, and transpire more water than nearby regions with a lower vegetation cover, increasing energy and water exchange between the Earth's surface and the atmosphere (Bonan, 2008; Duveiller et al., 2018b; Hoek van Dijke et al., 2022). On a local scale, the increased evaporation often has a cooling effect on the restored area (Feldman et al., 2022; Ruijsch et al., 2024; Zhang et al., 2024), which can provide comfort for the local population (Vancutsem et al., 2010; Wolff et al., 2018). However, globally, the decreased albedo of restored areas will increase surface temperatures. This so-called albedo warming is increasingly being acknowledged when implementing land restoration projects (Windisch et al., 2021; Hasler et al., 2024; Kirschbaum et al., 2024; Kristensen et al., 2024).

In addition to temperature, land restoration can also impact boundary layer development and cloud formation through land-atmosphere interaction. Regions with a high vegetation cover (e.g. forests) often have a low albedo which results in a higher amount of available energy at the surface. Combined with a high aerodynamic roughness, this provides the heat and turbulence necessary for daytime boundary layer growth. In addition, a relatively high evapotranspiration adds moisture to the atmosphere and lowers the lifting condensation level and level of free convection. This combination of available energy and moisture can result in enhanced cloud formation over areas with a high vegetation cover (Teuling et al., 2017b; Bosman et al., 2019). However, the enhanced evapotranspiration over vegetated areas also increases the allocation of available energy to the latent heat flux, at the expense of the sensible heat flux. This reduces boundary layer growth and can in some cases result in reduced cloud formation over vegetated areas compared to nearby sparsely vegetated regions. For example, although temperate and boreal forests in Europe, Asia and North America often show cloud enhancement, tropical forests in the Amazon and Central Africa

inhibit cloud formation (Xu et al., 2022). These regions with enhanced cloud formation correspond to regions where the forest has a higher sensible heat flux compared to reference regions, assuming there is enough water vapour present in the atmosphere to condensate (Taylor, Klein, Parker, et al., 2022; Xu et al., 2022).

However, the impact of vegetation on cloud formation also depends on its surroundings. If a forest borders sparsely vegetated areas, the differences in temperature and surface roughness can trigger thermally or dynamically driven mesoscale circulation and convergence (Garcia-Carreras et al., 2010; Birch et al., 2014; Spracklen et al., 2018), which are sometimes referred to as forest-breezes. Whether this is the restored region or the surrounding regions with lower vegetation cover depends on whether the restored region is relatively cold (due to increased evapotranspiration) or warm (due to the decreased albedo). In addition, the effect of forests on cloud formation can vary through time (Qin et al., 2025). Similarly, if evapotranspiration is limited by soil moisture, dry conditions result in a higher allocation of net radiation towards the sensible heat flux, increasing surface temperature (Miralles et al., 2012) and boundary layer development (Findell & Eltahir, 2003a; Ek & Holtslag, 2004). Through changes in the surface energy balance, soil moisture anomalies and gradients can impact convection, mesoscale circulations and precipitation (Taylor et al., 2007; Taylor et al., 2012; Westra et al., 2012; Taylor, 2015; Klein & Taylor, 2020). This important role of vegetation in cloud formation is often overlooked when restoration projects are implemented, as the complex interaction of these processes makes it difficult to predict how restoration will impact cloud formation in a particular region (Lawrence et al., 2022).

In West Africa, satellite observations have shown enhanced cloud formation over restored areas (Ruijsch et al., 2025). However, the existence of mesoscale circulation, convergence and forest-breezes suggests that the spatial context of land restoration projects is an important factor determining cloud enhancement. Cloud enhancement has been, for example, observed only over project areas larger than roughly 10 by 10 km (Ruijsch et al., 2025). In addition, previous research shows that simultaneously increasing tree heterogeneity and tree cover enhances cloud formation in Africa by 55.2% compared to a uniform increase in tree cover (Xie et al., 2025). Idealised land cover simulations show that sharp land cover boundaries initiate convective initiation at the land cover boundaries (Ascher et al., 2025), depending on the scale of the heterogeneities (Chen & Avissar, 1994; Lynn et al., 1998). Yet, it remains unknown how (realistic) spatial patterns in which the land restoration projects are implemented influence cloud formation, even though different types of land restoration projects may result in considerably different spatial patterns of vegetation. For example, farmer-managed natural regeneration is expected to result in smaller patches of vegetation within an agricultural or grassland region. Protected areas or active reforestation, on the other hand, will create large, continuous patches of vegetation.

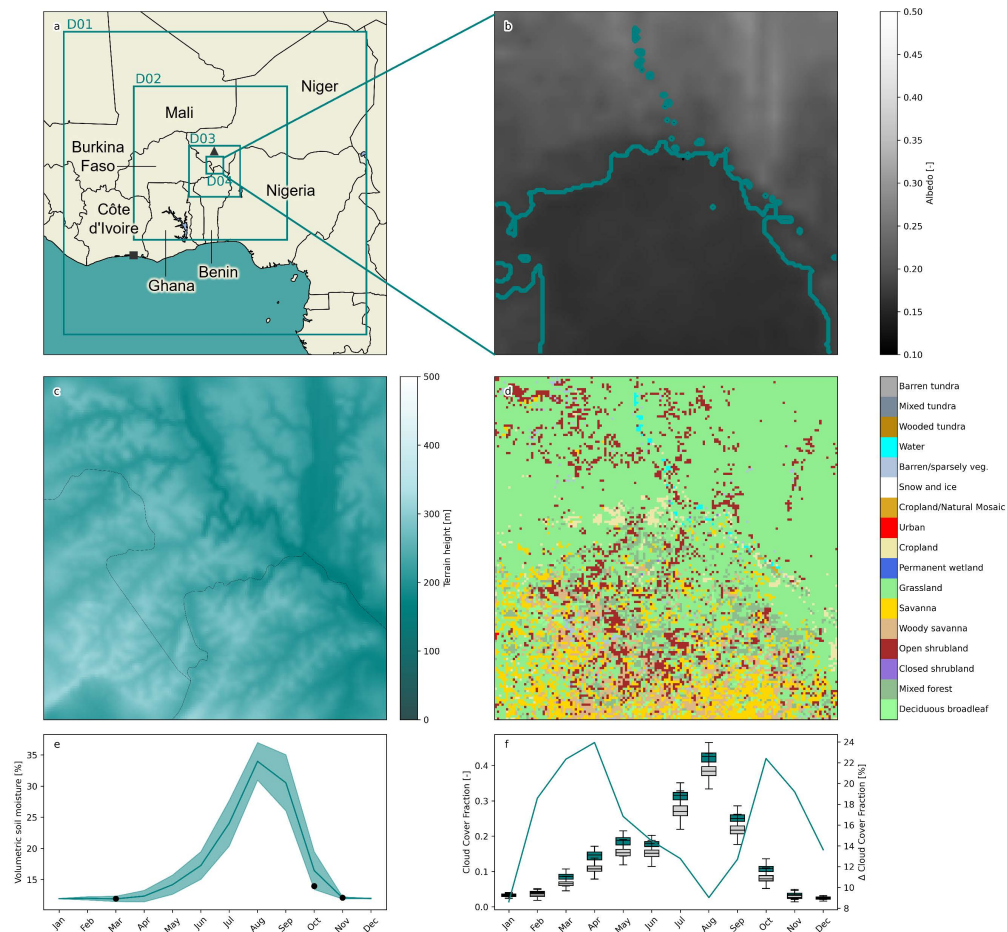


Figure 5.1 | Study area and period. (a) WRF model domains and validation locations in Niamey (grey triangle) and Abidjan (grey square). (b) MODIS albedo on 2017/10/01 in Domain 4. The line indicates the edge of the forest region. (c) Topography and (d) MODIS land cover as used in the model in Domain 4. (e) Climatology of soil moisture content from ERA-5 and (f) climatology of cloud cover fraction in the forested (blue boxes) and grassland (grey boxes) area. The line shows the relative difference in cloud cover fraction between those two regions. Data in this panel is obtained from (Ruijsch et al., 2025).

This research aims to close this gap by determining how the spatial pattern in which land restoration projects are implemented affects cloud formation in West African drylands. However, the many factors impacting cloud formation result in noisy signals, which would make it difficult to extract relations from observation data alone. On top of that, the limited flux measurements make it challenging to determine underlying cloud development mechanisms. To this end, we use the Weather Research and Forecasting (WRF) model (Skamarock et al., 2019) to simulate cloud formation in West Africa. First, we run the model with the current vegetation cover over a study region with a sharp boundary between forest and non-forest (Figure 5.1) to determine how different surface characteristics (i.e. albedo, surface roughness and soil moisture) affect

cloud formation. Even though land restoration can encompass a wide range of measures, we compare a forested protected area to a surrounding grassland area as a proxy for the potential effects of land restoration on cloud formation. Using this knowledge, we simulate several realistic land restoration scenarios with varying forest extent and spatial clustering to determine how the spatial pattern of land restoration affects cloud formation.

Our results can inform land restoration projects on how their project design may impact cloud formation through changes in vegetation cover. Ultimately, this may lead to the optimisation of project design to obtain maximum climate benefits. Clouds provide shade and play an important role in initiating convective rainfall in the Sahel (Mathon et al., 2002) through which land restoration can impact water availability on a larger scale (Hoek van Dijke et al., 2022; Te Wierik et al., 2024). This may be needed to sustain restoration projects in dryland regions. At the same time, clouds impact the energy balance of the Earth and have the potential to impact global climate patterns (Goessling et al., 2025), both through trapping heat emitted by the Earth's surface and reflecting incoming solar radiation. Determining the impact of land restoration on cloud formation is, therefore, a crucial next step to form a more complete understanding of the overall climate effect of land restoration.

5.2 Methodology

5.2.1 Case study description

We focus on a study region in West Africa. The region of interest is 150 by 150 km and located on the northernmost edge of the W-Arly-Pendjari Complex, a transnational protected area on the borders of Benin, Niger and Burkina Faso (11.7–13.1°N, 1.8–3.2°E) (Figure 5.1a). This case study area was selected because the border of the protected area shows a clear boundary in land cover and albedo (Figure 5.1b) and limited elevation differences (Figure 5.1c). The region inside the protected area mainly consists of natural vegetation types like savanna, shrublands and mixed forest, whereas the outside region largely consists of grassland (Figure 5.1d). Satellite observations between 2004 and 2024 show a structurally higher cloud cover fraction over the protected area compared to the surrounding region, with large relative differences at the start and end of the wet season (Figure 5.1f) (Ruijsch et al., 2025). To meet computational constraints, we selected three case study days (2017/10/01, 2004/11/05, and 2013/03/24), ahead of and following the rainy season (Figure 5.1e). These days were selected because they show a clear distinction in cloud development over the forested area compared to the grassland area, ensuring a day with land-atmosphere coupling and a potential effect of the forest cover on cloud formation. During these days, a light wind (roughly 5 knots) is coming from the southwest (Figure

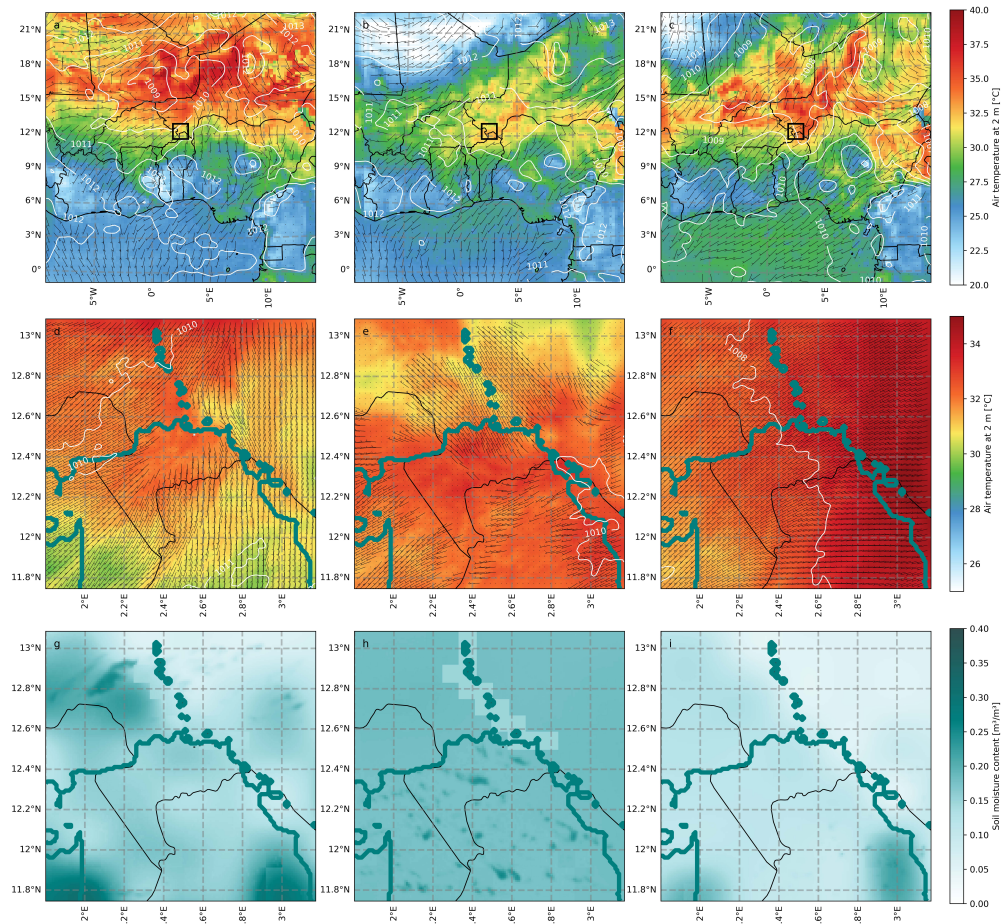


Figure 5.2 | Atmospheric and soil moisture conditions on study case study days. Simulated air temperature at 2m (colours), air pressure at sea level (white contours), and wind direction (black arrows) in Domain 1 (a-c) and Domain 4 (d-e) at 09:00 during case study Day 1 (left), Day 2 (middle) and Day 3 (right). Country borders are indicated with black lines. The location of Domain 4 is indicated with a black square in (a-c). The initial soil moisture content distribution as provided by ECMWF operational analysis across Domain 4 for the same days is shown in (g-h). The blue line in (d-i) indicates the edge of the forest region.

5.2a-f). In addition, the soil moisture content in the southwest and southeast of the domain is relatively high compared to the forested area and the northeast grassland area (Figure 5.2g-i). On Day 2, the soil moisture content is more homogeneous across Domain 4.

5.2.2 Model description and configuration

The (Advanced Research) Weather Research and Forecasting model (WRF-ARW) version 4.1.4 is run for the three case study days with four nested model domains

Table 5.1 | Characteristics of the model domains. Domain name, number of horizontal and vertical grid cells, domain size, grid cell size and coordinates of the model domains.

Domain	Number of grid cells	Domain size	Grid cell size	Domain latitude and longitude (NW, SE)	Time step (Day 1 & Day 2, Day 3)
D01	100x100	2700x2700 km	27km	(22.683, -10.259), (-1.165, 14.260)	162 seconds, 100 seconds
D02	151x151	1359x1359 km	9km	(18.556, -4.230), (6.458, 8.226)	32.4 seconds, 20.0 seconds
D03	151x151	453x453 km	3km	(13.946, 0.376), (9.901, 4.513)	6.48 seconds, 4.00 seconds
D04	151x151	151x151 km	1km	(13.090, 1.794), (11.741, 3.175)	1.30 seconds, 0.80 seconds

Table 5.2 | WRF model schemes used in this study. The name of the model scheme used for different model components.

Name	Used scheme	Source
Boundary Layer	YSU scheme	Hong et al. (2006)
Surface Layer	Revised MM5 Monin-Obukhov scheme	Grell et al. (1994)
Land surface	Unified Noah land-surface model	Chen, Haase, et al. (2022)
Cumulus	Grell-Freitas ensemble scheme (domain 1 and 2)	Grell and Freitas (2014)
Microphysics	WSM 6-class graupel scheme	Hong and Lim (2006)
Shortwave radiation	rrtmg scheme	Oreopoulos and Barker (1999)
Longwave radiation	rrtmg scheme	Oreopoulos and Barker (1999)

(Figure 5.1a) with decreasing grid sizes of 27 km in the largest domain and 1 km in the smallest domain (Table 5.1). The initial and boundary conditions, including soil moisture, are provided by the European Centre for Medium-Range Weather Forecasts (ECMWF) operational analysis with a 0.25 spatial grid length and a 6-hour temporal resolution. The model albedo, land use classes and leaf area index values are based on MODIS climatology data (Broxton et al., 2014), with a 1 km grid length in the smallest domain.

In the two largest domains, cumulus development is parameterised using the Grell-Freitas ensemble scheme, while in the smallest domains, the spatial grid length (1-3 km) is low enough to assume that the cumulus development is resolved. The land surface is represented by the Unified Noah land-surface model. The other parameterisations, considered suitable for answering the research questions (Klein et al., 2015; Achugbu et al., 2020) are listed in Table 2. The start of the simulation was set to 00:00 UTC one day prior to the selected day, to act as spin-up, and run until 23:59

UTC the next day, resulting in a simulation period of 48 hours. The model top is set to 3000 Pa, with 8 levels in the lowest 1 km. For Day 1 and Day 2, the model is run with a timestep of 162 seconds (in Domain 1) and 61 vertical levels. To ensure model stability, Day 3 is run with a timestep of 100 seconds and 81 vertical levels. Output data is provided on a 15-minute temporal resolution.

5.2.3 Model evaluation

The model results are evaluated against multiple sources. We used radiosonde measurements from the University of Wyoming Upper Air Sounding Dataset (University of Wyoming, 2025) to evaluate vertical profiles of potential temperature, temperature, wind speed and wind direction. Because soundings are limited in Africa, no soundings were available in Domain 4. To this end, we compared model results in Domain 3 and Domain 1 with radiosonde measurements in, respectively, Niamey, Niger (13.48°N, 2.16°E) and Abidjan, Côte d'Ivoire (5.25°N, 3.93°W) (Figure 5.1a). The soundings are available for the three case study days at 12:00 UTC, except on 2004/11/05, where data were only available in Niamey.

To evaluate the modelled cloud formation, we use cloud masks derived from the High Resolution Visible band of the SEVIRI sensor onboard the Meteosat Second Generation Satellites (Ruijsch et al., 2025). Because we are interested in cloud formation over forest and grassland areas, we separate the study area into a 'forest' area and a 'grassland' area. The forest area is defined as having a mean albedo lower than 0.175 on 2017/10/01, similar to the forest area in Ruijsch et al. (2025) and visibly matching the land cover boundary (Figure 5.1b). The grassland area is the remaining part of the domain. The same forest boundary is used for all case study days. Since cloud masks are not directly provided by the WRF model outputs, we defined a cloud mask based on locations where the liquid water path (LWP) in the vertical column exceeds 1 mm (1000 g/m²) (Supplementary Figure 5.1). The fractional cloud cover can then be defined as the fraction of clouds compared to the total area (the forest area, the grassland area or across the entire domain). The cloud cover fraction development over the forest and grassland area during the case study days is then compared to the cloud cover fraction observed with the satellite data. We compared the observed cloud cover fraction to the simulated cloud cover fraction in Domain 4 between 11.7°N and 13.0°N.

5.2.4 Sensitivity analysis

To provide more insight into underlying relations between forests and cloud development, we carried out a sensitivity analysis by varying the albedo, surface roughness and soil moisture, all of which are expected to impact cloud formation. The parameters are varied over the forest area only, by multiplying the reference value provided by the MODIS and ECMWF operational analysis data with a certain

Table 5.3 | Multiplicative factors for the sensitivity analysis. The albedo, surface roughness and soil moisture content area all changed in three steps, resulting in a total of 27 model simulations for the sensitivity analysis.

Parameter	Step 1	Step 2	Step 3
Albedo	1.00	0.75	0.50
Surface roughness	1.00	1.50	2.00
Soil moisture	1.00	1.50	2.00

multiplication factor. Each parameter changed in three steps (Table 5.3), resulting in 27 parameter combinations (Supplementary Figure 5.2). The albedo is decreased, and the surface roughness and soil moisture content are increased relative to the grassland, as these are typical surface characteristics through which forests are hypothesised to impact cloud formation (e.g. Xu et al., 2022).

The albedo is changed within Domain 4 only. The soil moisture is changed in both Domain 4 and 3 across all vertical layers. Because the surface roughness is based on tabled data linked to the land use class, we multiply the minimum and maximum roughness length ($Z_{0\min}$, $Z_{0\max}$) for the evergreen broadleaf forests, deciduous needleleaf forests, deciduous broadleaf forests, mixed forests, closed shrublands, woody savannas, savannas and croplands classes across the model domain. To study the effect of these parameters on cloud formation, we determined for each time step the cloud cover fraction over the forest and grassland areas. In addition, to provide more insight into the underlying processes, we retrieve other variables such as the sensible heat flux, latent heat flux, planetary boundary layer height, lifting condensation level and vertical wind profiles. The planetary boundary layer height is defined as the lowest height where the bulk Richardson number exceeds the critical threshold (in this case, 0.25).

5.2.5 Restoration scenarios

To determine the effect of forest size and heterogeneity on cloud formation, we simulated different restoration scenarios with varying forest extent and spatial clustering. The land cover scenarios were simulated for one of the case study days (2017/10/01) with a model configuration similar to that of the reference simulation. To reduce the number of variables, we created restoration scenarios using only the 'grassland' and 'mixed forest' MODIS land covers. We created random patterns with varying forest cover and spatial clustering, following Lennon (2000), generating two-dimensional random patterns similar to patterns found in natural systems. In total, we created 27 restoration scenarios, using combinations of three forest covers: 21.3% (half

of the reference forest cover), 42.7% (the reference forest cover) and 85.4% (two times the reference forest cover). In addition, we used three dispersion values that represent the degree of spatial clustering (-1.0, -2.5 and -5.0), and three random variations (seed 1, seed 2 and seed 3) (Supplementary Figure 5.3). A detailed description of the generation of these patterns is given in Supplementary Information Chapter 5. In addition, we simulated a scenario with only grassland and only mixed forest for comparison.

To avoid sharp land cover boundaries between Domain 3 and Domain 4, we created the spatial pattern for Domain 3 on a 1 km grid size first. We then selected the pattern at the location of Domain 4 for this domain. For Domain 3, we converted the pattern to a 3 km size using a mode interpolation. In addition, because not all vegetation characteristics are directly coupled to the land use type in WRF, we also changed the leaf area index, fraction of green vegetation, vegetation type and annual minimum and maximum vegetation fraction. The values were assigned to grassland and mixed forest classes in Domain 3 and Domain 4 based on the mean value of the forest and grassland regions in Domain 4 in the reference simulation. In addition, we made the albedo dependent on look-up tables linked to the land use type rather than using the MODIS data for these simulations. To determine how forest pattern impacts cloud formation, we create conditions where we expect cloud development over the forest (as observations show for this case study day). We therefore used the domain average soil moisture in the grassland regions, and half the domain average in the grassland, as we expect soil moisture heterogeneities to be an important factor determining cloud formation (Taylor et al., 2011). In addition, we used a homogeneous soil type (sandy loam, the most common value) across the domain to reduce the impact of soil type. Based on these model simulations, we compared cloud development over forest and grassland areas in the same way as for the sensitivity analysis.

5.3 Results

5.3.1 Evaluation of model results

To validate the model results, we compared the reference model simulation with radiosonde measurements. On Day 1, the simulated height profiles (represented by air pressure) of temperature closely follow the measurements at Niamey (13.48°N, 2.16°E) (Figure 5.3a). However, near the surface (1000-800 hPa), the simulated dew point temperature is up to 9.3 °C lower than measured values, suggesting the model simulates a drier boundary layer, resulting in a higher simulated lifting condensation level (153.2 hPa). Also at a higher level, between 600 and 300 hPa, the dew point temperature is underestimated. The simulated Convective Available Potential Energy (CAPE) is lower (675.7 J/kg) than the measured value (3101.8 J/kg), while no Convective Inhibition

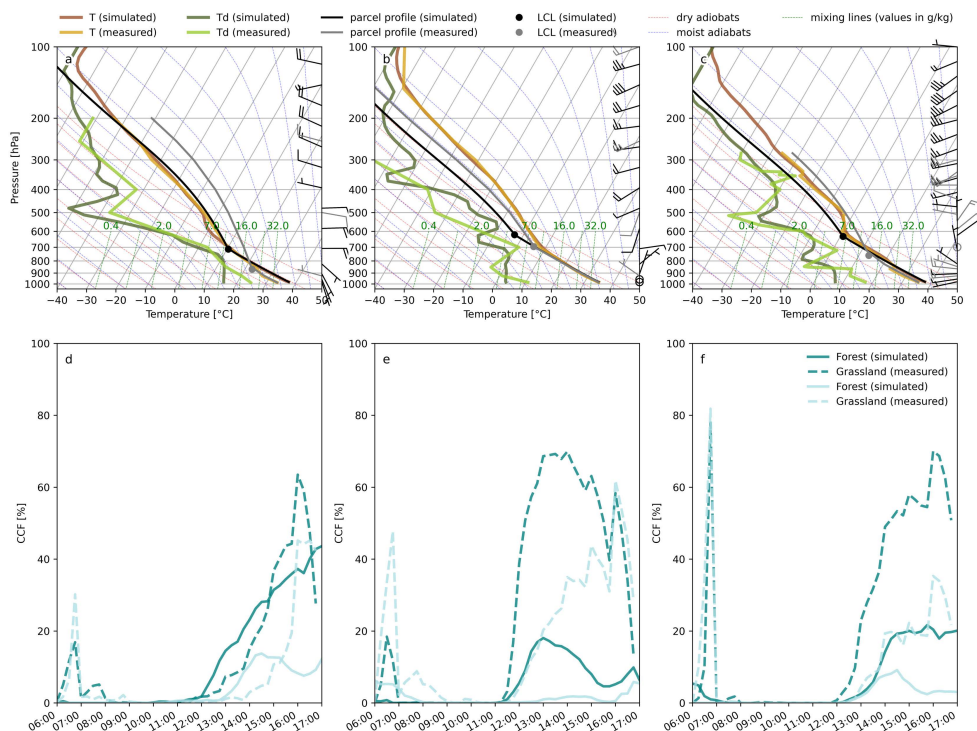


Figure 5.3 | Evaluation of model results. (a-c) Thermodynamic diagram of simulated (WRF) and measured (sounding) temperature (T), dew point temperature (Td), parcel profile, lifting condensation level (LCL) and wind speed and direction (barbs, simulated is black, measured is gray) at Niamey on (a) Day 1, (b) Day 2 and (c) Day 3. The same graphs in Abidjan are shown in Supplementary Figure 5.4. Simulated temperature, dew point temperature and pressure are obtained from Domain 3 at the location of Niamey. (d-f) Simulated and measured cloud cover fraction inside and outside the forest on (d) Day 1, (e) Day 2 and (f) Day 3 in Domain 4.

(CIN) is simulated, but a value of -56.76 J/kg is measured. On Day 2, simulations of dew point temperature are underestimated at the surface (1000-900 hPa), and the simulated lifting condensation level is 75.0 hPa higher than the measured value (Figure 5.3b). Both the measured and observed CAPE and CIN have a value of 0.0 J/kg. On Day 3, a similar pattern is observed, with an underestimation of dew point temperature (10.3 °C) between 1000 and 900 hPa and a higher simulated lifting condensation level (127.9 hPa). On this case study day, the model simulated a CAPE and CIN of 0.0 J/kg, while the measured values are 171.7 J/kg and -191.0 J/kg, respectively. So, during all three case study days, the simulated lifting condensation level is lower than the observed value due to a dry simulated boundary layer, although these local humidity biases are not unusual to occur in the Sahel (Taylor et al., 2007). In Abidjan (5.25°N , 3.93°W), the simulations follow the measurements more closely on Day 2 and Day 3, both in terms of the lifting condensation level and the dew point temperature near the surface (Supplementary Figure 5.4).

In addition, we evaluated simulations of cloud cover with satellite observations. Although the simulated cloud cover fraction inside the forest region on Day 1 is underestimated during the beginning of the afternoon and overestimated after around 15:00, the simulated development of the clouds follows the pattern of measurements (Root Mean Squared Error (RMSE) = 6.0%, maximum bias (bias_{max}) = 16.7%, between 06:00 and 16:45 UTC). Outside the forest, the model predicts a lower cloud cover than the observations, especially at the end of the afternoon (RMSE=9.9%, bias_{max} =37.0%) (Figure 5.3d). On Day 2, the cloud cover is underestimated by the model, both inside (RMSE=28.9%, bias_{max} =55.1%) and outside (RMSE=18.7%, bias_{max} =42.8%) the forest, compared to observations, but follows a similar diurnal pattern to the observations (Figure 5.3e). On Day 3, the simulated cloud cover is overestimated as well, both inside (RMSE=21.1%, bias_{max} =76.9%) and outside (RMSE=15.8%, bias_{max} =81.8%) the forest, but follows a similar development over the course of the day (Figure 5.3f). So, even though the model simulates a lower cloud cover than observational data, especially on Day 2 and Day 3, the cloud development follows a similar pattern and has a similar timing of cloud formation. In addition, during all three case study days, both the model simulations and the measurements show a higher cloud cover over the forest area than outside the forest area.

5.3.2 Relationship between vegetation characteristics and cloud formation

In this subsection, we will discuss results in our area of interest (Domain 4) only. On Day 1, changing the albedo, roughness length and soil moisture content in the forested area has a pronounced effect on cloud development in the case study area. Visual inspection of the model simulations reveals an enhanced cloud formation over the forest compared to the grassland, which is also visible in observational data (Figure 5.4a-c). Cloud cover is especially prevalent in the south-western part of the forest. For all parameter combinations, clouds start developing around 12:00 UTC, reaching a maximum cloud cover around 14:00-16:00 UTC (Figure 5.5a).

Compared to the reference simulation, a decrease in albedo or an increase in surface roughness increases cloud formation in the forested region. Multiplying the albedo in the forested region by 0.75 and 0.5 increases the afternoon (12:00-17:00 UTC) average cloud cover in the forested region with, respectively, +99.4% and +54.4% (Figure 5.5e). Increasing the surface roughness has a smaller effect on cloud formation, as multiplying the roughness length by 1.5 results in a decrease in cloud cover of -12.9%, whereas multiplying it by 2.0 increases the cloud cover by -1.9%. Increasing the soil moisture in the forested regions strongly inhibits cloud formation (Figure 5.4 & 5.5a). Compared to the reference simulation, multiplying the soil moisture content by 1.5 and 2.0 results in a strong cloud cover decrease of, respectively, -83.1% and -90.0%. Comparing all parameter combinations, the afternoon cloud cover fraction varies between +123.9% and -92.1% compared to the reference simulation.

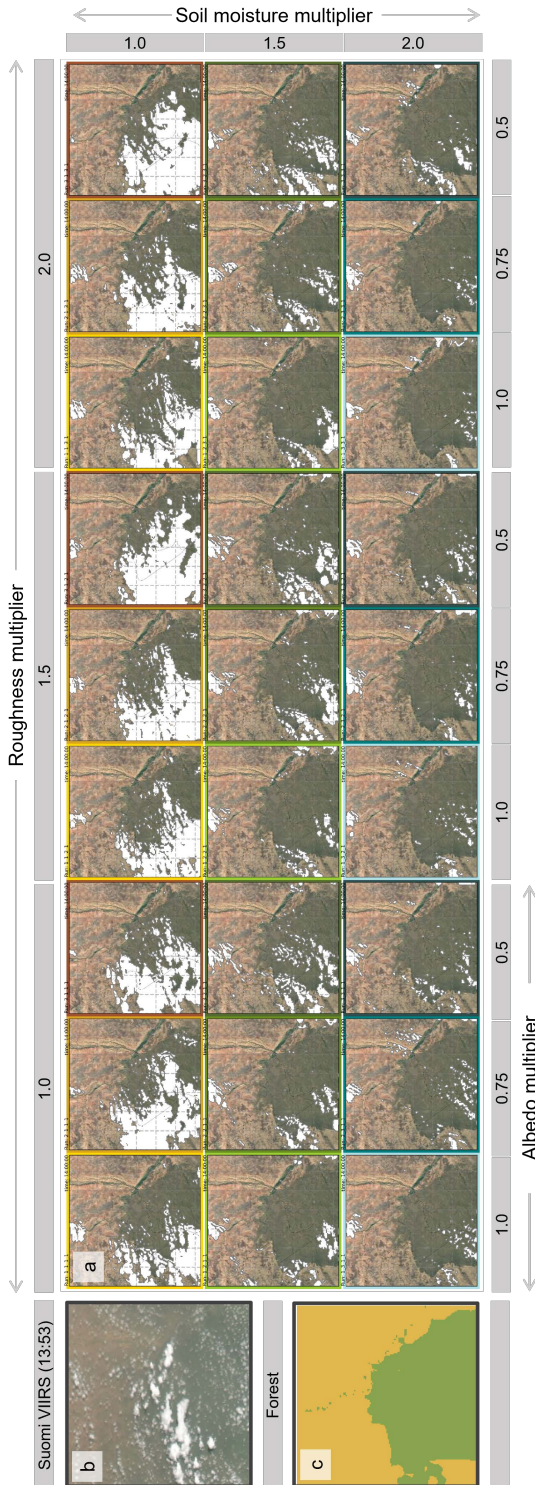


Figure 5.4 | Effect of albedo, soil moisture and surface roughness on cloud formation. Cloud cover (white) under different parameter combinations on Day 1 (2017/10/01) at 14:00 UTC in Domain 4 (a). Cloud cover is defined as having a liquid water path (LWP) higher than 0.001 m. The parameter combination is indicated at the top (roughness multiplier) and bottom (albedo multiplier) and side (soil moisture multiplier). The background image is obtained from Google Earth (Map data: Google, NASA). As a reference, the image on the left shows Suomi VIIRS reflectance image at 2017/10/01 13:53 UTC in Domain 4 (Wolfe et al., 2013) (b). The parameters are only changed in the forested areas (c). Visualisation of Day 2 and Day 3 is included in Supplementary Figures 5.5 and 5.6, respectively.

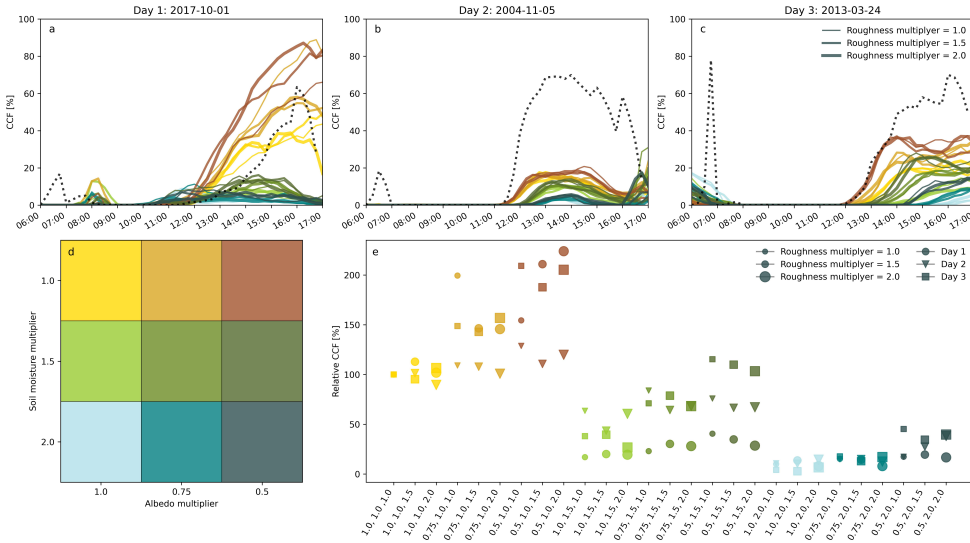


Figure 5.5 | Effect of albedo, soil moisture and surface roughness on cloud formation. (a-c) Cloud cover fraction (CCF) over the course of the day for Day 1, Day 2 and Day 3 over the forested area. Line colours indicate different parameter combinations of albedo and soil moisture as shown in (d), while the line thickness indicates different surface roughness parameter multipliers. The black dotted line indicates the observed CCF, based on Ruijch et al. (2025). (e) The afternoon (12:00-17:00 UTC) average CCF for the combinations of the albedo, soil moisture and surface roughness multipliers, respectively. The CCF is shown compared to the reference scenario, which has a value of 100%. Cloud cover is defined as having an LWP of more than 0.001 m.

The other case study days show a similar effect of changing the albedo, roughness length and soil moisture on cloud formation (Supplementary Figure 5.5 and 5.6). However, even though observational data shows a similar cloud cover as Day 1, both Day 2 and Day 3 show a lower cloud cover over the course of the day (Figure 5.5b-c). Yet, similar to Day 1, decreasing the albedo and increasing the roughness length results in an increase in cloud formation, whereas increasing the soil moisture reduces cloud formation. Interestingly, during these case study days, the maximum cloud cover is reached later during the day when the soil moisture is increased (Figure 5.5b-c). In general, decreasing the albedo and surface roughness thus enhances and advances cloud formation, whereas increasing the soil moisture strongly reduces and delays cloud formation. Yet, increasing surface roughness can also decrease cloud formation in some cases.

5.3.3 Potential underlying mechanisms for cloud formation

To determine potential underlying mechanisms for cloud formation over the forested region, we determined how changing the albedo, roughness length, and soil moisture affects the surface energy balance, boundary layer development and mesoscale circulation. To determine why cloud formation is more pronounced over the forested

region, we focus on the difference in these variables between the forest and grassland areas (Figure 5.6).

A lower albedo in the forest region results in an increase in sensible heat flux and, to a lesser extent, in latent heat flux for all case study days (Figure 5.6a-f). The latent heat flux is higher over the forested region over the course of the day, whereas the sensible heat flux is higher over the forested region until around 13:00 on Day 1, after which the sensible heat flux is higher over the grassland. During the other case study days, both the sensible and latent heat fluxes are higher over the forest region. A similar pattern can be seen in the boundary layer height (Figure 5.6g-i). Similarly, the difference in boundary layer height between the forest and grassland is higher (and positive) when the albedo is decreased. At the same time, the lifting condensation level is lower over the forest than over the grassland (Figure 5.6j-o). In addition, the decreased albedo results in a higher vertical velocity over the forested area (Figure 5.6p-r), which, combined with the higher boundary layer and lower lifting condensation level, results in a higher cloud formation in the forest compared grassland (Figure 5.6s-x).

Increasing the soil moisture in the forested region has a strong impact on surface energy balance and boundary layer development (Figure 5.6). A higher soil moisture results in an increased latent heat flux in the forest compared to the grassland. Simultaneously, the sensible heat flux reduces and becomes higher in the grassland than in the forests (Figure 5.6a-f). Consequently, in the high soil moisture simulations, the difference in boundary layer height between the forest and grassland region is lower, or even negative, indicating that the boundary layer is higher over the grassland than over the forest (Figure 5.6g-i). At the same time, the increased soil moisture lowers the lifting condensation level (Figure 6j-l). Interestingly, the boundary layer height over the grassland is not much affected by increasing the soil moisture in the forest, whereas the lifting condensation level decreases in both the forest and the grassland, although stronger in the forest (Supplementary Figure 5.7 and 5.8). The difference between the boundary layer height and lifting condensation level decreases on Day 1 and Day 2, and shows a delayed effect on Day 3 when soil moisture is increased. In addition, the higher soil moisture content results in a decrease in vertical velocity over the forest area, where the forest afternoon average turns from positive (rising air) for the dry soil to negative (sinking air) with the wet soil during Day 1 and 2 (Figure 5.6p-r, Supplementary Figure 5.7p-r). In addition, increasing the soil moisture content not only decreases the cloud development over the forested area, but it becomes stronger over the grassland area than over the forest (Figure 5.6s-u). Changing the surface roughness has a limited impact on the sensible and latent heat flux and boundary layer development during all three case study days. However, the model simulations show generally stronger vertical wind velocities under simulations with a higher surface roughness (Figure 5.6p-r).

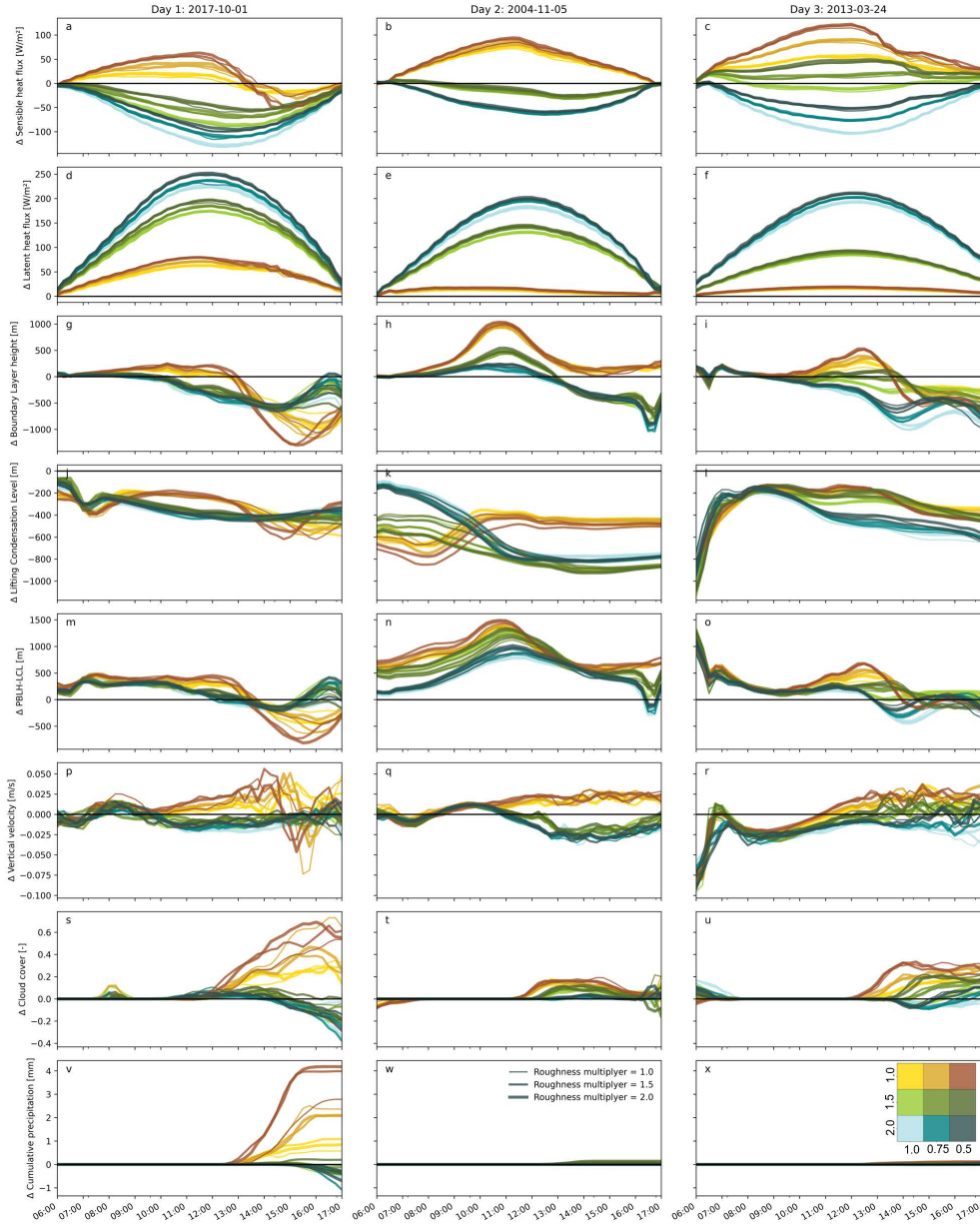


Figure 5.6 | Effect of surface properties on surface fluxes, boundary layer growth and precipitation. Difference in (a-c) surface sensible heat flux, (d-f) surface latent heat flux, (g-i) boundary layer height, (j-l) lifting condensation level, (m-o) difference between boundary layer height and lifting condensation level, (p-r) vertical velocity, (s-u) cloud cover fraction and (v-x) cumulative precipitation between the forest and grassland area over the course of Day 1, Day 2 and Day 3 (06:00-17:00 UTC). The colours are similar to Figure 5.5. The inset in (x) shows the colour legend with albedo (horizontal) and soil moisture (vertical) multipliers. Positive values indicate the value is higher in the forest area. Clouds are defined as areas with a LWP higher than 0.001 m.

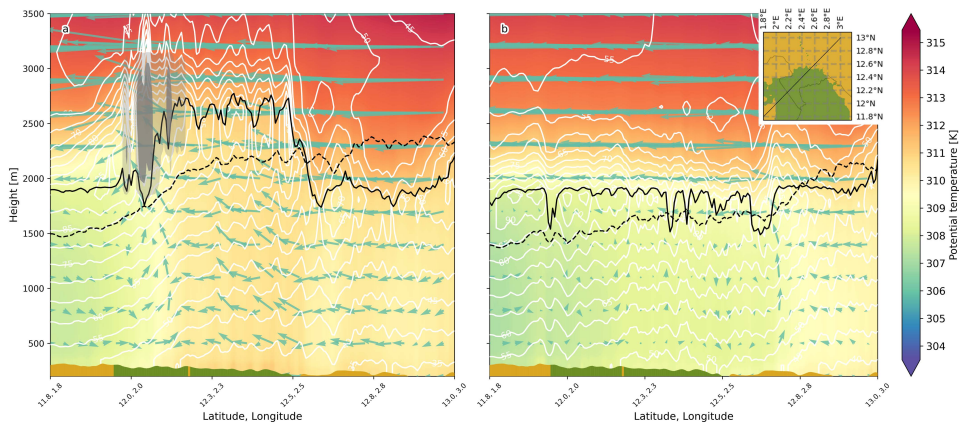


Figure 5.7 | Vertical cross section of boundary layer development over wet and dry soils. The vertical velocity (blue arrows), relative humidity (white lines) and potential temperature (colour) across height above sea level over a transect across the study domain on Day 1 at 12:45 UTC under (a) dry soil and (b) wet soil conditions. The colours on the bottom show topography and forest (green) and grassland (yellow). The planetary boundary layer height is indicated with the continuous black line, and the lifting condensation level with the dotted black line. The dry soil conditions are represented by the run with maximum albedo, minimum soil moisture and maximum surface roughness. The wet soil conditions have a maximum albedo, maximum soil moisture and maximum surface roughness.

On Day 2 and Day 3, the cloud formation results in limited precipitation throughout the day, with a maximum cumulative precipitation of 0.16 mm. On Day 1, however, changing the albedo, surface roughness and soil moisture results in precipitation changes with similar patterns as the cloud cover (Figure 5.6v-x). The maximum cumulative precipitation in the forested area (4.83 mm) is found with a maximum surface roughness, minimum albedo and minimum soil moisture. Whereas an increase in soil moisture strongly reduces the cumulative precipitation to 0.003 mm. Increasing the soil moisture does, however, increase the precipitation in the grassland regions to 1.15 mm (Supplementary Figure 5.7 and 5.8).

To provide more insight into the difference in cloud formation mechanisms between a dry soil (reference soil moisture) and wet soil (soil moisture multiplied by 2.0 in the forest domain), we created a transect from the south-west (11.8°N, 1.8°E) to north-east (13.0°N, 3.0°E) within the model domain, roughly aligned with the wind direction (Figure 5.7). At 12:45 UTC on Day 1, just before the onset of cloud development, the south-western grassland part of the transect (left) has a relatively cool and moist atmosphere, whereas the north-eastern grassland part of the transect has a drier and warmer atmosphere. When the soil moisture is low, the atmosphere over the forested region is relatively warm and dry, whereas under high soil moisture, the potential temperature gradually increases from the south-west to the north-eastern part of the transect, consistent with the large-scale meridional temperature gradient that characterises the Sahel. Under dry soil conditions, the lifting condensation level

increases from 1469m to a maximum of 2386m over the forest and north-western grassland region in the south-west of the domain. The boundary layer reaches as high as 2774 m, compared to a maximum of 2199m over the grassland. Under wet soil conditions, the boundary layer has a relatively constant height with an average height of 1850m, while the lifting condensation level gradually increases from 1370m to 2145m in the north-eastern grassland. In addition, under dry soil conditions, the wind speed near the surface is higher, with strong vertical velocities and wind convergence near the forest-grassland edge in the south-western part of the domain, which is not present under wet soil conditions.

5.3.4 Effect of land restoration patterns on cloud formation

Visual inspection of cloud development shows that forest cover and clustering both impact the amount of cloud cover and the location of cloud formation for this case study. We studied cloud formation over 27 different restoration scenarios, consisting of three different forest covers, three degrees of spatial clustering (controlled by the dispersion parameter β) and three random variations (seeds) on Day 1 (Figure 5.8). At 14:00 UTC, clouds are visibly more present under restoration scenarios with a higher spatial clustering (Figure 5.8j-r) than with a more small-scale heterogeneous distribution of forest across the landscape (Figure 5.8a-i). In addition, under the highest clustering (Figure 5.8s-a1), clouds develop more at the edge between forest and grasslands (Supplementary Animation 5.1). The restoration scenario with the highest afternoon cloud cover is different per random variation (Supplementary Figure 5.9), varying between 4% (scenario in Figure 5.8a) and 25% (scenario in Figure 5.8w). Yet, averaged over the random variations (Figure 5.9), we find the highest cloud cover under scenarios with a high spatial clustering (more negative dispersion) and intermediate forest cover of 42.7% (e.g. Figure 5.8w). Under these scenarios, the afternoon cloud cover is on average 21.1% across the domain. Interestingly, doubling the forest cover to 85.4% strongly reduces the cloud cover from 21.1% to 14.4%. In addition, distributing the forest cover with more small-scale heterogeneities over the domain (low clustering, top row) reduces the cloud cover to 6.4%. This suggests that it is not an increase in forest cover but rather a certain amount of land cover variation (with certain length scales) which increases cloud formation in this case study. The afternoon cloud cover fraction under a scenario with only grassland (6.3%) is similar to scenarios with a low spatial clustering, whereas under a scenario with 100% forest cover, the afternoon cloud cover fraction increases to 21.0%.

The spatial pattern of forest barely impacts the area-averaged sensible and latent heat flux within the forest and grassland regions (Figure 5.10a, b, e, f). However, the forest cover does impact the average fluxes across the model domain (Figure 5.10c, g). Under small-scale heterogeneous forest covers (with limited clustering), the boundary layer grows higher than with more clustering (Figure 5.10i-l).

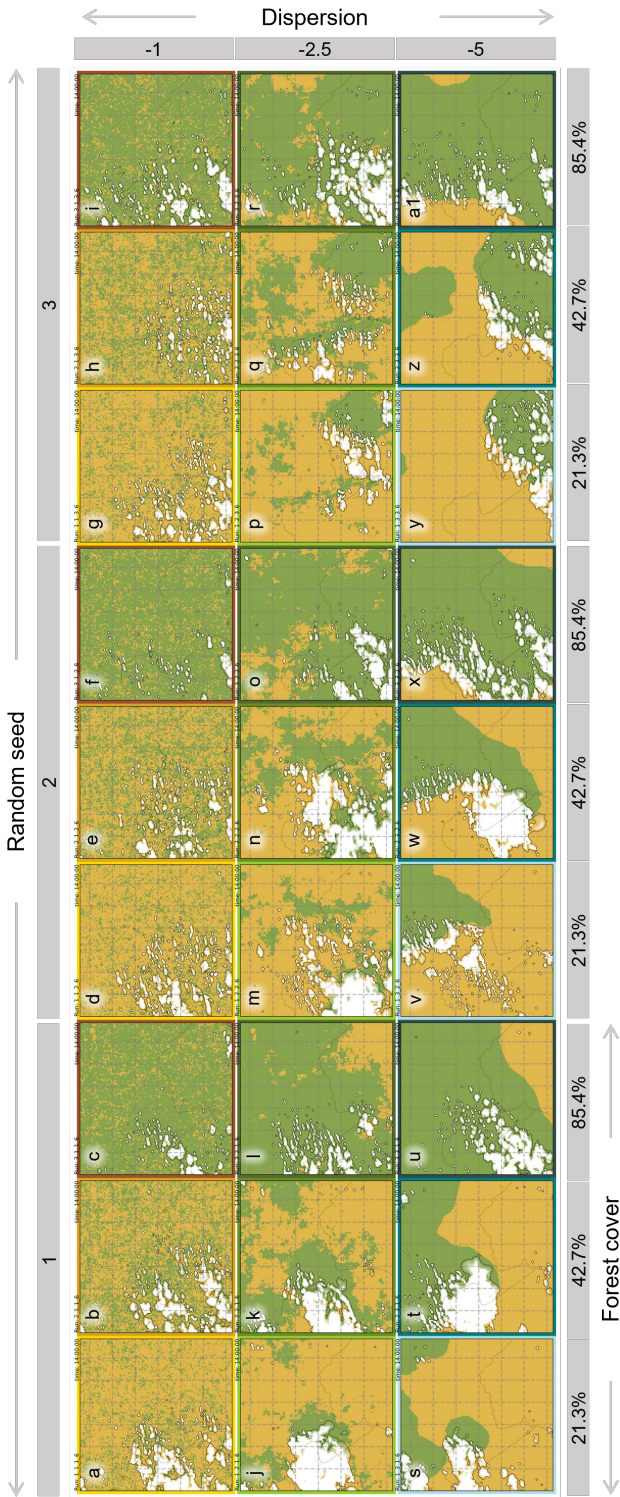


Figure 5.8 | Effect of restoration topology on the spatial distribution of clouds. Cloud cover (white) under different restoration scenarios on Day 1 (2017/10/01) at 14:00 UTC in Domain 4. Cloud cover is defined as having a liquid water path (LWP) higher than 0.001 m. The background image shows the created land cover map, with forest in green and grassland in yellow, with different forest cover (indicated at the bottom), spatial dispersion (indicated on the right, more negative values indicate higher clustering) and random variations (indicated at the top), resulting in 27 land cover simulations. Supplementary Animation 1 shows the cloud development between 09:00 and 15:00 UTC.

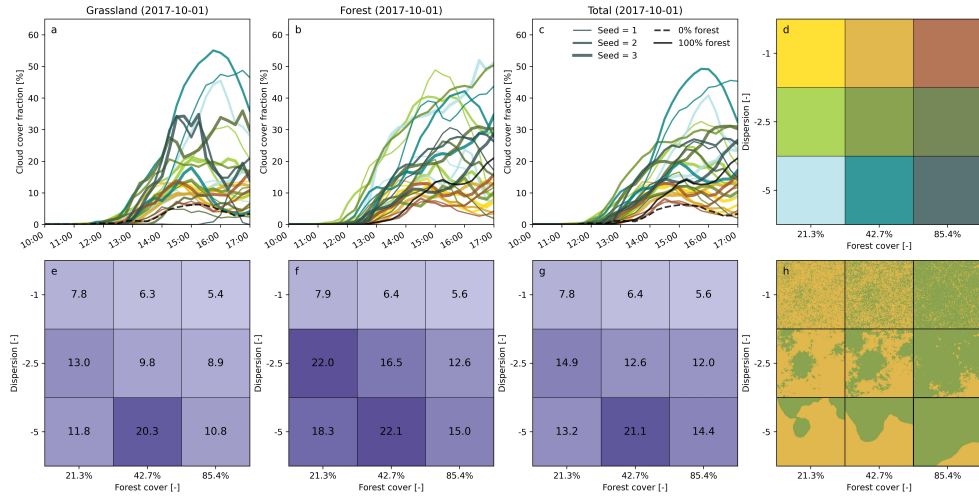


Figure 5.9 | Effect of restoration design on cloud development. Cloud cover fraction over the course of the day (a) over the grassland, (b) over the forest and (c) over the total domain. The line colours indicate different restoration scenarios with varying forest cover and spatial dispersion, as shown in (d) (and similar to the box outlined in Figure 5.8). Afternoon (12:00-17:00 UTC) average cloud cover fraction (%) (e) over the grassland, (f) over the forest and (g) over the total domains for the same restoration scenarios. The black striped and continuous line represents the 0% and 100% forest cover scenarios, respectively.

However, since the lifting condensation level is also higher (Figure 5.10m-p), the difference between the boundary layer height and lifting condensation level is similar for the different spatial configurations (Figure 5.10q-t). After 13:00 UTC, the boundary layer continues to grow for the small-scale heterogeneous forest cover, while the boundary layer height decreases under clustered forests. At the same time, land restoration configurations with the highest cloud cover show a more negative (downward) vertical velocity over the grassland and a positive (upward) vertical velocity over the forest, especially at the end of the afternoon (Figure 5.10u-b2). We also observe that the cloud formation in this case study also results in precipitation, with, in general, a higher cumulative precipitation for configurations with a high cloud cover and more spatial clustering (Figure 5.10y-f2). Inside the forest, we find the highest average cumulative precipitation under scenarios with a high spatial clustering and the lowest forest cover (seed 3), with 1.89 mm. A low spatial clustering generally results in an average cumulative precipitation between 0.43 mm and 0.05 mm. All these scenarios have, however, a higher cumulative precipitation than the scenario with only grass (0.03 mm).

To provide more insight into the boundary layer development and mesoscale circulations, we created a vertical transect across the model domain for nine different spatial configurations with varying forest cover and spatial clustering (Figure 5.11). The nine transects correspond to Random Seed 2 in Figure 5.8. At 14:00 UTC, relatively shallow clouds have developed over a small-scale heterogeneous forest cover (Figure

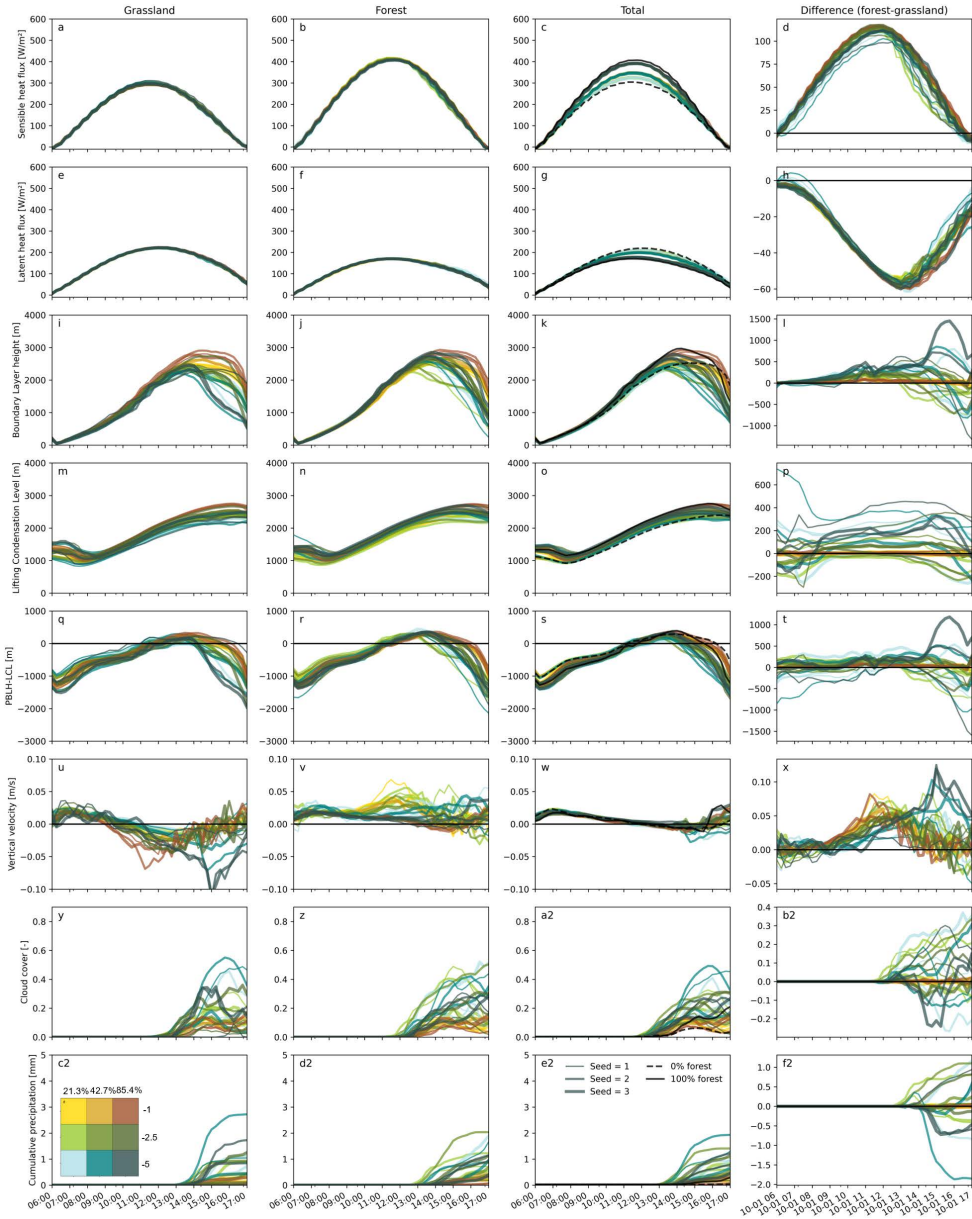


Figure 5.10 | Effect of restoration design on surface fluxes, boundary layer growth and precipitation. Diurnal variation in the grassland, the forest, the total domain and the difference between the forest and grassland for (a-d) sensible heat flux, (e-h) latent heat flux, (i-l) boundary layer height, (m-p) lifting condensation level, (q-t) difference between boundary layer height and lifting condensation level, (u-x) vertical wind velocity, (y-b2) cloud cover fraction and (c2-f2) cumulative precipitation between the forest and grassland area over the course of Day 1 (06:00-17:00 UTC). Clouds are defined as areas with an LWP higher than 0.001 m. The black striped and continuous line represents the 0% and 100% forest cover scenarios, respectively. The colors are similar to Figure 5.9. The inset in (c2) shows the colour legend for precipitation values.

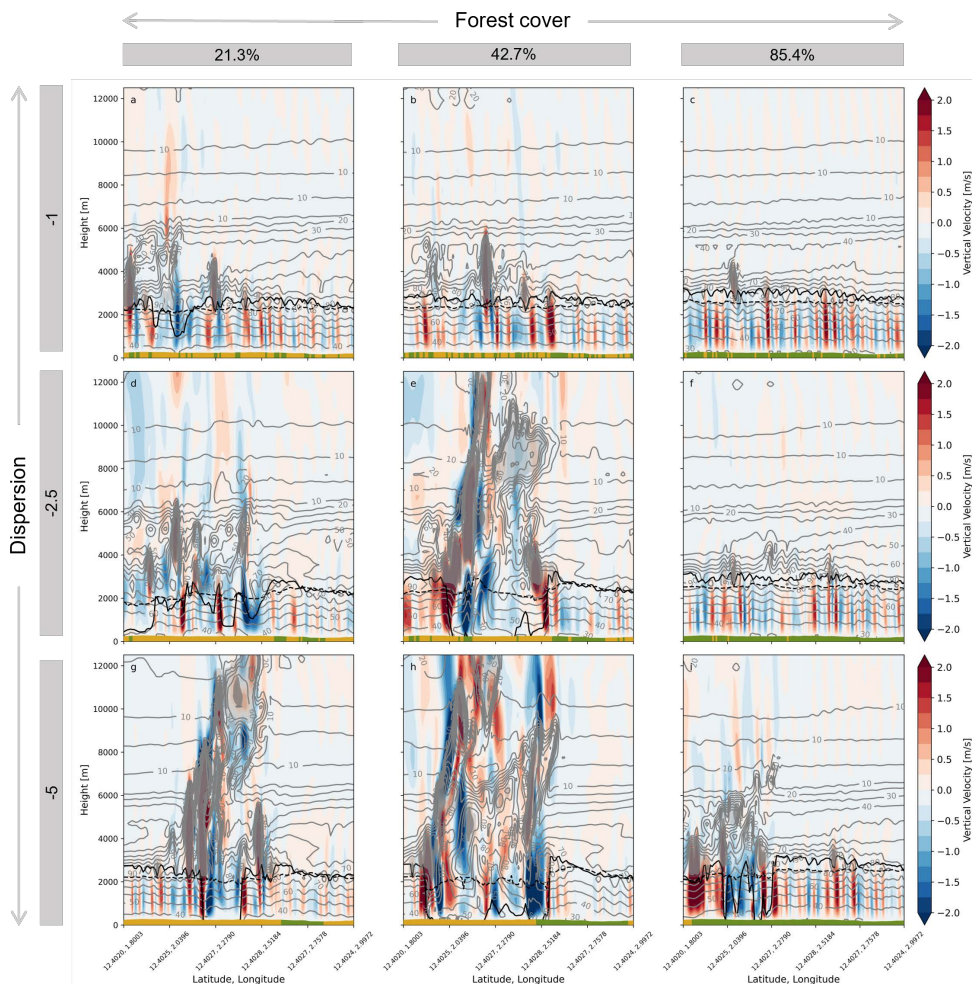


Figure 5.11 | Vertical cross-section of boundary layer development over different spatial patterns of restoration. Vertical wind velocity (colours) at a west (left)-east (right) vertical cross section at a latitude of 12.4°N at 14:15 UTC for nine different restoration scenarios corresponding to Random Seed 2 in Figure 5.8. The black continuous line indicates the boundary layer height, the striped black line the lifting condensation level and the grey lines the relative humidity contours [%]. The land cover type is indicated by the yellow (grass) and green (forest) shading at the bottom. The grey opaque and transparent shading indicates a cloud water mixing ratio of, respectively, more than 0.001 and 0.1 g/kg. Supplementary Animation 2 shows the cloud development between 09:00 and 15:00 UTC.

5.11a-c) and the high forest cover scenarios (Figure 5.11c, f, i). Over the clustered forest, especially with intermediate and lower forest cover, we see the development of deep convections, with clouds reaching as high as 12 km (Figure 5.11e, g, h). These clouds first develop at the forest-grassland edge and later expand mainly into the grassland (Supplementary Animation 5.2). At the edges of larger forest patches, wind convergence and a strong reduction in boundary layer height develop, with a strong

upward vertical velocity at the cloud edges, and a downward wind at the centre. This landscape-induced mesoscale circulation provides favourable conditions for triggering deep convection and precipitation.

5.4 Discussion and conclusions

In this study, we used the WRF atmospheric model to determine how the spatial pattern of land restoration projects impacts cloud formation in West African drylands. We selected three case study days that show an enhanced cloud formation over the W-Arly-Pendjari Complex at the border of Benin, Niger and Burkina Faso, and ran the model with varying albedo, surface roughness and soil moisture content to determine mechanisms behind observed cloud formation over forested regions to determine how these parameters impact cloud formation. According to existing research, clouds can either be enhanced or inhibited over forested regions. In temperate regions, observational analysis has shown cloud enhancement over forest, while in some parts of the Amazon, the high evapotranspiration of forests inhibits cloud formation (Duveiller et al., 2021; Xu et al., 2022). The low albedo and high surface roughness over forests increase boundary layer growth, which can result in enhanced cloud formation over regions with a high sensible heat flux (Teuling et al., 2017b; Bosman et al., 2019). In addition, the high evaporation provides atmospheric moisture and lowers the lifting condensation level, enhancing cloud formation over regions with a high evaporation if the sensible heat flux is large enough to stimulate boundary layer growth (Findell & Eltahir, 2003a; Garcia-Carreras et al., 2017).

In this study, model simulations show that increasing the surface roughness and albedo inside the forest enhances the afternoon cloud cover fraction up to +123.9% due to the increased net radiation and sensible heat flux. During these simulations, the sensible heat flux and boundary layer height are larger over the forested region than over the surrounding grassland. Similar results have been found for case studies in Europe, where the high sensible heat flux is essential for the onset of cloud development over forested regions (Bosman et al., 2019; Noual et al., 2023). However, increasing the soil moisture content in the forest strongly reduces the cloud formation, up to -97.2%, over the forest. Because the evapotranspiration in dryland regions is strongly water-limited, increasing the soil moisture content strongly enhances the latent heat flux in the forest region, at the expense of the sensible heat flux, resulting in a lower boundary layer compared to the grassland region. Thus, under dry soil moisture conditions, the forest has a higher sensible heat flux, boundary layer growth and cloud formation. Under wet soil moisture conditions, the forest region has a lower sensible heat flux, boundary layer and cloud formation than the surrounding grassland region, which is in line with the negative relationships between soil moisture and cloud formation in West Africa that have been found in other studies (Taylor et al., 2012; Taylor et al., 2013; Klein & Taylor,

2020). Based on these results, an increase in sensible heat flux appears to be more critical for cloud formation than a decrease in atmospheric moisture, again in line with Bosman et al. (2019) and Noual et al. (2023).

In addition, differences in surface roughness and albedo between the forest and adjacent grassland can trigger thermally and dynamically driven mesoscale circulations, which enhance cloud formation over warm and rough regions (Birch et al., 2014; Khanna & Medvigy, 2014; Spracklen et al., 2018). In this study, the relatively high soil moisture in the south-western part of the case study domain (Figure 5.2) in combination with the dry and dark forest, cause a sharp contrast in boundary layer height and potential temperature, resulting in updraft and wind convergence, and ultimately cloud formation, at the forest-grassland edge. During the wet soil moisture conditions, wind convergence and mesoscale circulation needed for cloud development do not develop in the same way as during dry soil moisture conditions. This suggests that these circulations play an important role in cloud development, at least during the case study days. Although these only represent conditions during these three case study days, observations show enhanced cloud formation over regions with a negative soil moisture anomaly due to the enhanced sensible heat flux over longer time scales (Taylor et al., 2011; Taylor et al., 2012).

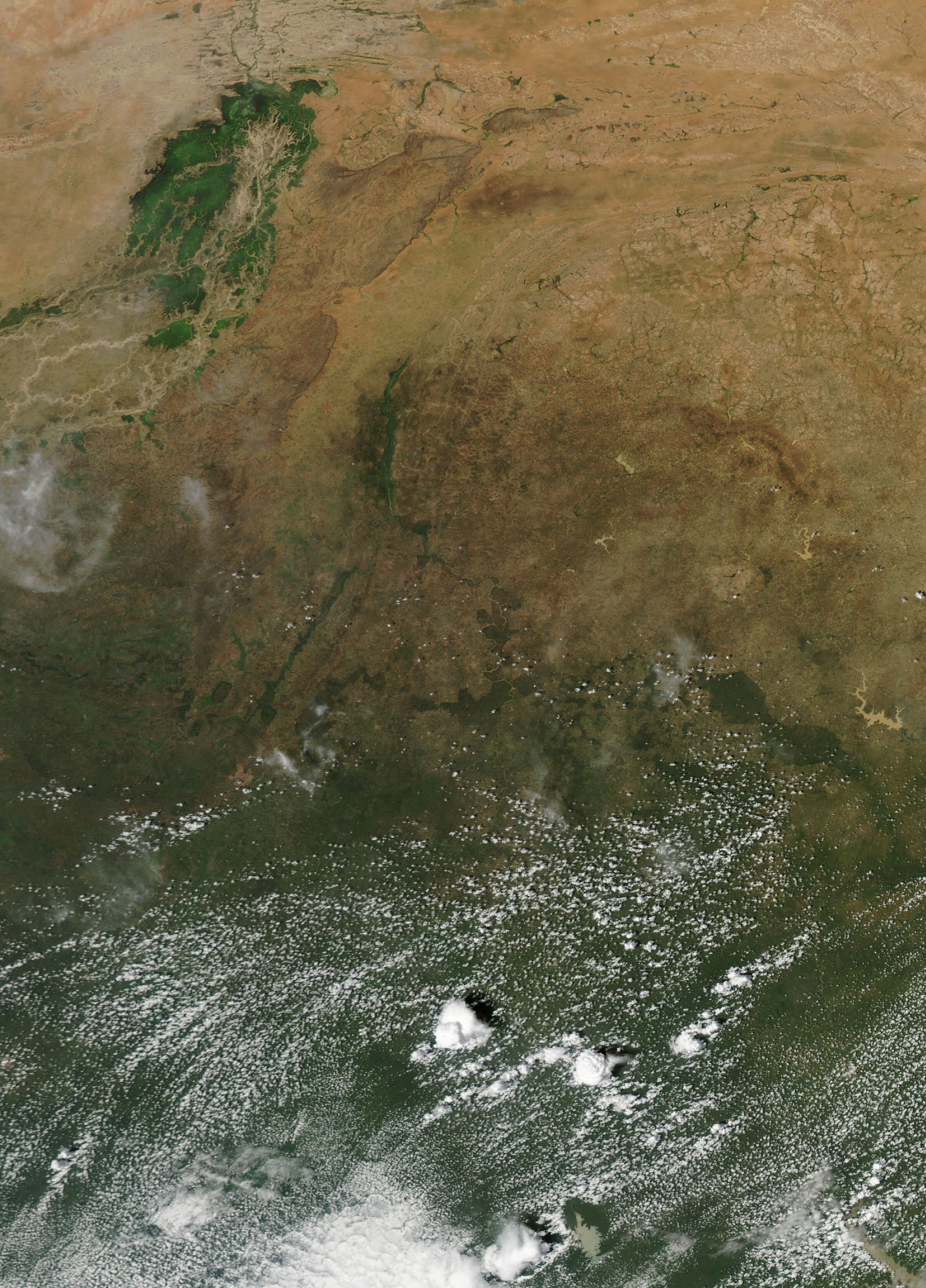
To determine the effect of spatial patterns of restoration, we ran 27 land restoration scenarios with forest cover and spatial clustering. Model simulations show that a more clustered forest cover results in cloud cover enhancement compared to a more scattered forest. Furthermore, increasing forest cover decreases cloud cover development. This suggests that a certain degree of variation in land cover, of certain length scales, increases cloud formation in this region. Because the sensible and latent heat flux do not depend on the spatial pattern of the forest, and the boundary layer is higher over the scattered forest scenarios (which have lower cloud formation), the difference in cloud formation likely has other underlying mechanisms and differences in mesoscale circulation and convergence contribute to the cloud formation over a clustered forest. The variation in surface roughness and temperature of the boundary layer over the forest and grassland contributes to thermally (temperature) and dynamically (roughness) driven mesoscale circulations caused by frictional convergence, resulting in cloud formation on the forest-grassland boundary. Similar results were seen with observational data, where only larger protected areas in West Africa show cloud enhancement (Ruijsch et al., 2025). In addition, previous observational and modelling studies have shown mesoscale circulation to cause cloud cover enhancement over the warm and rough edge of land cover heterogeneities (Garcia-Carreras et al., 2010; Taylor et al., 2011; Spracklen et al., 2018; Ascher et al., 2025), which is, in this case, the forested side due to the relatively dry soil.

Because the cloud formation is strongly coupled to soil moisture heterogeneities, it is, however, expected that the cloud enhancement under land restoration scenarios varies

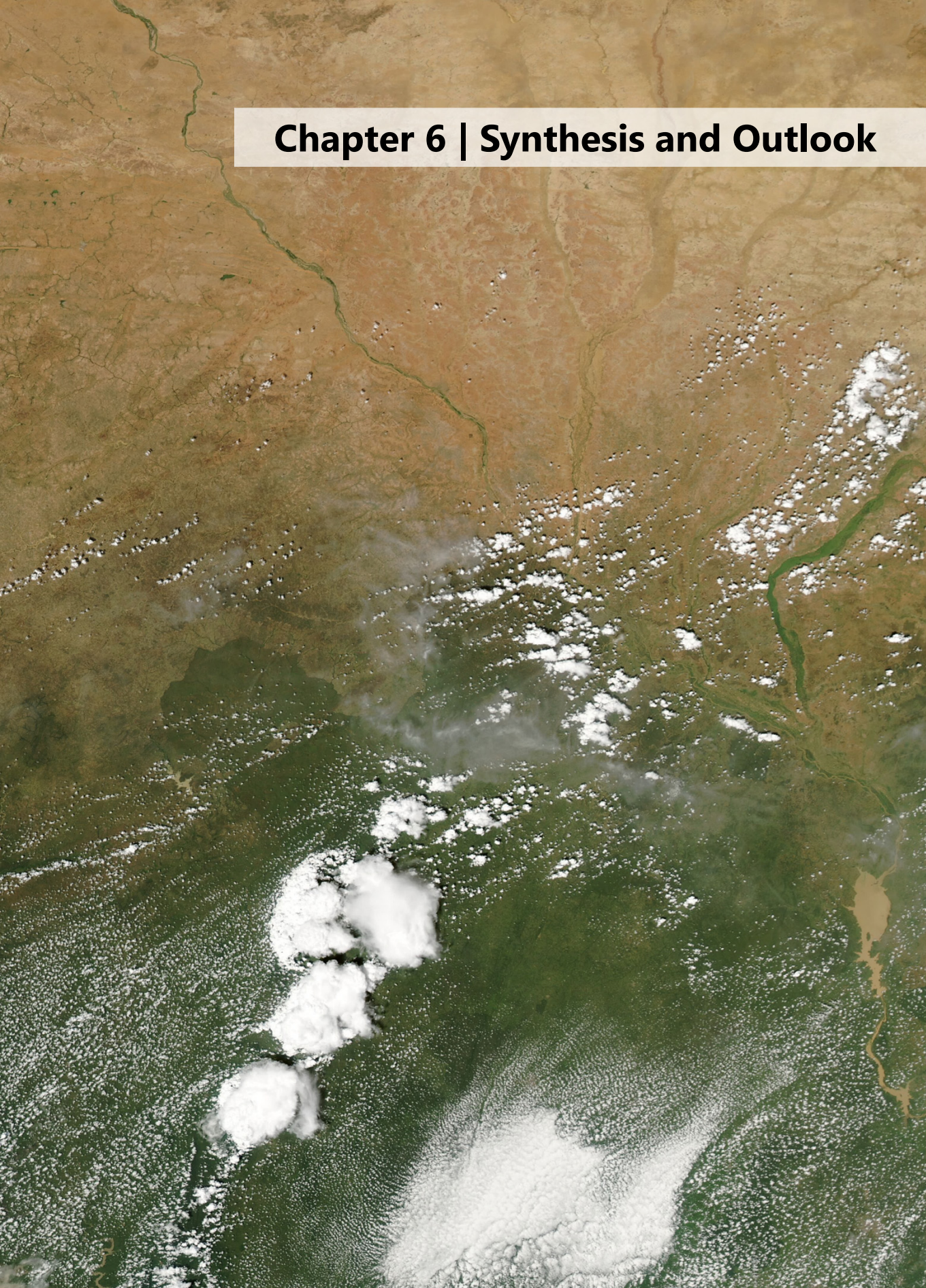
throughout the year. Other studies have indeed found that the effect of deforestation strongly depends on seasonality in Asia and South America (Leung et al., 2024; Qin et al., 2025). In addition, multi-year satellite observations show that the relative difference in cloud cover fraction between the forest and grassland in a similar case study region is 8% (Ruijsch et al., 2025), which is lower than the strong cloud enhancement during these specific case study days. While computational limitations restricted longer model simulations, further research on the overall long-term effect of the patterns of land restoration on cloud formation would therefore be insightful. This will also provide more insights into potential feedbacks, both between soil moisture and cloud formation, and to the vegetation itself. In addition, because this is a modelling study, the accuracy of the representation of the model and the input data results also impacts the accuracy of the results. Yet, as limited flux measurements are available in this region, validation of the surface energy balance is challenging.

Despite these limitations, this study shows that spatial patterns of land restoration projects strongly influence cloud formation, with a stronger cloud enhancement of vegetation over clustered forests. This suggests that, if cloud (or rainfall) enhancement is a goal of the project, larger patches of forest (e.g. protected areas) in a grassland region are more effective in generating clouds than smaller patches of forests (e.g. farmer-managed natural regeneration). Although the scattered forest cover does not result in a considerable increase in cloud cover compared to grassland only, the results do show an increased cumulative precipitation with scattered forest cover (up to 0.43 mm) compared to the grassland simulation (0.03 mm). A high spatial clustering can, however, increase the domain-averaged cumulative precipitation up to 1.89 mm. This study, therefore, suggests that restoration can locally impact water availability, as found in previous global analyses (e.g. Hoek van Dijke et al., 2022).

To this end, this research can provide insights for policymakers on how the design of restoration projects in West African drylands impacts cloud cover or precipitation. In addition, given the many restoration projects currently being implemented under, for example, the United Nations Decade of Ecosystem Restoration or the Great Green Wall of Africa, and the strong effect of changes in cloud cover on the global climate (Goessling et al., 2025), both through trapping heat emitted by the Earth's surface and reflecting incoming solar radiation, more insight into the cloud impacts of land restoration projects is essential to understand their overall climate effect and look beyond their carbon sequestration potential (Ibisch et al., 2025).



Chapter 6 | Synthesis and Outlook



Abstract | Land degradation is a globally recognised problem, decreasing food production, water availability, biodiversity and human welfare. As a reaction, several restoration initiatives have emerged that aim to reduce or reverse land degradation and its negative consequences. The increase in vegetation cover caused by land restoration projects can affect the regional and global climate, not only through carbon sequestration, but also by changing the biophysical properties of the earth's surface (e.g. albedo, surface roughness or evapotranspiration). Some land restoration initiatives explicitly focus on improving the regional climate through these biophysical processes. However, how these mechanisms apply to the often small-scale restoration projects remains uncertain. As a result, it is unknown how restoration through changes in vegetation can contribute to climate change adaptation. In this thesis, I aim to contribute to closing this gap by determining the biophysical climate effects of land restoration projects, focusing on Africa.

6.1 Introduction

The word latent in the title of this thesis comes from the Latin word 'latens', meaning 'lying hidden'. It can be defined as '(a quality or state) existing but not yet developed or manifest'. This also gives rise to the term 'latent heat flux', as referred to many times in this thesis, because the latent heat flux does not result in a detectable change in air temperature at the surface. So, based on the results of this thesis, can it be concluded that there is a 'latent potential of restoration', a potential that is currently not being used? Below, I summarise the main findings of each research question (Chapter 6.2). In the remainder of the chapter, I synthesise these results by discussing how uncertainties may have impacted these findings (Chapter 6.3), how this thesis contributes to our understanding of the latent potential of restoration (Chapter 6.4) and my recommendations for future research lines to further explore the latent potential of restoration (Chapter 6.5).

6.2 Main findings

6.2.1 How does land restoration contribute to vegetation greening?

Although many land restoration projects are being implemented across Africa to improve biodiversity, combat land degradation and sequester carbon, it has remained largely unknown how these projects exactly impacted vegetation greening, due to the lack of a complete database of land restoration projects in Africa, the numerous organisations involved and the low survival rate of the planted vegetation. In addition, climatic influences, which impact the vegetation greening simultaneously with the restoration projects, complicate the allocation of vegetation greening to the restoration projects.

A critical first step in this thesis was, therefore, to determine how land restoration contributes to vegetation greening across Africa (Chapter 2). To account for changes in the background climate, I applied a spatial-context method to 20 years (2001-2021) of MODIS satellite data, where I compared the Normalized Difference Vegetation Index (NDVI) and Enhanced Vegetation Index (EVI) at each location to its surrounding area. By assuming that the climate impacts vegetation on a larger scale than land restoration, I removed factors such as natural climate variability and climate change from the vegetation greenness time series. In addition, I applied the Breaks For Additive Seasonal and Trend (BFAST) algorithm to detect sudden changes in vegetation trends across Africa.

The results highlight that land restoration visibly contributes to vegetation greening in Africa. Specifically, 2.1% of the continent (roughly 400,000 km²) has experienced a sudden increase in vegetation greenness compared to surrounding areas. The amount

of greening shows clear patterns related to aridity, as semi-arid regions experience more of this local greening compared to more humid or arid regions. In addition, the amount of location greening is significantly higher around sustainable land management projects than in reference regions with a comparable aridity and land use. Interestingly, active revegetation results in a high amount of local greening, whereas natural regeneration causes less greening, but over a larger area.

Considering these results only represent the 2001-2021 period, it is expected that more small-scale greening will be observed across Africa in the future. Even though only roughly 30% of the Great Green Wall project has currently been completed, the original objective of the Great Green Wall is to restore one million square kilometres of degraded land by 2030. In addition, under the current UN Decade of Ecosystem Restoration, countries in Sub-Saharan Africa have pledged to restore more than 400 million hectares (PBL, 2020). It should be kept in mind, however, that there has been an increasing amount of attention towards the type of restoration that is implemented, as tree planting in regions without a native tree cover may have negative consequences on biodiversity (Parr et al., 2024). In addition, ongoing climate change may affect the regions that are suitable for restoration in the future (Roebroek et al., 2025). Nonetheless, it can be concluded that land restoration increases vegetation across the African continent, although the effectiveness (in terms of greening) depends on the type of intervention and the aridity of the location where the project is implemented. Because land restoration impacts vegetation greening, these projects also have the potential to impact land-atmosphere interactions.

6.2.2 What is the local biophysical cooling potential of land restoration?

To determine whether these restoration-induced changes in vegetation cover impact the local surface temperature, I extended the analysis with remotely sensed observations of temperature and albedo over a 22-year period (2001-2023) (Chapter 3). I compared the NDVI, albedo and land surface temperature to surrounding regions, which indicates whether greener regions are either cooler or warmer than their surroundings. In addition, I used a random forest algorithm to extrapolate the results and determine the local cooling potential of land restoration across Africa.

On a continental scale, land restoration has the potential to decrease the local surface temperature in Africa by 0.2 K on average due to a strong cooling potential in semi-arid regions. However, observed vegetation-temperature relationships vary both spatially across Africa and temporally over different time scales. In most regions, especially semi-arid and dry sub-humid regions, vegetation-temperature relationships are negatively correlated, suggesting a decrease in temperature during periods when the vegetation greenness is higher. However, vegetation greening increases the temperature in the driest areas of the continent. Because these regions also show a negative correlation between vegetation greenness and albedo (suggesting an albedo

warming effect), it is expected that these dryland regions do not have sufficient moisture to compensate for the albedo warming effect of increased vegetation greenness with evaporative cooling. Increasing the vegetation cover will therefore result in a higher surface temperature in the more arid regions.

6.2.3 To what extent can land restoration affect cloud development?

In Chapter 4, I zoomed in on West Africa to determine the impact of land restoration on cloud formation. After all, if land restoration has the ability to impact land surface temperature through changes in vegetation greenness, it may also impact cloud formation through changes in albedo, surface roughness (providing a lifting mechanism) and evapotranspiration (providing moisture). Using 20 years of data from the geostationary Meteosat Second Generation satellites, I developed a statistical algorithm to detect cloud cover from the High Resolution Visible band. Applying this algorithm to more than 300,000 images allowed me to compare cloud occurrence to vegetation greenness and protected areas, obtaining observational evidence for the relationship between land restoration and cloud formation in West African drylands and diurnal and seasonal variation herein.

The results highlight a scale-dependent relationship between land restoration and cloud formation. On average, the cloud cover fraction between 2004 and 2024 is higher over greener regions (with a high NDVI) and over protected areas, with a high relative difference at the start and end of the wet season. However, observations show a significant increase in cloud formation only over protected areas larger than about 10x10 km, while the difference for the smaller project is positive but not significant or even negative in some cases. This suggests that land restoration can indeed increase cloud formation, but only for sufficiently large projects. However, satellite data alone is unfortunately not able to determine the underlying relations for cloud formation.

6.2.4 How does the spatial pattern of land restoration projects affect cloud development?

To improve our understanding of how land restoration can impact cloud formation, I used the WRF atmospheric model to simulate cloud formation over the W-Arly-Pendjari national park complex in West Africa, which has a sharp contrast between a forested area inside the park and surrounding grasslands and croplands (Chapter 5). The aim was to determine how the spatial pattern of land restoration projects impacts cloud formation. First, I ran a sensitivity analysis for three case study days with enhanced cloud formation over the forest. Changing the albedo, soil moisture and surface roughness inside the protected forest area shows that a lower albedo and higher surface roughness increase cloud formation, while increasing soil moisture strongly reduces cloud formation, because the low contrast in temperature and boundary layer growth inhibits mesoscale circulation and cloud formation. Next, I ran 27 land

restoration scenarios with varying forest cover and varying extents of spatial clustering of forests.

This shows that, under atmospheric conditions where cloud enhancement is expected over forested regions, a higher clustering of forests cause enhanced cloud formation (with an average cloud cover fraction of 21.1%) compared to a scattered forest distributed across the domain (with an average cloud cover fraction of 6.4%), caused by enhanced mesoscale circulation and convergence at the forest edge. Interestingly, increasing the total forest cover in the study domain does not result in higher cloud formation because this results in less spatial heterogeneity needed for these mesoscale circulations. These results show that in this case study, larger patches of forest, through, for example, area protection or reforestation, may result in a higher cloud formation than, for example, farmer-managed natural regeneration, which may result in smaller patches of forest scattered across the region.

6.3 A reflection on the applied methodology

Like every research, this thesis also comes with uncertainties that should be considered when interpreting the results. Uncertainties of the separate research questions have been discussed in the respective chapters. Below, I will discuss the uncertainties related to the broader methodology and how these uncertainties affect the conclusions of this thesis. Specifically, I focus on: the used definition of land restoration; the use of remote sensing data and modelling; potential feedbacks that are not included and how the results may differ from the land user's perspectives.

6.3.1 Uncertainties related to the definition of land restoration

Throughout this thesis, I studied land restoration mainly from a 'greening' perspective, where I assume that land restoration results in greening and that (small-scale) greening can be viewed as land restoration. This rather simplified definition of land restoration was chosen because vegetation greening can be directly observed with remote sensing. In addition, the biophysical climate effects of restoration are expected to be linked mostly to the amount of vegetation.

However, it also leads to several uncertainties when interpreting the results. On the one hand, not all land restoration practices will result in observable vegetation greening. As the aim of land restoration is often to increase biodiversity and restore ecosystem services, it can encompass a wide range of activities. Even though land restoration in general results in greening (as shown in Chapter 2), not all land restoration practices will have a similar result. For example, the conversion of a monocultural plantation into a more diverse forest can be considered land restoration,



Figure 6.1 | Greening is not always good. Image of woody encroachment by *Prosopis* in Shompole falls in Soralo, Kenya. Image obtained from Sonak (2023).

but it will not result in a considerable change in vegetation greenness. Consequently, the results of this thesis are, therefore, only applicable to restoration practices that result in changes in vegetation greenness.

At the same time, not all greening arises from land restoration and should be considered beneficial. Even though forest restoration is still being pledged for restoration regions that do not contain native forests (Parr et al., 2024), more and more studies have called for considering native ecosystems when implementing land restoration, especially concerning tree planting in non-forested ecosystems (Di Sacco et al., 2021; Briske et al., 2024; Parr et al., 2024) because it can lead to the destruction of intact native ecosystems. Especially an increase in tree cover can result in degradation of grassland and savanna ecosystems (Bond et al., 2019). Restoration through monocultures or non-native vegetation can have similar negative impacts (Veldman et al., 2015). On top of that, not all greening is caused by land restoration. Woody encroachment of non-native or invasive vegetation species can negatively impact native ecosystems (Figure 6.1), but is difficult to distinguish from restored areas using vegetation indices such as the NDVI or EVI, especially in large-scale studies (Brandt et al., 2017).

Ideally, data on the amount of vegetation should be combined with information on biodiversity and vegetation type (Scogings, 2023). As new remote sensing techniques are being developed (Pettorelli et al., 2024), studying biophysical climate effects across context-specific restoration practices would give the opportunity to provide more realistic predictions on the climate effect of land restoration, while harnessing other benefits (and trade-offs). In this thesis, however, I did not consider the suitability and type of vegetation during the assessment of land restoration (Chapter 3). When applying the results of this thesis to a local context, it should, therefore, be kept in mind that the results may change under different vegetation types that are appropriate to that local context.



Figure 6.2 | Shade provides comfort, but is not included in the analysis. Maasai herder taking a break to cool off near the water pan under a tree. Image obtained from Sonak (2023).

6.3.2 Uncertainties related to the use of remote sensing and modelling

In this thesis, I used remote sensing (Chapter 2-4) and atmospheric modelling (Chapter 5) to determine how changes in vegetation affect properties such as albedo, temperature and cloud formation. However, even though the satellite and model results are validated using field measurements in Chapter 3 and Chapter 5, using satellite data as a main source comes with uncertainty. For example, the satellites monitor restoration and temperature at the top of the canopy under clear-sky conditions and estimated that the corresponding change in air temperature may only be 15-30% of the change in surface temperature (Li et al., 2025). It is therefore expected that the surface cooling potential of restoration, as found in this study, is higher than the potential to change in air temperature (at least under clear-sky conditions). Vegetation can also provide comfort through shade (Figure 6.2), which is not considered in the (top-of-canopy) land surface temperature. The microclimate inside a forest is often different from the surface temperature (Wilson et al., 2000; Su et al., 2021), depending on the leaf density (Von Arx et al., 2013), season (Haesen et al., 2021) and tree type (Luyssaert et al., 2014; Luyssaert et al., 2018). In general, the temperature inside a forest is milder than outside the forest (Aalto et al., 2021; De Frenne et al., 2021) with a lower diurnal temperature range (Ismaeel et al., 2024). Unfortunately, the limited availability of eddy covariance and other field measurements in Africa limits extensive analysis of air temperature and forest microclimates.

In addition, I often use a so-called ‘space-for-time’ approach to study the effect of land restoration on, for example, cloud cover (Chapter 4). In this approach, it is assumed that the changing vegetation cover over time (i.e. land restoration) can be studied by comparing regions with different vegetation cover over space. However, often, such a space-for-time approach overestimates the effect of land cover change (Chen & Dirmeyer, 2020). I also considered increases and decreases in vegetation greening to have a similar impact (Chapter 3). Recent studies have shown that forest loss and forest gain may have an asymmetric impact on land surface temperature due to structural differences in vegetation, although studies conflict on the magnitude of this asymmetry (Su et al., 2023; Zhang et al., 2024).

On top of that, when using observational data, it always comes with a risk of covariation with other variables, such as elevation (Sandel & Svenning, 2013). Although these effects can partially be solved by using modelling studies, the parameterisation of vegetation in the model strongly influences the outcome (Breil et al., 2021). Combining model predictions with observational data is, therefore, essential to get a more accurate view of the climate effects of land restoration.

6.3.3 Uncertainties related to potential feedbacks

As a consequence of studying the climate effect of land restoration separately, some potential feedbacks are not included. For example, in Chapter 3, I only considered daytime clear-sky land surface temperature. Consequently, the effect of the increased cloud formation found in Chapters 4 and 5 is not included in the temperature effects studied in Chapter 3. Because clouds change the incoming shortwave and outgoing longwave radiation, it is estimated that the effect of vegetation changes on air temperature is less extreme than on clear-sky land surface temperature (Alkama & Cescatti, 2016). This can also be observed during the three case study days in Chapter 5, as cloud formation is quickly followed by a decrease in potential temperature close to the surface. However, because different cloud types have been shown to respond to incoming shortwave and outgoing longwave radiation differently, modelling studies that simulate longer time scales are needed to determine the total effect of land restoration on temperature. In addition, changes in atmospheric circulation can further impact the local and non-local temperature after restoration (Winckler et al., 2019), which are not included in the analysis in Chapter 3.

Similarly, vegetation in Africa plays an important role in moisture recycling (Te Wierik et al., 2024) through which land restoration can impact water availability over larger scales (Hoek van Dijke et al., 2022; Engel et al., 2025). Because the amount of vegetation in many regions across Africa is limited by water availability, restoration-induced changes in water availability may impact the potential of vegetation to grow in this region, the energy balance partitioning and other potential feedback mechanisms to cloud formation. These indirect effects and feedbacks are not considered in the data-



Figure 6.3 | Digging bunts in East Africa. Risa bunds in Soralo (Kenya) in November 2022. Images made by (Sonak, 2023).

driven analysis or short model runs. As a result, the effect of large-scale restoration across Africa may differ from the results obtained in this thesis, which rather show the local and immediate climate effect if restoration is implemented in a certain location. Modelling studies with longer time-scales and dynamic vegetation can be used in the future to study the impact land restoration on feedbacks between climate and vegetation.

6.3.4 Uncertainties related to the land user's perspective

The benefits and trade-offs of land restoration projects are often (also in this thesis) assessed using qualitative tools such as remote sensing, modelling or field measurements (e.g. Meroni et al., 2017; Sacande et al., 2021; van der Vliet et al., 2024). The perspective of local communities and land users is, in these cases, not considered in the analysis, even though the success or failure of land restoration projects is often tightly connected to the local perceptions. More and more studies argue that context-specific approaches are needed (Brancalion & Holl, 2020; Holl & Brancalion, 2020; Di Sacco et al., 2021; Briske et al., 2024). It is therefore important to determine to what extent local residents experience the same biophysical effects of a restoration project as shown by the remotely-sensed data.

The MSc thesis from Ishani Sonak, for example, aimed to integrate remote sensing with the local land users' perspective to assess the biophysical effect of rainwater harvesting structures (Figure 6.3) and formalisation of grazing management in Amboseli and South Rift Valley in the south of Kenya (Sonak, 2023). During field interviews, the

Maasai community members mentioned temperature benefits even though no significant difference in temperature could be observed with satellite data:

“When rain falls, bunds will hold water and grasses will appear. The grass absorbs heat. There is lesser heat released and lesser heating of the ground. Therefore, no heating of the air right above ground. Perhaps the reason we feel cooler weather and lower temperature.” - Maasai community elder.

In addition, the local communities mention several benefits of land restoration, including increased vegetation to feed the animals, water retention, decreased temperature and increased biodiversity such as insects.

*“Digging these bunds will help reduce the velocity and increase infiltration. This will lead to increase in soil moisture which will help in regeneration of nutritional grass. Retention of soil water with enough vegetation will also cool down the temperature and potentially induce rain. It is the only way to ensure survival of my livestock.”
- Community elder.*

This example case study highlights that community perceptions can be different from objective measurements, such as through satellite data. In addition, even if the original goals of the project are not reached, project evaluation can shed light on other indirect benefits that were not expected before.

6.4 The latent potential of restoration

6.4.1 The biophysical climate effects of land restoration

Despite these uncertainties, the results in this thesis show that land restoration has the potential to affect the local climate through biophysical processes, depending on the type of projects, aridity and soil moisture conditions, and the size and spatial patterns of the land restoration projects. This makes it difficult to predict the biophysical effect of restoration projects. Therefore, I explain the expected biophysical climate effects of land restoration projects under different aridity (or soil moisture) conditions and spatial clustering of restoration projects, using four conceptual figures (Figure 6.4).

The lower albedo of the restored area compared to a nearby region with a lower vegetation cover increases the absorption of incoming solar radiation (Figure 6.4a). Under conditions where the restored area has a high soil moisture, much water is available for the vegetation to evaporate. As a result, the increased net radiation will mainly result in an enhanced latent heat flux and a decreased sensible heat flux in the restored area compared to surrounding regions. Combined with the higher surface roughness, the surface temperature in the restored area will be lower. Because the

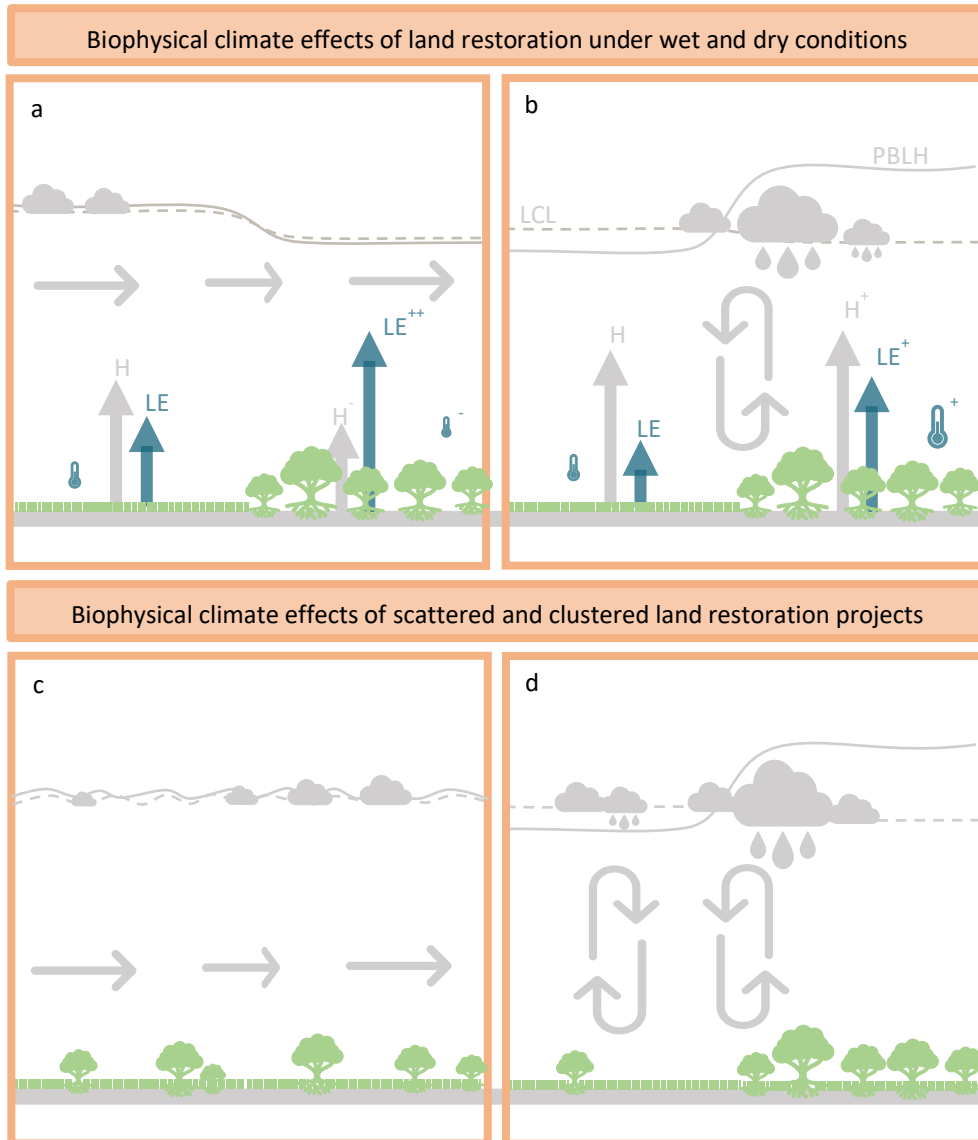


Figure 6.4 | Biophysical climate effects of land restoration in Africa. Local effects of an increase in vegetation cover on the energy balance, boundary layer development and cloud formation. The arrows show the sensible heat flux (H , grey) and latent heat flux (LE , blue). The grey lines show the boundary layer height (PBLH, continuous) and lifting condensation level (LCL, dotted). The grey arrows show the wind patterns. The top row show the effect of land restoration under wet (a) and dry (b) conditions in the restored area. The bottom row shows the effect of the spatial configuration, with scattered (c) and clustered projects (d)

boundary layer height is lower over the restored area, cloud formation is inhibited, despite the lower lifting condensation level. Under conditions where the soil moisture is relatively low in the restored area, for example, in arid regions (Chapter 3) or on drier days (Chapter 5), a rather different effect is expected (Figure 6.4b). Due to the lack of moisture available for evaporation, the increased available energy caused by the low albedo cannot be allocated to the latent heat flux only, but will also result in an increased sensible heat flux. This will lead to a higher surface temperature in the restored area, as well as an increased boundary layer height. The combination of a high surface roughness and a relatively high and warm boundary layer will result in wind convergence and mesoscale circulations, enhancing cloud formation and potentially precipitation over the restored area.

Under conditions where restoration enhances cloud formation, the cloud enhancement is especially strong over larger, clustered protected areas because these conditions enhance the mesoscale circulation triggered by thermally and dynamically driven convergence (Figure 6.4d). If the same amount of land were restored, but scattered across a larger area, there would be no strong gradients in temperature or height of the boundary layer (Figure 6.4c). As a result, such a scattered restoration pattern will result in less cloud formation.

These results build, of course, on a vast number of existing literature studying land-atmosphere interactions. It has been known that changes in vegetation can affect the local climate through biophysical processes (e.g. Duveiller et al., 2018b, 2018a; Chen & Dirmeyer, 2020) and that these processes vary across climate regions (e.g. Bonan, 2008; Perugini et al., 2017; Li et al., 2025). It was known that soil moisture anomalies impact cloud formation and rainfall patterns (Taylor, 2000; Taylor & Blyth, 2000; Taylor et al., 2012) in regions with strong soil moisture-atmosphere coupling (Koster et al., 2004). In regions such as the Sahel, dry soils increase the intensity of convection due to increased instability, convergence and wind shear across the Sahel (Klein & Taylor, 2020). The boundary layer over dry soils is found to be twice as high as over wet soils (Taylor et al., 2007). This effect is especially strong over mesoscale soil moisture heterogeneities, where length scales of 10-40 km enhance convective cloud initiation and precipitation (Garcia-Carreras et al., 2010; Taylor et al., 2011). It has also been known that changes in forest cover can impact cloud formation and precipitation (Taylor, Klein, Parker, et al., 2022; Crook et al., 2023), and that the size of the forest cover changes is important (Garcia-Carreras & Parker, 2011; Spracklen et al., 2018).

However, this thesis sheds new light on these mechanisms by explicitly focusing on land restoration in Africa, combining changes in vegetation cover across different climate regions, taking soil moisture conditions as well a project size and heterogeneity into account.

6.4.2 Biophysical climate effects in the context of land restoration

Land restoration can have many goals and benefits, but also trade-offs, both locally and globally. In this thesis, I mainly discuss the local climate effects of land restoration across Africa, but designing and implementing land restoration only based on potential local biophysical climate effects will ignore these other potential benefits and trade-offs. It is, therefore, important to zoom out and consider the broader context in which the restoration projects are implemented.

Land restoration can be implemented for many reasons, including reversing land degradation, enhancing biodiversity, improving livelihoods or preventing floods (Edwards et al., 2021; Edwards & Cerullo, 2024). Considering the broader climate impacts, land restoration can sequester carbon through increases in vegetation cover. Not only tree planting, but also natural regeneration and forest management may increase carbon sequestration (Roebroek et al.; Williams et al., 2024), showing wide potential for restoring existing natural regions (Rayden et al., 2023). However, the change in albedo should be taken into account as well (Hasler et al., 2024; Kristensen et al., 2024). Accounting for both carbon sequestration and changes in surface albedo, land restoration in dryland regions in Africa may have a net warming effect because the change in albedo, as shown in Chapter 3, offsets the cooling effect due to carbon sequestration (Rohatyn et al., 2022; Kristensen et al., 2024). These studies do, however, not include potential cloud feedbacks shown in Chapter 4 and 5, and how this potentially affects the top-of-atmosphere albedo. This makes it difficult to predict the overall climate effect, including biophysical and biogeochemical effects, of land restoration projects across Africa.

It is advised that restoration projects acknowledge both synergies and trade-offs and invest in sustainable and equitable land restoration (Edwards et al., 2021) and biodiversity enhancement to ensure the long-term success of restoration (Edwards & Cerullo, 2024). Trade-offs could include reduced water availability (Hoek van Dijke et al., 2022; Peng et al., 2024), grassland degradation (Wieczorkowski & Lehmann, 2022; Parr et al., 2024) decreases in cropland or deforestation, and social inequity (Brancalion & Holl, 2020; Holl & Brancalion, 2020). It is therefore important to keep societal and equity implications in mind when designing and implementing a land restoration project (Schultz et al., 2022; Mensah et al., 2024) by allowing local communities and organisations to be involved in management (Erbaugh et al., 2020; Walters et al., 2021; Nsikani et al., 2023).

For example, it is possible to determine how land restoration actually contributes to adaptation to extreme events. Does land restoration provide benefits for local land users and do these benefits align with their needs? Together with Vivian Onyango, I tried to answer these questions using a combination of remote sensing and field ethnographies (focus group discussions, key informant interviews and participatory

mapping) (Figure 6.5) for two villages in Laisamis, Kenya, called Ndikiir and Korr, where farmer-managed natural regeneration has been implemented by World Vision in 2019. Remote sensing data, using high-resolution NDVI data from Planet (Planet Team, 2017), highlights an increase in vegetation greening within the project area compared to surrounding areas after project implementation (Figure 6.6). Field ethnographies confirm that after a long period of degradation, the number of acacia trees has increased due to better management within the project area. A local pastoralist in Ndikiir says:

“They came up with bylaws that prohibited shaking the trees. Whoever was found shaking the trees would be fined 50,000 shillings, and if they had an expectant cow, it would be taken. From that time, the landscape changed, and people began to respect the environment up to now, you can see a forested area.”

These acacia trees provide several benefits to adapt to extreme events, especially droughts. According to local pastoralists, the seeds of the acacia (pods) are a crucial feed for the livestock during droughts, when other vegetation is limited. They also sell the pods or wood from the trees to provide extra income. In addition, the pastoralists are aware of the continuous nature of extreme events and use the pods to prepare for future droughts. A pastoralist in Korr highlights:

“Yes, trees have many benefits. They produce acacia pods that contribute to the health of animals and can be sold at a good price. They also provide shade. The acacia pods produce flowers, which goat kids feed on, and the trees' leaves, when they shed, are also consumed by goat kids. Additionally, the trees help attract rainfall.”

However, the trees only provide benefits during shorter droughts. Due to the increasing intensity of extreme events, restoration alone is not enough to adapt, and pastoralists mention that other interventions, such as government support and relief, diversification of income and education, may help to adapt to future climate change. This research illustrates that land restoration provides benefits in Kenyan drylands, but is in itself not enough to adapt to droughts, and a multi-method approach provides important local context on the adaptation benefits and adaptation gaps of land restoration projects.

6.4.3 Recommendations for restoration policy and project design

Based on the results in this thesis and existing literature, I make the following recommendations for restoration projects in Africa. Land restoration has an observable impact on temperature and cloud formation across Africa and should therefore be incorporated in decision-making and planning, both to optimise potential benefits and to avoid unwanted potential trade-offs. From a biophysical perspective, land restoration in arid regions will likely result in local warming. This should be considered and weighed against other benefits when projects are implemented in these regions. If



Figure 6.5 | A multi-method approach to study land restoration. Field ethnographies such as participatory mapping here in Korr (Kenya) can provide a local land user's perspective on benefits and challenges of land restoration. Image made by Vivian Onyango.

local cooling is the aim of the projects, restoration in semi-arid or subhumid regions will be more effective. If the aim is to increase cloud formation, larger restoration areas and clustered projects will likely have a larger impact than smaller projects scattered across the region. However, even though land restoration projects are expected to impact rainfall and water availability in the long term, these impacts remain mostly unknown. On a large scale, I argue for the inclusion of biophysical effects in climate mitigation as the effect on land restoration on the Earth's energy balance has been shown to be broader than carbon sequestration alone, both through changes in surface albedo as well as cloud formation. Despite these potential large-scale benefits, I believe it is important to incorporate the small-scale and local community perspective in the evaluation of these projects to avoid inequity.

6.4.4 Applicability to other study regions

Land restoration is a widely used measure to combat land degradation across the world. Under the current Decade of Ecosystem Restoration, large-scale global projects, such as the Bonn Challenge or the Trillion Trees initiative, aim to restore millions of hectares in

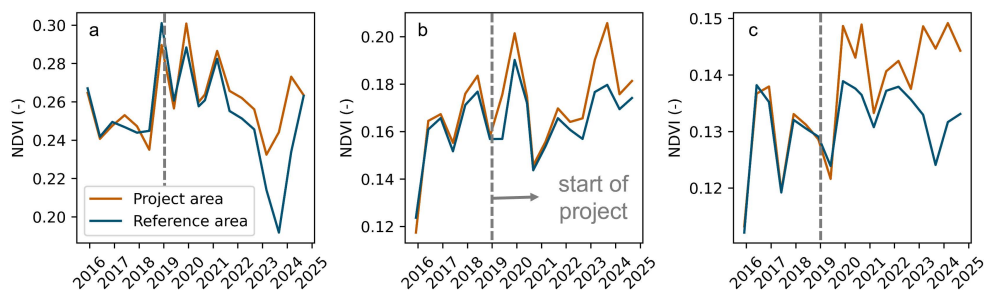


Figure 6.6 | The impact of farmer-managed natural regeneration on vegetation. Time series of the Normalized Difference Vegetation Index (NDVI) within the project area and a surrounding reference area in (a) Ndikiir and (b, c) two locations in Korr. The dotted lines indicate the moment of intervention. Data is obtained from Planet (Planet Team, 2017).

the coming years (UNEP, 2021). However, because the biophysical climate impact of land restoration projects depends on background climate and aridity, the results in this thesis cannot be directly applied to other study areas. Global studies have shown that the temperature impact of vegetation changes strongly varies across the globe, where land restoration will likely result in biophysical cooling in tropical regions and warming in boreal regions (e.g. Bonan, 2008; Perugini et al., 2017; Duveiller et al., 2020). In more boreal regions such as northern Europe, the relatively strong albedo reduction of forested areas in high snow cover counterweights any potential evaporative cooling, resulting in a relative increase in surface temperature with offsets climate benefits cause by carbon sequestration (Windisch et al., 2021; Hasler et al., 2024; Kristensen et al., 2024). In tropical regions such as the Amazon, a combination of high moisture availability and incoming solar radiation results in a high evaporative cooling (Huang et al., 2022; da Silva et al., 2024). Being in-between tropical and boreal climates, temperate regions such as the Netherlands often show a limited or unclear biophysical climate effect of changes in vegetation cover. Studies show that deforestation in the temperate regions likely will result in an increased temperature during the day (Chen & Dirmeyer, 2020) and a decrease at night (Li et al., 2015a; Hamberg et al., 2022), depending on the vegetation type (Huang et al., 2020).

Although the fact that changes in vegetation cover can impact cloud formation is recognised (Duveiller et al., 2021), there is less scientific consensus on the magnitude and direction of this effect, with discrepancies between satellite observations and models (Caporaso et al., 2024), across regions (Duveiller et al., 2021; Xu et al., 2022) and scales (Garcia-Carreras et al., 2010; Spracklen et al., 2018). This highlights that although similar mechanisms may play a role in the biophysical climate effect of land restoration across the world, it is difficult to directly transfer the results of this thesis to other study areas.

6.5 Future outlook

The effect of deforestation, reforestation and vegetation on the climate has been studied and debated for many years (e.g. Brown, 1877). In 1888, the Philosophical Society of Washington organised a symposium to discuss the question “Do forests influence rainfall?” where scholars did not seem to agree with the answer to this seemingly simple question (Science, 1888; Bonan, 2023). Although research has come a long way since then, the debate is continuing (Ellison et al., 2012). Main uncertainties exist in the greening potential of land restoration, how the biophysical climate effects varied across climate regions, and to what extent the small-scale restoration project can impact the climate. This thesis shows that land restoration projects in Africa can increase vegetation greenness (Chapter 2), decrease the local surface temperature in semi-arid regions (Chapter 3) and increase cloud formation in West Africa, especially larger or clustered projects (Chapter 4 and 5). Yet, there is much left to learn before it is possible to make accurate predictions on the broader climate impact of land restoration in Africa and elsewhere.

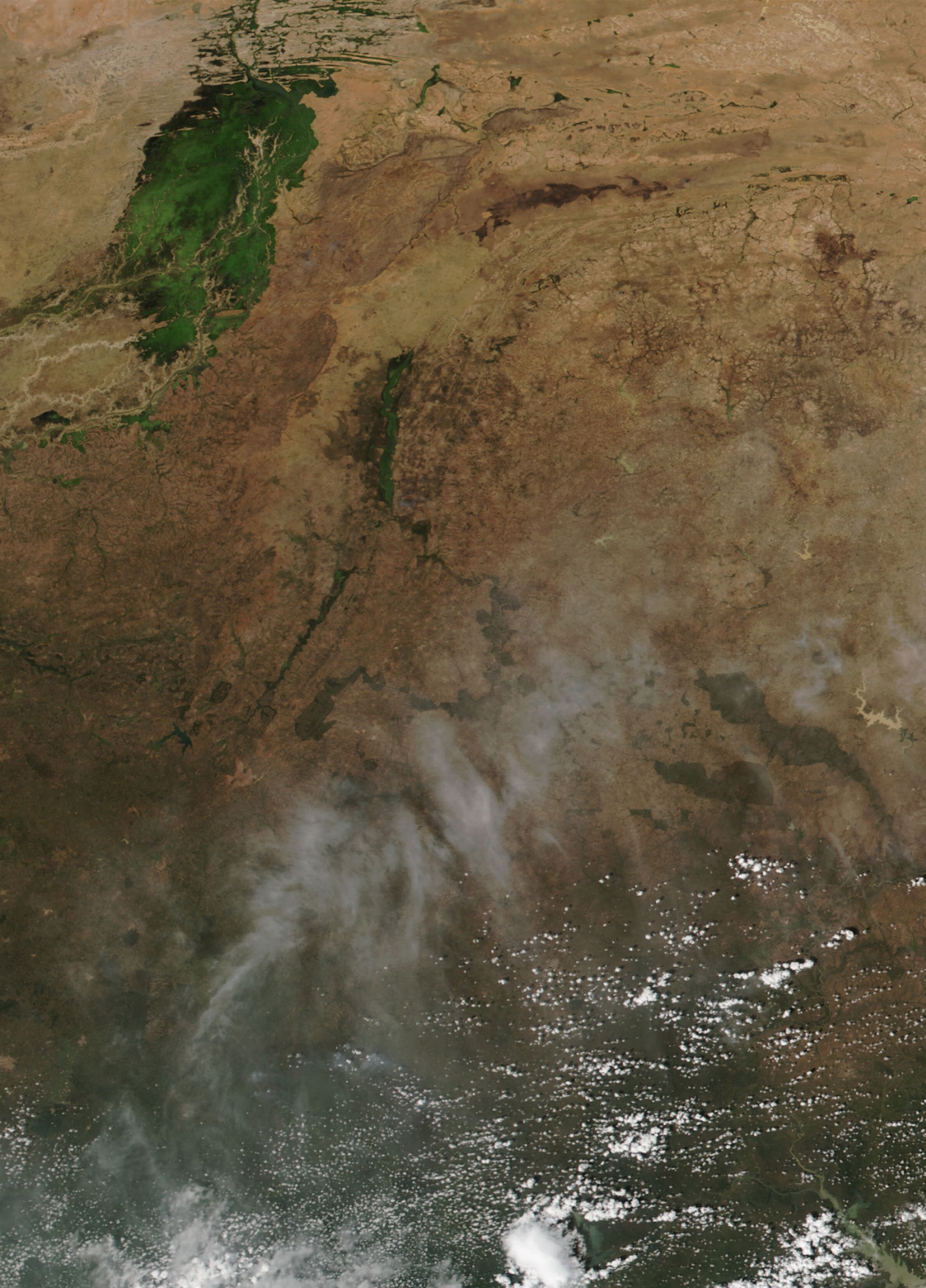
In Chapter 4 and Chapter 5, I showed that the size and spatial patterns of land restoration strongly impact cloud formation. Yet, it remains unknown how different vegetation types or heterogeneity within the restored areas impact these relations. In Europe, for example, it is found that forest management can considerably impact temperature (Luyssaert et al., 2014; Naudts et al., 2016; Luysaert et al., 2018; Windisch et al., 2021). In addition, I only studied these relations for a case study region in West Africa, so it is not known how these relationships vary across climate regions within Africa or over longer time scales. Newly developed datasets and tools, such as high-resolution tree cover maps (Reiner et al., 2023) in combination with geostationary satellite data or large-eddy simulation, will provide opportunities to study the relationships between different vegetation types and cloud formation across climate zones in Africa in the future.

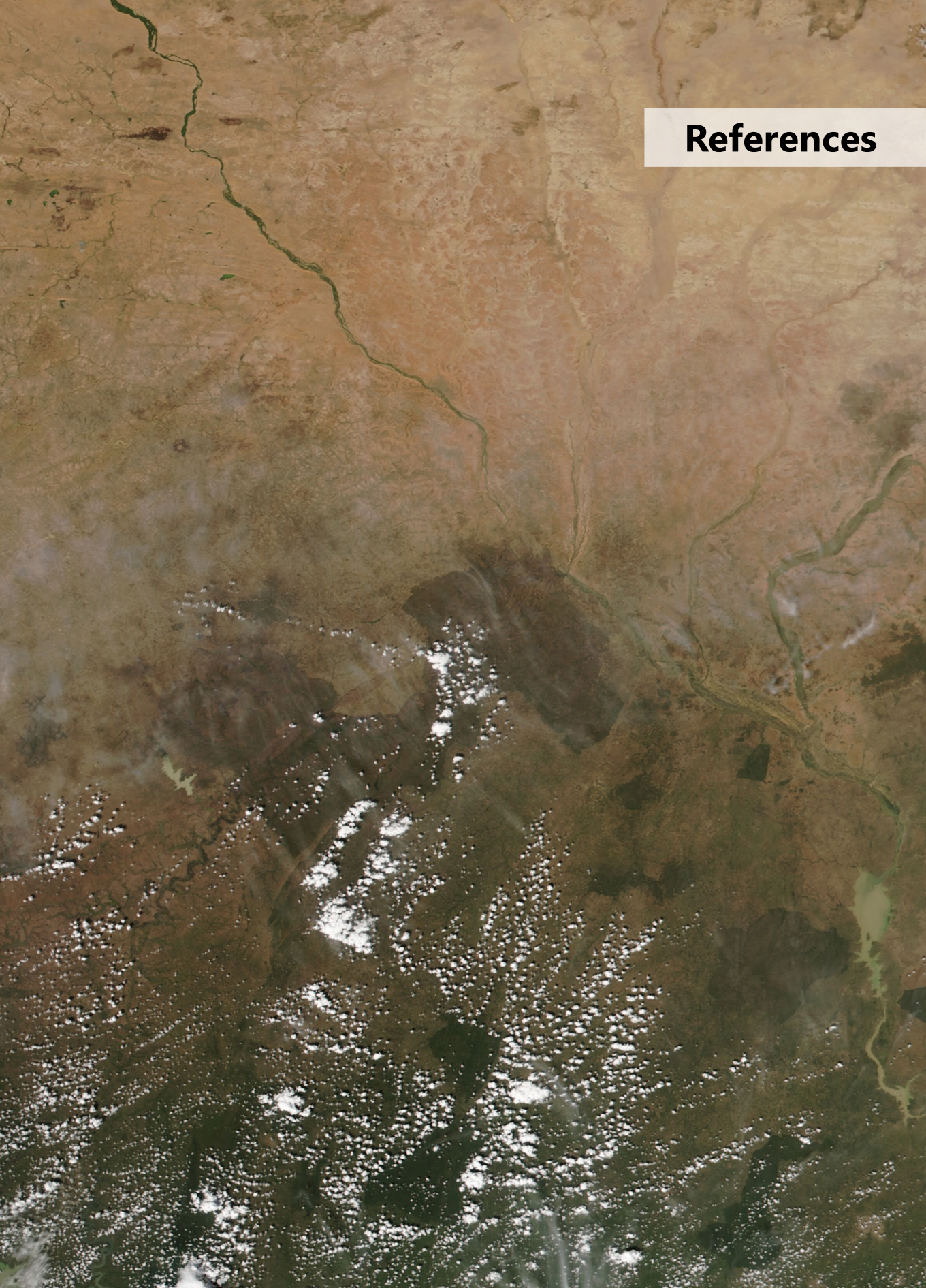
In addition to providing shade and rainfall, changes in cloud cover can have a profound effect on the global climate (Goessling et al., 2025). In general, high-altitude clouds trap longwave radiation emitted by the Earth’s surface, while low-altitude clouds reflect incoming shortwave solar radiation. Yet, to what extent restoration-induced changes in cloud formation impact, for example, the Earth’s top-of-atmosphere albedo, remains uncertain (Ibisch et al., 2025). Even though research is moving beyond solely studying the climate impact of restoration from a carbon sequestration perspective (Hasler et al., 2024), studying the relation between land restoration-induced cloud formation and the Earth’s energy balance remains challenging due to the inherently noisy cloud signal and the conversion of cloud data to top-of-atmosphere albedo. From an observational perspective, opportunities may lie in using tools like machine learning to connect the discrepancy in spatial scales of land restoration (~100m), cloud cover (~1 km) and top-of-atmosphere albedo (~100 km) datasets (Ham et al., 2022; Ryan et al., 2022; Ryan,

2024). Nonetheless, neglecting the effect of cloud formation on the Earth's energy balance does not provide a complete picture of the climate impacts of land restoration.

In Chapter 3, I showed that the cooling potential of land restoration strongly depends on aridity and in Chapter 5, I determined that restoration-cloud interactions change with soil moisture conditions. With ongoing anthropogenic climate change, temperatures in Africa are expected to rise further, increasing drought frequency and duration across the continent (IPCC, 2021). It is expected that climate change will also impact land-atmosphere interactions and moisture recycling (Engel et al., 2025). In addition, climate change will also affect to what extent regions are suitable for restoration (Roebroek et al., 2025). To study the climate effects of land restoration across longer time scales, it is needed to include a dynamic vegetation cover in modelling studies, as well as to study the observed effect of anthropogenic climate change on the land-atmosphere interactions. This is needed to determine to what extent land restoration can actually help to (globally) mitigate and (locally) adapt to ongoing anthropogenic climate change.

With the many land restoration projects currently being implemented, providing a thorough understanding of the relevant land-atmosphere interactions is timely and essential. Throughout this thesis, I aimed to advance our current knowledge on the climate effects of land restoration and vegetation in general. Nonetheless, science still has a long road ahead before this thorough understanding can be reached. I personally believe that this does not mean that the implementation of land restoration should be paused or even stopped altogether, as anthropogenic climate change and other human pressures continue to degrade native ecosystems and the benefits of restoration, if done correctly, seem plentiful. However, evaluation and monitoring of land restoration projects, using both biophysical observations and land users' perspectives, remains essential. It should also not be forgotten that land restoration alone is not a golden solution to all our problems, and avoiding further degradation of ecosystems and limiting anthropogenic climate change is essential to reach a sustainable world in the future.



An aerial photograph of a landscape. The top half shows a light brown, textured area, possibly a dry riverbed or a road, with a thin green line running through it. The bottom half shows a dense green forest with a network of roads and paths. A white rectangular box is in the top right corner containing the word "References".

References

- Aalto, I. J., Maeda, E. E., Heiskanen, J., Aalto, E. K., & Pellikka, P. K. E. (2021). Strong influence of trees outside forest in regulating microclimate of intensively modified Afrotropical landscapes. *Biogeosciences Discussions*, 2021, 1-34.
- Abel, C., Horion, S., Tagesson, T., Brandt, M., & Fensholt, R. (2019). Towards improved remote sensing based monitoring of dryland ecosystem functioning using sequential linear regression slopes (SeRGS). *Remote Sensing of Environment*, 224, 317-332.
- Abel, C., Horion, S., Tagesson, T., De Keersmaecker, W., Seddon, A. W., Abdi, A. M., & Fensholt, R. (2020). The human–environment nexus and vegetation–rainfall sensitivity in tropical drylands. *Nature Sustainability*, 1-8.
- Abiodun, B. J., Adeyewa, Z. D., Oguntunde, P. G., Salami, A. T., & Ajayi, V. O. (2012). Modeling the impacts of reforestation on future climate in West Africa. *Theoretical and Applied Climatology*, 110(1-2), 77-96.
- Achugbu, I. C., Dudhia, J., Olufayo, A. A., Balogun, I. A., Adefisan, E. A., & Gbode, I. E. (2020). Assessment of WRF Land Surface Model Performance over West Africa. *Advances in Meteorology*, 2020(1), 6205308.
- Adler, B., Kalthoff, N., & Gantner, L. (2017). Nocturnal low-level clouds over southern West Africa analysed using high-resolution simulations. *Atmospheric Chemistry and Physics*, 17(2), 899-910.
- Akkermans, T., Thiery, W., & Van Lipzig, N. P. M. (2014). The regional climate impact of a realistic future deforestation scenario in the Congo basin. *Journal of Climate*, 27(7), 2714-2734.
- Alibakhshi, S., Naimi, B., Hovi, A., Crowther, T. W., & Rautiainen, M. (2020). Quantitative analysis of the links between forest structure and land surface albedo on a global scale. *Remote Sensing of Environment*, 246, 111854.
- Alkama, R., & Cescatti, A. (2016). Biophysical climate impacts of recent changes in global forest cover. *science*, 351(6273), 600-604.
- Allen, S., Wallace, J., Gash, J., & Sivakumar, M. (1994). Measurements of albedo variation over natural vegetation in the Sahel. *International journal of climatology*, 14(6), 625-636.
- Amani, S., & Shafizadeh-Moghadam, H. (2023). A review of machine learning models and influential factors for estimating evapotranspiration using remote sensing and ground-based data. *Agricultural Water Management*, 284, 108324.
- Archibald, S., Kirton, A., Van der Merwe, M. R., Scholes, R., Williams, C., & Hanan, N. (2009). Drivers of inter-annual variability in Net Ecosystem Exchange in a semi-arid savanna ecosystem, South Africa. *Biogeosciences*, 6(2), 251-266.
- Ardö, J., Mölder, M., El-Tahir, B. A., & Elkhidir, H. A. M. (2008). Seasonal variation of carbon fluxes in a sparse savanna in semi arid Sudan. *Carbon Balance and Management*, 3, 1-18.
- Arora, V. K., & Montenegro, A. (2011). Small temperature benefits provided by realistic afforestation efforts. *Nature geoscience*, 4(8), 514-518.
- Aryee, J. N., Amekudzi, L. K., & Yamba, E. I. (2021). Low-Level Cloud Development and Diurnal Cycle in Southern West Africa During the DACCIWA Field Campaign: Case Study of Kumasi Supersite, Ghana. *Journal of Geophysical Research: Atmospheres*, 126(11), e2020JD034028.
- Ascher, B. D., Saleeby, S. M., Marinescu, P. J., & van den Heever, S. C. (2025). Forest Breeze–Cold Pool Interactions Drive Convective Organization over Heterogeneous Vegetation. *Journal of the Atmospheric Sciences*, 82(1), 71-94.

- Bala, G., Caldeira, K., Wickett, M., Phillips, T., Lobell, D., Delire, C., & Mirin, A. (2007). Combined climate and carbon-cycle effects of large-scale deforestation. *Proceedings of the national academy of sciences*, 104(16), 6550-6555.
- Baldocchi, D., Falge, E., Gu, L., Olson, R., Hollinger, D., Running, S., Anthoni, P., Bernhofer, C., Davis, K., & Evans, R. (2001). FLUXNET: A new tool to study the temporal and spatial variability of ecosystem-scale carbon dioxide, water vapor, and energy flux densities. *Bulletin of the American Meteorological Society*, 82(11), 2415-2434.
- Barbier, E. B., & Hochard, J. P. (2018). Land degradation and poverty. *Nature Sustainability*, 1(11), 623-631.
- Bastin, J.-F., Finegold, Y., Garcia, C., Mollicone, D., Rezende, M., Routh, D., Zohner, C. M., & Crowther, T. W. (2019). The global tree restoration potential. *science*, 365(6448), 76-79.
- Bechara, F. C., Dickens, S. J., Farrer, E. C., Larios, L., Spotswood, E. N., Mariotte, P., & Suding, K. N. (2016). Neotropical rainforest restoration: comparing passive, plantation and nucleation approaches. *Biodiversity and Conservation*, 25(11), 2021-2034.
- Bennett, B. M., & Barton, G. A. (2018). The enduring link between forest cover and rainfall: a historical perspective on science and policy discussions. *Forest Ecosystems*, 5(1), 1-9.
- Betts, A. K., & Ball, J. H. (1997). Albedo over the boreal forest. *Journal of Geophysical Research: Atmospheres*, 102(D24), 28901-28909.
- Betts, R. A. (2000). Offset of the potential carbon sink from boreal forestation by decreases in surface albedo. *Nature*, 408(6809), 187-190.
- Biasutti, M. (2019). Rainfall trends in the African Sahel: Characteristics, processes, and causes. *Wiley Interdisciplinary Reviews: Climate Change*, 10(4), e591.
- Birch, C. E., Marsham, J. H., Parker, D. J., & Taylor, C. M. (2014). The scale dependence and structure of convergence fields preceding the initiation of deep convection. *Geophysical Research Letters*, 41(13), 4769-4776.
- Bley, S., & Deneke, H. (2013). A threshold-based cloud mask for the high-resolution visible channel of Meteosat Second Generation SEVIRI. *Atmospheric Measurement Techniques*, 6(10), 2713-2723.
- Boisier, J., de Noblet-Ducoudré, N., Pitman, A., Cruz, F., Delire, C., Van den Hurk, B., Van der Molen, M., Müller, C., & Voldoire, A. (2012). Attributing the impacts of land-cover changes in temperate regions on surface temperature and heat fluxes to specific causes: Results from the first LUCID set of simulations. *Journal of Geophysical Research: Atmospheres*, 117(D12).
- Bonan, G. (2023). *Seeing the Forest for the Trees* [Book]. Cambridge University Press.
- Bonan, G. B. (2008). Forests and climate change: forcings, feedbacks, and the climate benefits of forests. *science*, 320(5882), 1444-1449.
- Bonan, G. B. (2016). Forests, climate, and public policy: A 500-year interdisciplinary odyssey. *Annual Review of Ecology, Evolution, and Systematics*, 47, 97-121.
- Bond, W. J., Stevens, N., Midgley, G. F., & Lehmann, C. E. R. (2019). The Trouble with Trees: Afforestation Plans for Africa. *Trends in Ecology & Evolution*, 34(11), 963-965.
- Bosman, P. J., van Heerwaarden, C. C., & Teuling, A. J. (2019). Sensible heating as a potential mechanism for enhanced cloud formation over temperate forest. *Quarterly Journal of the Royal Meteorological Society*, 145(719), 450-468.

- Boysen, L. R., Brovkin, V., Arora, V. K., Cadule, P., de Noblet-Ducoudré, N., Kato, E., Pongratz, J., & Gayler, V. (2014). Global and regional effects of land-use change on climate in 21st century simulations with interactive carbon cycle. *Earth System Dynamics*, 5(2), 309-319.
- Boysen, L. R., Brovkin, V., Pongratz, J., Lawrence, D. M., Lawrence, P., Vuichard, N., Peylin, P., Liddicoat, S., Hajima, T., & Zhang, Y. (2020). Global climate response to idealized deforestation in CMIP6 models. *Biogeosciences*, 17(22), 5615-5638.
- Brancalion, P. H., & Holl, K. D. (2020). Guidance for successful tree planting initiatives. *Journal of Applied Ecology*, 57(12), 2349-2361.
- Branch, O., & Wulfmeyer, V. (2019). Deliberate enhancement of rainfall using desert plantations. *Proceedings of the national academy of sciences*, 116(38), 18841-18847.
- Brandt, M., Rasmussen, K., Peñuelas, J., Tian, F., Schurgers, G., Verger, A., Mertz, O., Palmer, J. R., & Fensholt, R. (2017). Human population growth offsets climate-driven increase in woody vegetation in sub-Saharan Africa. *Nature ecology & evolution*, 1(4), 1-6.
- Brandt, M., Tucker, C. J., Kariryaa, A., Rasmussen, K., Abel, C., Small, J., Chave, J., Rasmussen, L. V., Hiernaux, P., & Diouf, A. A. (2020). An unexpectedly large count of trees in the West African Sahara and Sahel. *Nature*, 587(7832), 78-82.
- Breil, M., Davin, E. L., & Rechid, D. (2021). What determines the sign of the evapotranspiration response to afforestation in European summer? *Biogeosciences*, 18(4), 1499-1510.
- Breil, M., Krawczyk, F., & Pinto, J. G. (2023). The response of the regional longwave radiation balance and climate system in Europe to an idealized afforestation experiment. *Earth System Dynamics*, 14(1), 243-253.
- Breiman, L. (2001). Random forests. *Machine learning*, 45, 5-32.
- Bright, R. M., Zhao, K., Jackson, R. B., & Cherubini, F. (2015). Quantifying surface albedo and other direct biogeophysical climate forcings of forestry activities. *Global change biology*, 21(9), 3246-3266.
- Briske, D. D., Vetter, S., Coetsee, C., & Turner, M. D. (2024). Rangeland afforestation is not a natural climate solution. *Frontiers in Ecology and the Environment*, 22(5), e2727.
- Brown, J. C. (1877). *Forests and moisture: or effects of forests on humidity of climate* [Book]. Oliver and Boyd.
- Broxton, P. D., Zeng, X., Sulla-Menashe, D., & Troch, P. A. (2014). A Global Land Cover Climatology Using MODIS Data. *Journal of Applied Meteorology and Climatology*, 53(6), 1593-1605.
- Caporaso, L., Duveiller, G., Giuliani, G., Giorgi, F., Stengel, M., Massaro, E., Piccardo, M., & Cescatti, A. (2024). Converging Findings of Climate Models and Satellite Observations on the Positive Impact of European Forests on Cloud Cover. *Journal of Geophysical Research: Atmospheres*, 129(11).
- Castelli, G., Castelli, F., & Bresci, E. (2019). Mesoclimate regulation induced by landscape restoration and water harvesting in agroecosystems of the horn of Africa. *Agriculture, ecosystems & environment*, 275, 54-64.
- Chacón, A., Sushama, L., & Beltrami, H. (2016). Biophysical impacts of land use change over North America as simulated by the Canadian regional climate model. *Atmosphere*, 7(3).

- Chapman, S., Syktus, J., Trancoso, R., Salazar, A., Thatcher, M., Watson, J. E., Meijaard, E., Sheil, D., Dargusch, P., & McAlpine, C. A. (2020). Compounding impact of deforestation on Borneo's climate during El Niño events. *Environmental Research Letters*, 15(8), 084006.
- Chen, C., Ge, J., Guo, W., Cao, Y., Liu, Y., Luo, X., & Yang, L. (2022). The biophysical impacts of idealized afforestation on surface temperature in China: local and nonlocal effects. *Journal of Climate*, 35(23), 4233-4252.
- Chen, C., Li, D., Li, Y., Piao, S., Wang, X., Huang, M., Gentine, P., Nemani, R. R., & Myneni, R. B. (2020). Biophysical impacts of Earth greening largely controlled by aerodynamic resistance. *Science advances*, 6(47), eabb1981.
- Chen, F., & Avissar, R. (1994). Impact of Land-Surface Moisture Variability on Local Shallow Convective Cumulus and Precipitation in Large-Scale Models. *Journal of Applied Meteorology and Climatology*, 33(12), 1382-1401.
- Chen, J., Dai, A., Zhang, Y., & Rasmussen, K. L. (2020). Changes in convective available potential energy and convective inhibition under global warming. *Journal of Climate*, 33(6), 2025-2050.
- Chen, L., & Dirmeyer, P. A. (2020). Reconciling the disagreement between observed and simulated temperature responses to deforestation. *Nature communications*, 11(1), 202.
- Chen, S., Haase, D., Qureshi, S., & Firozjaei, M. K. (2022). Integrated Land Use and Urban Function Impacts on Land Surface Temperature: Implications on Urban Heat Mitigation in Berlin with Eight-Type Spaces. *Sustainable Cities and Society*, 83.
- Cherlet, M., Hutchinson, C., Reynolds, J., Hill, J., Sommer, S., & von Maltitz, G. E. (2018). *World Atlas of Desertification* (3rd ed.) [Book]. Publication Office of the European Union.
- Chiti, T., Certini, G., Grieco, E., & Valentini, R. (2010). The role of soil in storing carbon in tropical rainforests: the case of Ankasa Park, Ghana. *Plant and soil*, 331, 453-461.
- Choobari, O. A., Zawar-Reza, P., & Sturman, A. (2014). The global distribution of mineral dust and its impacts on the climate system: A review. *Atmospheric Research*, 138, 152-165.
- Closset, M., Feindouno, S., Guillaumont, P., & Simonet, C. (2018). A Physical Vulnerability to Climate Change Index: Which are the most vulnerable developing countries? *FERDI Working paper*, P213.
- Constenla-Villoslada, S., Liu, Y., Wen, J., Sun, Y., & Chonabayashi, S. (2022). Large-scale land restoration improved drought resilience in Ethiopia's degraded watersheds. *Nature Sustainability*, 5(6), 1-10.
- Cook-Patton, S. C., Leavitt, S. M., Gibbs, D., Harris, N. L., Lister, K., Anderson-Teixeira, K. J., Briggs, R. D., Chazdon, R. L., Crowther, T. W., Ellis, P. W., Griscom, H. P., Herrmann, V., Holl, K. D., Houghton, R. A., Larrosa, C., Lomax, G., Lucas, R., Madsen, P., Malhi, Y., . . . Griscom, B. W. (2020). Mapping carbon accumulation potential from global natural forest regrowth. *Nature*, 585(7826), 545-550.
- Cooke, S. J., Bennett, J. R., & Jones, H. P. (2019). We have a long way to go if we want to realize the promise of the "Decade on Ecosystem Restoration". *Conservation Science and Practice*, 1(12), e129.
- Cordero, R. R., Feron, S., Sepúlveda, E., Damiani, A., Carrera, J. M., Jorquera, J., Alfonso, J. A., Fuenzalida, R., Rivas, M., & MacDonell, S. (2021). Evaluation of MODIS-

- derived estimates of the albedo over the Atacama Desert using ground-based spectral measurements. *Scientific Reports*, 11(1), 19822.
- Crook, J., Klein, C., Folwell, S., Taylor, C. M., Parker, D. J., Bamba, A., & Kouadio, K. (2023). Effects on early monsoon rainfall in West Africa due to recent deforestation in a convection-permitting ensemble. *Weather and Climate Dynamics*, 4(1), 229-248.
- da Silva, H. J. F., Gonçalves, W. A., Bezerra, B. G., Santos e Silva, C. M., de Oliveira, C. P., Júnior, J. B. C., Rodrigues, D. T., & Silva, F. D. S. (2024). Analysis of environmental variables and deforestation in the amazon using logistical regression models. *Environmental Monitoring and Assessment*, 196(10), Article 911.
- Davin, E. L., & de Noblet-Ducoudré, N. (2010). Climatic impact of global-scale deforestation: Radiative versus nonradiative processes. *Journal of Climate*, 23(1), 97-112.
- de Arellano, J. V.-G., Van Heerwaarden, C. C., & Lelieveld, J. (2012). Modelled suppression of boundary-layer clouds by plants in a CO₂-rich atmosphere. *Nature geoscience*, 5(10), 701-704.
- De Frenne, P., Lenoir, J., Luoto, M., Scheffers, B. R., Zellweger, F., Aalto, J., Ashcroft, M. B., Christiansen, D. M., Decocq, G., De Pauw, K., Govaert, S., Greiser, C., Gril, E., Hampe, A., Jucker, T., Klings, D. H., Koelemeijer, I. A., Lembrechts, J. J., Marrec, R., . . . Hylander, K. (2021). Forest microclimates and climate change: Importance, drivers and future research agenda. *Global change biology*, 27(11), 2279-2297.
- De Hertog, S. J., Havermann, F., Vanderkelen, I., Guo, S., Luo, F., Manola, I., Coumou, D., Davin, E. L., Duveiller, G., Lejeune, Q., Pongratz, J., Schleussner, C. F., Seneviratne, S. I., & Thiery, W. (2022). The biogeophysical effects of idealized land cover and land management changes in Earth system models. *Earth System Dynamics*, 13(3), 1305-1350.
- Dhakal, S., J.C. Minx, F.L. Toth, A. Abdel-Aziz, M.J. Figueroa Meza, K. Hubacek, I.G.C. Jonckheere, Yong-Gun Kim, G.F. Nemet, S. Pachauri, X.C. Tan, & Wiedmann, T. (2022). Emissions Trends and Drivers (In *Climate Change 2022: Mitigation of Climate Change. Contribution of Working Group III to the Sixth Assessment Report of the Intergovernmental Panel on Climate Change*). Cambridge University Press.
- Di Sacco, A., Hardwick, K. A., Blakesley, D., Brancalion, P. H., Breman, E., Cecilio Rebola, L., Chomba, S., Dixon, K., Elliott, S., & Ruyonga, G. (2021). Ten golden rules for reforestation to optimize carbon sequestration, biodiversity recovery and livelihood benefits. *Global change biology*, 27(7), 1328-1348.
- Didan, K. (2021). *MODIS/Terra Vegetation Indices 16-Day L3 Global 250m SIN Grid V061* [Dataset]. <https://doi.org/10.5067/MODIS/MOD13Q1.061>
- Dintwe, K., Okin, G. S., & Xue, Y. (2017). Fire-induced albedo change and surface radiative forcing in sub-Saharan Africa savanna ecosystems: Implications for the energy balance. *Journal of Geophysical Research: Atmospheres*, 122(12), 6186-6201.
- Dotterweich, M. (2013). The history of human-induced soil erosion: Geomorphic legacies, early descriptions and research, and the development of soil conservation—A global synopsis. *Geomorphology*, 201, 1-34.

- Dudley, N., Eufemia, L., Fleckenstein, M., Periago, M. E., Petersen, I., & Timmers, J. F. (2020). Grasslands and savannahs in the UN Decade on Ecosystem Restoration. *Restoration Ecology*, 28(6), 1313-1317.
- Durieux, L., Toledo Machado, L. A., & Laurent, H. (2003). The impact of deforestation on cloud cover over the Amazon arc of deforestation. *Remote Sensing of Environment*, 86(1), 132-140.
- Duveiller, G., Caporaso, L., Abad-Viñas, R., Perugini, L., Grassi, G., Arneth, A., & Cescatti, A. (2020). Local biophysical effects of land use and land cover change: towards an assessment tool for policy makers. *Land Use Policy*, 91, 104382.
- Duveiller, G., Filipponi, F., Ceglar, A., Bojanowski, J., Alkama, R., & Cescatti, A. (2021). Revealing the widespread potential of forests to increase low level cloud cover. *Nature communications*, 12(1), 4337.
- Duveiller, G., Hooker, J., & Cescatti, A. (2018a). A dataset mapping the potential biophysical effects of vegetation cover change. *Scientific data*, 5(1), 1-15.
- Duveiller, G., Hooker, J., & Cescatti, A. (2018b). The mark of vegetation change on Earth's surface energy balance. *Nature communications*, 9(1), 679.
- Edwards, D. P., & Cerullo, G. R. (2024). Biodiversity is central for restoration. *Current Biology*, 34(9), R371-R379.
- Edwards, D. P., Cerullo, G. R., Chomba, S., Worthington, T. A., Balmford, A. P., Chazdon, R. L., & Harrison, R. D. (2021). Upscaling tropical restoration to deliver environmental benefits and socially equitable outcomes. *Current Biology*, 31(19), R1326-R1341.
- Ek, M. B., & Holtslag, A. A. M. (2004). Influence of Soil Moisture on Boundary Layer Cloud Development. *Journal of Hydrometeorology*, 5(1), 86-99.
- ELD Initiative. (2015). *Report for policy and decision makers: Reaping economic and environmental benefits from sustainable land management*. [Report]. E. o. L. Degradation.
- Ellis, E. C., Gauthier, N., Klein Goldewijk, K., Bliege Bird, R., Boivin, N., Díaz, S., Fuller, D. Q., Gill, J. L., Kaplan, J. O., Kingston, N., Locke, H., McMichael, C. N. H., Ranco, D., Rick, T. C., Shaw, M. R., Stephens, L., Svenning, J.-C., & Watson, J. E. M. (2021). People have shaped most of terrestrial nature for at least 12,000 years. *Proceedings of the national academy of sciences*, 118(17), e2023483118.
- Ellison, D., Morris, C. E., Locatelli, B., Sheil, D., Cohen, J., Murdiyarsa, D., Gutierrez, V., Van Noordwijk, M., Creed, I. F., & Pokorny, J. (2017). Trees, forests and water: Cool insights for a hot world. *Global Environmental Change*, 43, 51-61.
- Ellison, D., N. Futter, M., & Bishop, K. (2012). On the forest cover–water yield debate: from demand-to supply-side thinking. *Global change biology*, 18(3), 806-820.
- Ellison, D., Pokorný, J., & Wild, M. (2024). Even cooler insights: On the power of forests to (water the Earth and) cool the planet. *Global change biology*, 30(2), e17195.
- Ellison, D., & Speranza, C. I. (2020). From blue to green water and back again: Promoting tree, forest and vegetation-based landscape resilience in the Sahel. *Science of the Total Environment*, 140002.
- Engdaw, M. M., Ballinger, A. P., Hegerl, G. C., & Steiner, A. K. (2022). Changes in temperature and heat waves over Africa using observational and reanalysis data sets. *International journal of climatology*, 42(2), 1165-1180.
- Engel, F., Hoek van Dijke, A. J., Roebroek, C. T. J., & Benedict, I. (2025). Can large-scale tree cover change negate climate change impacts on future water availability? *Hydrology and earth system sciences*, 29(7), 1895-1918.

- Erbaugh, J. T., Pradhan, N., Adams, J., Oldekop, J. A., Agrawal, A., Brockington, D., Pritchard, R., & Chhatre, A. (2020). Global forest restoration and the importance of prioritizing local communities. *Nature ecology & evolution*, 4(11), 1472-1476.
- EUMETSAT. (2015). *MSG meteorological products extraction facility: Algorithm specification document* [Report]. EUMETSAT.
- Fagan, M. E., Reid, J. L., Holland, M. B., Drew, J. G., & Zahawi, R. A. (2020). How feasible are global forest restoration commitments? *Conservation Letters*, 13(3), e12700.
- Fan, Y., Li, H., & Miguez-Macho, G. (2013). Global patterns of groundwater table depth. *science*, 339(6122), 940-943.
- Fan, Y., Miguez-Macho, G., Jobbágy, E. G., Jackson, R. B., & Otero-Casal, C. (2017). Hydrologic regulation of plant rooting depth. *Proceedings of the national academy of sciences*, 114(40), 10572-10577.
- FAO. (2023). *The State of Food and Agriculture 2023. Revealing the true cost of food to transform agrifood systems* [Report]. F. a. A. Ogranisation.
- Feldman, A. F., Short Gianotti, D. J., Dong, J., Trigo, I. F., Salvucci, G. D., & Entekhabi, D. (2022). Tropical surface temperature response to vegetation cover changes and the role of drylands. *Global change biology*, 29, 110-125.
- Feng, X., Fu, B., Piao, S., Wang, S., Ciais, P., Zeng, Z., Lü, Y., Zeng, Y., Li, Y., & Jiang, X. (2016). Revegetation in China's Loess Plateau is approaching sustainable water resource limits. *Nature Climate Change*, 6(11), 1019-1022.
- Filoso, S., Bezerra, M. O., Weiss, K. C., & Palmer, M. A. (2017). Impacts of forest restoration on water yield: A systematic review. *PloS one*, 12(8), e0183210.
- Findell, K. L., & Eltahir, E. A. (2003a). Atmospheric controls on soil moisture-boundary layer interactions. Part I: Framework development. *Journal of Hydrometeorology*, 4(3), 552-569.
- Findell, K. L., & Eltahir, E. A. (2003b). Atmospheric controls on soil moisture-boundary layer interactions. Part II: Feedbacks within the continental United States. *Journal of Hydrometeorology*, 4(3), 570-583.
- Fitzpatrick, R. G. J., Parker, D. J., Marsham, J. H., Rowell, D. P., Guichard, F. M., Taylor, C. M., Cook, K. H., Vizy, E. K., Jackson, L. S., Finney, D., Crook, J., Stratton, R., & Tucker, S. (2020). What drives the intensification of mesoscale convective systems over the West African Sahel under climate change? *Journal of Climate*, 33(8), 3151-3172.
- Forzieri, G., Alkama, R., Miralles, D. G., & Cescatti, A. (2017). Satellites reveal contrasting responses of regional climate to the widespread greening of Earth. *science*, 356(6343), 1180-1184.
- Friedlingstein, P., O'Sullivan, M., Jones, M. W., Andrew, R. M., Hauck, J., Olsen, A., Peters, G. P., Peters, W., Pongratz, J., & Sitch, S. (2020). Global carbon budget 2020. *Earth System Science Data*, 12(4), 3269-3340.
- Funk, C., Peterson, P., Landsfeld, M., Pedreros, D., Verdin, J., Shukla, S., Husak, G., Rowland, J., Harrison, L., Hoell, A., & Michaelsen, J. (2015). The climate hazards infrared precipitation with stations—a new environmental record for monitoring extremes. *Scientific data*, 2(1), 150066.
- Garcia-Carreras, L., Marsham, J. H., & Spracklen, D. V. (2017). Observations of increased cloud cover over irrigated agriculture in an arid environment. *Journal of Hydrometeorology*, 18(8), 2161-2172.

- Garcia-Carreras, L., & Parker, D. (2011). How does local tropical deforestation affect rainfall? *Geophysical Research Letters*, *38*(19).
- Garcia-Carreras, L., Parker, D. J., Taylor, C. M., Reeves, C. E., & Murphy, J. G. (2010). Impact of mesoscale vegetation heterogeneities on the dynamical and thermodynamic properties of the planetary boundary layer. *Journal of Geophysical Research: Atmospheres*, *115*(D3).
- Gatebe, C., Ichoku, C., Poudyal, R., Román, M., & Wilcox, E. (2014). Surface albedo darkening from wildfires in northern sub-Saharan Africa. *Environmental Research Letters*, *9*(6), 065003.
- Ghilain, N., Arboleda, A., & Gellens-Meulenberghs, F. (2011). Evapotranspiration modelling at large scale using near-real time MSG SEVIRI derived data. *Hydrology and earth system sciences*, *15*(3), 771-786.
- Ghilain, N., Arboleda, A., Sepulcre-Cantò, G., Batelaan, O., Ardö, J., & Gellens-Meulenberghs, F. (2011). Improving evapotranspiration in land surface models by using biophysical parameters derived from MSG/SEVIRI satellite. *Hydrology and Earth System Sciences Discussions*, *8*(5).
- Giannini, A. (2015). Hydrology: climate change comes to the Sahel. *Nature Climate Change*, *5*(8), 720-721.
- Giannini, A., Biasutti, M., & Verstraete, M. M. (2008). A climate model-based review of drought in the Sahel: desertification, the re-greening and climate change. *Global and planetary Change*, *64*(3-4), 119-128.
- Giannini, A., Saravanan, R., & Chang, P. (2003). Oceanic forcing of Sahel rainfall on interannual to interdecadal time scales. *science*, *302*(5647), 1027-1030.
- Gibbs, H., & Salmon, J. M. (2015). Mapping the world's degraded lands. *Applied geography*, *57*, 12-21.
- Goessling, H. F., Rackow, T., & Jung, T. (2025). Recent global temperature surge intensified by record-low planetary albedo. *science*, *387*(6729), 68-73.
- Gorelick, N., Hancher, M., Dixon, M., Ilyushchenko, S., Thau, D., & Moore, R. (2017). Google Earth Engine: Planetary-scale geospatial analysis for everyone. *Remote Sensing of Environment*, *202*, 18-27.
- Grell, G. A., Dudhia, J., & Stauffer, D. R. (1994). A description of the fifth-generation Penn State/NCAR Mesoscale Model (MM5). *University Corporation for Atmospheric Research*.
- Grell, G. A., & Freitas, S. R. (2014). A scale and aerosol aware stochastic convective parameterization for weather and air quality modeling. *Atmospheric Chemistry and Physics*, *14*(10), 5233-5250.
- Hackländer, J., Parente, L., Ho, Y.-F., Hengl, T., Simoes, R., Consoli, D., Şahin, M., Tian, X., Jung, M., & Herold, M. (2023). Land potential assessment and trend-analysis using 2000–2021 FAPAR monthly time-series at 250 m spatial resolution. *PeerJ*, *12*(e16972).
- Haesen, S., Lembrechts, J. J., De Frenne, P., Lenoir, J., Aalto, J., Ashcroft, M. B., Kopecký, M., Luoto, M., Maclean, I., & Nijs, I. (2021). ForestTemp–Sub-canopy microclimate temperatures of European forests. *Global change biology*, *27*(23), 6307-6319.
- Ham, S.-H., Kato, S., Rose, F. G., Sun-Mack, S., Chen, Y., Miller, W. F., & Scott, R. C. (2022). Combining Cloud Properties from CALIPSO, CloudSat, and MODIS for Top-of-Atmosphere (TOA) Shortwave Broadband Irradiance Computations: Impact of

- Cloud Vertical Profiles. *Journal of Applied Meteorology and Climatology*, 61(10), 1449-1471.
- Hamberg, L. J., Fisher, J. B., Ruppert, J. L. W., Tureček, J., Rosen, D. H., & James, P. M. A. (2022). Assessing and modeling diurnal temperature buffering and evapotranspiration dynamics in forest restoration using ECOSTRESS thermal imaging. *Remote Sensing of Environment*, 280.
- Hammerle, A., Haslwanter, A., Tappeiner, U., Cernusca, A., & Wohlfahrt, G. (2008). Leaf area controls on energy partitioning of a temperate mountain grassland. *Biogeosciences*, 5(2), 421-431.
- Hamunyela, E., Rosca, S., Mirt, A., Engle, E., Herold, M., Gieseke, F., & Verbesselt, J. (2020). Implementation of BFASTmonitor algorithm on google earth engine to support large-area and sub-annual change monitoring using earth observation data. *Remote sensing*, 12(18), 2953.
- Hamunyela, E., Verbesselt, J., & Herold, M. (2016). Using spatial context to improve early detection of deforestation from Landsat time series. *Remote Sensing of Environment*, 172, 126-138.
- Harris, I. C., Jones, P. D., & Osborn, T. (2020). *CRU TS4.04: Climatic Research Unit (CRU) Time-Series (TS) version 4.04 of high-resolution gridded data of month-by-month variation in climate (Jan. 1901- Dec. 2019)* [Dataset]. <https://catalogue.ceda.ac.uk/uuid/89e1e34ec3554dc98594a5732622bce9>
- Hasler, N., Williams, C. A., Denney, V. C., Ellis, P. W., Shrestha, S., Terasaki Hart, D. E., Wolff, N. H., Yeo, S., Crowther, T. W., Werden, L. K., & Cook-Patton, S. C. (2024). Accounting for albedo change to identify climate-positive tree cover restoration. *Nature communications*, 15(1), 2275.
- Hengl, T., Miller, M. A. E., Križan, J., Shepherd, K. D., Sila, A., Kilibarda, M., Antonijević, O., Glušica, L., Dobermann, A., Haefele, S. M., McGrath, S. P., Acquah, G. E., Collinson, J., Parente, L., Sheykhmousa, M., Saito, K., Johnson, J.-M., Chamberlin, J., Silatsa, F. B. T., . . . Crouch, J. (2021). African soil properties and nutrients mapped at 30 m spatial resolution using two-scale ensemble machine learning. *Scientific Reports*, 11(1), 6130.
- Hoek van Dijke, A. J., Herold, M., Mallick, K., Benedict, I., Machwitz, M., Schlerf, M., Pranindita, A., Theeuwens, J. J., Bastin, J.-F., & Teuling, A. J. (2022). Shifts in regional water availability due to global tree restoration. *Nature geoscience*, 15(5), 363-368.
- Holl, K. (2020). *Primer of ecological restoration* [Book]. Island Press.
- Holl, K. D., & Brancalion, P. H. (2020). Tree planting is not a simple solution. *science*, 368(6491), 580-581.
- Hong, S.-Y., & Lim, J.-O. J. (2006). The WRF single-moment 6-class microphysics scheme (WSM6). *Asia-Pacific Journal of Atmospheric Sciences*, 42(2), 129-151.
- Hong, S.-Y., Noh, Y., & Dudhia, J. (2006). A new vertical diffusion package with an explicit treatment of entrainment processes. *Monthly Weather Review*, 134(9), 2318-2341.
- Horion, S., Cornet, Y., Erpicum, M., & Tychon, B. (2013). Studying interactions between climate variability and vegetation dynamic using a phenology based approach. *International journal of applied earth observation and geoinformation*, 20, 20-32.
- Hovi, A., Lindberg, E., Lang, M., Arumäe, T., Peuhkurinen, J., Sirparanta, S., Pyankov, S., & Rautiainen, M. (2019). Seasonal dynamics of albedo across European boreal

- forests: Analysis of MODIS albedo and structural metrics from airborne LiDAR. *Remote Sensing of Environment*, 224, 365-381.
- Huang, A., Xu, X., Jia, G., & Shen, R. (2022). Asymmetrical cooling effects of Amazonian protected areas across spatiotemporal scales. *Environmental Research Letters*, 17(5), Article 054038.
- Huang, B., Hu, X., Fuglstad, G. A., Zhou, X., Zhao, W., & Cherubini, F. (2020). Predominant regional biophysical cooling from recent land cover changes in Europe. *Nature communications*, 11(1).
- Huete, A. R., HuiQing, L., & van Leeuwen, W. J. D. (1997, 3-8 Aug. 1997). The use of vegetation indices in forested regions: issues of linearity and saturation. IEEE International Geoscience and Remote Sensing Symposium Proceedings. Remote Sensing - A Scientific Vision for Sustainable Development (IGARSS'97).
- Huxman, T. E., Smith, M. D., Fay, P. A., Knapp, A. K., Shaw, M. R., Loik, M. E., Smith, S. D., Tissue, D. T., Zak, J. C., & Weltzin, J. F. (2004). Convergence across biomes to a common rain-use efficiency. *Nature*, 429(6992), 651-654.
- Ibisch, P. L., Sheil, D., Baudena, M., Coumou, D., Dellasala, D., Ellison, D., Gaasbeek, T., Gohr, C., De Laet, R., Nobre, C., & Teuling, A. J. (2025). Cloudy outlook for forests [eLetter]. *science*.
- Ilstedt, U., Bargués Tobella, A., Bazié, H. R., Bayala, J., Verbeeten, E., Nyberg, G., Sanou, J., Benegas, L., Murdiyarsa, D., Laudon, H., Sheil, D., & Malmer, A. (2016). Intermediate tree cover can maximize groundwater recharge in the seasonally dry tropics. *Scientific Reports*, 6(1), 21930.
- IPCC. (2019). *Climate Change and Land: an IPCC special report on climate change, desertification, land degradation, sustainable land management, food security, and greenhouse gas fluxes in terrestrial ecosystems* [Report]. I. P. o. C. Change.
- IPCC. (2021). *Climate Change 2021: The Physical Science Basis. Contribution of Working Group I to the Sixth Assessment Report of the Intergovernmental Panel on Climate Change* [Report].
- IPCC. (2023). *Summary for Policymakers*. [Report](Climate Change 2023: Synthesis Report. Contribution of Working Groups I, II and III to the Sixth Assessment Report of the Intergovernmental Panel on Climate Change, Issue. I. P. o. C. Change.
- Irons, J. R., Dwyer, J. L., & Barsi, J. A. (2012). The next Landsat satellite: The Landsat data continuity mission. *Remote Sensing of Environment*, 122, 11-21.
- Ismaeel, A., Tai, A. P. K., Santos, E. G., Maraia, H., Aalto, I., Altman, J., Doležal, J., Lembrechts, J. J., Camargo, J. L., Aalto, J., Sam, K., Avelino do Nascimento, L. C., Kopecký, M., Svátek, M., Nunes, M. H., Matula, R., Plichta, R., Abera, T., & Maeda, E. E. (2024). Patterns of tropical forest understory temperatures. *Nature communications*, 15(1), 549.
- IUCN. (2019). *Reviving land and restoring landscapes: Policy convergence between forest landscape restoration and land degradation neutrality* [Gichuki, L., Brouwer, R., Davies, J., Vidal, A., Kuzee, M., Magero, C., Walter, S., Lara, P., Oragbade, C., Gilbey, B.] [Report].
- IUCN, U.-W. a. (2024). *Protected Planet: The World Database on Protected Areas (WDPA)* [Dataset]. <https://www.protectedplanet.net/en/thematic-areas/wdpa?tab=WDPA>

- Jackson, R. B., Randerson, J. T., Canadell, J. G., Anderson, R. G., Avissar, R., Baldocchi, D. D., Bonan, G. B., Caldeira, K., Diffenbaugh, N. S., & Field, C. B. (2008). Protecting climate with forests. *Environmental Research Letters*, 3(4), 044006.
- Jansen, F. A., Jongen, H. J., Jacobs, C. M., Bosveld, F. C., Buzacott, A. J., Heusinkveld, B. G., Kruijt, B., van der Molen, M., Moors, E., & Steeneveld, G. J. (2023). Land cover control on the drivers of evaporation and sensible heat fluxes: An observation-based synthesis for the Netherlands. *Water Resources Research*, e2022WR034361.
- Jarvis, A., Reuter, H. I., Nelson, A., & Guevara, E. (2008). *Hole-filled SRTM for the globe Version 4, available from the CGIAR-CSI SRTM 90m Database* [Dataset]. <https://srtm.csi.cgiar.org>
- Kalele, D. N., Ogara, W. O., Oludhe, C., & Onono, J. O. (2021). Climate change impacts and relevance of smallholder farmers' response in arid and semi-arid lands in Kenya. *Scientific African*, 12, e00814.
- Keys, P. W., Wang-Erlandsson, L., & Gordon, L. J. (2016). Revealing Invisible Water: Moisture Recycling as an Ecosystem Service. *PloS one*, 11(3), e0151993.
- Khanna, J., & Medvigy, D. (2014). Strong control of surface roughness variations on the simulated dry season regional atmospheric response to contemporary deforestation in Rondônia, Brazil. *Journal of Geophysical Research: Atmospheres*, 119(23), 13,067-013,078.
- Khanna, J., Medvigy, D., Fueglistaler, S., & Walko, R. (2017). Regional dry-season climate changes due to three decades of Amazonian deforestation. *Nature Climate Change*, 7(3), 200-204.
- Kiehl, J. T., & Trenberth, K. E. (1997). Earth's annual global mean energy budget. *Bulletin of the American Meteorological Society*, 78(2), 197-208.
- Kirschbaum, M. U. F., Cowie, A. L., Peñuelas, J., Smith, P., Conant, R. T., Sage, R. F., Brandão, M., Cotrufo, M. F., Luo, Y., Way, D. A., & Robinson, S. A. (2024). Is tree planting an effective strategy for climate change mitigation? *Science of the Total Environment*, 909, 168479.
- Kirschbaum, M. U. F., Zeng, G., Ximenes, F., Giltrap, D. L., & Zeldis, J. R. (2019). Towards a more complete quantification of the global carbon cycle. *Biogeosciences*, 16(3), 831-846.
- Klein, C., Heinzeller, D., Bliefernicht, J., & Kunstmann, H. (2015). Variability of West African monsoon patterns generated by a WRF multi-physics ensemble. *Climate Dynamics*, 45(9), 2733-2755.
- Klein, C., & Taylor, C. M. (2020). Dry soils can intensify mesoscale convective systems. *Proceedings of the National Academy of Sciences of the United States of America*, 117(35), 21132-21137.
- Knox, R., Bisht, G., Wang, J., & Bras, R. (2011). Precipitation Variability over the Forest-to-Nonforest Transition in Southwestern Amazonia. *Journal of Climate*, 24(9), 2368-2377.
- Knyazikhin, Y., Martonchik, J., Myneni, R. B., Diner, D., & Running, S. W. (1998). Synergistic algorithm for estimating vegetation canopy leaf area index and fraction of absorbed photosynthetically active radiation from MODIS and MISR data. *Journal of Geophysical Research: Atmospheres*, 103(D24), 32257-32275.
- Kodikara, K. A. S., Mukherjee, N., Jayatissa, L. P., Dahdouh-Guebas, F., & Koedam, N. (2017). Have mangrove restoration projects worked? An in-depth study in Sri Lanka. *Restoration Ecology*, 25(5), 705-716.

- Koster, R. D., Dirmeyer, P. A., Guo, Z., Bonan, G., Chan, E., Cox, P., Gordon, C. T., Kanae, S., Kowalczyk, E., Lawrence, D., Liu, P., Lu, C.-H., Malyshev, S., McAvaney, B., Mitchell, K., Mocko, D., Oki, T., Oleson, K., Pitman, A., . . . Yamada, T. (2004). Regions of Strong Coupling Between Soil Moisture and Precipitation. *science*, 305(5687), 1138-1140.
- Kristensen, J. Å., Barbero-Palacios, L., Barrio, I. C., Jacobsen, I. B. D., Kerby, J. T., López-Blanco, E., Malhi, Y., Le Moullec, M., Mueller, C. W., Post, E., Raundrup, K., & Macias-Fauria, M. (2024). Tree planting is no climate solution at northern high latitudes. *Nature geoscience*, 17(11), 1087-1092.
- Kuusinen, N., Tomppo, E., Shuai, Y., & Berninger, F. (2014). Effects of forest age on albedo in boreal forests estimated from MODIS and Landsat albedo retrievals. *Remote Sensing of Environment*, 145, 145-153.
- Laguë, M. M., & Swann, A. L. (2016). Progressive midlatitude afforestation: Impacts on clouds, global energy transport, and precipitation. *Journal of Climate*, 29(15), 5561-5573.
- Lal, P., Shekhar, A., & Kumar, A. (2021). Quantifying Temperature and Precipitation Change Caused by Land Cover Change: A Case Study of India Using the WRF Model. *FRONTIERS IN ENVIRONMENTAL SCIENCE*, 9.
- Lawrence, D., Coe, M., Walker, W., Verchot, L., & Vandecar, K. (2022). The unseen effects of deforestation: biophysical effects on climate. *Frontiers in Forests and Global Change*, 5, 756115.
- Le Houérou, H. N. (1984). Rain use efficiency: a unifying concept in arid-land ecology. *Journal of arid environments*, 7(3), 213-247.
- Le, Q. B., Nkonya, E., & Mirzabaev, A. (2016). Biomass productivity-based mapping of global land degradation hotspots. *Nkonya, E. Mirzabaev, A. and von Braun, J.(eds.). Economics of Land Degradation and Improvement—A Global Assessment for Sustainable Development. New York: Springer*, 55-84.
- Lennon, J. J. (2000). Red-shifts and red herrings in geographical ecology. *Ecography*, 23(1), 101-113.
- Leung, G. R., Grant, L. D., & van den Heever, S. C. (2024). Deforestation-Driven Increases in Shallow Clouds Are Greatest in Drier, Low-Aerosol Regions of Southeast Asia. *Geophysical Research Letters*, 51(10), e2023GL107678.
- Lhermitte, S., Verbesselt, J., Verstraeten, W. W., & Coppin, P. (2010). A pixel based regeneration index using time series similarity and spatial context. *Photogrammetric Engineering & Remote Sensing*, 76(6), 673-682.
- Lhermitte, S., Verbesselt, J., Verstraeten, W. W., & Coppin, P. (2011). A comparison of time series similarity measures for classification and change detection of ecosystem dynamics. *Remote Sensing of Environment*, 115(12), 3129-3152.
- Li, S., Yan, Q., Liu, Z., Wang, X., Yu, F., Teng, D., Sun, Y., Lu, D., Zhang, J., & Gao, T. (2023). Seasonality of albedo and fraction of absorbed photosynthetically active radiation in the temperate secondary forest ecosystem: A comprehensive observation using Qingyuan Ker towers. *Agricultural and Forest Meteorology*, 333, 109418.
- Li, Y., Li, Z.-L., Wu, H., Liu, X., Lian, X., Si, M., Li, J., Zhou, C., Tang, R., Duan, S., Zhao, W., Leng, P., Song, X., Shi, Q., Zhao, E., & Gao, C. (2025). Observed different impacts of potential tree restoration on local surface and air temperature. *Nature communications*, 16(1), 2335.

- Li, Y., Noblet-Ducoudré, D., Davin, E. L., Motesharrei, S., Zeng, N., Li, S., & Kalnay, E. (2016). The role of spatial scale and background climate in the latitudinal temperature response to deforestation. *Earth System Dynamics*, 7(1), 167-181.
- Li, Y., Zhao, M., Motesharrei, S., Mu, Q., Kalnay, E., & Li, S. (2015a). Local cooling and warming effects of forests based on satellite observations. *Nature communications*, 6(1), 6603.
- Li, Y., Zhao, M., Motesharrei, S., Mu, Q., Kalnay, E., & Li, S. (2015b). Local cooling and warming effects of forests based on satellite observations. *Nature communications*, 6(1), 1-8.
- Liang, S., Strahler, A. H., & Walthall, C. (1999). Retrieval of land surface albedo from satellite observations: A simulation study. *Journal of Applied Meteorology*, 38(6), 712-725.
- Lin, H., Li, Y., & Zhao, L. (2022). Partitioning of sensible and latent heat fluxes in different vegetation types and their spatiotemporal variations based on 203 FLUXNET sites. *Journal of Geophysical Research: Atmospheres*, 127(21), e2022JD037142.
- Liu, J., Schaaf, C., Strahler, A., Jiao, Z., Shuai, Y., Zhang, Q., Roman, M., Augustine, J. A., & Dutton, E. G. (2009). Validation of Moderate Resolution Imaging Spectroradiometer (MODIS) albedo retrieval algorithm: Dependence of albedo on solar zenith angle. *Journal of Geophysical Research: Atmospheres*, 114(D1).
- Liu, Y., Jiang, Q., & Gleasure, R. (2023). Hitting Net-Zero Without Stopping Flying: Increasing Air Travelers' Likelihood to Opt-in to Voluntary Carbon Offsetting. *Journal of Travel Research*, 62(1), 21-38.
- Lohou, F., Kergoat, L., Guichard, F., Boone, A., Cappelaere, B., Cohard, J. M., Demarty, J., Galle, S., Grippa, M., Peugeot, C., Ramier, D., Taylor, C. M., & Timouk, F. (2014). Surface response to rain events throughout the West African monsoon. *Atmospheric Chemistry and Physics*, 14(8), 3883-3898.
- Luyssaert, S., Jammot, M., Stoy, P. C., Estel, S., Pongratz, J., Ceschia, E., Churkina, G., Don, A., Erb, K., Ferlicoq, M., Gielen, B., Grünwald, T., Houghton, R. A., Klumpp, K., Knohl, A., Kolb, T., Kuemmerle, T., Laurila, T., Lohila, A., . . . Dolman, A. J. (2014). Land management and land-cover change have impacts of similar magnitude on surface temperature. *Nature Climate Change*, 4(5), 389-393.
- Luyssaert, S., Marie, G., Valade, A., Chen, Y.-Y., Njakou Djomo, S., Ryder, J., Otto, J., Naudts, K., Lansø, A. S., & Ghattas, J. (2018). Trade-offs in using European forests to meet climate objectives. *Nature*, 562(7726), 259-262.
- Lynn, B. H., Tao, W.-K., & Wetzel, P. J. (1998). A Study of Landscape-Generated Deep Moist Convection. *Monthly Weather Review*, 126(4), 928-942.
- Mahmood, R., Pielke Sr, R. A., Hubbard, K. G., Niyogi, D., Dirmeyer, P. A., McAlpine, C., Carleton, A. M., Hale, R., Gameda, S., & Beltrán-Przekurat, A. (2014). Land cover changes and their biogeophysical effects on climate. *International journal of climatology*, 34(4), 929-953.
- Maranan, M., Fink, A. H., & Knippertz, P. (2018). Rainfall types over southern West Africa: Objective identification, climatology and synoptic environment. *Quarterly Journal of the Royal Meteorological Society*, 144(714), 1628-1648.
- Martin, M. P., Woodbury, D. J., Doroski, D. A., Nagele, E., Storace, M., Cook-Patton, S. C., Pasternack, R., & Ashton, M. S. (2021). People plant trees for utility more often than for biodiversity or carbon. *Biological Conservation*, 261, 109224.

- Masih, I., Maskey, S., Mussá, F., & Trambauer, P. (2014). A review of droughts on the African continent: a geospatial and long-term perspective. *Hydrology and earth system sciences*, 18(9), 3635-3649.
- Mathon, V., Laurent, H., & Lebel, T. (2002). Mesoscale Convective System Rainfall in the Sahel. *Journal of Applied Meteorology*, 41(11), 1081-1092.
- Meier, J., Zabel, F., & Mauser, W. (2018). A global approach to estimate irrigated areas – a comparison between different data and statistics. *Hydrology and earth system sciences*, 22(2), 1119-1133.
- Meinshausen, N., & Ridgeway, G. (2006). Quantile regression forests. *Journal of machine learning research*, 7(6).
- Mensah, E. R., Shinde, N., Kakpo, A. T., & Djenontin, I. N. S. (2024). The human well-being outcomes of tree plantations in sub-Saharan Africa: A reassessment of evidence using longitudinal subnational-year data. *Forest Policy and Economics*, 160, 103141.
- Merbold, L., Ardö, J., Arneth, A., Scholes, R. J., Nouvellon, Y., De Grandcourt, A., Archibald, S., Bonnefond, J.-M., Boulain, N., & Brueggemann, N. (2009). Precipitation as driver of carbon fluxes in 11 African ecosystems. *Biogeosciences*, 6(6), 1027-1041.
- Meroni, M., Schucknecht, A., Fasbender, D., Rembold, F., Fava, F., Mauclair, M., Goffner, D., Di Lucchio, L. M., & Leonardi, U. (2017). Remote sensing monitoring of land restoration interventions in semi-arid environments with a before–after control-impact statistical design. *International journal of applied earth observation and geoinformation*, 59, 42-52.
- Meyfroidt, P., Rudel, T. K., & Lambin, E. F. (2010). Forest transitions, trade, and the global displacement of land use. *Proceedings of the national academy of sciences*, 107(49), 20917-20922.
- Mganga, K. Z. (2023). Agricultural Land Degradation in Kenya (In *Impact of Agriculture on Soil Degradation I: Perspectives from Africa, Asia, America and Oceania* (pp. 273-300)). Springer International Publishing.
- Middleton, N., & Thomas, D. (1997). *World Atlas of Desertification* (2nd ed.) [Book]. United Nations Environment Program.
- Miralles, D. G., Nieto, R., McDowell, N. G., Dorigo, W. A., Verhoest, N. E., Liu, Y. Y., Teuling, A. J., Dolman, A. J., Good, S. P., & Gimeno, L. (2016). Contribution of water-limited ecoregions to their own supply of rainfall. *Environmental Research Letters*, 11(12), 124007.
- Miralles, D. G., van den Berg, M. J., Teuling, A. J., & de Jeu, R. A. M. (2012). Soil moisture-temperature coupling: A multiscale observational analysis. *Geophysical Research Letters*, 39(21).
- Murekezi, J., Nduwamungu, J., & Munyanziza, E. (2013). Investigation of survival rate of trees planted in agroforestry and forest plantations in Huye District from 2007 to 2011 and underlying factors. *Rwanda Journal*, 1(1), 52-61.
- Naudts, K., Chen, Y., McGrath, M. J., Ryder, J., Valade, A., Otto, J., & Luyssaert, S. (2016). Europe's forest management did not mitigate climate warming. *science*, 351(6273), 597-600.
- Negri, A. J., Adler, R. F., Xu, L., & Surratt, J. (2004). The impact of Amazonian deforestation on dry season rainfall. *Journal of Climate*, 17(6), 1306-1319.

- Nistor, M. M., Man, T. C., Benzaghta, M. A., Nedumpallile Vasu, N., Dezsi, Ş., & Kizza, R. (2018). Land cover and temperature implications for the seasonal evapotranspiration in Europe. *Geographia Technica*, 13(1), 85-108.
- Noual, G., Brunet, Y., Le Moigne, P., & Lac, C. (2023). Simulating the effects of regional forest cover and windthrow-induced cover changes on mid-latitude boundary-layer clouds. *Journal of Geophysical Research: Atmospheres*, e2023JD038477.
- Nsikani, M. M., Anderson, P., Bouragaoui, Z., Geerts, S., Gornish, E. S., Kairo, J. G., Khan, N., Madikizela, B., Mganga, K. Z., Ntshotsho, P., Okafor-Yarwood, I., Webster, K. M. E., & Peer, N. (2023). UN Decade on Ecosystem Restoration: key considerations for Africa. *Restoration Ecology*, 31(3), e13699.
- Nunes, A., Oliveira, G., Mexia, T., Valdecantos, A., Zucca, C., Costantini, E. A., Abraham, E. M., Kyriazopoulos, A. P., Salah, A., & Prasse, R. (2016). Ecological restoration across the Mediterranean Basin as viewed by practitioners. *Science of the Total Environment*, 566, 722-732.
- Oke, T. R. (1987). *Boundary Layer Climates* (2nd ed.). Routledge.
- Oreopoulos, L., & Barker, H. W. (1999). Accounting for subgrid-scale cloud variability in a multi-layer 1D solar radiative transfer algorithm. *Quarterly Journal of the Royal Meteorological Society*, 125(553), 301-330.
- Ouedraogo, I., Runge, J., Eisenberg, J., Barron, J., & Sawadogo-Kaboré, S. (2014). The re-greening of the Sahel: Natural cyclicity or human-induced change? *Land*, 3(3), 1075-1090.
- Palmer, P. I., Wainwright, C. M., Dong, B., Maidment, R. I., Wheeler, K. G., Gedney, N., Hickman, J. E., Madani, N., Folwell, S. S., Abdo, G., Allan, R. P., Black, E. C. L., Feng, L., Gudoshava, M., Haines, K., Huntingford, C., Kilavi, M., Lunt, M. F., Shaaban, A., & Turner, A. G. (2023). Drivers and impacts of Eastern African rainfall variability. *Nature Reviews Earth & Environment*, 4(4), 254-270.
- Parr, C. L., te Beest, M., & Stevens, N. (2024). Conflation of reforestation with restoration is widespread. *science*, 383(6684), 698-701.
- PBL. (2020). *Global Restoration Commitments Database* [Dataset]. <https://www.pbl.nl/en/publications/goals-and-commitments-for-the-restoration-decade>
- Peng, S., Terrer, C., Smith, B., Ciais, P., Han, Q., Nan, J., Fisher, J. B., Chen, L., Deng, L., & Yu, K. (2024). Carbon restoration potential on global land under water resource constraints. *Nature Water*.
- Perugini, L., Caporaso, L., Marconi, S., Cescatti, A., Quesada, B., de Noblet-Ducoudre, N., House, J. I., & Arneth, A. (2017). Biophysical effects on temperature and precipitation due to land cover change. *Environmental Research Letters*, 12(5), 053002.
- Pettorelli, N., Williams, J., Schulte to Bühne, H., & Crowson, M. (2024). Deep learning and satellite remote sensing for biodiversity monitoring and conservation. *Remote Sensing in Ecology and Conservation*, 11, 123-132.
- Piao, S., Wang, X., Park, T., Chen, C., Lian, X., He, Y., Bjerke, J. W., Chen, A., Ciais, P., & Tømmervik, H. (2020). Characteristics, drivers and feedbacks of global greening. *Nature Reviews Earth & Environment*, 1(1), 14-27.
- Pitman, A., Avila, F., Abramowitz, G., Wang, Y., Phipps, S., & de Noblet-Ducoudré, N. (2011). Importance of background climate in determining impact of land-cover change on regional climate. *Nature Climate Change*, 1(9), 472-475.

- Pitman, A. J. (2003). The evolution of, and revolution in, land surface schemes designed for climate models [Article]. *International journal of climatology*, 23(5), 479-510.
- Planet Team, A. (2017). Planet application program interface: In space for life on Earth. *San Francisco*.
- Prach, K., & del Moral, R. (2015). Passive restoration is often quite effective: response to Zahawi et al.(2014). *Restoration Ecology*, 23(4), 344-346.
- Právělie, R. (2021). Exploring the multiple land degradation pathways across the planet. *Earth-Science Reviews*, 220, 103689.
- Prevedello, J. A., Winck, G. R., Weber, M. M., Nichols, E., & Sinervo, B. (2019). Impacts of forestation and deforestation on local temperature across the globe. *PloS one*, 14(3), e0213368.
- Probst, B. S., Toetzke, M., Kontoleon, A., Díaz Anadón, L., Minx, J. C., Haya, B. K., Schneider, L., Trotter, P. A., West, T. A. P., Gill-Wiehl, A., & Hoffmann, V. H. (2024). Systematic assessment of the achieved emission reductions of carbon crediting projects. *Nature communications*, 15(1), 9562.
- Proud, S. R., & Rasmussen, L. V. (2011). The influence of seasonal rainfall upon Sahel vegetation. *Remote sensing letters*, 2(3), 241-249.
- Qin, Y., Wang, D., Ziegler, A. D., Fu, B., & Zeng, Z. (2025). Impact of Amazonian deforestation on precipitation reverses between seasons. *Nature*, 639(8053), 102-108.
- Ranasinghe, R., Ruane, A. C., Vautard, R., Arnell, N., Coppola, E., Cruz, F. A., Dessai, S., Saiful Islam, A., Rahimi, M., & Carrascal, D. R. (2021). Climate change information for regional impact and for risk assessment (In *Climate Change 2021: The Physical Science Basis. Contribution of Working Group I to the Sixth Assessment Report of the Intergovernmental Panel on Climate Change* (pp. 1767–1926)). Cambridge University Press.
- Rasmussen, K., D'haen, S., Fensholt, R., Fog, B., Horion, S., Nielsen, J. O., Rasmussen, L. V., & Reenberg, A. (2016). Environmental change in the Sahel: reconciling contrasting evidence and interpretations. *Regional Environmental Change*, 16(3), 673-680.
- Rayden, T., Jones, K. R., Austin, K., & Radachowsky, J. (2023). Improving climate and biodiversity outcomes through restoration of forest integrity. *Conservation biology*, 37(6), e14163.
- Reiner, F., Brandt, M., Tong, X., Skole, D., Kariryaa, A., Ciais, P., Davies, A., Hiernaux, P., Chave, J., Mugabowindekwe, M., Igel, C., Oehmcke, S., Gieseke, F., Li, S., Liu, S., Saatchi, S., Boucher, P., Singh, J., Taugourdeau, S., . . . Fensholt, R. (2023). More than one quarter of Africa's tree cover is found outside areas previously classified as forest. *Nature communications*, 14(1), 2258.
- Reuter, H. I., Nelson, A., & Jarvis, A. (2007). An evaluation of void-filling interpolation methods for SRTM data. *International Journal of Geographical Information Science*, 21(9), 983-1008.
- Roe, S., Streck, C., Obersteiner, M., Frank, S., Griscom, B., Drouet, L., Fricko, O., Gusti, M., Harris, N., Hasegawa, T., Hausfather, Z., Havlík, P., House, J., Nabuurs, G.-J., Popp, A., Sánchez, M. J. S., Sanderman, J., Smith, P., Stehfest, E., & Lawrence, D. (2019). Contribution of the land sector to a 1.5 °C world. *Nature Climate Change*, 9(11), 817-828.

- Roebroek, C. T., Duveiller, G., Seneviratne, S. I., Davin, E. L., & Cescatti, A. (2023). Releasing global forests from human management: How much more carbon could be stored? *science*, 380(6646), 749-753.
- Roebroek, C. T. J., Caporaso, L., Duveiller, G., Davin, E. L., Seneviratne, S. I., & Cescatti, A. (2025). Potential tree cover under current and future climate scenarios. *Scientific data*, 12(1), 564.
- Rohatyn, S., Yakir, D., Rotenberg, E., & Carmel, Y. (2022). Limited climate change mitigation potential through forestation of the vast dryland regions. *science*, 377(6613), 1436-1439.
- Rotenberg, E., & Yakir, D. (2010). Contribution of Semi-Arid Forests to the Climate System. *science*, 327(5964), 451-454.
- Roy, D. P., Boschetti, L., Justice, C., & Ju, J. (2008). The collection 5 MODIS burned area product—Global evaluation by comparison with the MODIS active fire product. *Remote Sensing of Environment*, 112(9), 3690-3707.
- Roy, S. B. (2009). Mesoscale vegetation-atmosphere feedbacks in Amazonia. *Journal of Geophysical Research: Atmospheres*, 114(D20).
- Ruijsch, J., Hutjes, R. W., & Teuling, A. J. (2023). *Heeft landgebruik effect op ons weer?: Literatuuronderzoek relatie landgebruik en klimaat op regionale en lokale schaal: De Kleine Waterkringloop* [Report].
- Ruijsch, J., Taylor, C. M., Hutjes, R. W. A., & Teuling, A. J. (2025). Scale-dependent cloud enhancement from land restoration in West African drylands. *Communications Earth & Environment*, 6(1), 174.
- Ruijsch, J., Teuling, A. J., Duveiller, G., & Hutjes, R. W. A. (2024). The local cooling potential of land restoration in Africa. *Communications Earth & Environment*, 5(1), 495.
- Ruijsch, J., Teuling, A. J., Verbesselt, J., & Hutjes, R. W. A. (2023). Landscape restoration and greening in Africa. *Environmental Research Letters*, 18(6), 064020.
- Ryan, J. C. (2024). Contribution of surface and cloud radiative feedbacks to Greenland Ice Sheet meltwater production during 2002–2023. *Communications Earth & Environment*, 5(1), 538.
- Ryan, J. C., Smith, L. C., Cooley, S. W., Pearson, B., Wever, N., Keenan, E., & Lenaerts, J. T. M. (2022). Decreasing surface albedo signifies a growing importance of clouds for Greenland Ice Sheet meltwater production. *Nature communications*, 13(1), 4205.
- Sacande, M., Martucci, A., & Vollrath, A. (2021). Monitoring Large-Scale Restoration Interventions from Land Preparation to Biomass Growth in the Sahel. *Remote sensing*, 13(18), 3767.
- Saley, I. A., Salack, S., Sanda, I. S., Moussa, M. S., Bonkaney, A. L., Ly, M., & Fodé, M. (2019). The possible role of the Sahel Greenbelt on the occurrence of climate extremes over the West African Sahel. *Atmospheric Science Letters*, 20(8), e927.
- Sandel, B., & Svenning, J.-C. (2013). Human impacts drive a global topographic signature in tree cover. *Nature communications*, 4(1), 2474.
- Schaaf, C., & Wang, Z. (2015). *MCD43A3 MODIS/Terra+Aqua BRDF/Albedo Daily L3 Global - 500m V006* [Dataset]. <https://doi.org/10.5067/MODIS/MCD43A3.006>
- Schmetz, J., Pili, P., Tjemkes, S., Just, D., Kerkmann, J., Rota, S., & Ratier, A. (2002). An Introduction to Meteosat Second Generation. *Bulletin of the American Meteorological Society*, 83(7), 977-992.

- Schowengerdt, R. A. (2006). *Remote sensing: models and methods for image processing* [Book]. elsevier.
- Schulte to Bühne, H., Wegmann, M., Durant, S. M., Ransom, C., de Ornellas, P., Grange, S., Beatty, H., & Petteorelli, N. (2017). Protection status and national socio-economic context shape land conversion in and around a key transboundary protected area complex in West Africa. *Remote Sensing in Ecology and Conservation*, 3(4).
- Schultz, B., Brockington, D., Coleman, E. A., Djenontin, I., Fischer, H. W., Fleischman, F., Kashwan, P., Marquardt, K., Pfeifer, M., & Pritchard, R. (2022). Recognizing the equity implications of restoration priority maps. *Environmental Research Letters*, 17(11), 114019.
- Schuster, R., Fink, A. H., & Knippertz, P. (2013). Formation and maintenance of nocturnal low-level stratus over the southern West African monsoon region during AMMA 2006. *Journal of the Atmospheric Sciences*, 70(8), 2337-2355.
- Science. (1888). The influence of forests on the quantity and frequency of rainfall. Do forests influence rainfall?
- Scogings, P. F. (2023). Perspective: Monitoring global forests using only structural metrics – problems and solutions from a savanna viewpoint. *Forest Ecology and Management*, 546, 121381.
- Semeena, V. S., Klein, C., Taylor, C. M., & Webster, S. (2023). Impact of land surface processes on convection over West Africa in convection-permitting ensemble forecasts: A case study using the MOGREPS ensemble. *Atmospheric Science Letters*, 24(8), Article e1167.
- Seneviratne, S. I., Corti, T., Davin, E. L., Hirschi, M., Jaeger, E. B., Lehner, I., Orlowsky, B., & Teuling, A. J. (2010). Investigating soil moisture–climate interactions in a changing climate: A review. *Earth-Science Reviews*, 99(3-4), 125-161.
- Sheil, D. (2018). Forests, atmospheric water and an uncertain future: the new biology of the global water cycle. *Forest Ecosystems*, 5(1), 1-22.
- Shevliakova, E., Stouffer, R. J., Malyshev, S., Krasting, J. P., Hurtt, G. C., & Pacala, S. W. (2013). Historical warming reduced due to enhanced land carbon uptake. *Proceedings of the national academy of sciences*, 110(42), 16730-16735.
- Skamarock, W. C., Klemp, J. B., Dudhia, J., Gill, D. O., Liu, Z., Berner, J., Wang, W., Powers, J. G., Duda, M. G., & Barker, D. M. (2019). A description of the advanced research WRF model version 4. *National Center for Atmospheric Research: Boulder, CO, USA*, 145, 145.
- Smith, C., Baker, J., & Spracklen, D. (2023). Tropical deforestation causes large reductions in observed precipitation. *Nature*, 615(7951), 270-275.
- Soares, P. M., Careto, J. A., Cardoso, R. M., Goergen, K., & Trigo, R. M. (2019). Land-atmosphere coupling regimes in a future climate in Africa: from model evaluation to projections based on CORDEX-Africa. *Journal of Geophysical Research: Atmospheres*, 124(21), 11118-11142.
- Sonak, I. (2023). *Integrating Maasai perception and satellite data to assess the biophysical climate effects and social impacts of land restoration efforts in South Kenya* Wageningen University & Research]. Wageningen.
- Spinoni, J., Vogt, J., Naumann, G., Carrao, H., & Barbosa, P. (2015). Towards identifying areas at climatological risk of desertification using the Köppen–Geiger classification and FAO aridity index. *International journal of climatology*, 35(9), 2210-2222.

- Spracklen, D., Baker, J., Garcia-Carreras, L., & Marsham, J. (2018). The effects of tropical vegetation on rainfall. *Annual Review of Environment and Resources*, 43, 193–218.
- Staal, A., Tuinenburg, O. A., Bosmans, J. H., Holmgren, M., van Nes, E. H., Scheffer, M., Zemp, D. C., & Dekker, S. C. (2018). Forest-rainfall cascades buffer against drought across the Amazon. *Nature Climate Change*, 8(6), 539–543.
- Stephens, L., Fuller, D., Boivin, N., Rick, T., Gauthier, N., Kay, A., Marwick, B., Armstrong, C. G., Barton, C. M., Denham, T., Douglass, K., Driver, J., Janz, L., Roberts, P., Rogers, J. D., Thakar, H., Altaweel, M., Johnson, A. L., Sampietro Vattuone, M. M., . . . Ellis, E. (2019). Archaeological assessment reveals Earth's early transformation through land use. *science*, 365(6456), 897–902.
- Su, Y., Zhang, C., Chen, X., Liu, L., Ciais, P., Peng, J., Wu, S., Wu, J., Shang, J., Wang, Y., Yuan, W., Yang, Y., Wu, Z., & Laforzezza, R. (2021). Aerodynamic resistance and Bowen ratio explain the biophysical effects of forest cover on understory air and soil temperatures at the global scale. *Agricultural and Forest Meteorology*, 308–309.
- Su, Y., Zhang, C., Ciais, P., Zeng, Z., Cescatti, A., Shang, J., Chen, J. M., Liu, J., Wang, Y.-P., Yuan, W., Peng, S., Lee, X., Zhu, Z., Fan, L., Liu, X., Liu, L., Laforzezza, R., Li, Y., Ren, J., . . . Chen, X. (2023). Asymmetric influence of forest cover gain and loss on land surface temperature. *Nature Climate Change*, 13(8), 823–831.
- Sühring, M., Maronga, B., Herbort, F., & Raasch, S. (2014). On the Effect of Surface Heat-Flux Heterogeneities on the Mixed-Layer-Top Entrainment. *Boundary-Layer Meteorology*, 151(3), 531–556.
- Sulla-Menashe, D., Gray, J. M., Abercrombie, S. P., & Friedl, M. A. (2019). Hierarchical mapping of annual global land cover 2001 to present: The MODIS Collection 6 Land Cover product. *Remote Sensing of Environment*, 222, 183–194.
- Syktus, J. I., & McAlpine, C. A. (2016). More than carbon sequestration: biophysical climate benefits of restored savanna woodlands. *Scientific Reports*, 6(1), 1–11.
- Tagesson, T., Fensholt, R., Guiro, I., Rasmussen, M. O., Huber, S., Mbow, C., Garcia, M., Horion, S., Sandholt, I., & Holm-Rasmussen, B. (2015). Ecosystem properties of semiarid savanna grassland in West Africa and its relationship with environmental variability. *Global change biology*, 21(1), 250–264.
- Tang, H., Armston, J., Hancock, S., Marselis, S., Goetz, S., & Dubayah, R. (2019). Characterizing global forest canopy cover distribution using spaceborne lidar. *Remote Sensing of Environment*, 231, 111262.
- Taylor, C. M. (2000). The influence of antecedent rainfall on Sahelian surface evaporation. *Hydrological Processes*, 14(7), 1245–1259.
- Taylor, C. M. (2015). Detecting soil moisture impacts on convective initiation in Europe. *Geophysical Research Letters*, 42(11), 4631–4638.
- Taylor, C. M., Birch, C. E., Parker, D. J., Dixon, N., Guichard, F., Nikulin, G., & Lister, G. M. S. (2013). Modeling soil moisture-precipitation feedback in the Sahel: Importance of spatial scale versus convective parameterization. *Geophysical Research Letters*, 40(23), 6213–6218.
- Taylor, C. M., & Blyth, E. M. (2000). Rainfall controls on evaporation at the regional scale: An example from the Sahel. *Journal of Geophysical Research: Atmospheres*, 105(D12), 15469–15479.
- Taylor, C. M., de Jeu, R. A., Guichard, F., Harris, P. P., & Dorigo, W. A. (2012). Afternoon rain more likely over drier soils. *Nature*, 489(7416), 423–426.

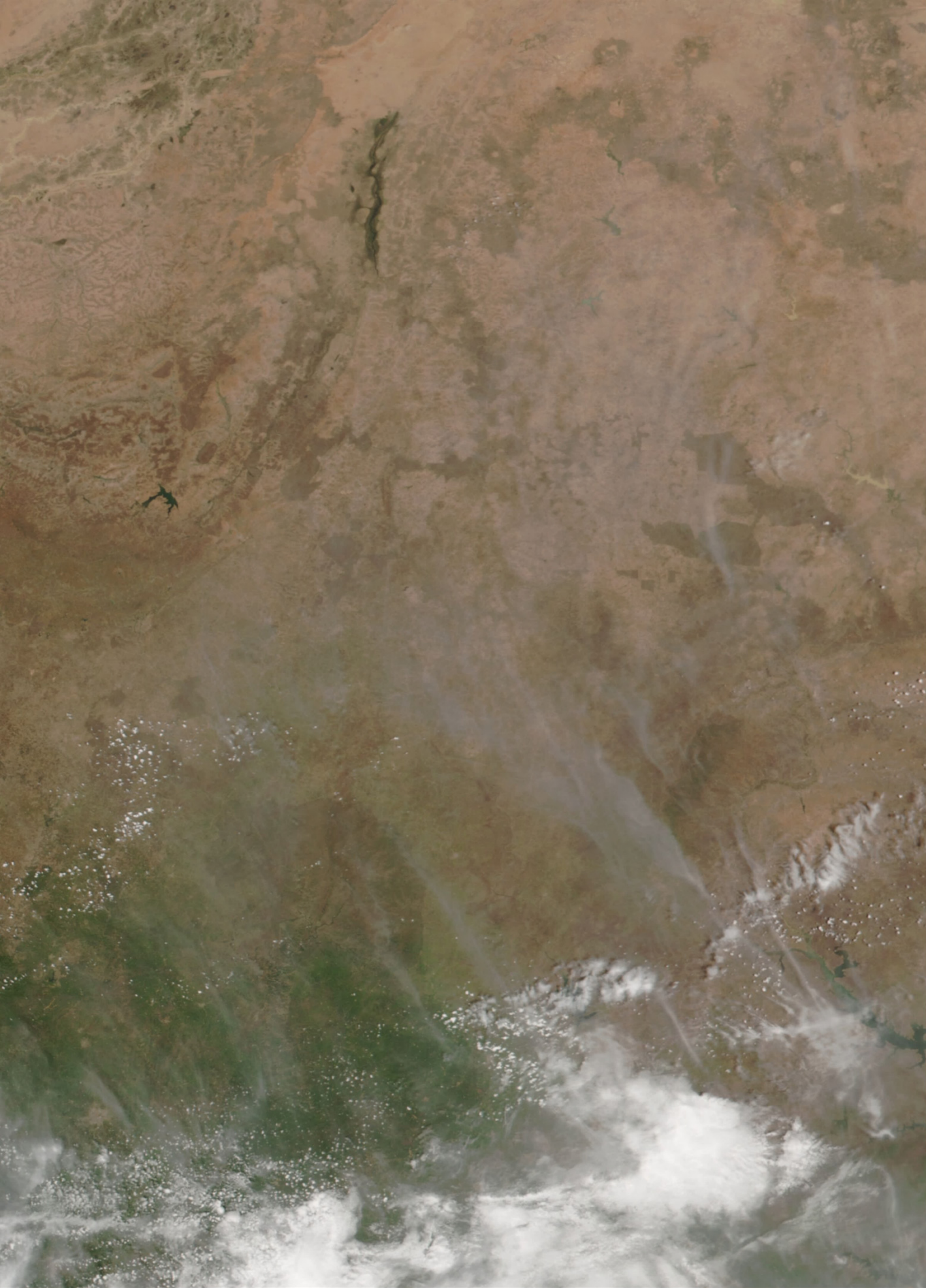
- Taylor, C. M., Gounou, A., Guichard, F., Harris, P. P., Ellis, R. J., Couvreur, F., & De Kauwe, M. (2011). Frequency of Sahelian storm initiation enhanced over mesoscale soil-moisture patterns. *Nature geoscience*, 4(7), 430-433.
- Taylor, C. M., Klein, C., Dione, C., Parker, D. J., Marsham, J., Abdoulahat Diop, C., Fletcher, J., Saidou Chaibou, A. A., Nafissa, D. B., Semeena, V. S., Cole, S. J., & Anderson, S. R. (2022). Nowcasting tracks of severe convective storms in West Africa from observations of land surface state. *Environmental Research Letters*, 17(3), Article 034016.
- Taylor, C. M., Klein, C., Parker, D. J., Gerard, F., Semeena, V. S., Barton, E. J., & Harris, B. L. (2022). "Late-stage" deforestation enhances storm trends in coastal West Africa. *Proceedings of the national academy of sciences*, 119(2), e2109285119.
- Taylor, C. M., Parker, D. J., & Harris, P. P. (2007). An observational case study of mesoscale atmospheric circulations induced by soil moisture. *Geophysical Research Letters*, 34(15).
- te Wierik, S. A., Cammeraat, E. L., Gupta, J., & Artzy-Randrup, Y. A. (2021). Reviewing the impact of land use and land-use change on moisture recycling and precipitation patterns. *Water Resources Research*, 57(7), e2020WR029234.
- Te Wierik, S. A., Keune, J., Miralles, D. G., Gupta, J., Artzy-Randrup, Y. A., Cammeraat, L. H., & van Loon, E. E. (2024). Critical Importance of Tree and Non-Tree Vegetation for African Precipitation. *Geophysical Research Letters*, 51(20), e2023GL103274.
- Te Wierik, S. A., Keune, J., Miralles, D. G., Gupta, J., Artzy-Randrup, Y. A., Gimeno, L., Nieto, R., & Cammeraat, L. H. (2022). The Contribution of Transpiration to Precipitation Over African Watersheds. *Water Resources Research*, 58(11), e2021WR031721.
- Teuling, A. J., Seneviratne, S. I., Stöckli, R., Reichstein, M., Moors, E., Ciais, P., Luysaert, S., Van Den Hurk, B., Ammann, C., & Bernhofer, C. (2010). Contrasting response of European forest and grassland energy exchange to heatwaves. *Nature geoscience*, 3(10), 722-727.
- Teuling, A. J., Taylor, C. M., Meirink, J. F., Melsen, L. A., Miralles, D. G., Van Heerwaarden, C. C., Vautard, R., Stegehuis, A. I., Nabuurs, G.-J., & de Arellano, J. V.-G. (2017a). Observational evidence for cloud cover enhancement over western European forests. *Nature communications*, 8(1), 1-7.
- Teuling, A. J., Taylor, C. M., Meirink, J. F., Melsen, L. A., Miralles, D. G., Van Heerwaarden, C. C., Vautard, R., Stegehuis, A. I., Nabuurs, G.-J., & de Arellano, J. V.-G. (2017b). Observational evidence for cloud cover enhancement over western European forests. *Nature communications*, 8(1), 14065.
- Tian, J., Zhang, Y., Klein, S. A., Öktem, R., & Wang, L. (2022). How Does Land Cover and Its Heterogeneity Length Scales Affect the Formation of Summertime Shallow Cumulus Clouds in Observations From the US Southern Great Plains? *Geophysical Research Letters*, 49(7), Article e2021GL097070.
- Toledo-Aceves, T., Trujillo-Miranda, A. L., & López-Barrera, F. (2021). Tree regeneration in active and passive cloud forest restoration: Functional groups and timber species. *Forest Ecology and Management*, 489, 119050.
- Trac, C. J., Harrell, S., Hinckley, T. M., & Henck, A. C. (2007). Reforestation programs in Southwest China: reported success, observed failure, and the reasons why. *Journal of Mountain Science*, 4(4), 275-292.

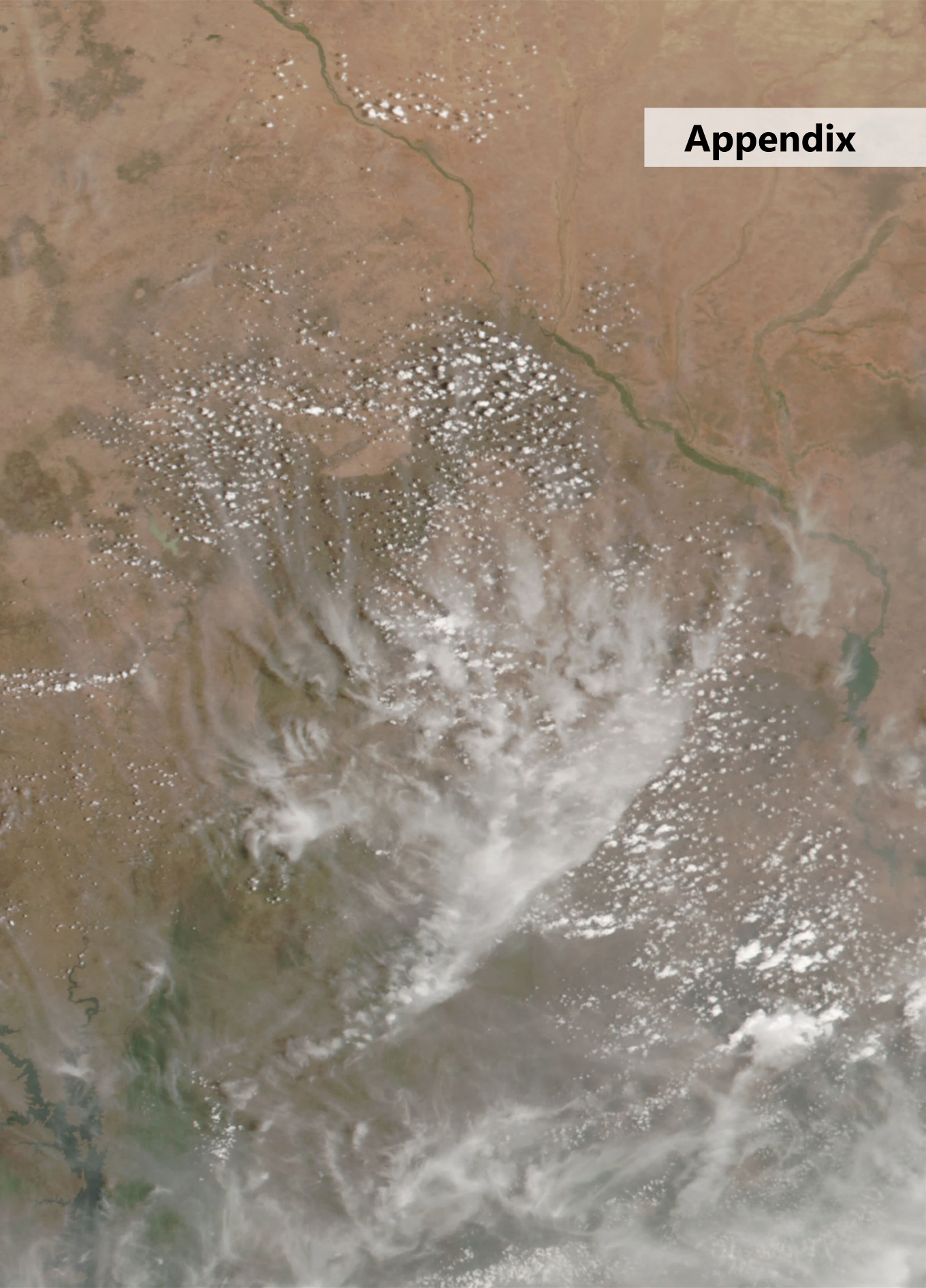
- Trenberth, K. E., Fasullo, J. T., & Kiehl, J. (2009). Earth's global energy budget. *Bulletin of the American Meteorological Society*, 90(3), 311-324.
- Trisos, C. H., Adelekan, I. O., Totin, E., Ayanlade, A., Efitre, J., Gameda, A., Kalaba, K., Lennard, C., Masao, C., Mgaya, Y., Ngaruiya, G., Olago, D., Simpson, N. P., & Zakieldean, S. (2022). Africa (In *Climate Change 2022: Impacts, Adaptation, and Vulnerability. Contribution of Working Group II to the Sixth Assessment Report of the Intergovernmental Panel on Climate Change* (pp. 1285–1455)). Cambridge University Press, Cambridge.
- Tucker, C. J. (1979). Red and photographic infrared linear combinations for monitoring vegetation. *Remote Sensing of Environment*, 8(2), 127-150.
- Tuinenburg, O., Hutjes, R., Jacobs, C., & Kabat, P. (2011). Diagnosis of local land-atmosphere feedbacks in India. *Journal of Climate*, 24(1), 251-266.
- UNCCD. (2017). *Global Land Outlook* [Report]. U. N. C. t. C. Desertification.
- UNCCD. (2020). *The Great Green Wall Implementation Status and Way Ahead to 2030* [Report]. U. N. C. t. C. Desertification.
- UNCCD. (2022). *Global Land Outlook* [Report]. U. N. C. t. C. Desertification.
- Underwood, A. (1991). Beyond BACI: experimental designs for detecting human environmental impacts on temporal variations in natural populations. *Marine and Freshwater Research*, 42(5), 569-587.
- Underwood, A. (1992). Beyond BACI: the detection of environmental impacts on populations in the real, but variable, world. *Journal of experimental marine biology and ecology*, 161(2), 145-178.
- UNEP-WCMC. (2022). *Protected Area Profile for South Africa from the World Database on Protected Areas* [Dataset]. www.protectedplanet.net
- UNEP. (2019). *Resolution 73/284: United Nations Decade on Ecosystem Restoration (2021–2030)*. [Report]. U. N. E. Programme.
- UNEP. (2021). *Becoming #GenerationRestoration: Ecosystem restoration for people, nature and climate*. [Report]. U. N. E. Programme.
- University of Wyoming. (2025). *Upper air soundings dataset*. [Dataset]. <https://weather.uwyo.edu/upperair/sounding.html>
- van der Vliet, M., Malbeteau, Y., Ghent, D., Haas, S. d., Veal, K. L., van der Zaan, T., Sinha, R., Dash, S. K., Houborg, R., & de Jeu, R. A. (2024). Quantifiable impact: monitoring landscape restoration from space. A regreening case study in Tanzania. *FRONTIERS IN ENVIRONMENTAL SCIENCE*, 12, 1352058.
- van Heerwaarden, C. C., & Teuling, A. J. (2014). Disentangling the response of forest and grassland energy exchange to heatwaves under idealized land-atmosphere coupling. *Biogeosciences*, 11(21), 6159-6171.
- Vancutsem, C., Ceccato, P., Dinku, T., & Connor, S. J. (2010). Evaluation of MODIS land surface temperature data to estimate air temperature in different ecosystems over Africa. *Remote Sensing of Environment*, 114(2), 449-465.
- Vaughan, M. A., Winker, D. M., & Powell, K. A. (2005). *CALIOP algorithm theoretical basis document, part 2, feature detection and layer properties algorithms* [Report]. NASA.
- Veldman, J. W., Aleman, J. C., Alvarado, S. T., Anderson, T. M., Archibald, S., Bond, W. J., Boutton, T. W., Buchmann, N., Buisson, E., Canadell, J. G., Dechoum, M. d. S., Diaz-Toribio, M. H., Durigan, G., Ewel, J. J., Fernandes, G. W., Fidelis, A., Fleischman, F., Good, S. P., Griffith, D. M., . . . Zaloumis, N. P. (2019). Comment on "The global tree restoration potential". *science*, 366(6463), eaay7976.

- Veldman, J. W., Overbeck, G. E., Negreiros, D., Mahy, G., Le Stradic, S., Fernandes, G. W., Durigan, G., Buisson, E., Putz, F. E., & Bond, W. J. (2015). Where tree planting and forest expansion are bad for biodiversity and ecosystem services. *Bioscience*, *65*(10), 1011-1018.
- Verbesselt, J., Hyndman, R., Newnham, G., & Culvenor, D. (2010). Detecting trend and seasonal changes in satellite image time series. *Remote Sensing of Environment*, *114*(1), 106-115.
- Verbesselt, J., Hyndman, R., Zeileis, A., & Culvenor, D. (2010). Phenological change detection while accounting for abrupt and gradual trends in satellite image time series. *Remote Sensing of Environment*, *114*(12), 2970-2980.
- Verbesselt, J., Zeileis, A., & Herold, M. (2012). Near real-time disturbance detection using satellite image time series. *Remote Sensing of Environment*, *123*, 98-108.
- Vermote, E. F. (2015). *MOD09A1 MODIS Surface Reflectance 8-Day L3 Global 500m SIN Grid V006* [Dataset]. NASA EOSDIS Land Processes DAAC. <https://doi.org/10.5067/MODIS/MYD09A1.006>
- Vilà-Guerau de Arellano, J., Van Heerwaarden, C., Van Stratum, B., & van den Dries, K. (2015). *Atmospheric boundary layer: Integrating air chemistry and land interactions* [Book]. Cambridge University Press.
- Villani, L., Castelli, G., Sambalino, F., Almeida Oliveira, L. A., & Bresci, E. (2021). Influence of trees on landscape temperature in semi-arid agro-ecosystems of East Africa. *Biosystems Engineering*, *212*, 185-199.
- Villani, L., Castelli, G., Sambalino, F., Oliveira, L. A. A., & Bresci, E. (2020, 4-6 Nov. 2020). Integrating UAV and satellite data to assess the effects of agroforestry on microclimate in Dodoma region, Tanzania. IEEE International Workshop on Metrology for Agriculture and Forestry (MetroAgriFor),
- Vollset, S. E., Goren, E., Yuan, C.-W., Cao, J., Smith, A. E., Hsiao, T., Bisignano, C., Azhar, G. S., Castro, E., Chalek, J., Dolgert, A. J., Frank, T., Fukutaki, K., Hay, S. I., Lozano, R., Mokdad, A. H., Nandakumar, V., Pierce, M., Pletcher, M., . . . Murray, C. J. L. (2020). Fertility, mortality, migration, and population scenarios for 195 countries and territories from 2017 to 2100: a forecasting analysis for the Global Burden of Disease Study. *The Lancet*, *396*(10258), 1285-1306.
- Von Arx, G., Graf Pannatier, E., Thimonier, A., & Rebetez, M. (2013). Microclimate in forests with varying leaf area index and soil moisture: potential implications for seedling establishment in a changing climate. *Journal of ecology*, *101*(5), 1201-1213.
- Walters, G., Baruah, M., Karambiri, M., Osei-Wusu Adjei, P., Samb, C., & Barrow, E. (2021). The power of choice: How institutional selection influences restoration success in Africa. *Land Use Policy*, *104*, 104090.
- Wan, Z., & Dozier, J. (1996). A generalized split-window algorithm for retrieving land-surface temperature from space. *IEEE Transactions on geoscience and remote sensing*, *34*(4), 892-905.
- Wan, Z., Hook, S., & Hulley, G. (2021). *MODIS/Terra Land Surface Temperature/Emissivity Daily L3 Global 1km SIN Grid V061* [Dataset]. <https://doi.org/10.5067/MODIS/MOD11A1.061>
- Wang, J., Chagnon, F. J., Williams, E. R., Betts, A. K., Renno, N. O., Machado, L. A., Bisht, G., Knox, R., & Bras, R. L. (2009). Impact of deforestation in the Amazon basin on cloud climatology. *Proceedings of the national academy of sciences*, *106*(10), 3670-3674.

- Westra, D., Steeneveld, G. J., & Holtslag, A. A. M. (2012). Some Observational Evidence for Dry Soils Supporting Enhanced Relative Humidity at the Convective Boundary Layer Top. *Journal of Hydrometeorology*, 13(4), 1347-1358.
- Wieczorkowski, J. D., & Lehmann, C. E. R. (2022). Encroachment diminishes herbaceous plant diversity in grassy ecosystems worldwide. *Global change biology*, 28(18), 5532-5546.
- Williams, B. A., Beyer, H. L., Fagan, M. E., Chazdon, R. L., Schmoeller, M., Sprengle-Hyppolite, S., Griscom, B. W., Watson, J. E. M., Tedesco, A. M., Gonzalez-Roglich, M., Daldegan, G. A., Bodin, B., Celentano, D., Wilson, S. J., Rhodes, J. R., Alexandre, N. S., Kim, D.-H., Bastos, D., & Crouzeilles, R. (2024). Global potential for natural regeneration in deforested tropical regions. *Nature*, 636(8041), 131-137.
- Williams, P. A., Simpson, N. P., Totin, E., North, M. A., & Trisos, C. H. (2021). Feasibility assessment of climate change adaptation options across Africa: an evidence-based review. *Environmental Research Letters*, 16(7), 073004.
- Williamson, S. N., Barrio, I. C., Hik, D. S., & Gamon, J. A. (2016). Phenology and species determine growing-season albedo increase at the altitudinal limit of shrub growth in the sub-Arctic. *Global change biology*, 22(11), 3621-3631.
- Wilson, K. B., Hanson, P. J., & Baldocchi, D. D. (2000). Factors controlling evaporation and energy partitioning beneath a deciduous forest over an annual cycle. *Agricultural and Forest Meteorology*, 102(2-3), 83-103.
- Winckler, J., Lejeune, Q., Reick, C. H., & Pongratz, J. (2019). Nonlocal effects dominate the global mean surface temperature response to the biogeophysical effects of deforestation. *Geophysical Research Letters*, 46(2), 745-755.
- Windisch, M. G., Davin, E. L., & Seneviratne, S. I. (2021). Prioritizing forestation based on biogeochemical and local biogeophysical impacts. *Nature Climate Change*, 11(10), 867-871.
- Winker, D. M., Pelon, J. R., & McCormick, M. P. (2003). CALIPSO mission: spaceborne lidar for observation of aerosols and clouds. Lidar remote sensing for industry and environment monitoring III,
- Winker, D. M., Vaughan, M. A., Omar, A., Hu, Y., Powell, K. A., Liu, Z., Hunt, W. H., & Young, S. A. (2009). Overview of the CALIPSO Mission and CALIOP Data Processing Algorithms. *Journal of Atmospheric and Oceanic Technology*, 26(11), 2310-2323.
- WOCAT. (2022). *Global Sustainable Land Management Database* [Dataset]. <https://www.wocat.net/en/>
- Wolfe, R. E., Lin, G., Nishihama, M., Tewari, K. P., Tilton, J. C., & Isaacman, A. R. (2013). Suomi NPP VIIRS prelaunch and on-orbit geometric calibration and characterization. *Journal of Geophysical Research: Atmospheres*, 118(20), 5108-5115, 5115-5121.
- Wolff, N. H., Masuda, Y. J., Meijaard, E., Wells, J. A., & Game, E. T. (2018). Impacts of tropical deforestation on local temperature and human well-being perceptions. *Global Environmental Change*, 52, 181-189.
- World Bank. (2024). *Transforming Education for Inclusive Growth* [Report](Africa's Pulse, Issue. W. Bank.
- Xie, D., Caporaso, L., Reichstein, M., Zhong, D., & Duveiller, G. (2025). Beyond Canopy Cover: How Tree Distribution Shapes Cloud Formation Across Africa. In.

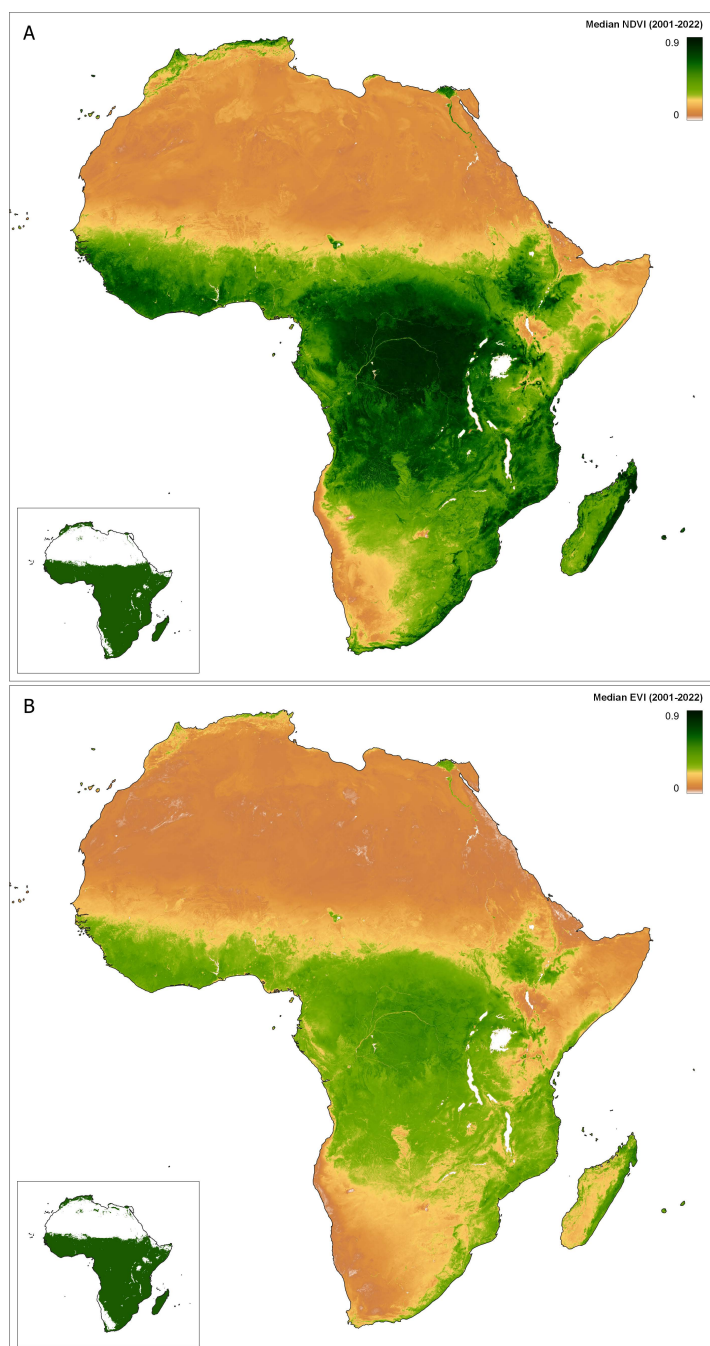
- Xu, R., Li, Y., Teuling, A. J., Zhao, L., Spracklen, D. V., Garcia-Carreras, L., Meier, R., Chen, L., Zheng, Y., & Lin, H. (2022). Contrasting impacts of forests on cloud cover based on satellite observations. *Nature communications*, *13*(1), 670.
- Yang, J., Li, Z., Zhai, P., Zhao, Y., & Gao, X. (2020). The influence of soil moisture and solar altitude on surface spectral albedo in arid area. *Environmental Research Letters*, *15*(3), 035010.
- Yosef, G., Walko, R., Avisar, R., Tatarinov, F., Rotenberg, E., & Yakir, D. (2018). Large-scale semi-arid afforestation can enhance precipitation and carbon sequestration potential. *Scientific Reports*, *8*(1), 996.
- Zahawi, R. A., Reid, J. L., & Holl, K. D. (2014). Hidden costs of passive restoration. *Restoration Ecology*, *22*(3), 284-287.
- Zeng, Z., Piao, S., Li, L. Z., Zhou, L., Ciais, P., Wang, T., Li, Y., Lian, X., Wood, E. F., & Friedlingstein, P. (2017). Climate mitigation from vegetation biophysical feedbacks during the past three decades. *Nature Climate Change*, *7*(6), 432-436.
- Zhang, Y., Wang, X., Lian, X., Li, S., Li, Y., Chen, C., & Piao, S. (2024). Asymmetric impacts of forest gain and loss on tropical land surface temperature. *Nature geoscience*, 1-7.
- Zheng, L., Zhao, G., Dong, J., Ge, Q., Tao, J., Zhang, X., Qi, Y., Doughty, R. B., & Xiao, X. (2019). Spatial, temporal, and spectral variations in albedo due to vegetation changes in China's grasslands. *ISPRS Journal of Photogrammetry and Remote Sensing*, *152*, 1-12.
- Zhu, Z., Piao, S., Myneni, R. B., Huang, M., Zeng, Z., Canadell, J. G., Ciais, P., Sitch, S., Friedlingstein, P., & Arneth, A. (2016). Greening of the Earth and its drivers. *Nature Climate Change*, *6*(8), 791-795.
- Zomer, R. J., Xu, J., & Trabucco, A. (2022). Version 3 of the Global Aridity Index and Potential Evapotranspiration Database. *Scientific data*, *9*(1), 409.



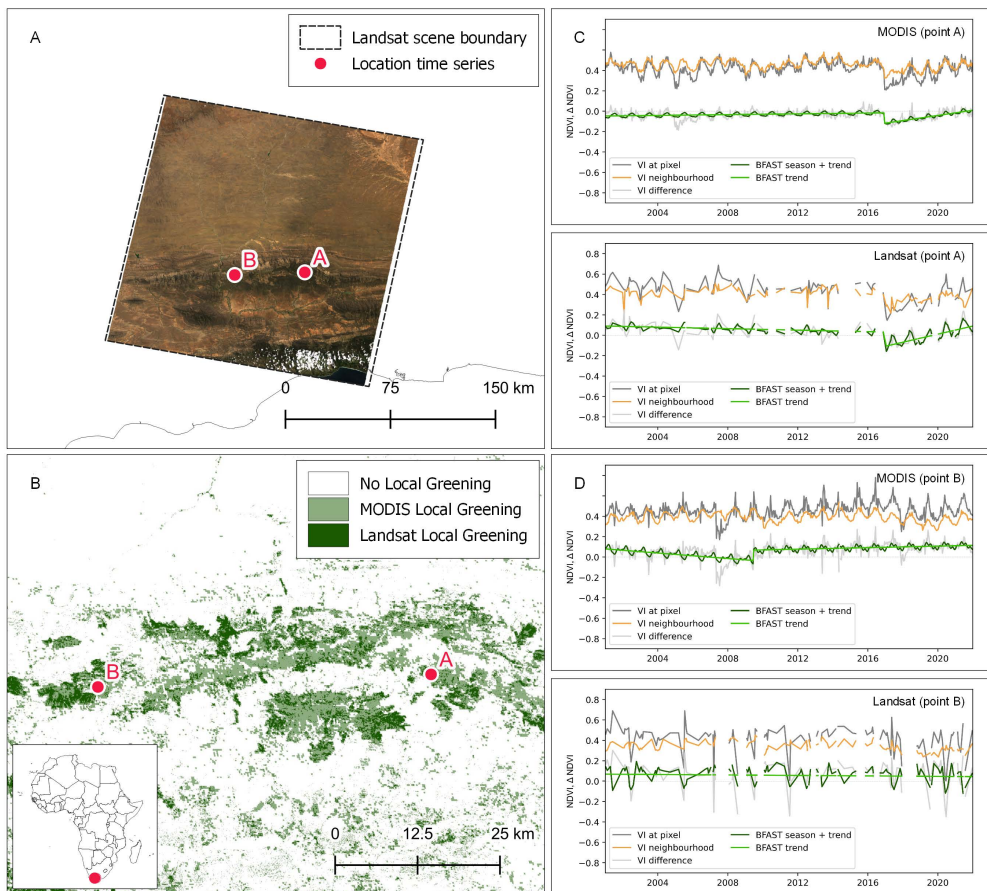
An aerial photograph of a river delta system. The water is a muddy brown color. A large, irregular white plume of water or sediment is visible in the center of the delta, extending from the top towards the bottom. The plume has a textured, almost crystalline appearance. The surrounding water shows various channels and distributaries. In the top right corner, there is a white rectangular box containing the word "Appendix" in black text.

Appendix

Appendix A | Supplementary Material Chapter 2



Supplementary Figure 2.1 | Spatial distribution of NDVI and EVI. Median Normalized Difference Vegetation Index (A) and Enhanced Vegetation Index (B) from MODIS, calculated for 2001-01-01 to 2022-01-01. The inserted maps show the areas where the NDVI and EVI are higher than 0.15 and 0.11, respectively. Areas in Africa with a NDVI higher than 0.15 are considered to be part of the study area.

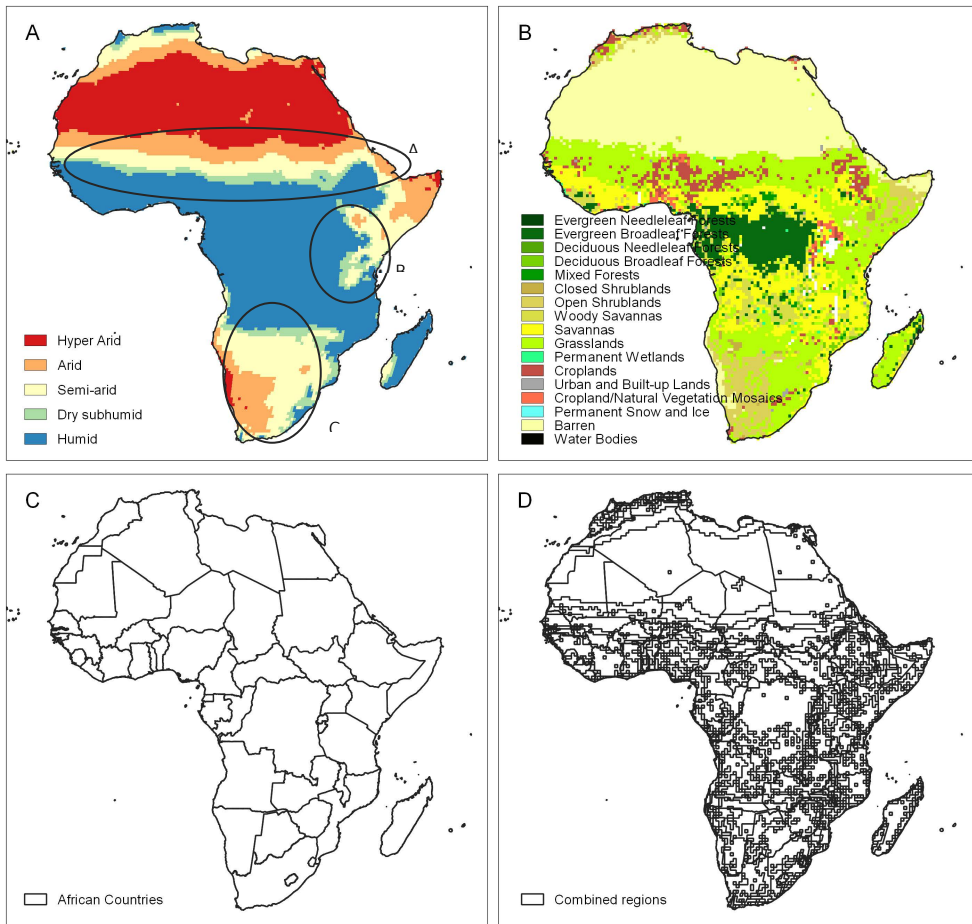


Supplementary Figure 2.2 | Comparison between spatial context approach with MODIS and Landsat NDVI. RGB image for a single Landsat-7 scene on 9 January 2001 in South-Africa (A). Local greening as calculated with MODIS (250m) and Landsat-7 (30m) (B). Due to the higher resolution of Landsat-7, the local greening is calculated with a 5 km neighbourhood radius for both MODIS and Landsat, instead of a 25 km neighbourhood. Time series of MODIS (top) and Landsat (bottom) at point A (C) and B (D). The time series are calculated with a 5 km neighbourhood radius.

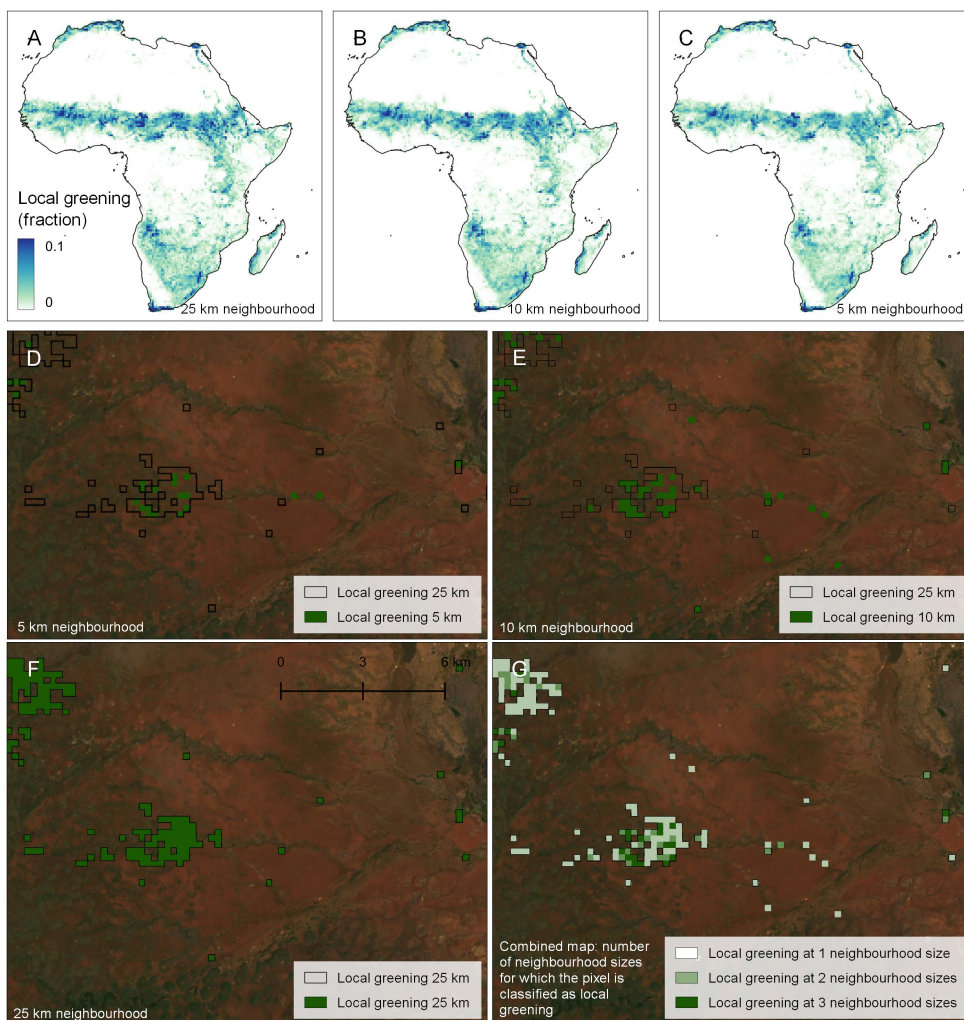
To explore the uncertainty caused by the moderate resolution (250m) of the MODIS data, the analysis was also performed with Landsat-7 ETM+ data for a smaller area in South-Africa (WRS-2 173_83). USGS Landsat-7 Level 2, Collection 2, Tier 1 atmospherically corrected surface reflectance data were used because this data is available for the whole 2001-2021 period in Google Earth Engine. The data has a 30 m spatial resolution and a temporal resolution of 16 days. Images with a cloud cover fraction higher than 10% were excluded from this analysis. For each image, the NDVI was calculated using the Red and NIR bands. Next, the spatial context method and BFASST were applied in a similar way as for the MODIS data. Due to computational limitations, the analysis was performed using a 5 km neighbourhood radius. It should

be noted that Landsat-7 experienced a Scan Line Corrector failure in the ETM+ sensor in May 2003, which caused striped data gaps in the imagery after this data.

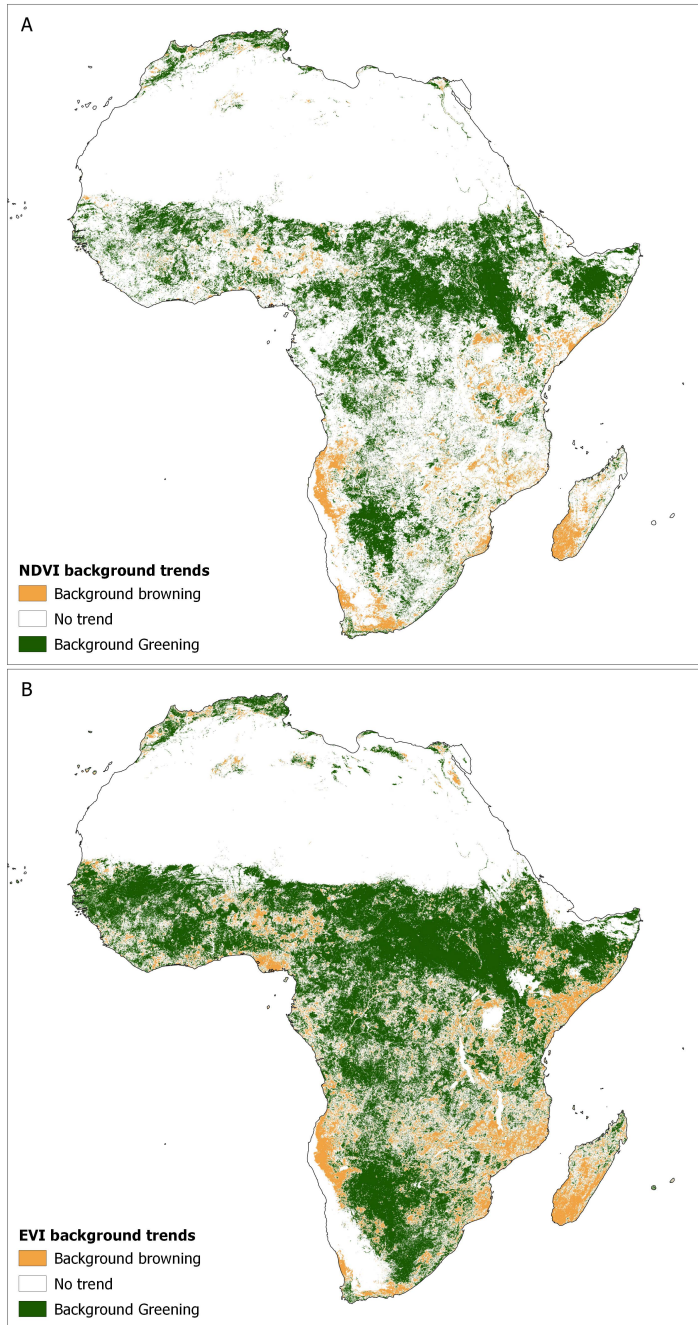
The analysis shows that the spatial patterns of local greening as calculated with Landsat data and MODIS data are similar. To be more precise, in 90.3% of the study area, MODIS and Landsat detect the same (both local greening or no local greening), in 8.1% of the study area, MODIS detects local greening but Landsat not, and in 1.6% of the area Landsat detects local greening but MODIS not. A smaller area is thus classified as local greening with Landsat than with MODIS, which can likely be explained by the lower temporal resolution of Landsat as well as the data gaps resulting from clouds and the Scan Line failure. This can also be observed in the time series at point B, where no breakpoint is detected when there are large gaps in the data. Despite these differences, the time series show a similar pattern and the breakpoint is detected at the same moment.



Supplementary Figure 2.3 | Surface properties used for the analysis of local greening pixels and the evaluation of sustainable land management projects: (A) Aridity Index classification, (B) MODIS land cover for 2001, (C) Countries in Africa and (D) combined regions with the same aridity index, land cover and country values. These combined areas are used for the evaluation of the WOCAT sustainable land management projects. The labels in the Aridity Index map mark rough boundaries of the Sahel region (A), Kenya and Tanzania (B) and southern Africa (C).



Supplementary Figure 2.4 | Sensitivity analysis of local greening pixels to neighbourhood size. The figures show local greening pixels with (A) a 25 km neighbourhood radius, (B) a 10 km neighbourhood radius and (C) a 5 km neighbourhood radius. We calculated local greening pixels with the spatial-context method. In all three figures, only significant trends are considered ($p=0.05$). For visualization purposes, the figures are downscaled to a 50 km resolution. Each downscaled pixel now shows the fraction of 250 m resolution local greening pixels. The bottom figures show local greening pixels in Kenya (37.8°E, 2.9°S) with (D) a 5 km neighbourhood radius, (E) a 10 km neighbourhood radius and (F) a 25 km neighbourhood radius. (G) shows a combination of the other three maps, where the amount of local greening pixels of the different neighbourhood sizes is shown.



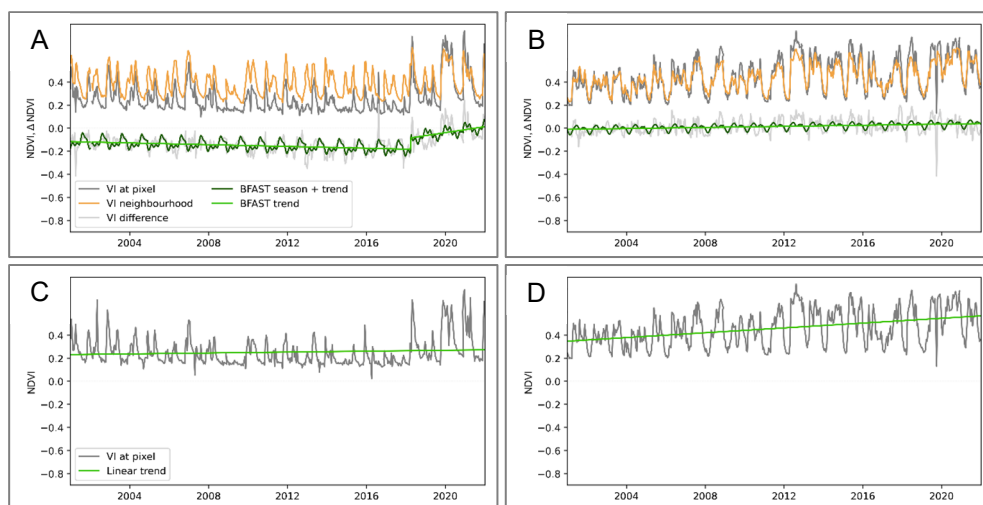
Supplementary Figure 2.5 | Spatial distribution of NDVI and EVI background greening. Normalized Difference Vegetation Index (A) and Enhanced Vegetation Index (B) background trends, as calculated with a linear least squares regression over the 2001-01-01 to 2022-01-01 period. Negative trends are shown as browning, positive trends as greening and non-significant trends as no trend ($p=0.05$). These two maps are used to create the map of combined background greening and browning in Fig. 1D.



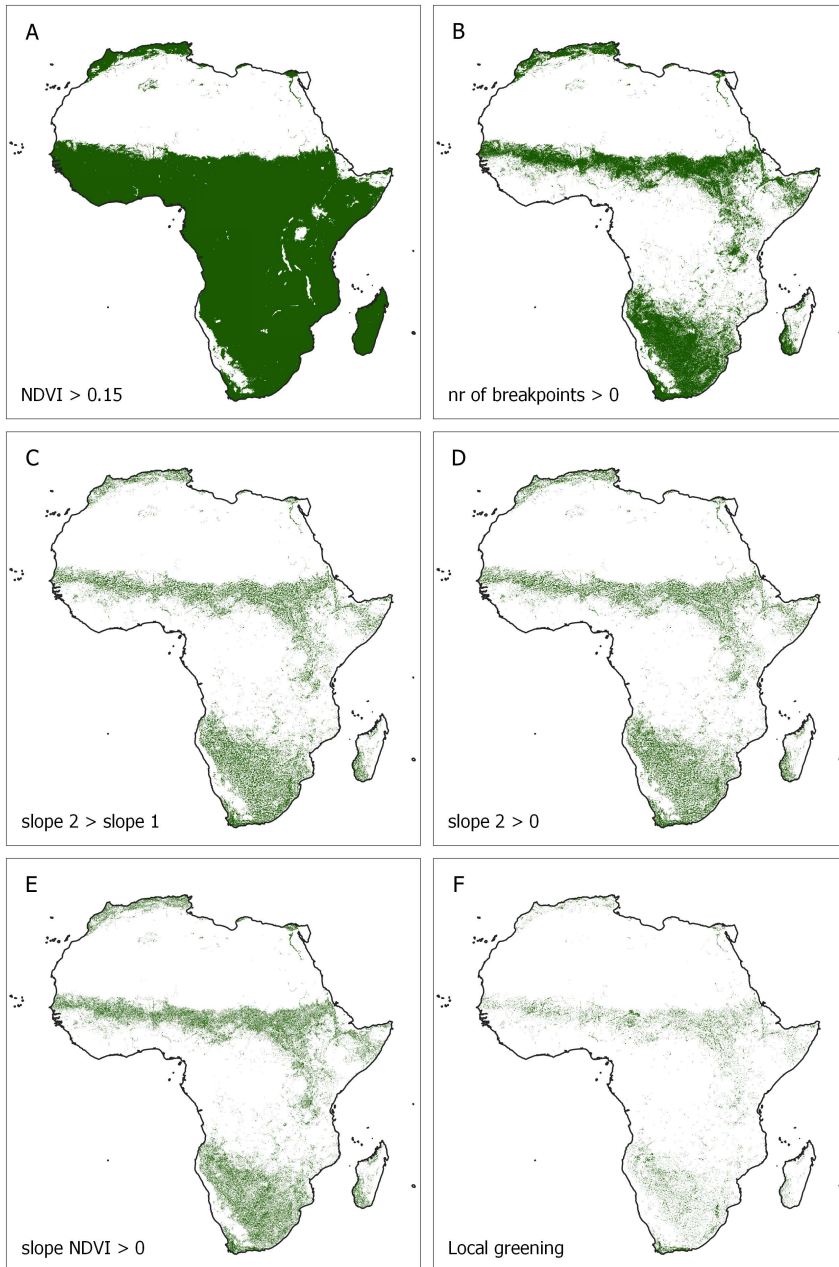
Supplementary Figure 2.6 | Spatial distribution of local browning pixels. The local browning pixels calculated in the same way as the local greening pixels, with the spatial context method and a 25 km neighbourhood, but the pixels should show a negative trend after a breakpoint in the spatially corrected time series as well the original NDVI and EVI time series. Using this method, 1.9% of the study area shows this type of local browning.

Supplementary Table 2.1 | Distribution of local greening pixels over land cover type and aridity index classes. Percentages indicate the area of combined NDVI and EVI local greening per class divided over the total greening area. The row and column "Total" show the total percentage of local greening over the row or column (e.g. the percentage of local greening that occurs in semi-arid areas). In the last row and column, relative size of each land cover and aridity class is given.

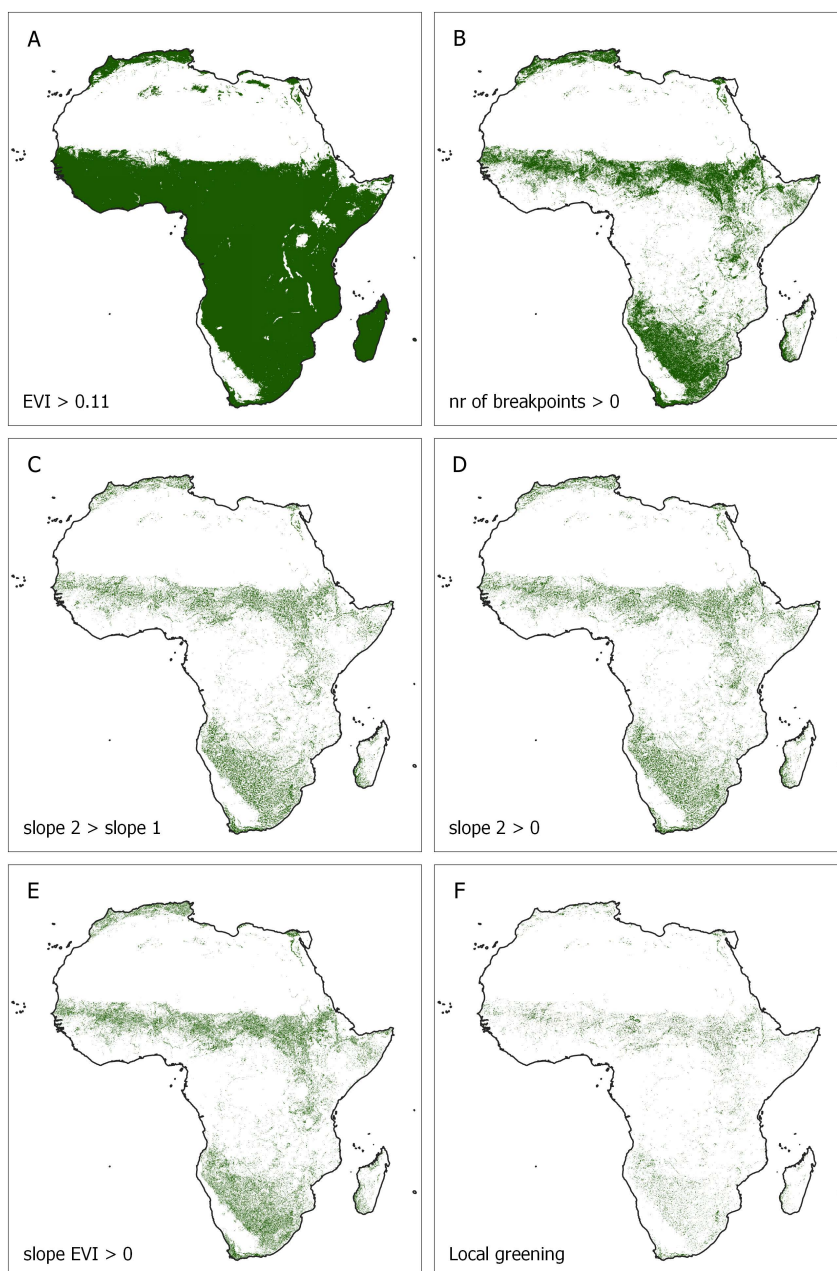
	Hyper arid	Arid	Semi-arid	Dry subhumid	Humid	Total	% of study area
Evergreen Needleleaf Forest	0.00%	0.00%	0.01%	0.01%	0.16%	0.2%	0.0%
Evergreen Broadleaf Forest	0.00%	0.00%	0.15%	0.28%	1.79%	2.2%	11.8%
Deciduous Needleleaf Forest	0.00%	0.00%	0.00%	0.00%	0.00%	0.0%	0.0%
Deciduous Broadleaf Forest	0.00%	0.00%	0.23%	0.09%	0.61%	0.9%	1.8%
Mixed Forest	0.00%	0.00%	0.00%	0.00%	0.33%	0.3%	1.0%
Closed Shrublands	0.00%	0.01%	1.25%	0.19%	0.29%	1.8%	0.9%
Open Shrublands	0.32%	3.82%	4.98%	0.30%	0.23%	9.7%	7.5%
Woody Savannas	0.00%	0.00%	0.12%	0.18%	1.78%	2.1%	6.4%
Savannas	0.03%	0.03%	0.91%	1.42%	12.10%	14.5%	22.6%
Grasslands	0.27%	6.44%	26.13%	10.12%	10.05%	53.0%	38.0%
Permanent wetlands	0.00%	0.01%	0.12%	0.04%	0.25%	0.4%	0.4%
Croplands	0.49%	0.58%	4.57%	3.14%	3.72%	12.5%	6.9%
Urban	0.03%	0.03%	0.08%	0.02%	0.06%	0.2%	0.2%
Cropland and Natural	0.01%	0.08%	0.37%	0.03%	0.56%	1.1%	1.4%
Permanent Snow and Ice	0.00%	0.00%	0.00%	0.00%	0.00%	0.0%	0.0%
Barren	0.42%	0.57%	0.11%	0.01%	0.00%	1.1%	0.8%
Water	0.00%	0.00%	0.01%	0.01%	0.03%	0.0%	0.1%
Total	1.6%	11.6%	39.1%	15.8%	32.0%		
% of study area	0.5%	8.4%	25.8%	10.1%	55.2%		



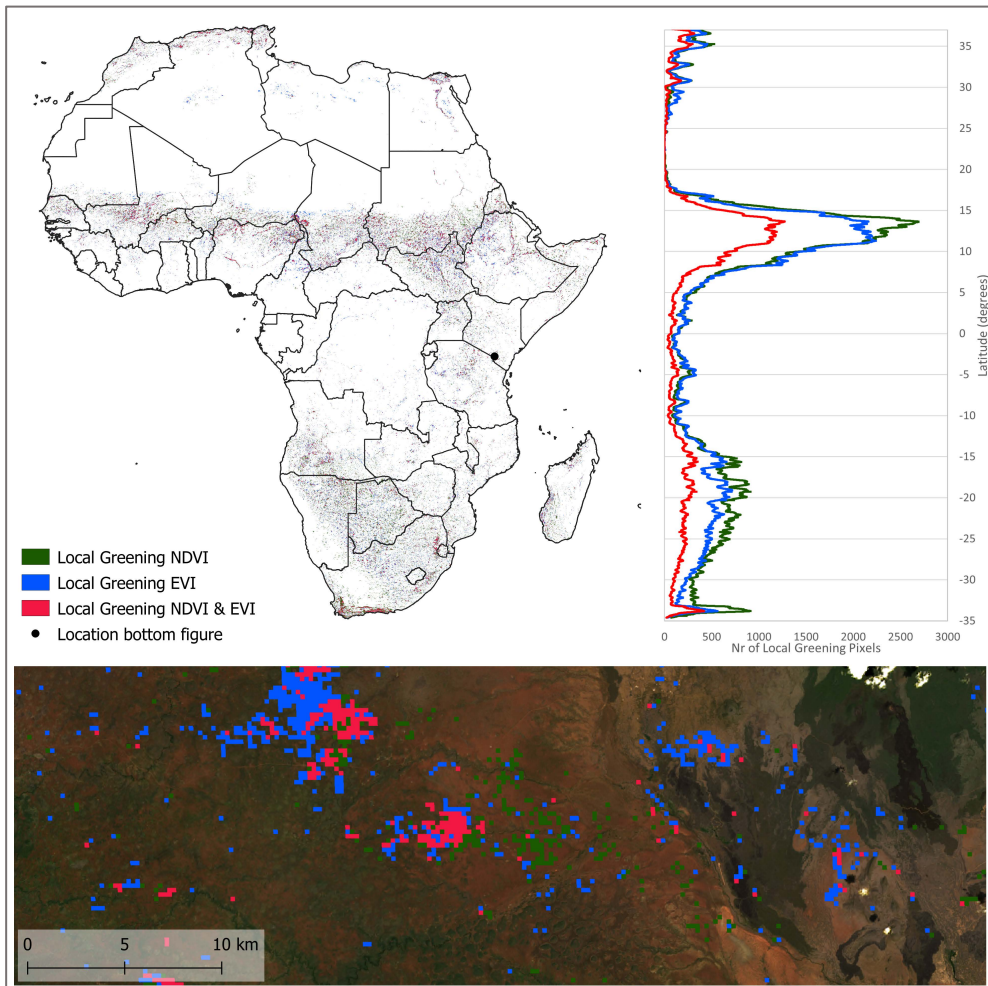
Supplementary Figure 2.7 | Illustration of spatial-context approach and background trends. Time series of NDVI as calculated with a spatial context approach (**top**) and linear regression (**bottom**) at point A (**left**) and B (**right**). At point A, a breakpoint is detected by using the spatial context method, while there is no background trend. At point B, there is a steep background trend detected, but the spatial context method does show this same trend. This suggests that the greening at point A is caused by small-scale processes, while the greening at point B is caused by large-scale processes.



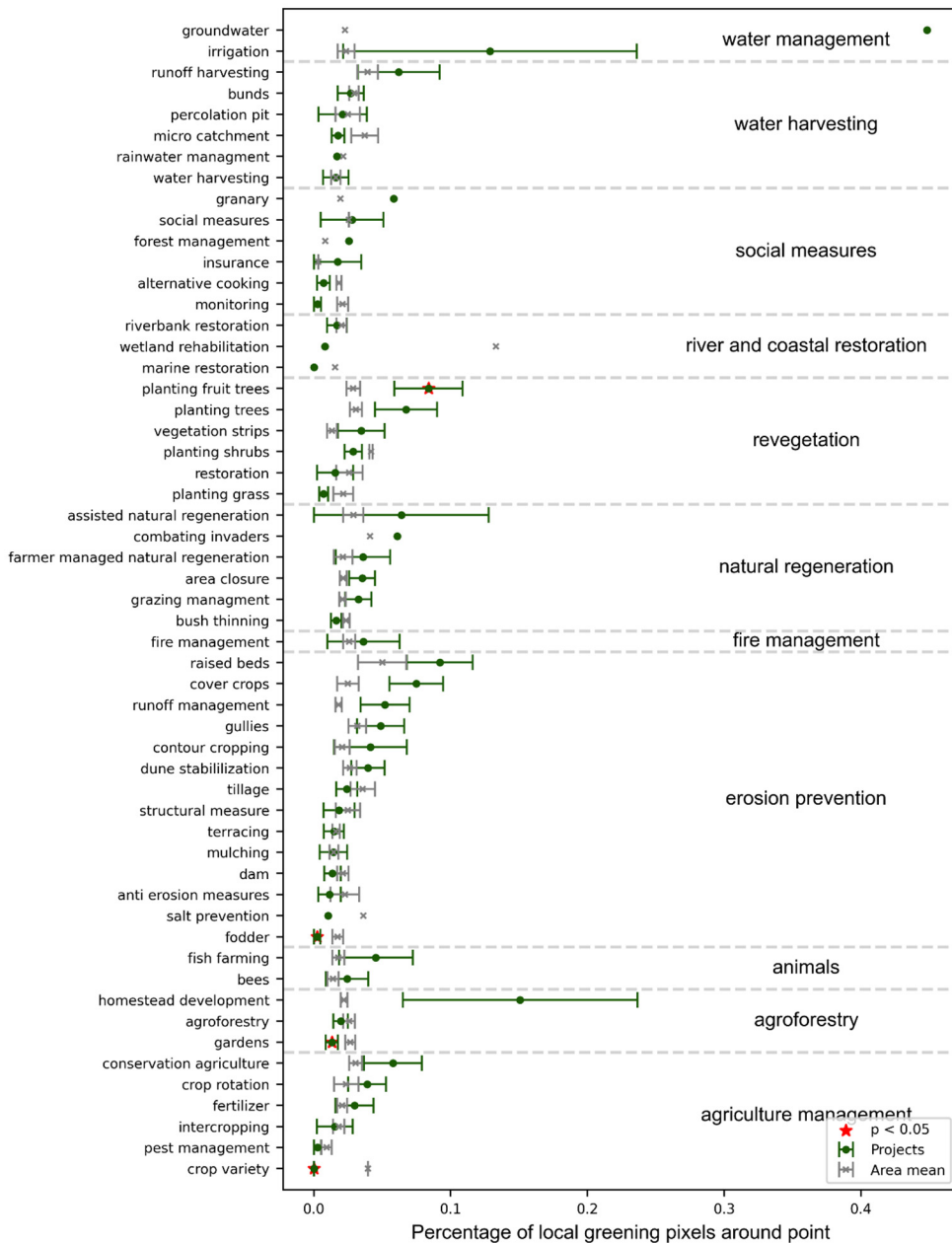
Supplementary Figure 2.8 | Intermediate results of Local Greening (NDVI). Regions where the median NDVI is higher than 0.15 (64% of Africa) (**A**), the BFAST algorithm detects a breakpoint (22% of study area) (**B**), the slope after the breakpoint is larger than before the breakpoint (51% of breakpoints) (**C**), the slope after the breakpoint is significantly positive (45% of breakpoints) (**D**) and the slope of the original (pixel) NDVI after the breakpoint is positive (52% of breakpoints) (**E**) and the areas classified as local greening (4.8% of study area) (**F**).



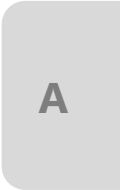
Supplementary Figure 2.9 | Intermediate results of Local Greening (EVI). Regions where the median EVI is higher than 0.11 (63% of Africa) (A), the BFAST algorithm detects a breakpoint (18% of study area) (B), the slope after the breakpoint is larger than before the breakpoint (50% of breakpoints) (C), the slope after the breakpoint is significantly positive (43% of breakpoints) (D) and the slope of the original (pixel) EVI after the breakpoint is positive (54% of breakpoints) (E) and the areas classified as local greening (4.3% of the study area) (F).



Supplementary Figure 2.10 | Spatial distribution of NDVI, EVI and combined local greening. Local greening, calculated with the NDVI and EVI spatial-context method and a 25 km neighbourhood at a 250 m resolution. Also, the areas that are classified as both NDVI and EVI local greening are shown. This combined NDVI and EVI is used in the main figures. On the right side, the number of NDVI, EVI and combined local greening pixels per degrees latitude is shown. The bottom figure shows local greening at a smaller area in Kenya, as indicated by the black dot.

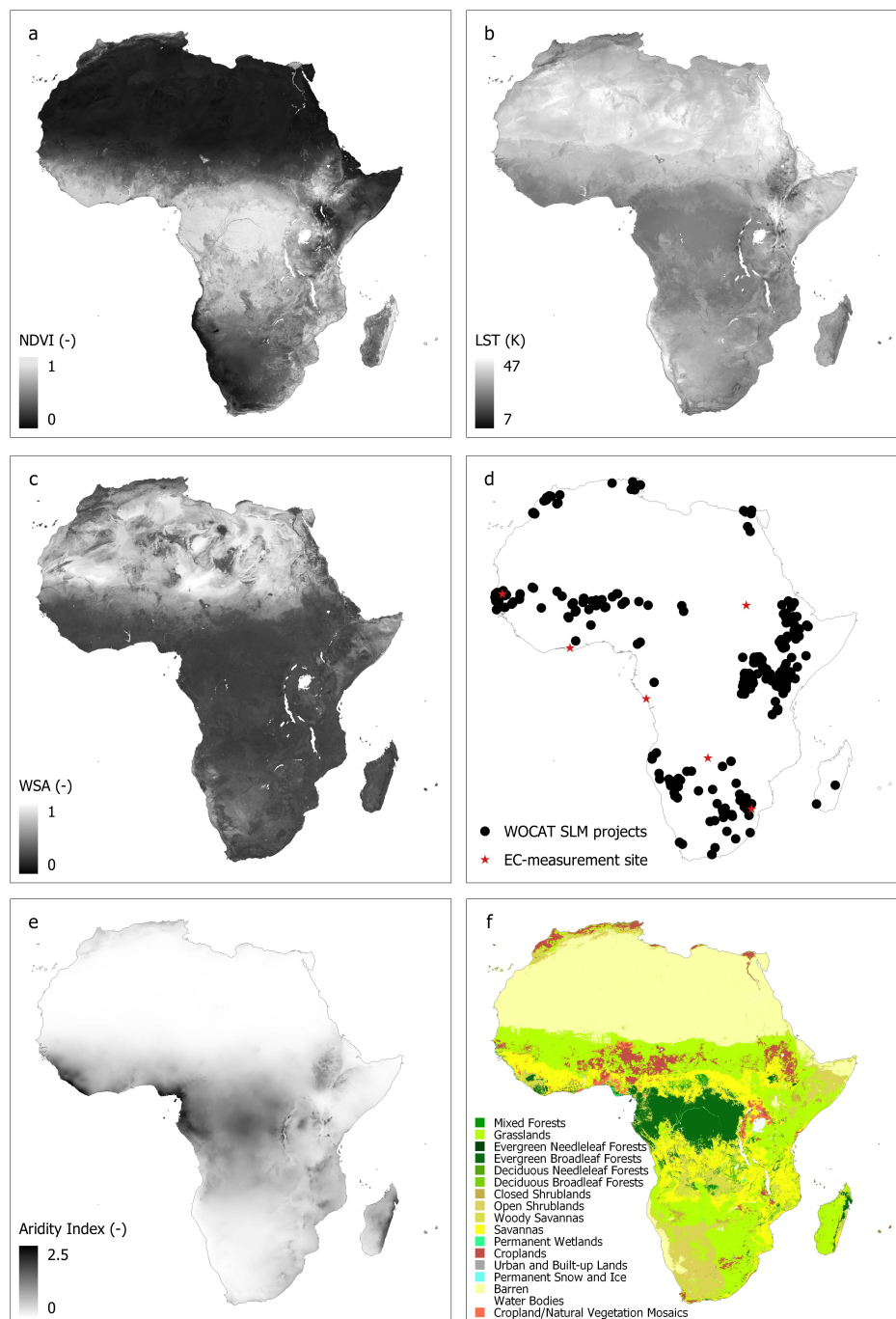


Supplementary Figure 2.11 | Comparison of sustainable land management types with regional averages. The error plot shows the mean and standard error of the percentage of combined NDVI and EVI local greening pixels (Fig. 1A) within 2000 m around the WOCAT SLM project point. The projects area categorized by subcategory of land management and compared to the mean percentage of local greening pixels in an area with the same aridity index, land cover type and country (Supplementary Figure 2.1D). Significant differences are marked with a star ($p = 0.05$).

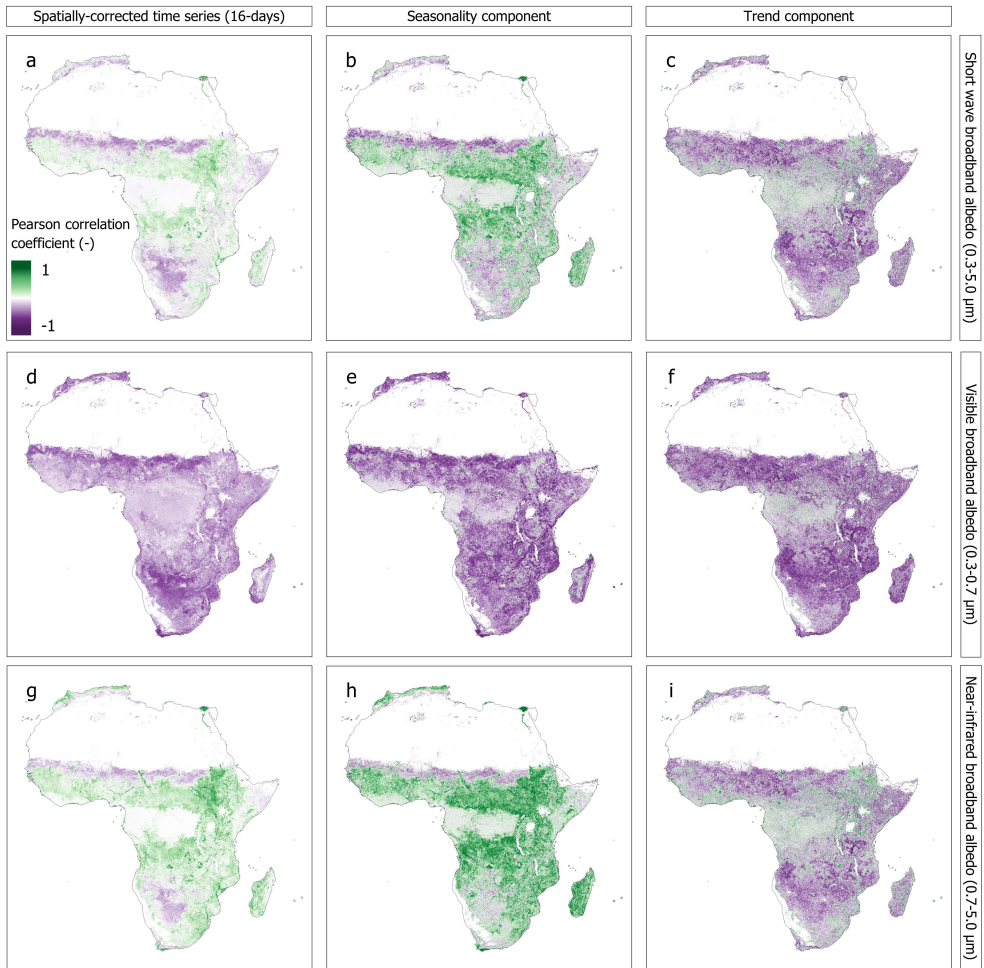


This figure is an extension of Figure 3, showing a comparison of local greening at SLM project with areas with a similar land cover and aridity in the same country. Instead of combined result for SLM, reforestation and natural regeneration, the results are calculated for each subcategory separately. It can be observed that the different categories show mixed results with respect to local greening. A limited number of SLM projects show a significant increase in local greening, which may be caused by the limited number of restoration projects for each category. As expected, project specifically aiming to increase vegetation cover, such as planting (fruit) trees show a large effect on local greening, while other categories, like social measures or water harvesting have limited or mixed effects.

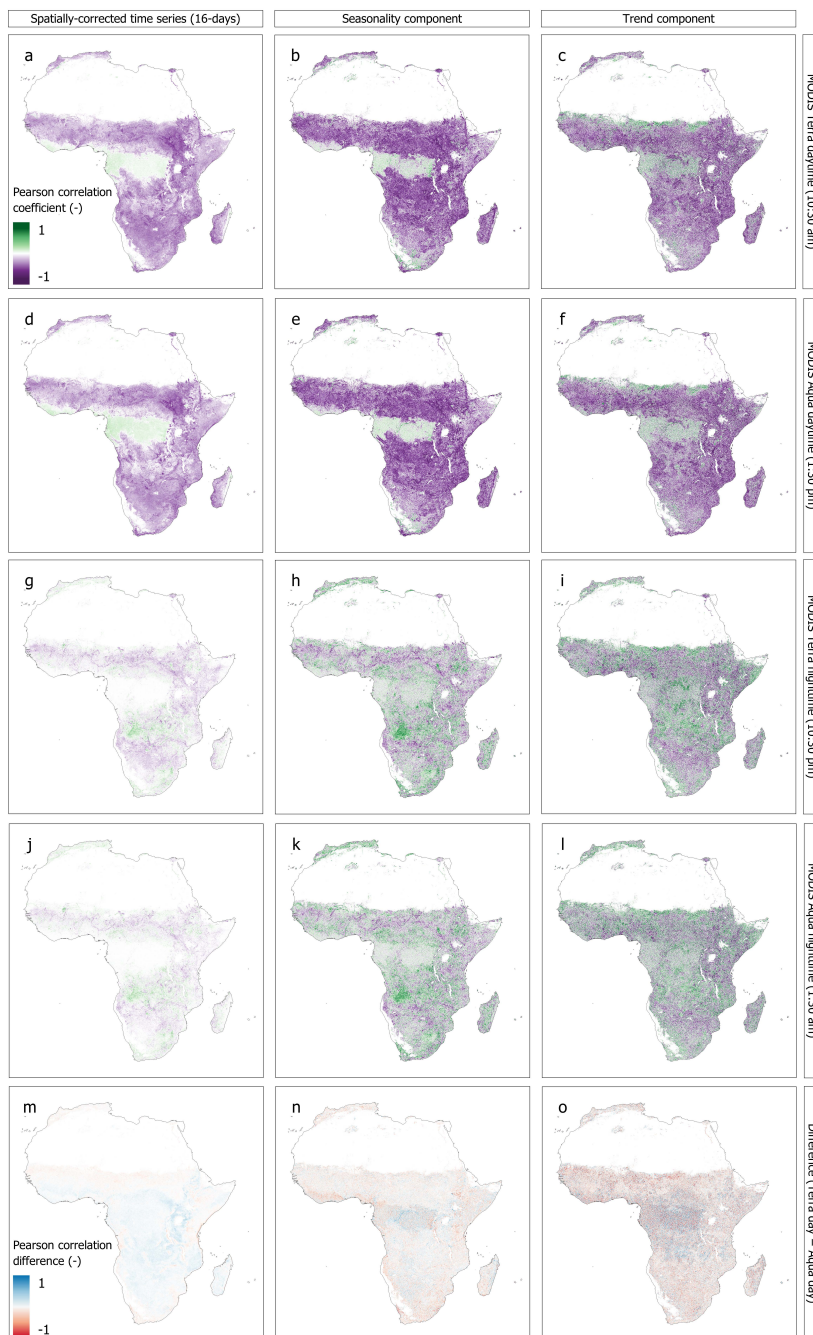
Appendix B | Supplementary Material Chapter 3



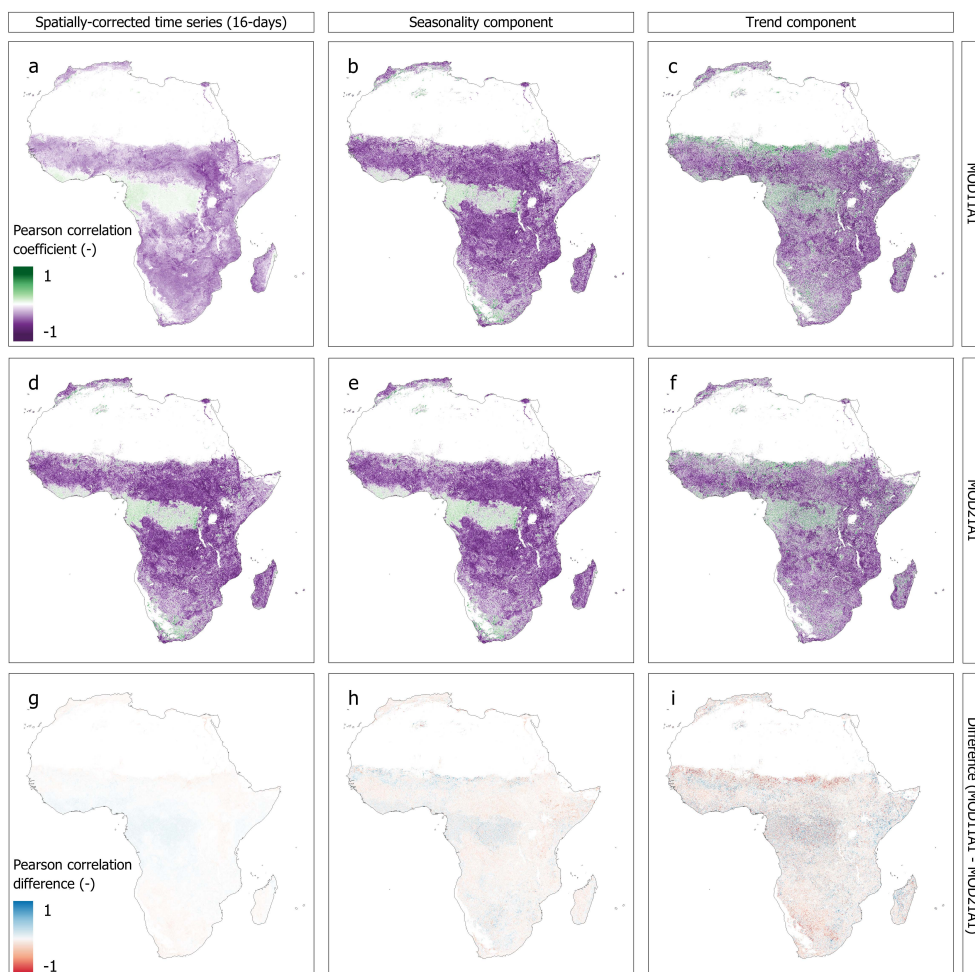
Supplementary Figure 3.1 | Input data. Median Normalized Difference Vegetation Index (NDVI) (a), land surface temperature (LST) (b) and white-sky albedo (c) over the study period. Location of WOCAT sustainable land management projects and Eddy-covariance (EC) flux tower sites (d). Aridity index and over 1970-2000 (e). Land cover in 2001 (f).



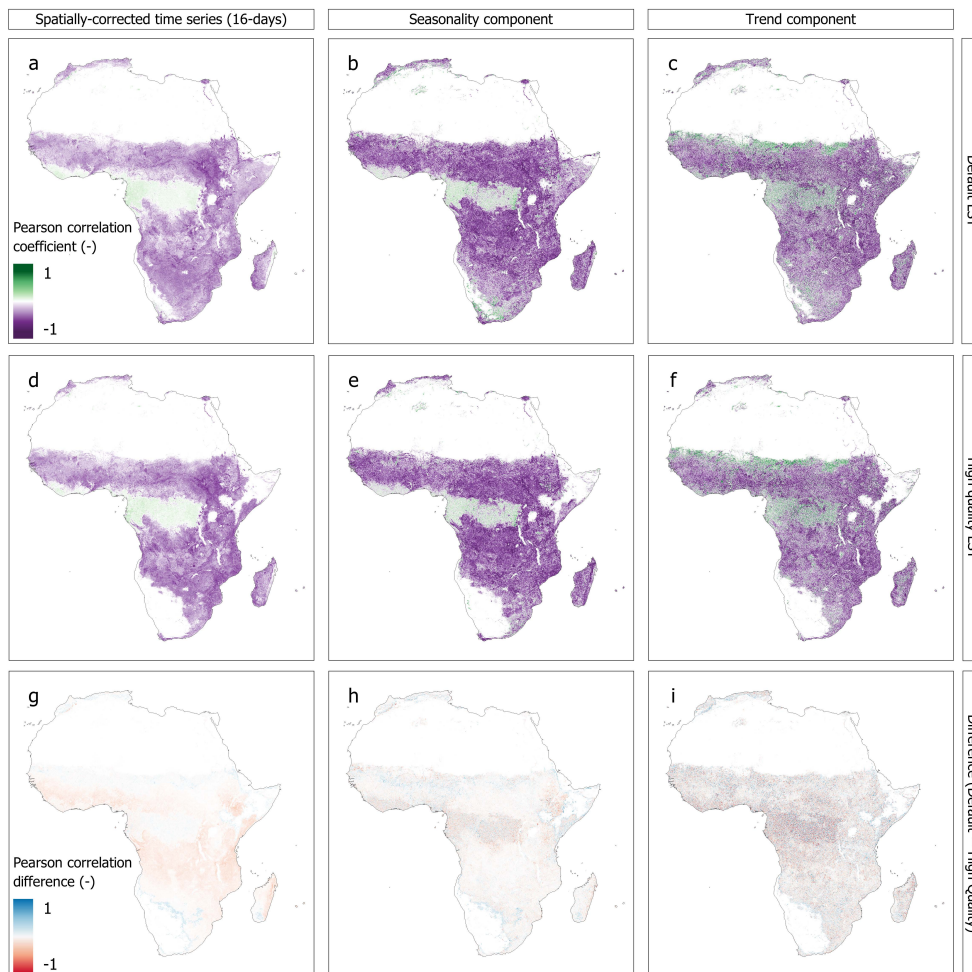
Supplementary Figure 3.2 | Effect of albedo range on NDVI-WSA correlation. The Pearson correlation coefficient between the NDVI and WSA for the shortwave broadband albedo (0.3-5.0 μm) (**a-c**), the visible broadband albedo (0.3-0.7 μm) (**d-f**) and the near-infrared broadband albedo (0.7-5.0 μm) (**g-i**) of the 16-day, seasonal and trend components.



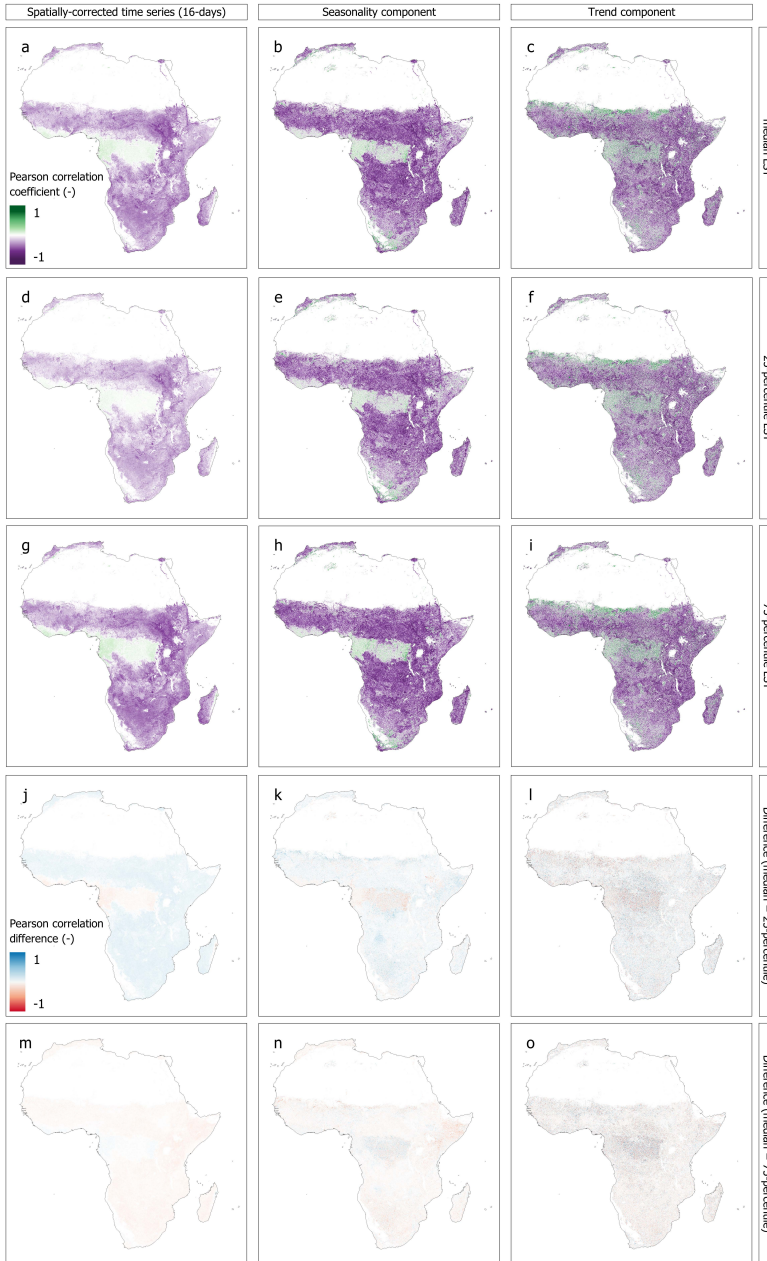
Supplementary Figure 3.3 | Effect of overpass time and algorithm on NDVI-LST correlation. The 16-day Pearson correlation coefficient between NDVI and LST for MODIS Terra day-time LST (overpass 10:30) (a-c), Aqua day-time LST (overpass 13:30) (d-f), Terra night-time (overpass 22:30) (g-i) and Aqua night-time LST (overpass 01:30) (j-l) of the 16-day, seasonal and trend components. (m-o) Difference in Pearson correlation between MODIS Terra day-time and MODIS Aqua day-time.



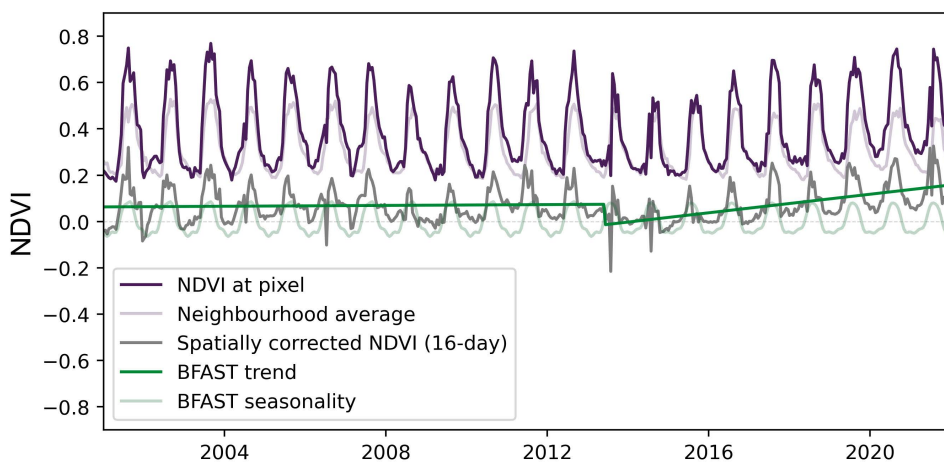
Supplementary Figure 3.4 | Effect of LST algorithm on NDVI-LST correlations. The Pearson correlation coefficient between the NDVI and LST for the MOD11A1 dataset (**a-c**) and the MOD21A1 dataset (**d-f**) of the 16-day, seasonal and trend components. (**g-i**) show the difference in Pearson correlation coefficient between the MOD11A1 dataset and the MOD21A1 dataset.



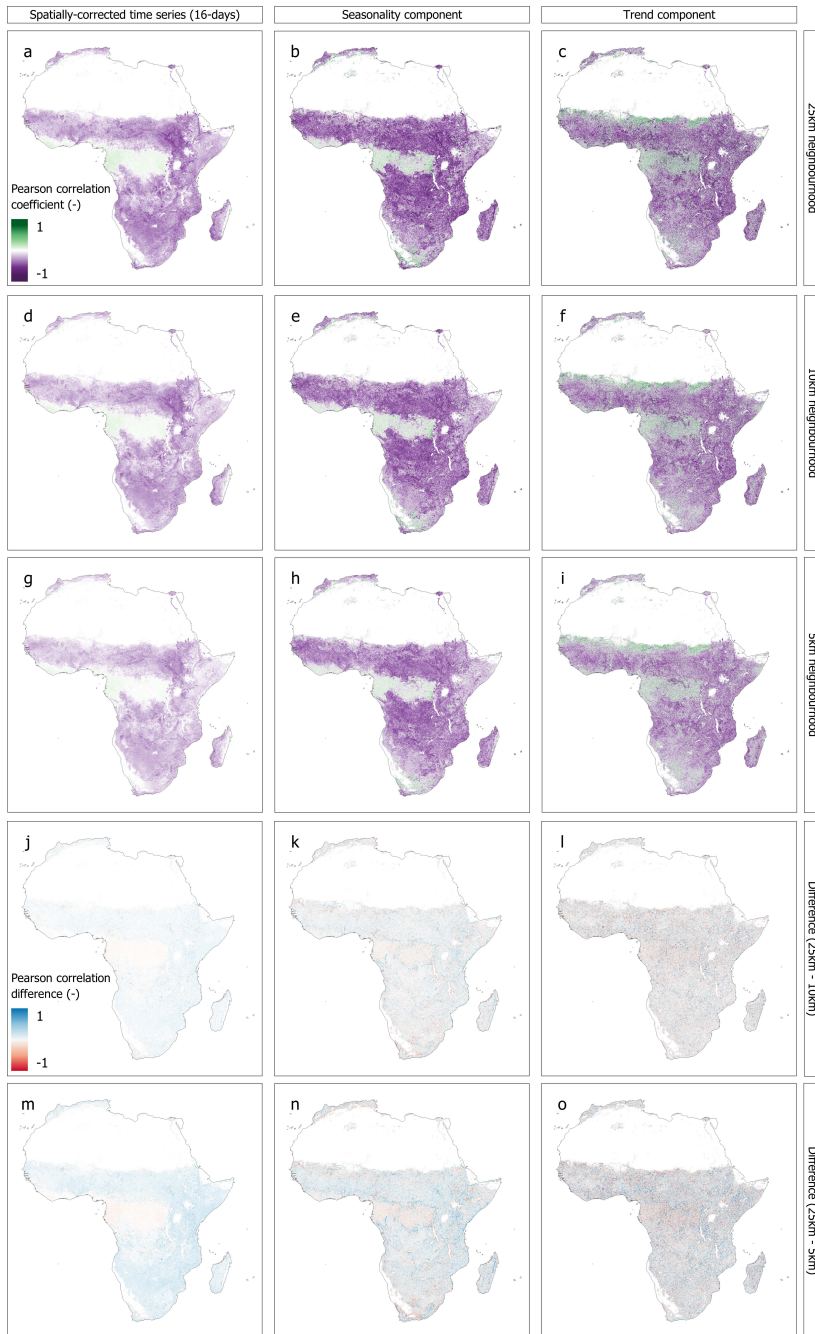
Supplementary Figure 3.5 | Effect of LST quality selection on NDVI-LST correlations. The Pearson correlation coefficient between the NDVI and LST for the uncorrected (**a-c**) and the quality corrected (**d-f**) of the 16-day, seasonal and trend components. (**g-i**) show the difference in Pearson correlation coefficient between the uncorrected dataset and the corrected dataset.



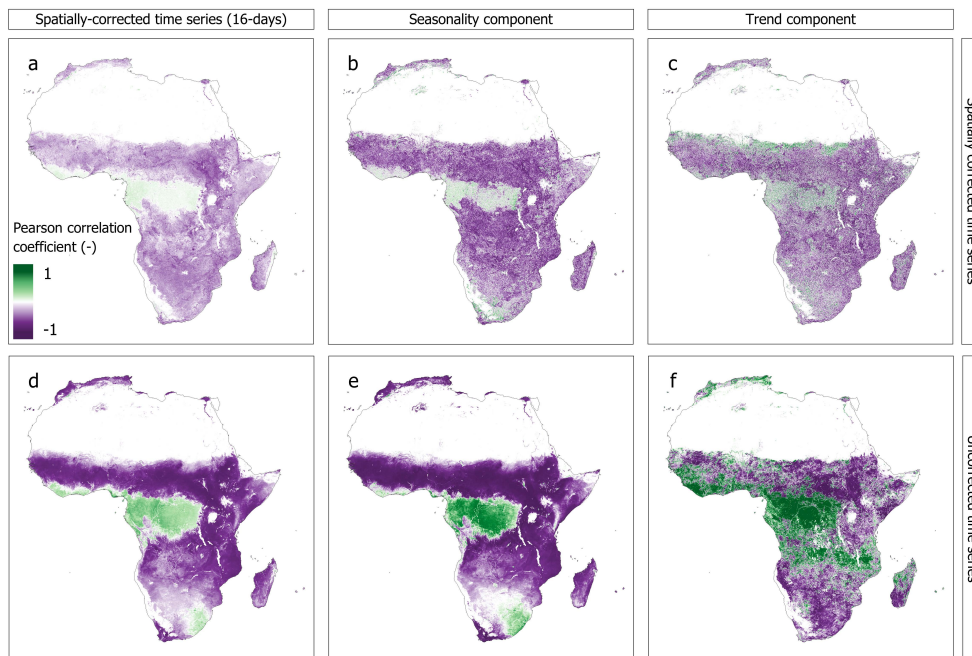
Supplementary Figure 3.6 | Effect of LST temporal downscaling on NDVI-LST correlations. The LST is downscaled to a 16-day period by taking the median value of this 16-day period. This figure shows the sensitivity of the NDVI-LST correlations to the downscaling method with: the pearson correlation coefficient between the NDVI and median LST (**a-c**), 25-percentile LST (**d-f**) and 75-percentile LST (**g-i**) of the 16-day, seasonal and trend components. (**j-l**) show the difference in pearson correlation coefficient between the median LST dataset and the 25-percentile dataset. (**m-o**) show the difference in pearson correlation coefficient between the median LST dataset and the 75-percentile dataset.



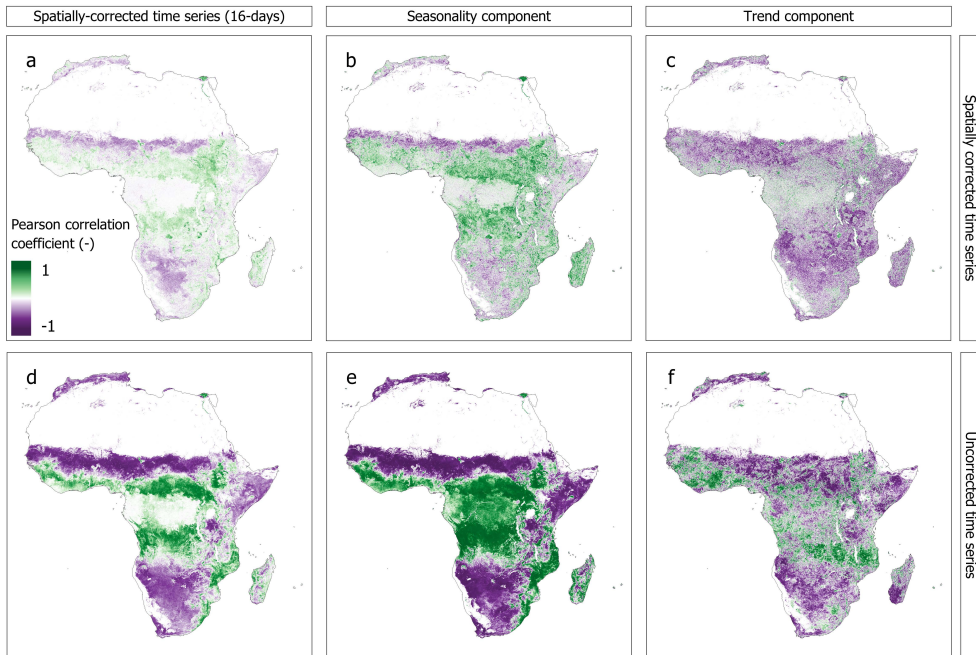
Supplementary Figure 3.7 | Visualization of spatial context method and BFAST algorithm. NDVI time series at pixel, time series averaged over a neighbourhood around the centre pixel and the spatially corrected time series (i.e. the difference between the pixel and neighbourhood NDVI). The BFAST algorithm is applied to the spatially corrected 16-day time series, resulting in a seasonality and trend component.



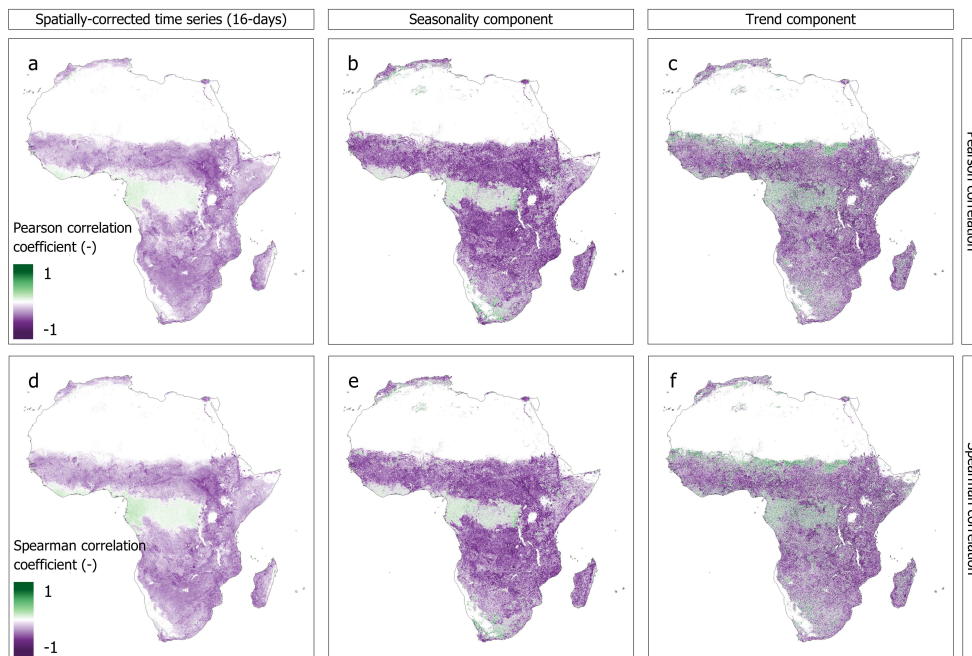
Supplementary Figure 3.8 | Effect of neighbourhood radius of spatial-context method on NDVI-LST correlations. The Pearson correlation coefficient between the NDVI and LST for a 25km neighbourhood (a-c), a 10km neighbourhood (d-f) and a 5km neighbourhood (g-i) of the 16-day, seasonal and trend components. (j-k) show the difference in Pearson correlation coefficient between a 25km and 10km radius, (m-o) between a 25km and 5km radius.



Supplementary Figure 3.9 | Effect of spatial context method on NDVI-LST correlations. The Pearson correlation coefficient between the NDVI and LST using the spatial context method (**a-c**) and the uncorrected time series (**d-f**) of the 16-day, seasonal and trend components.



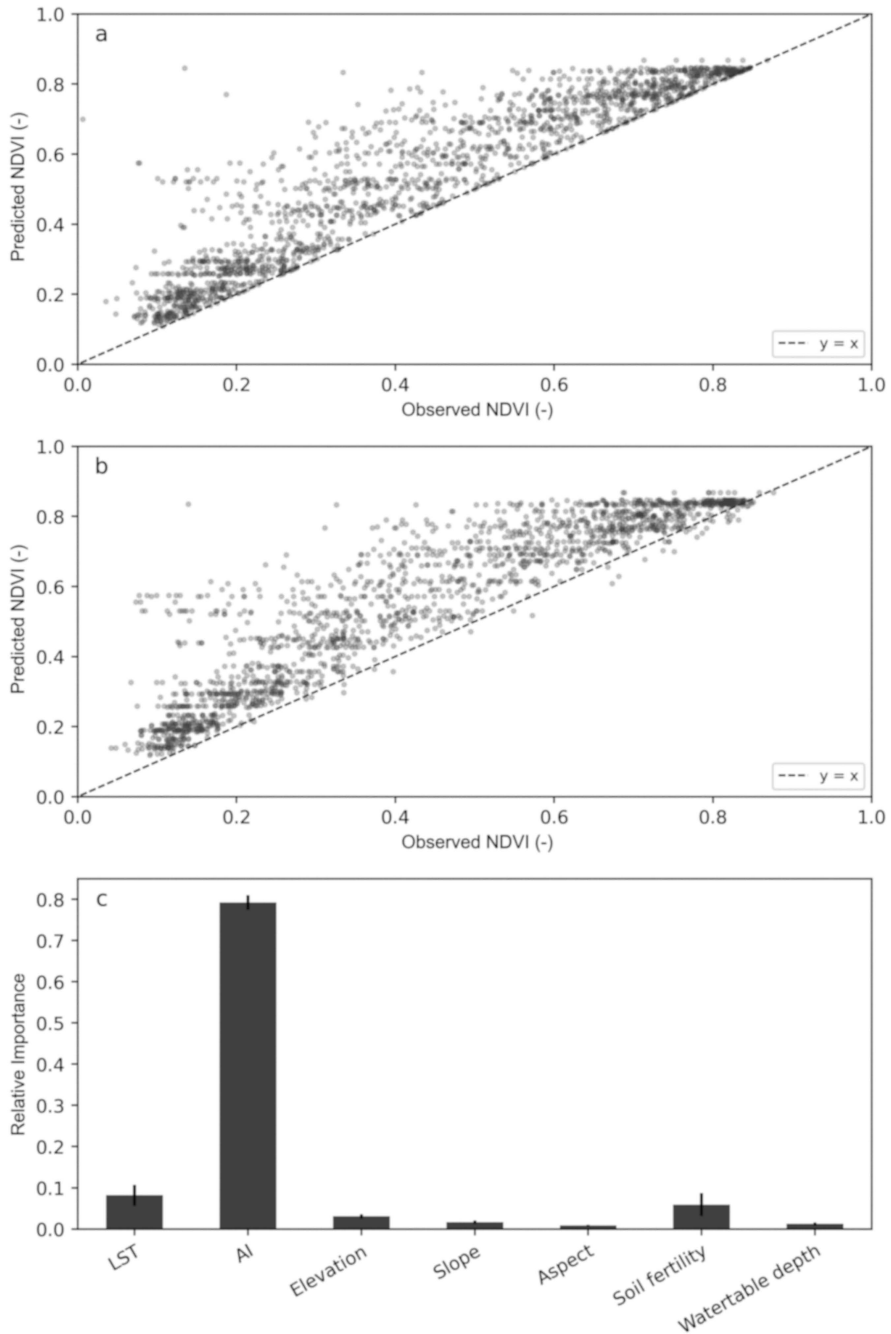
Supplementary Figure 3.10 | Effect of spatial context method on NDVI-WSA correlations. The Pearson correlation coefficient between the NDVI and WSA using the spatial context method (**a-c**) and the uncorrected time series (**d-f**) of the 16-day, seasonal and trend components.



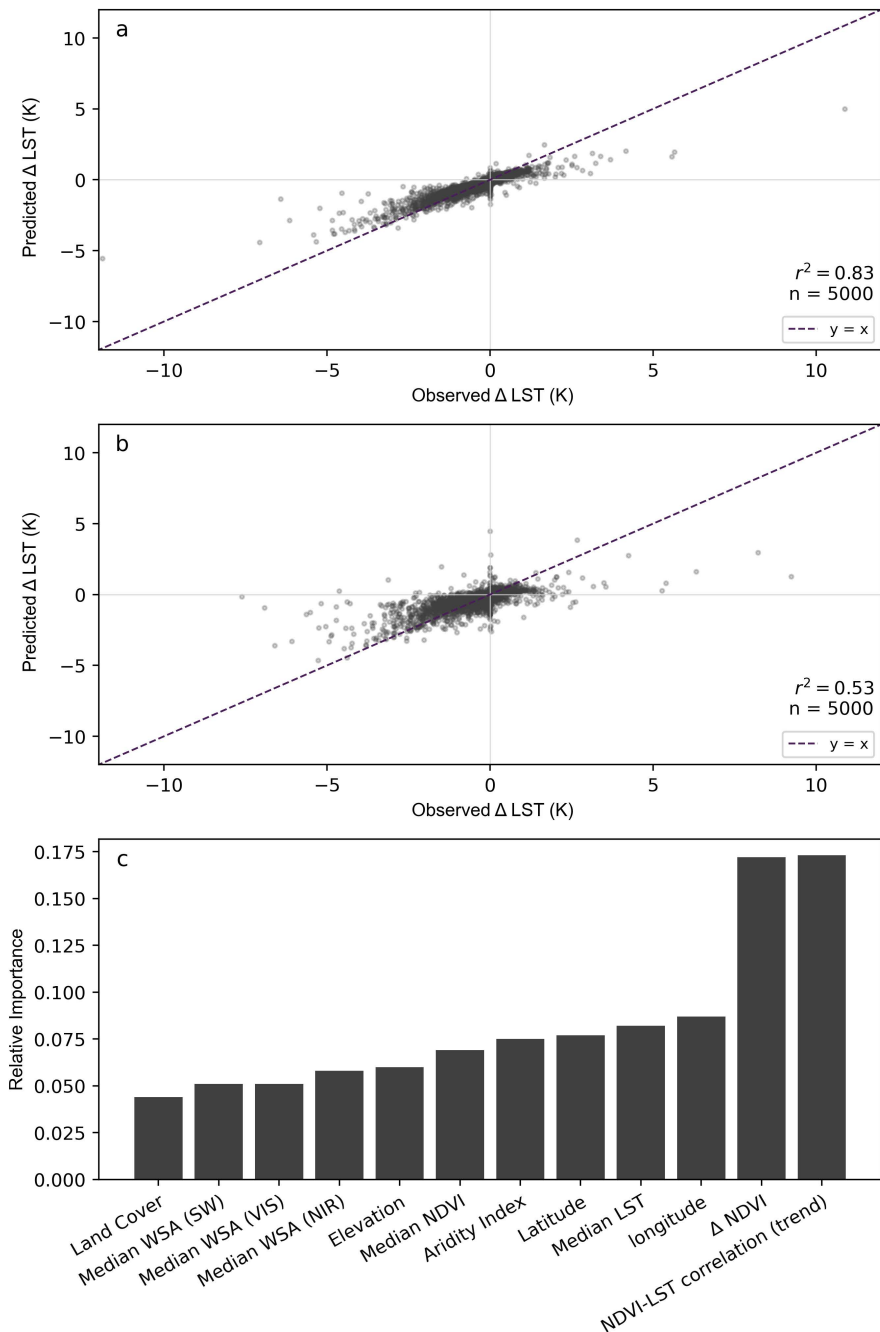
Supplementary Figure 3.11 | Effect of correlation type on NDVI-LST correlations. The Pearson (a-c) and Spearman (d-f) correlation coefficient between NDVI and LST of the 16-day, seasonal and trend components.

Supplementary Table 3.1 | Detailed information on Eddy-covariance (EC) measurement stations.

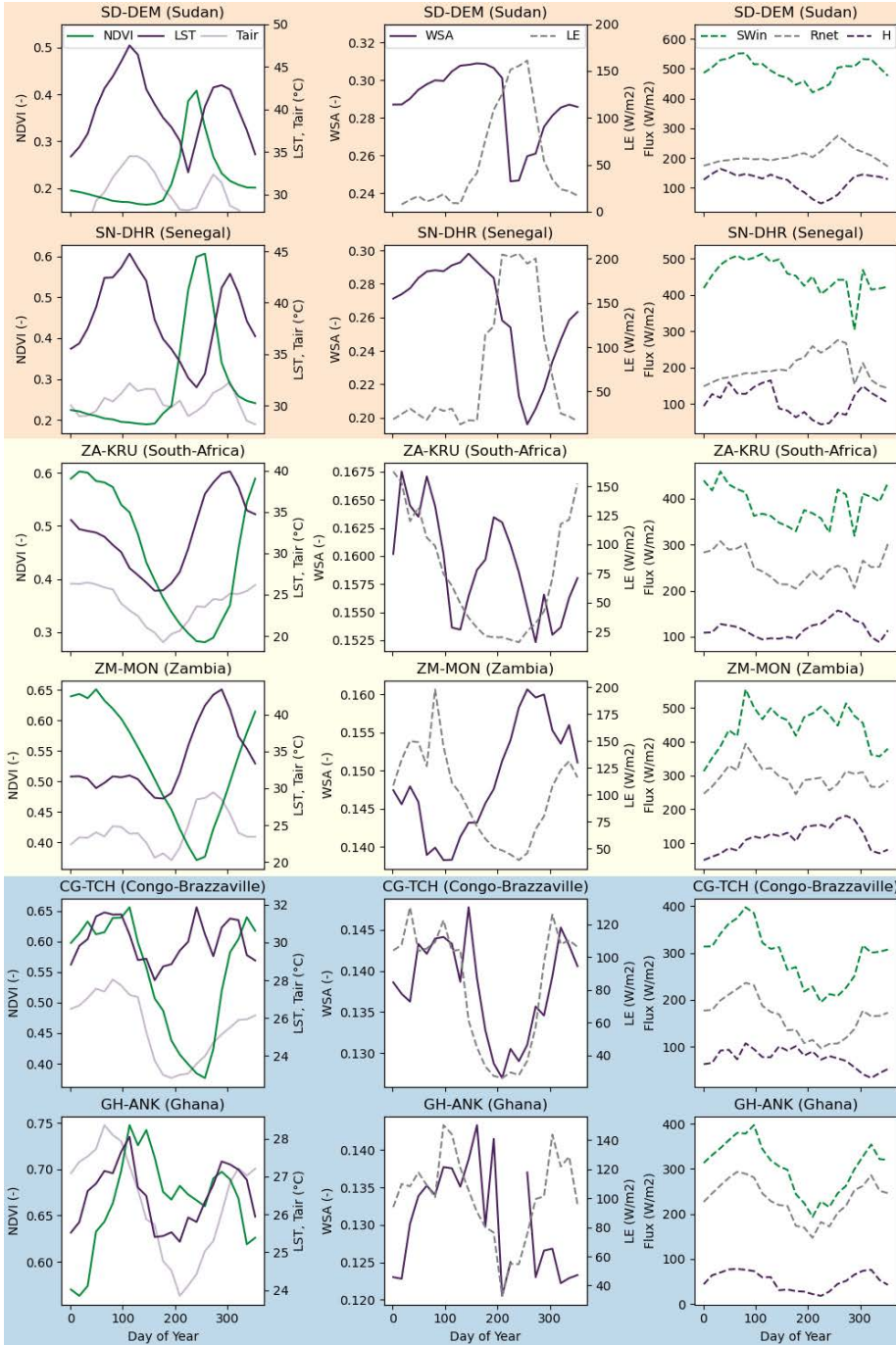
Aridity class	Station	Country	Time period included in analysis	Source	Land use
Arid	SD-Dem	Sudan	January 2005 – December 2008	Ardö et al. (2008)	Savannas
Arid	SN-DHR	Senegal	July 2010 – December 2012	Tagesson et al. (2015)	Savannas
Semi-arid	ZA-KRU	South-Africa	January 2001 – December 2013	Archibald et al. (2009)	Savannas
Semi-arid	ZM-MON	Zambia	September 2007 – December 2008	Merbold et al. (2009)	Deciduous broadleaf forest
Humid	CG-TCH	Congo-Brazzaville	September 2006 – December 2008	Merbold et al. (2009)	Savannas
Humid	GH-ANK	Ghana	January 2011 – December 2013	Chiti et al. (2010)	Evergreen broadleaf forest



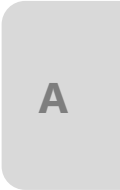
Supplementary Figure 3.12 | Evaluation of potential NDVI quantile random forest regression. Observed vs prediction NDVI of training data set (a) and validation data set as calculated with the maximum random forest regression (b). Relative variable importance of maximum random forest regression, defined as the mean decrease in impurity (c).

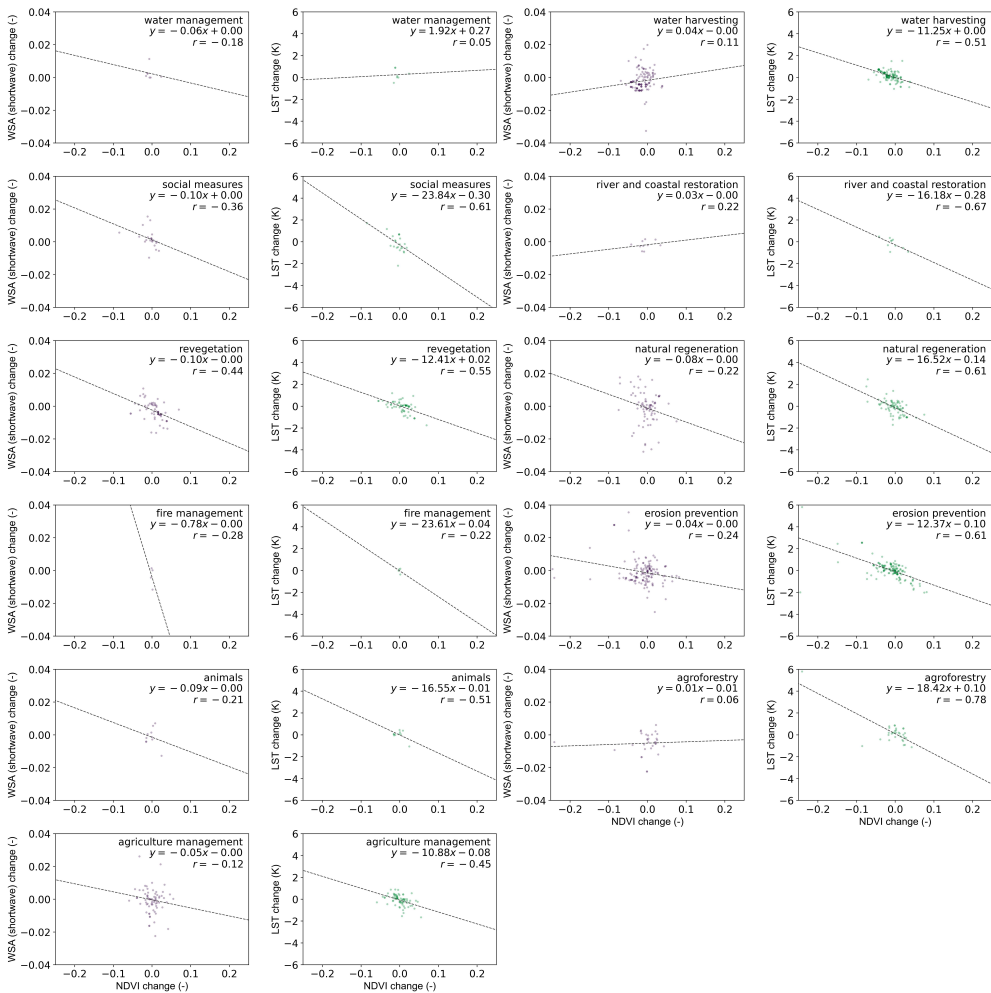


Supplementary Figure 3.13 |Evaluation of Δ LST/ Δ NDVI random forest regression. Observed vs prediction Δ LST/ Δ NDVI of training data set (a) and validation data set as calculated with the random forest regression (b). Relative variable importance of random forest regression, defined as the mean decrease in impurity(c).

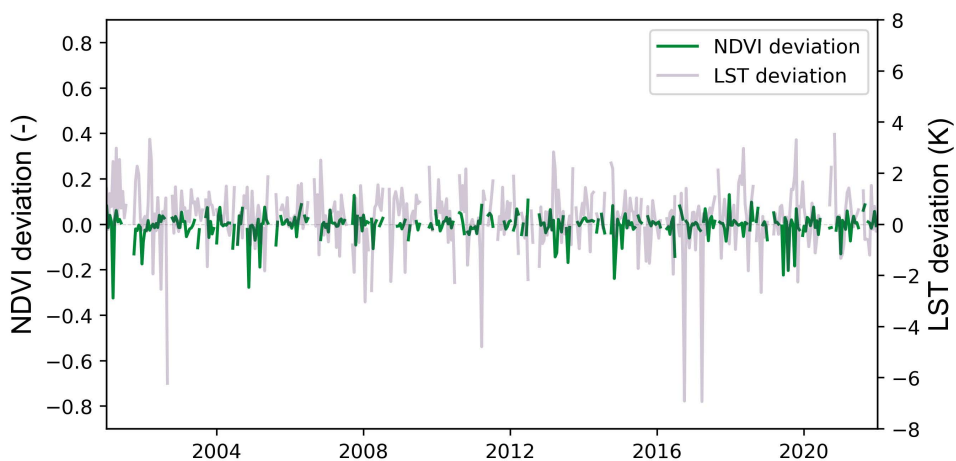


Supplementary Figure 3.14 | Eddy-covariance measurements at different locations in Africa. Mean uncorrected NDVI, LST, WSA, air temperature (Tair), latent heat flux (LE), sensible heat flux (H) and Net available radiation (Rnet) for each day of the year. LST is converted to °C to match Tair.

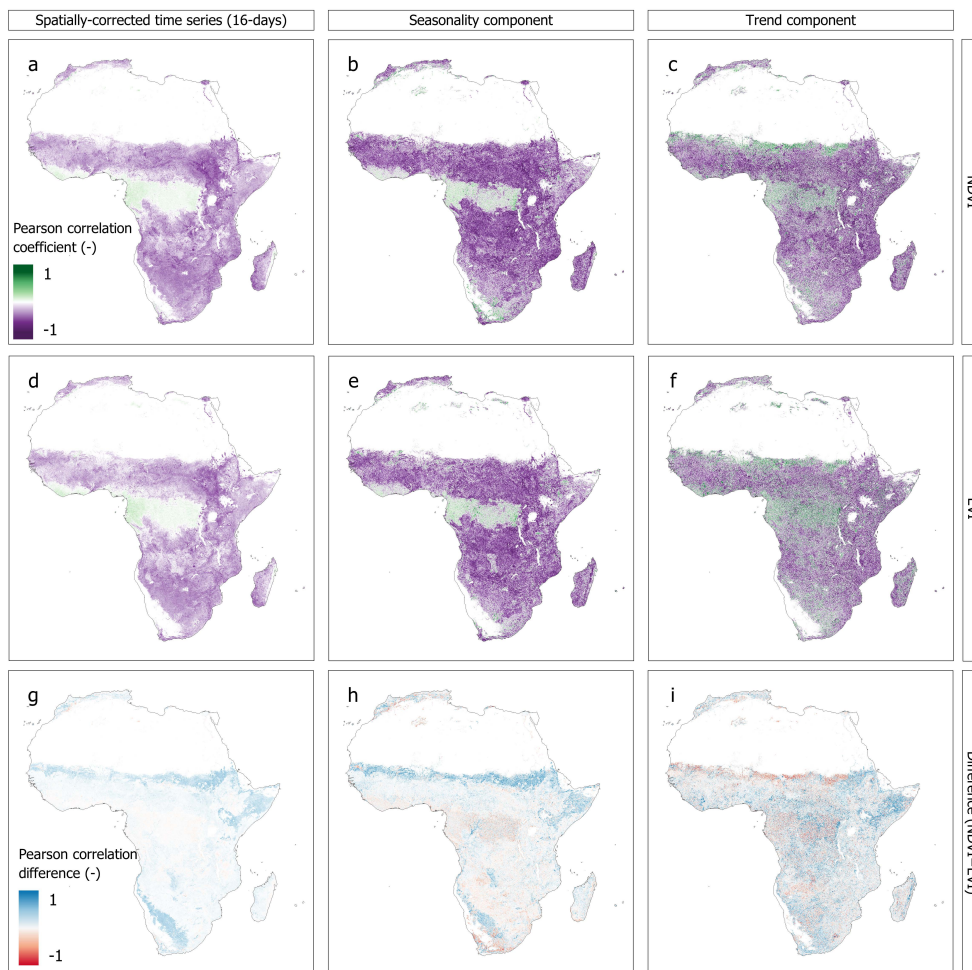




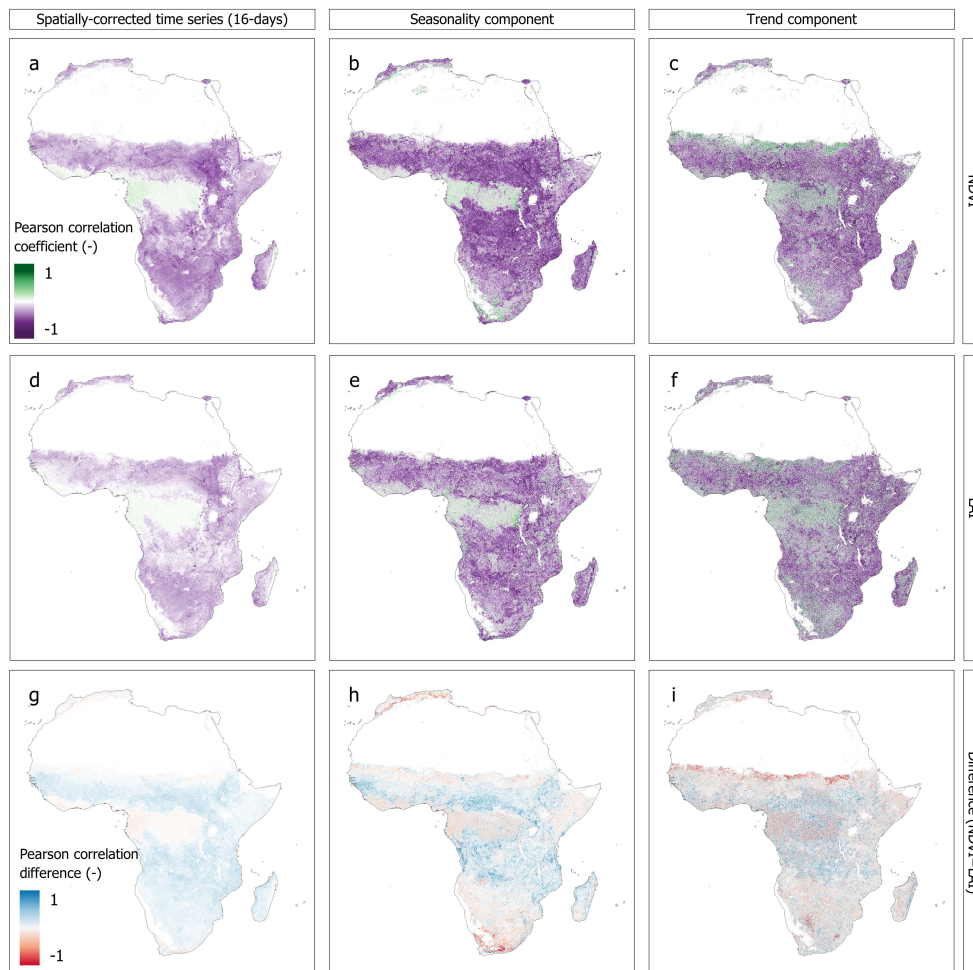
Supplementary Figure 3.15 | Effect of SLM type on NDVI-WSA and NDVI-LST relations. Relation between median change in trend component of the NDVI and WSA (purple) and the NDVI and LST (green) for different types of sustainable land management projects. The projects were classified based on their provided description. Strongest NDVI-WSA correlations are found for revegetation. Strongest NDVI-LST correlations are found for agroforestry. It should be noted that not all project types have the same number of projects.



Supplementary Figure 3.16 | Time series of NDVI and LST deviation. The spatially corrected NDVI and LST time series at 15.2°E, 1.77°N (Republic of the Congo). This time series is illustrative of humid regions, where there are large amounts of noise in the time series data.

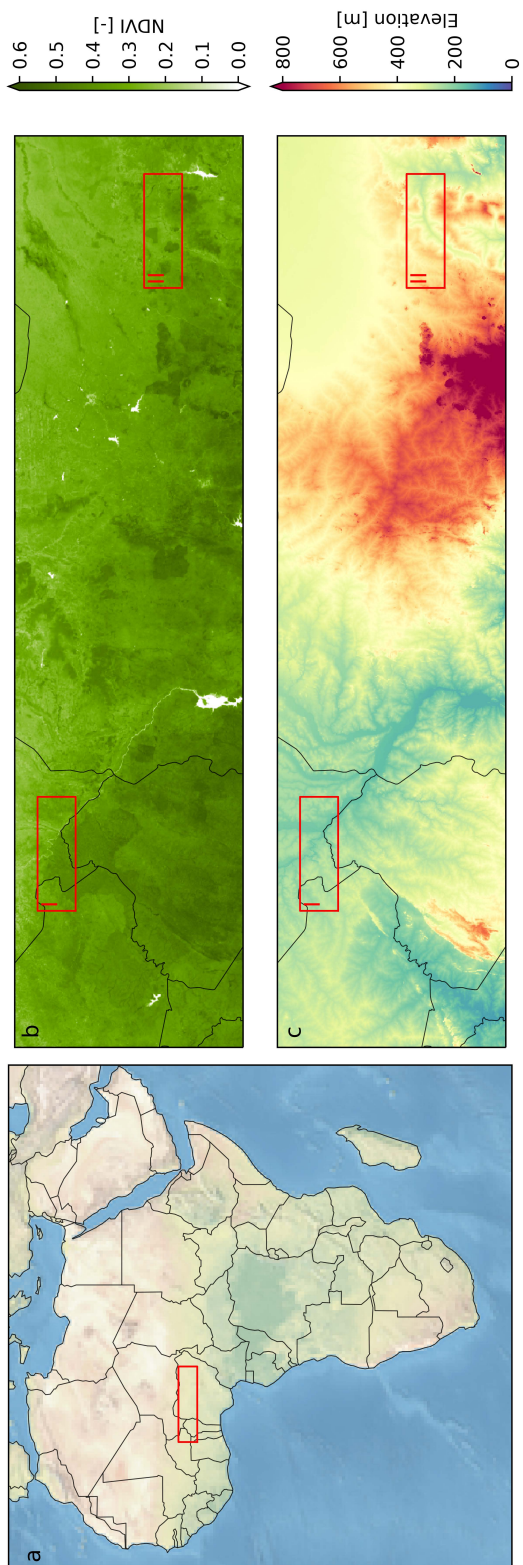


Supplementary Figure 3.17 | Effect of input data on NDVI-LST and EVI-LST correlations. The Pearson correlation coefficient between the NDVI and LST spatially corrected time series (**a-c**) and between the EVI and LST spatially corrected time series (**d-f**) of the 16-day, seasonal and trend components. (**g-i**) show the difference in Pearson correlation coefficient between the NDVI and EVI dataset (EVI subtracted from NDVI).

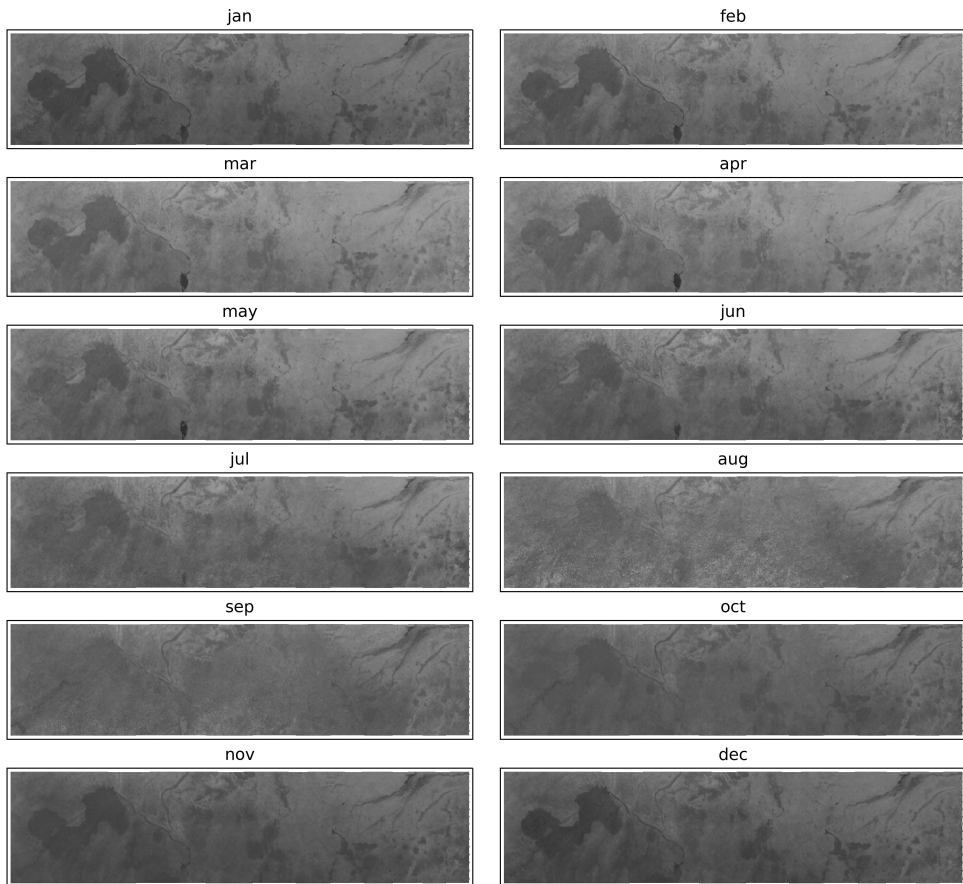


Supplementary Figure 3.18 | Effect of input data on NDVI-LST and LAI-LST correlations. The Pearson correlation coefficient between the NDVI and LST spatially corrected time series (**a-c**) and between the LAI and LST spatially corrected time series (**d-f**) of the 16-day, seasonal and trend components. (**g-i**) show the difference in Pearson correlation coefficient between the NDVI and LAI dataset (LAI subtracted from NDVI).

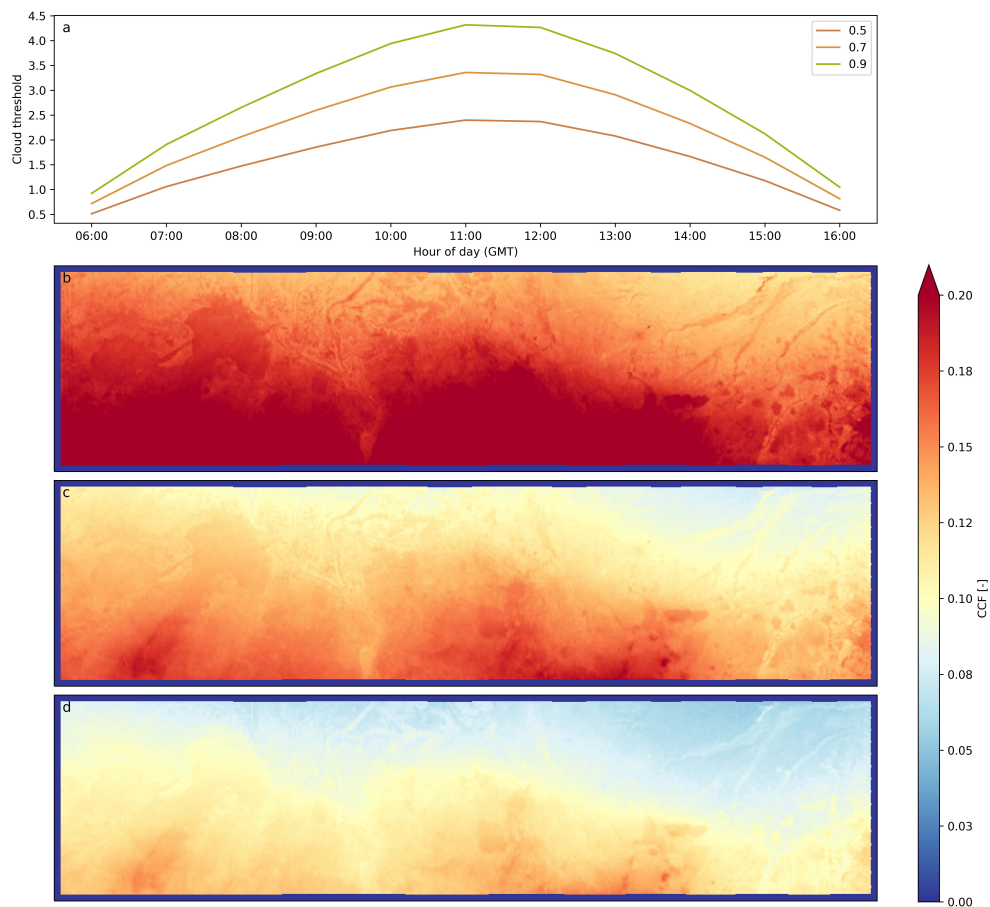
Appendix C | Supplementary Material Chapter 4



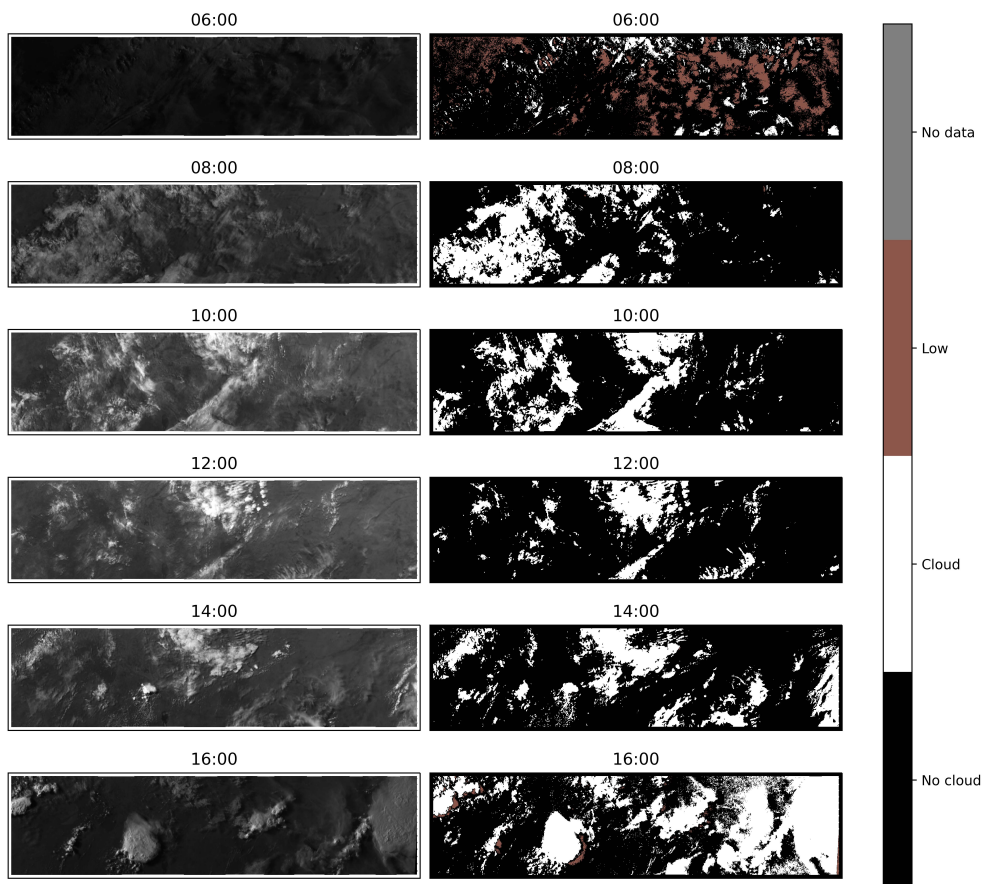
Supplementary Figure 4.1 | Locations of study region and subregions. Location of the study regions within Africa is indicated with the red box (a). Annual mean NDVI between 2004/01/01 and 2024/01/01 (b) and the elevation (c) within the study region. Locations of subregion I and subregion II are indicated with red boxes (b, c).



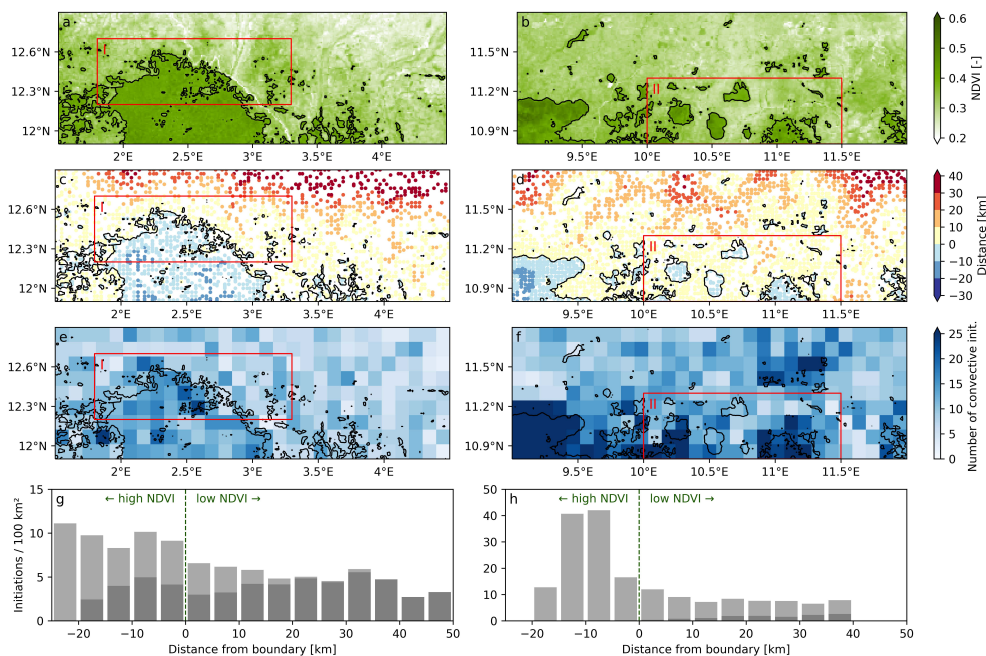
Supplementary Figure 4.2 | Clear-sky reflectance. Monthly (January – December) evolution of the clear-sky reflectance within the study region.



Supplementary Figure 4.3 | Calibration of HRV algorithm. Diurnal variation of cloud threshold (a) and overall cloud cover frequency (CCF) with a threshold of 0.5 (b), 0.7 (c) and 0.9 (d) within the case study area.



Supplementary Figure 4.4 | HRV cloud mask. HRV image (**left**) and HRV cloud mask (**right**) at 06:00, 08:00, 10:00, 12:00, 14:00 and 16:00 UTC 2018/05/14. Values of 'Low' indicate that the differences between the clear-sky reflectance and HRV image are higher than the threshold.



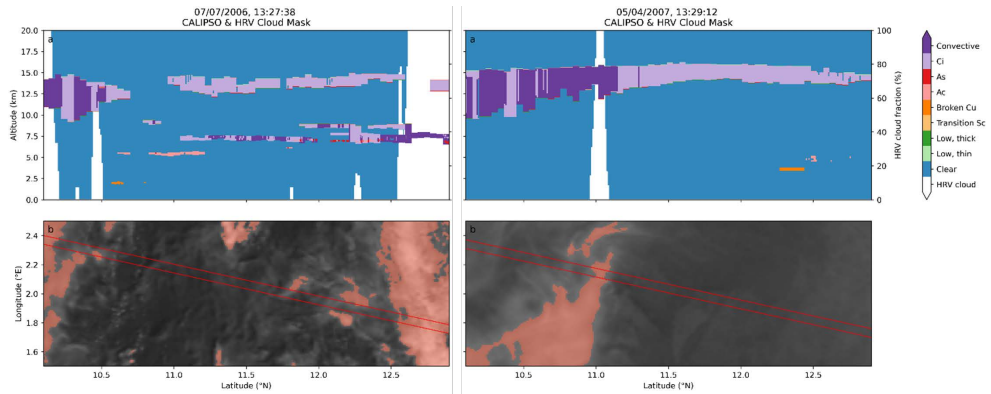
Supplementary Figure 4.5 | Convective Initiation and vegetation. Mean annual Normalized Difference Vegetation Index (NDVI) (a, b), locations of individual convective initiations (c, d) and total number of convective initiations gridded with a resolution of 0.11 degree (~ 12.3 km) (e, f) between 2004 and 2023 in Subregion I (left) and Subregion II (right). Black lines indicate the contours where the mean NDVI is 0.38, to distinguish between high and low vegetation areas. The colours in (c, d) show the distance to this contour. (g) and (h) show the number of convective initiations per distance to the NDVI contour boundary, relative to the total area with the same distance to the boundary. The lighter shades of grey in (h) include points of convective initiation over regions with topographical differences higher than 100 m over a distance of 25 km in all directions. The histograms in (g) and (h) are based on 2,389 and 3,952 moments of convective initiation, respectively. Negative (positive) distances indicate that the NDVI is higher (lower) than 0.38. The data includes convective initiations between 10:00 and 16:30 UTC over all months of the year (Similar to Figure 4.6, but with a 100 m topography threshold).

Supplementary Table 4.1 | Comparison of HRV cloud mask to CALIPSO. HRV cloud occurrences are derived from fractional cloud cover (FCC) within the CALIPSO scanning line, with clear ($FCC < 10\%$), partly clouded ($10\% < FCC < 90\%$) and clouded ($FCC > 90\%$). CALIPSO clouds are derived from the Vertical Feature Mask, where low overcast (transparent), transition stratocumulus, altostratus and cirrus types are classified as transparent clouds. Low overcast, low broken cumulus, altostratus and deep convective cloud types are classified as opaque clouds. The cloud types are aggregated over the altitude, selecting the most opaque cloud type. The values include all grid cells over all timesteps. Values are used for the verification in Supplementary Table 4.2.

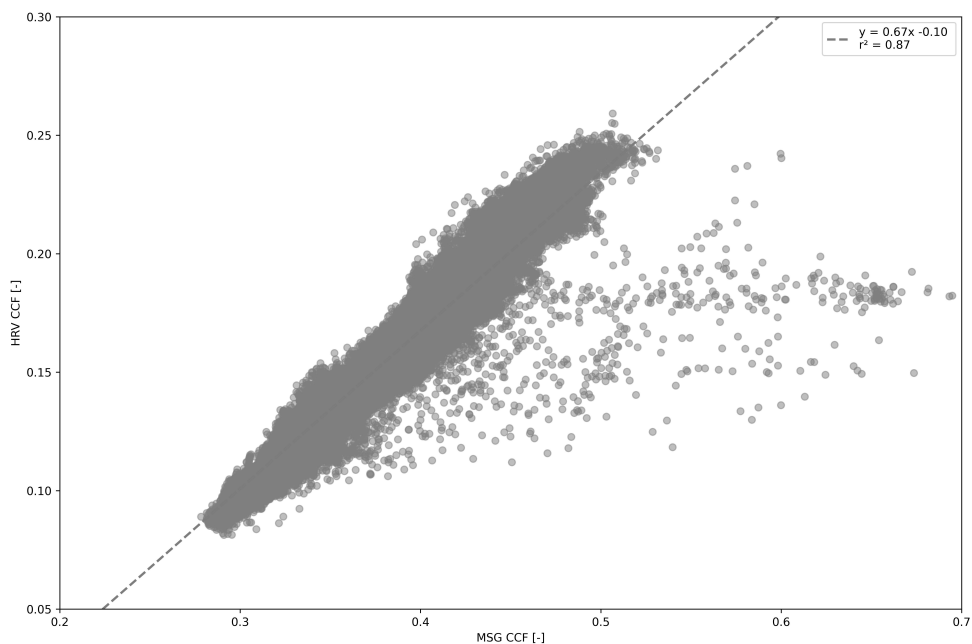
CALIPSO HRV	Clear + transparent clouds	Opaque clouds	Total
Clear	62756 (correct negatives)	16881 (misses)	79637
(Partly) clouded	1123 (false alarms)	9272 (hits)	10395
Total	63879	26153	90032

Supplementary Table 4.2 | Verification of HRV cloud mask to CALIPSO. Different methods, scores, perfect scores and descriptions of the accuracy of the HRV cloud mask compared to the CALIPSO cloud mask.

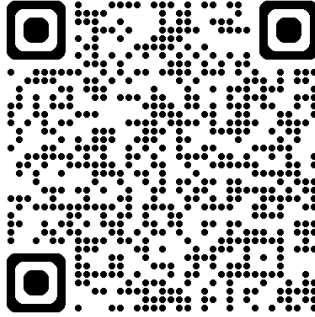
	Score	Perfect	Description
Accuracy	80.0%	100%	Overall, what fraction of the HRV classification is correct?
Frequency bias	39.7%	100%	How did the HRV frequency of "clouded" events compare to the CALIPSO frequency of "opaque clouds" events?
Probability of detection	35.5%	100%	What fraction of the HRV "clouded" events were correct compared to CALIPSO?
Probability of false detection	1.8%	0%	What fraction of the HRV "clear" events were incorrectly classified as "opaque clouds"?
False alarm ratio	10.8%	0%	What fraction of the HRV "clouded" event were "clear" in CALIPSO?
Success ratio	89.2%	100%	What fraction of the HRV "clouded" events were correctly classified?
Threat score	34.0%	100%	How well did the HRV "clouded" events correspond to the CALIPSO "opaque clouds" events?
Equitable threat score	25.8%	100%	How well did the HRV "clouded" events correspond to the CALIPSO "opaque clouds" (accounting for hits due to chance)?
Hanssen and Kuipers discriminant	33.7%	100%	How well did HRV separate the "clouded" events from the "clear" events?



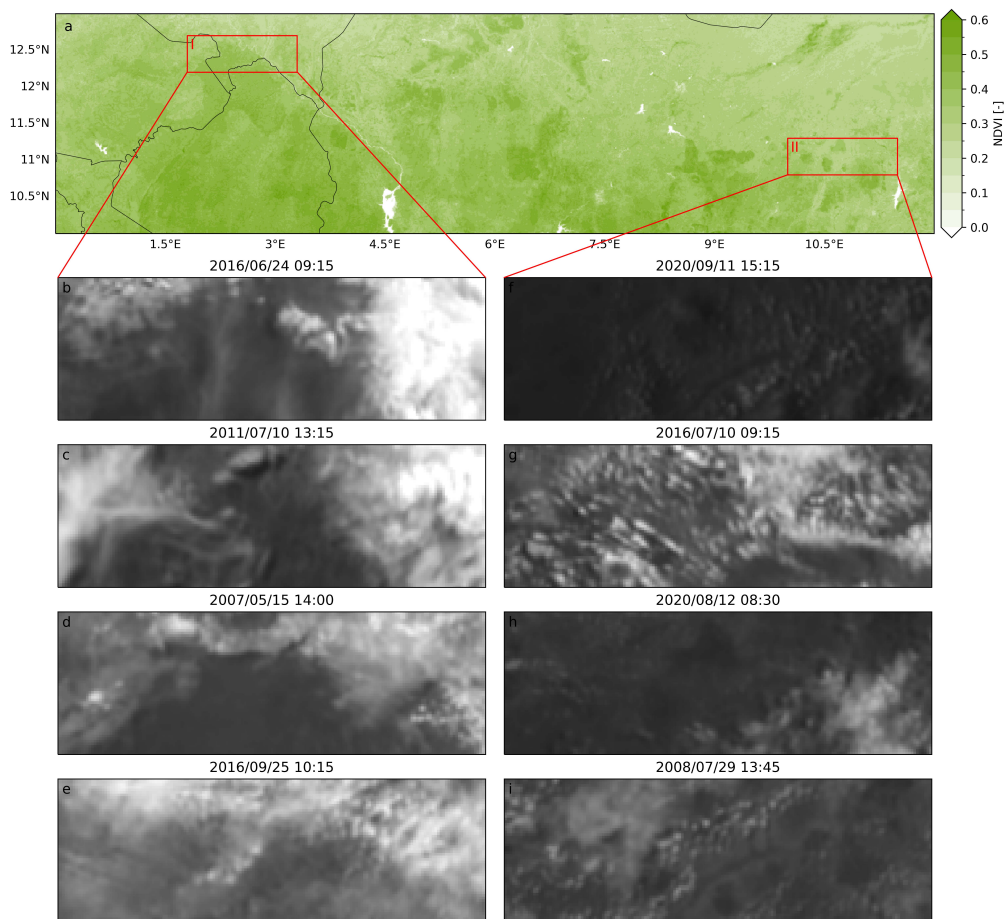
Supplementary Figure 4.6 | Validation based on CALIPSO Vertical Feature Mask (VFM). The cloud type profiles on 07/07/2006 (**left**) and 05/04/2007 (**right**). The colours indicate different cloud types where Low, thin=low overcast (transparent), Low, thick=low overcast (opaque), Transition Sc=transition stratocumulus, Broken Cu=low, broken cumulus, Ac=altocumulus (transparent), As=altostratus (opaque), Ci=cirrus (transparent) and Convective=deep convective (opaque). The corresponding scanning line (red lines), HRV cloud mask (red shading) and HRV image are shown in bottom figures. The figure shows that CALIPSO generally has a lower threshold for opaque cloud detection than HRV.



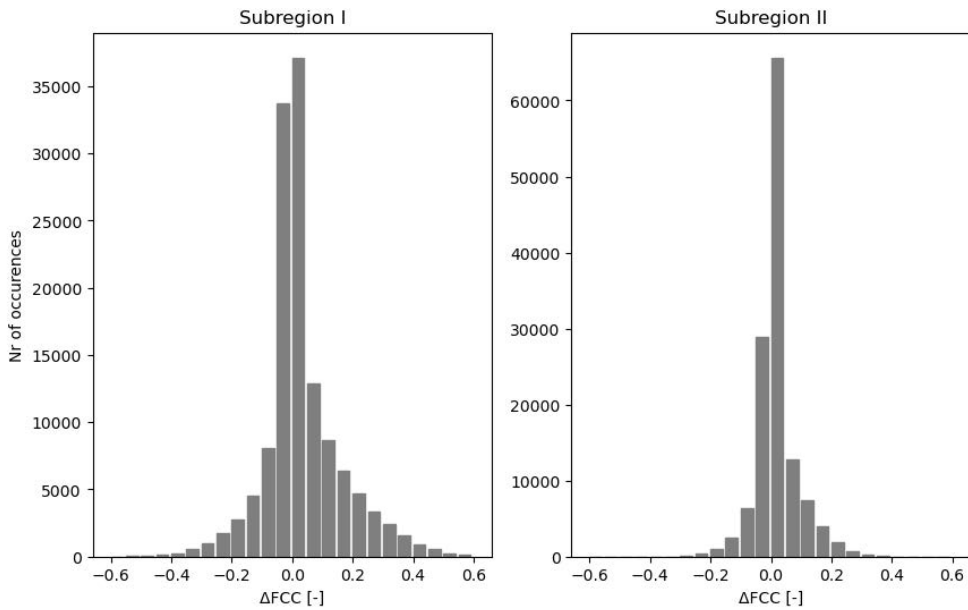
Supplementary Figure 4.7 | Spatial validation of cloud cover frequency. Spatial comparison between MSG cloud cover frequency (CCF) and HRV CCF. The 1 km HRV CCF is downscaled to the 3 km MSG CCF using a nearest neighbourhood interpolation. The dotted line indicates a linear fit between the two variables, with a coefficient of determination (r^2) of 0.87.



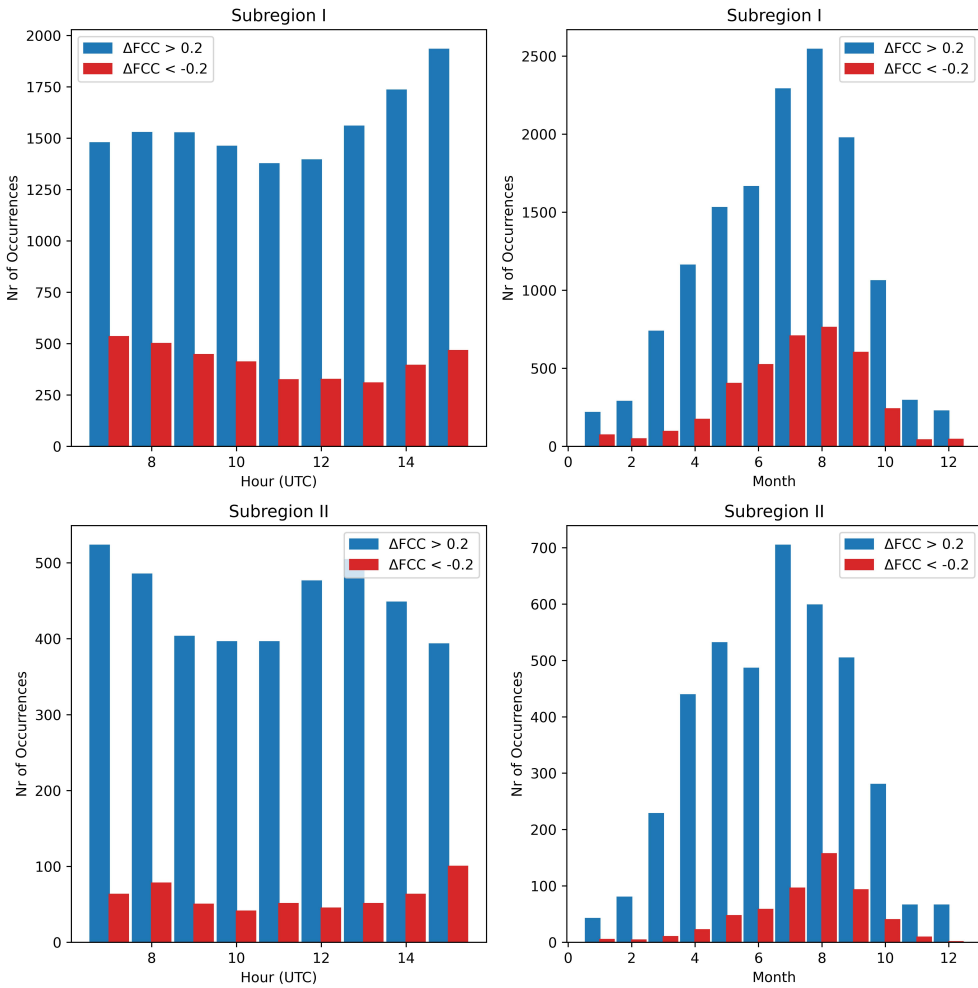
Supplementary Animation 4.1-4.8 | Cloud development over subregions. Animations of HRV images during specific days that show high contrast in cloud development between areas with high and low vegetation. Days correspond to Figure 4.2b-4.2i. Animations are available through the link or QR code below.



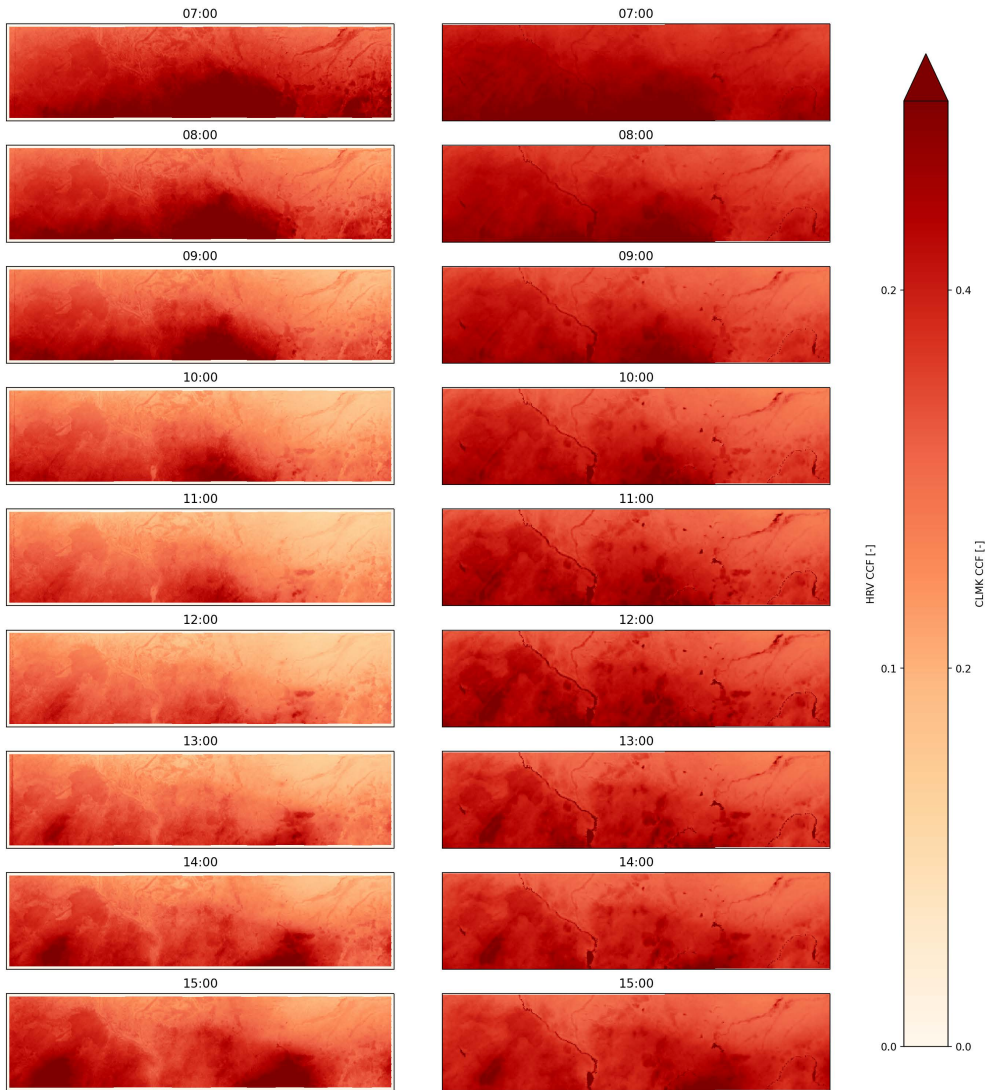
Supplementary Figure 4.8 |Vegetation and cloud development. Yearly mean NDVI between 2004/01/01 and 2024/01/01 in the study region (a). MSG HRV snapshots for subregion I (b-e) and subregion II (f-i) as indicated by the red boxes in (a).



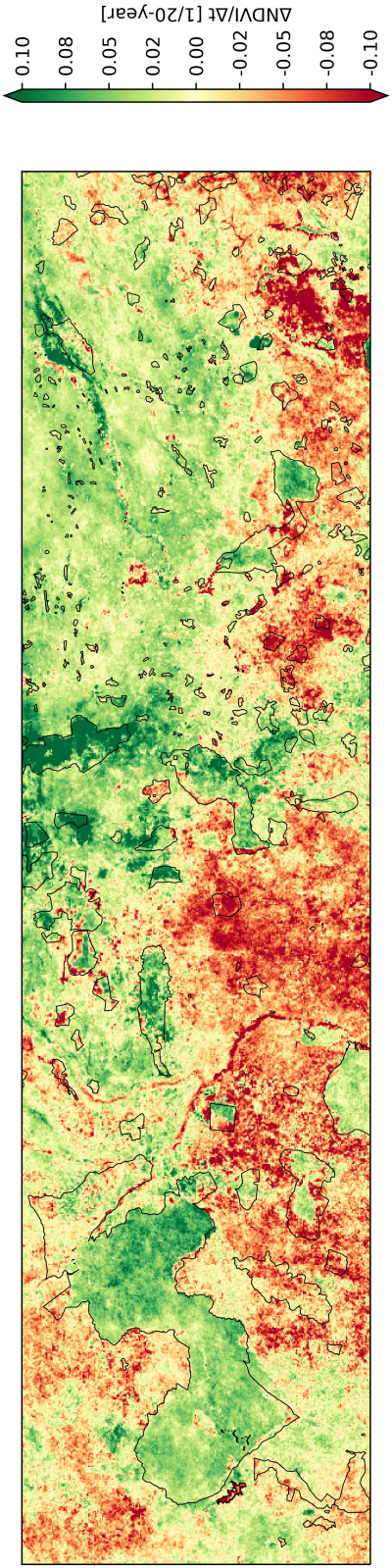
Supplementary Figure 4.9 | Distribution of difference in cloud cover frequency. Number of occurrences per difference in fractional cloud cover (ΔFCC) between green and less green areas in Subregion I (**left**) and II (**right**). In Subregion I (II), 30.1% (30.3%) of the values is positive and 20.1% (21.4%) is negative. The occurrences where ΔFCC is 0 (49.7% in Subregion I and 47.2% in Subregion II) are not included in the histogram. For both subregions, positive values are significantly more frequent than negative values ($p < 0.05$, using a binomial test) and positively skewed.



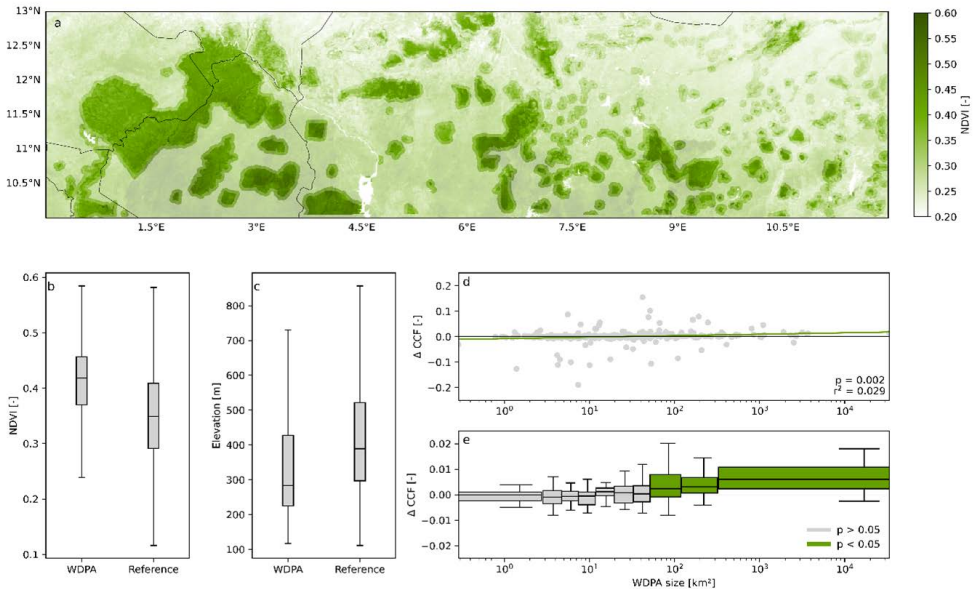
Supplementary Figure 4.10 | Characteristic hours and months of high differences in fractional cloud cover. Number of occurrences for each hour of the day between 07:00 and 15:00 UTC (**left**) and month of the year (**right**) for differences in fractional cloud cover (ΔFCC) lower than -0.2 (**red**) and higher than 0.2 (**blue**) within Subregion I (**top**) and Subregion II (**bottom**). Differences are calculated between green regions ($NDVI > 0.38$) and less green regions ($NDVI < 0.38$).



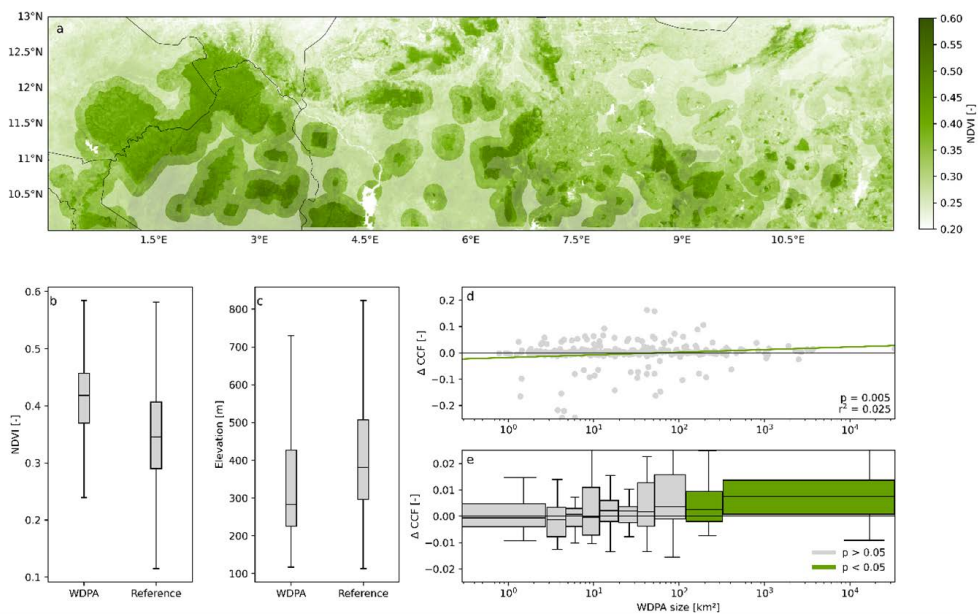
Supplementary Figure 4.11 | Diurnal validation. Hourly HRV cloud cover frequency (HRV CCF) (**left**) and MSG cloud cover frequency (CLMK CCF) (**right**). Cloud cover frequency values are calculated with all available (year-round) cloud mask within the specific hour. Note the scale difference between left and right.



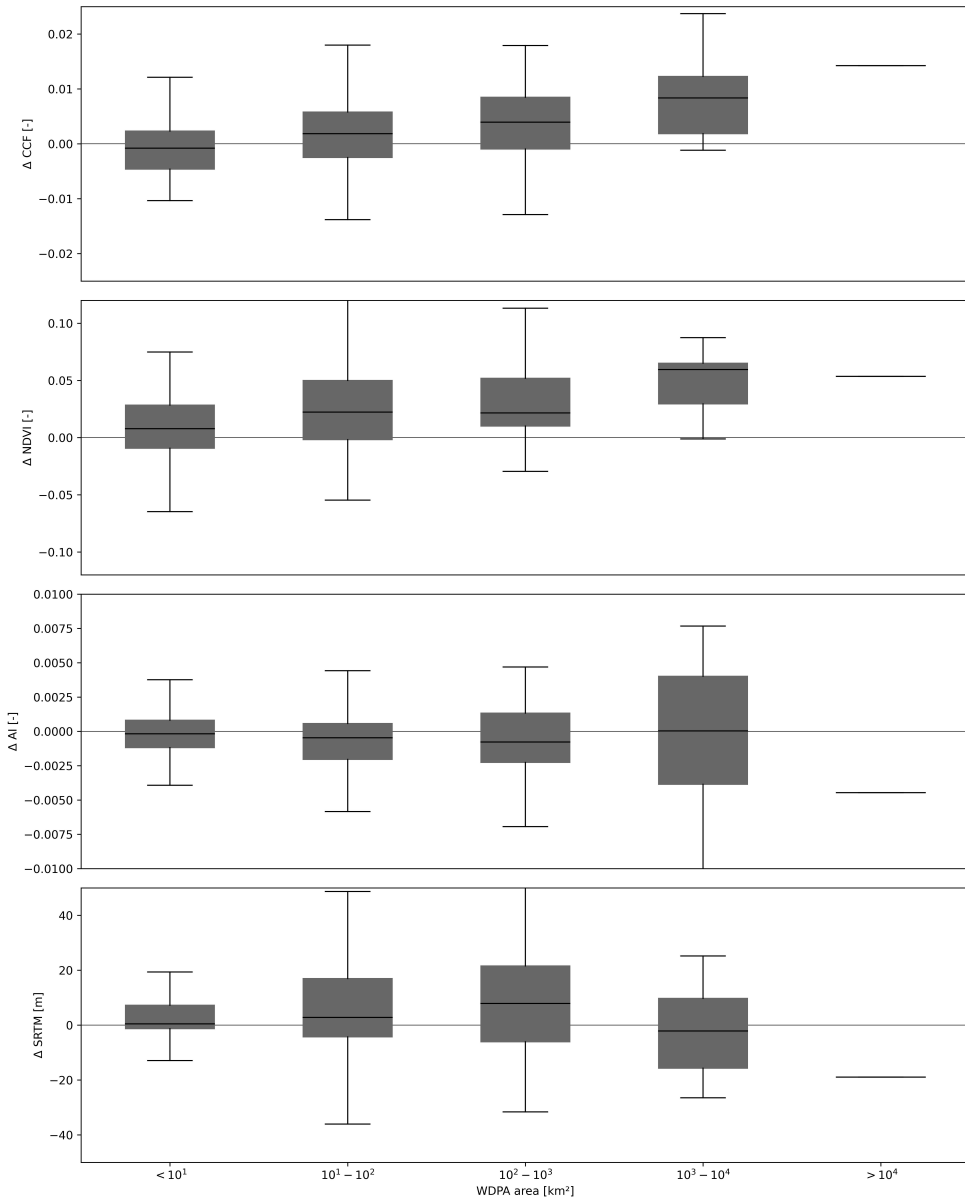
Supplementary Figure 4.12 | Vegetation changes within the World Database of Protected Areas (WDPA) regions. Linear trend in Normalized Difference Vegetation Index (NDVI) over the 2004/01/01 to 2024/01/01 period. Black lines indicate the WDPA boundaries.



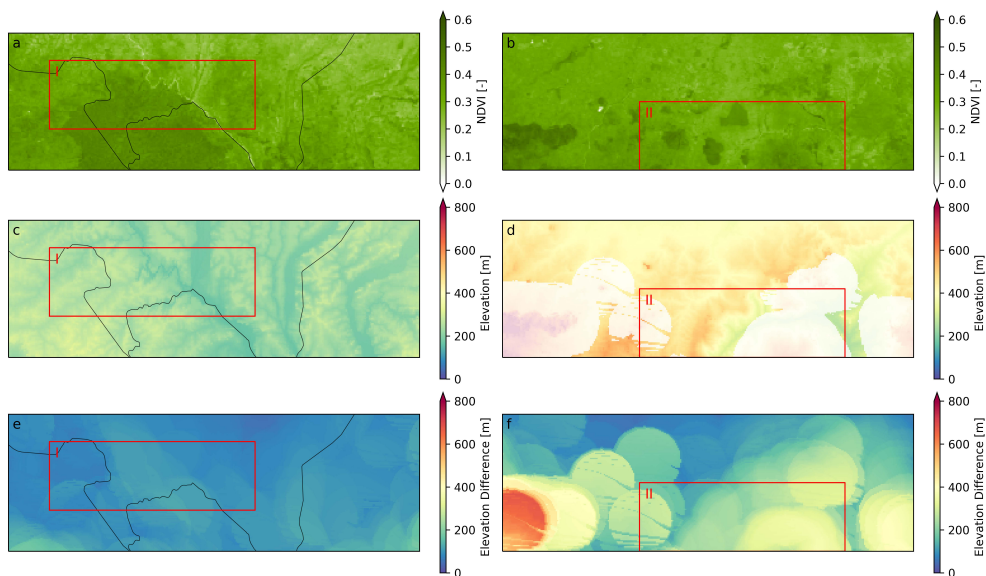
Supplementary Figure 4.13 | Scale dependent effects of area protection on cloud cover. Location of WDPA and reference areas in the study region (a). Difference in mean annual NDVI (b) and elevation (c) between the WDPA and reference areas. The difference in average April-September 07:00-15:45 cloud cover frequency (ΔCCF) between the WDPA and the corresponding reference area, per size of the WDPA area (d, e). The reference area consists of a 5 km buffer around the WDPA area, where overlapping WDPA areas are not considered. Points in d show ΔCCF for the individual areas. The line shows a linear regression between ΔCCF and $\log(\text{WDPA size})$. Boxes in e show the median (line/point), the interquartile range (box) and 1.5 times the interquartile range (whiskers) of the data grouped per 10-percentile of WDPA size. Each box contains 32 WDPA areas. The width of the boxes represents the range of WDPA sizes within the 10-percentile. Note that CCF is first averaged over time (based on $\sim 131,760$ individual images) and within the WDPA area and the reference areas, after which the ΔCCF is calculated. The boxes represent the variation in ΔCCF across WDPA areas only. Green boxes indicate that the median is significantly different to zero ($p < 0.05$, using the Wilcoxon signed-rank test).



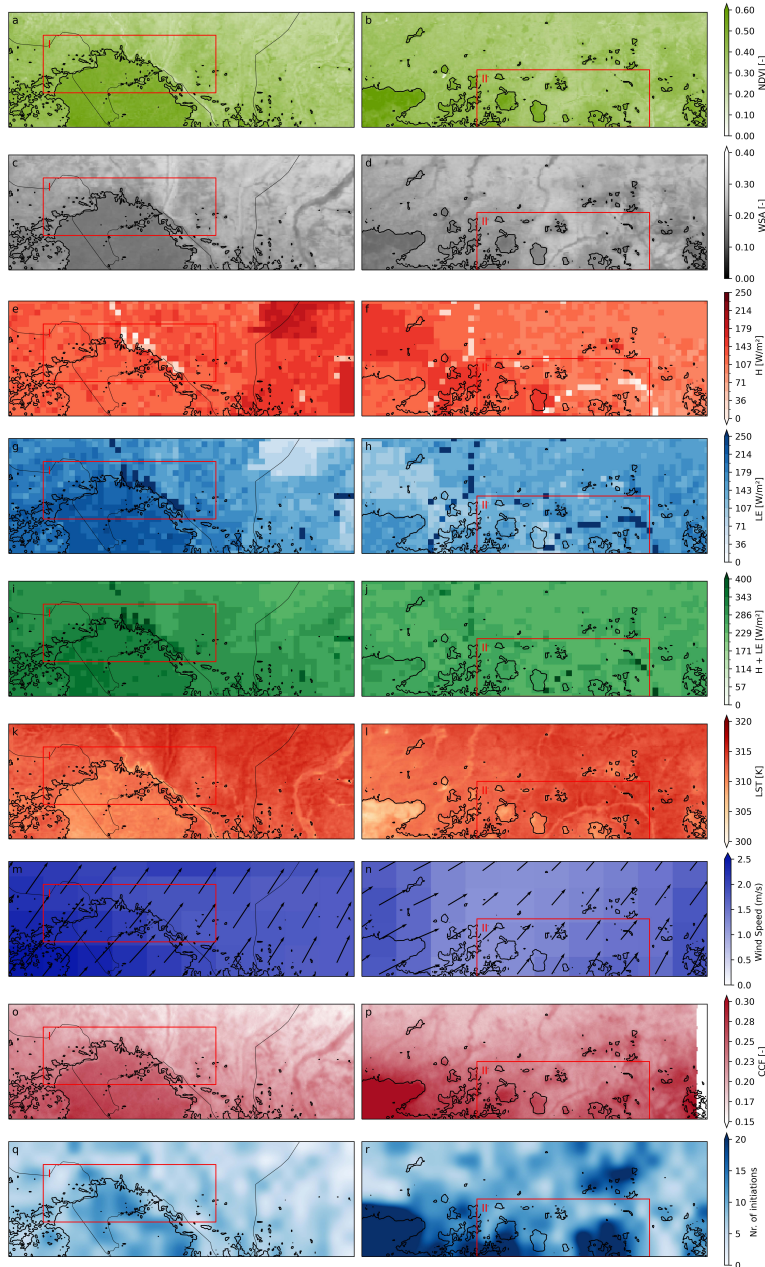
Supplementary Figure 4.14 | Scale dependent effects of area protection on cloud cover. Similar to Figure 4.4 and Supplementary Figure 4.10, but using a 15 km boundary, illustrating the effect of the buffer size on the results.



Supplementary Figure 4.15 | Properties of WDPA areas per size. Difference in cloud cover frequency (CCF), Normalized Difference Vegetation Index (NDVI), Aridity Index (AI) and Elevation (SRTM) between the protected and reference area, per project size class.



Supplementary Figure 4.16 | Areas with high topographical differences. Normalized Difference Vegetation Index around Subregion I (a) and Subregion II (b). Elevation in these regions is shown in (c,d). Light shades in Subregion II (d) show regions where the elevation changes more than 250 m within a circle with a radius of 25 km (i.e. high variations in topography). These areas are not present in Subregion I (c). The maximum elevation changes within a 25 km radius are shown in (e,f).



Supplementary Figure 4.17 | Earth Surface Properties and Cloud Cover. Mean April-September MODIS NDVI(Didan, 2021) (a, b), white-sky albedo (WSA)(Schaaf & Wang, 2015) (c, d), sensible heat flux (H) (e, f), latent heat flux (LE) (g, h), the sum of those (H+LE)(Ghilain, Arboleda, & Gellens-Meulenberghs, 2011; Ghilain, Arboleda, Sepulcre-Cantò, et al., 2011) (i, j) afternoon land surface temperature (LST)(Wan et al., 2021) (k, l), ERA-5 wind speed and direction (m, n), cloud cover frequency (CCF) (o, p) and number of convective initiations (q, r) between 2004/01/01 and 2024/01/01 in subregion I (left) and subregion II (right). Turbulent fluxes are calculated as the mean value between April and September for 2019-2023.

Appendix D | Supplementary Material Chapter 5

Supplementary Information Chapter 5

We created random patterns with spatial structures following Lennon (2000). This method generates two-dimensional $1/f$ noise patterns with a normal distribution, which is often similar to patterns found in natural systems. These patterns consist of two-dimensional waves across numerous frequencies. In frequency space, this is represented by:

$$f = (u^2 + v^2)^{1/2} \quad (\text{D.1})$$

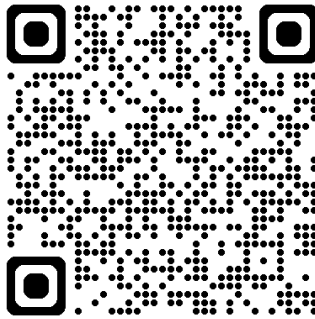
where f is the frequency grid, with u frequencies across rows and v frequencies across columns. Using a $1/f$ noise pattern, the spectral density is $S(f)$ is given by:

$$S(f) = f^\beta = (u^2 + v^2)^{\beta/2} \quad (\text{D.2})$$

The spatial clustering was changed through the dispersion parameter (β), which controls the weight of each frequency. If β is zero, each frequency has a similar weight, resulting in a pattern with low spatial correlation, whereas if β is negative, the lower frequencies are more important, resulting in smoother and clustered patterns with more spatial correlation. To add randomness, we give each frequency a random phase (φ) to create the different patterns. The spatial pattern x can then be given by applying the inverse Fourier transform operator F^{-1} on a complex spatial pattern with amplitude $\sqrt{S(f)}$ and phase $e^{i2\pi\varphi}$:

$$x = F^{-1}(\sqrt{S(f)} * e^{i2\pi\varphi}) = F^{-1}((u^2 + v^2)^{\beta/4} * (\cos(2\pi\varphi) + i \sin(2\pi\varphi))) \quad (\text{D.3})$$

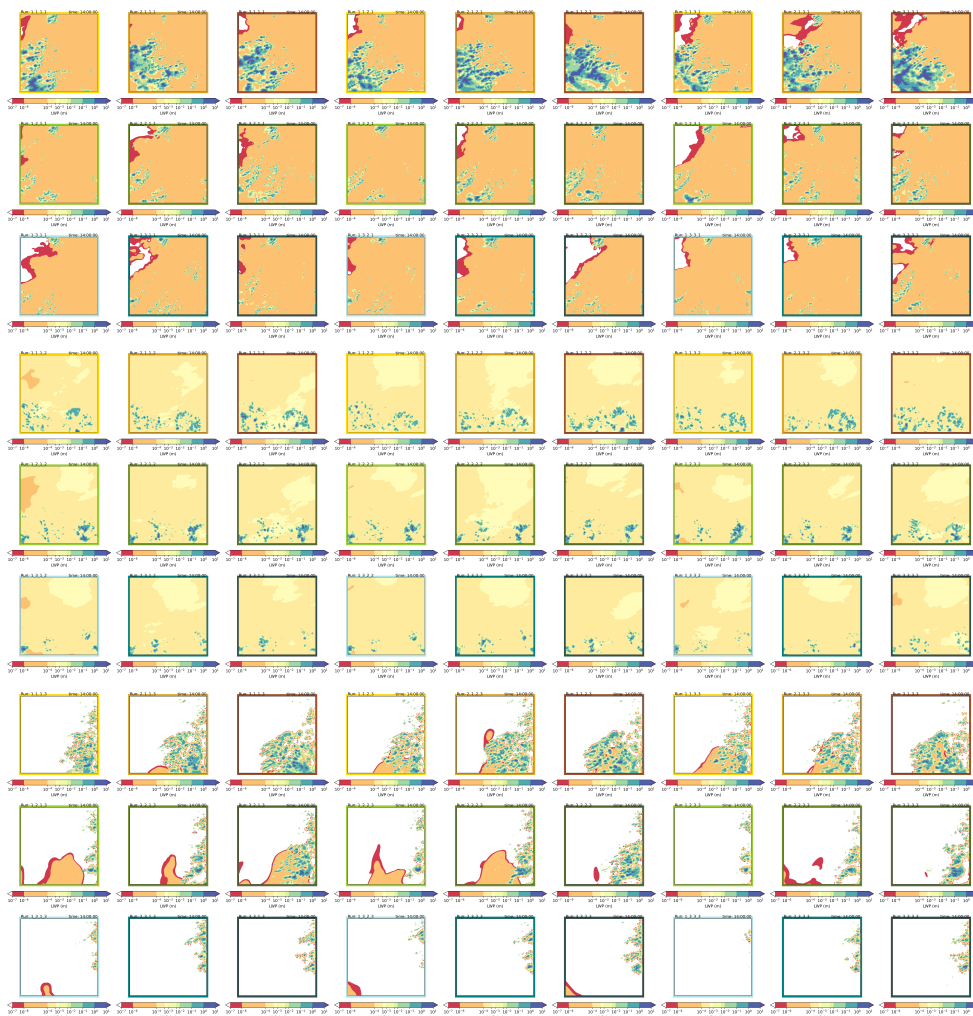
where we only consider the real part. The continuous field can then be classified into a binary forest and grassland map with a certain forest cover using the percentiles of values. In total, we created 27 restoration scenarios, using combinations of three forest covers (21.3%, 42.7% and 85.4%), three dispersion values (-1.0, -2.5 and -5.0), and three random variations (random phase) (seed 1, seed 2 and seed 3) (Supplementary Figure 5.2).



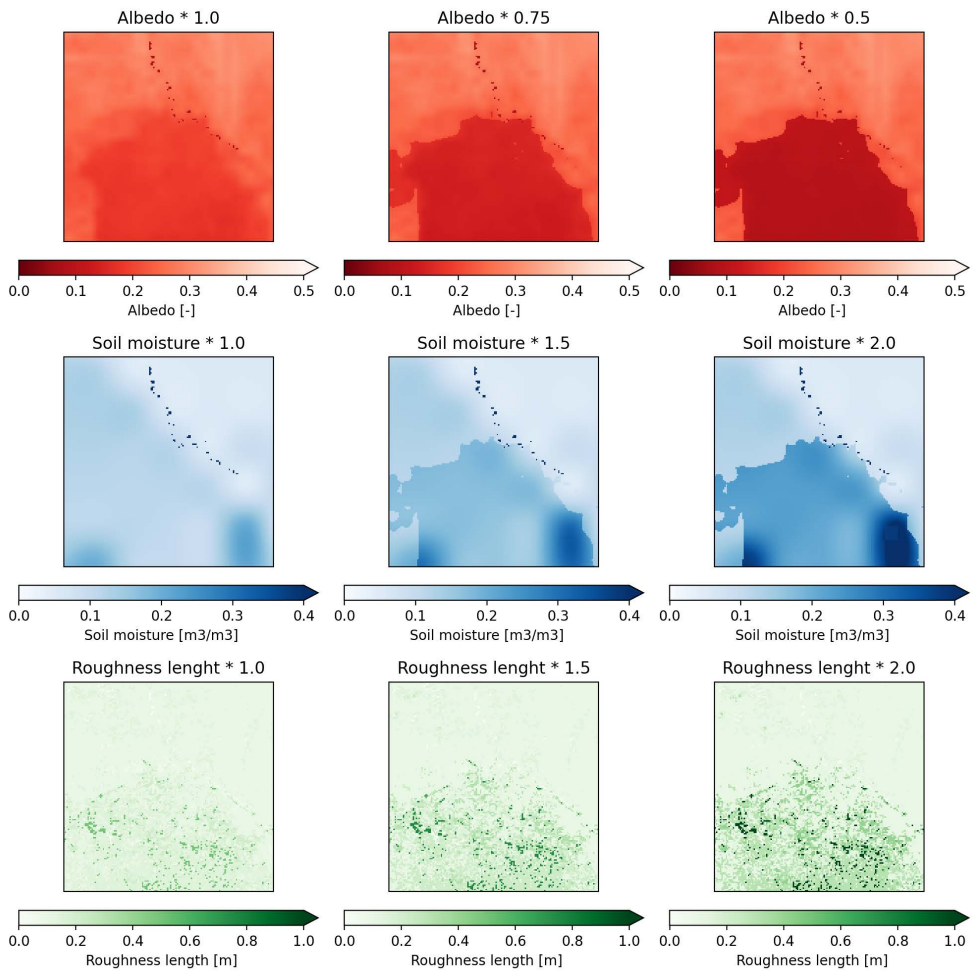
<https://figshare.com/s/44b19d12bc157543599f>

Supplementary Animation 5.1 | Effect of restoration on the spatial distribution of clouds. Animation of cloud cover (white) under different restoration scenarios on Day 1 (2017/10/01) at between 09:00 and 15:00 UTC in Domain 4. Cloud cover is defined as having a liquid water path (LWP) higher than 0.001 m. The background image shows the created land cover map, with forest in green and grassland in yellow, with different forest cover (indicated at the bottom), spatial dispersion (indicated on the right) and random variations (indicated at the top), resulting in 27 land cover simulations.

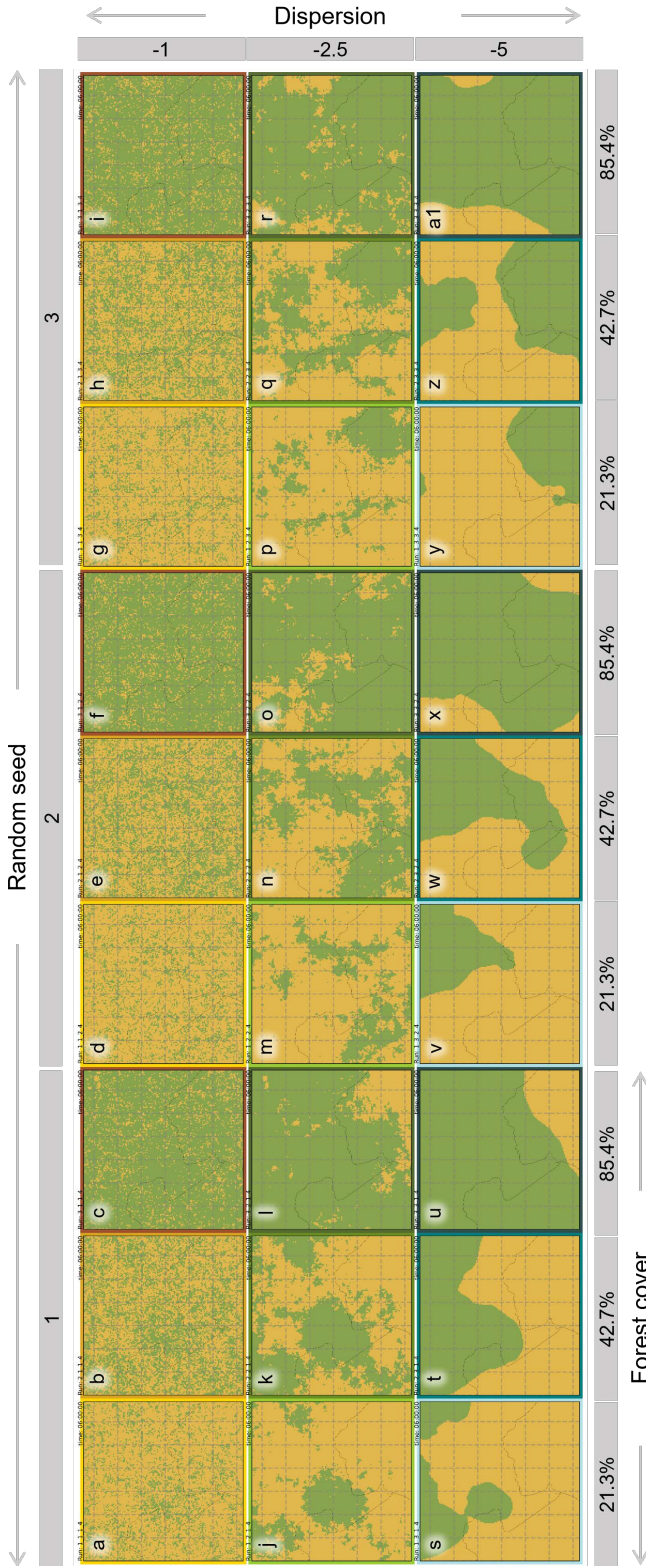
Supplementary Animation 5.2 | Vertical cross-section of boundary layer development over different spatial patterns of restoration. Potential temperature (left image) and vertical wind velocity (right image) at a west (left)-east (right) vertical cross section at a latitude of 12.4 °N for nine different restoration scenarios corresponding to Random Seed 2 in Figure 5.8 between 09:00 and 15:00 UTC. The black continuous line indicates the boundary layer height, the striped black line the lifting condensation level and the grey lines the relative humidity contours [%]. The land cover type is indicated by the yellow (grass) and green (forest) shading at the bottom. The grey opaque and transparent shading indicates a cloud water mixing ratio of, respectively, more than 0.001 and 0.1 g/kg. The blue shading indicates a precipitation mixing ratio of the same values.



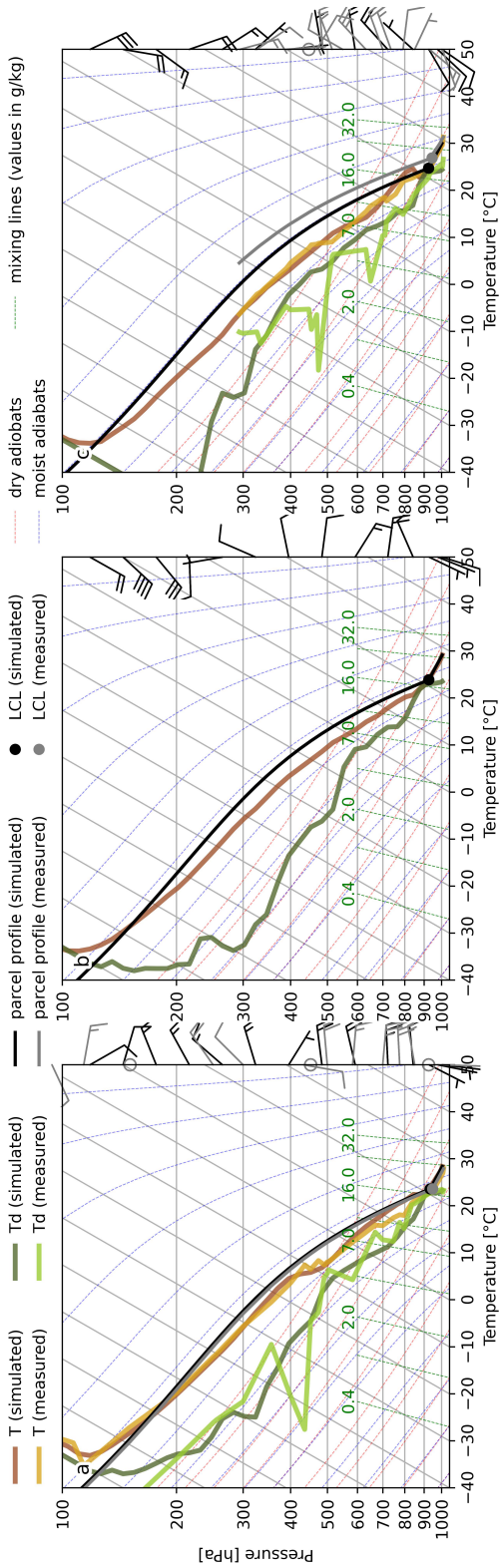
Supplementary Figure 5.1 | Liquid water path threshold for clouds. Liquid water path (LWP) at 14:00 UTC in Domain 4 on Day 1 (**top**), Day 2 (**middle**) and Day 3 (**bottom**). The parameter combinations are the same as in Figure 5.4. In this study, we selected clouds to have a higher liquid water path than 0.001 (m), visually matching the cloud edge. White regions have an LWP lower than 10^{-7} m.



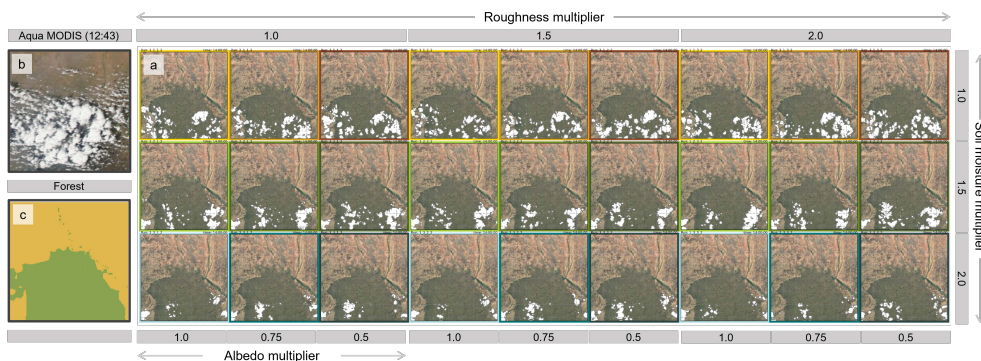
Supplementary Figure 5.2 | Input data for sensitivity analysis on Day 1. Albedo (**top**), soil moisture content (**middle**) and surface roughness (**bottom**) are changed in the region with high vegetation. Variables are changed by multiplication.



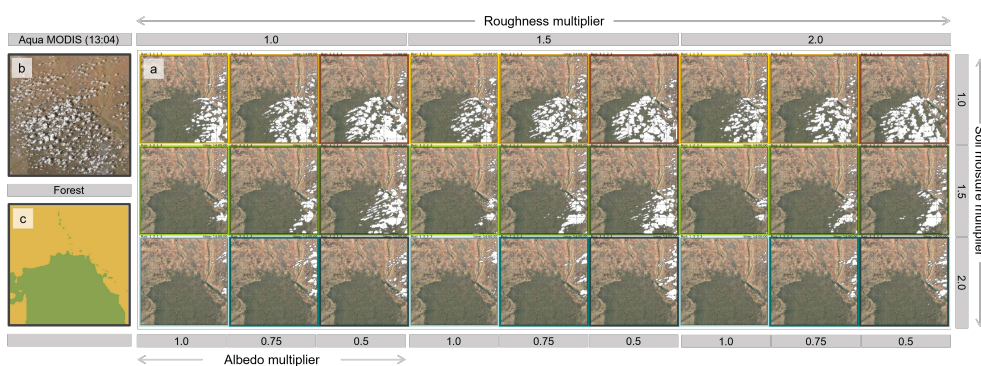
Supplementary Figure 5.3 | Restoration scenarios with varying forest cover and spatial heterogeneity. Green areas indicate mixed forest, whereas yellow areas indicate grassland. The random seed represents three random patterns with the same forest cover and dispersion coefficient. In total, 27 spatial patterns were created.



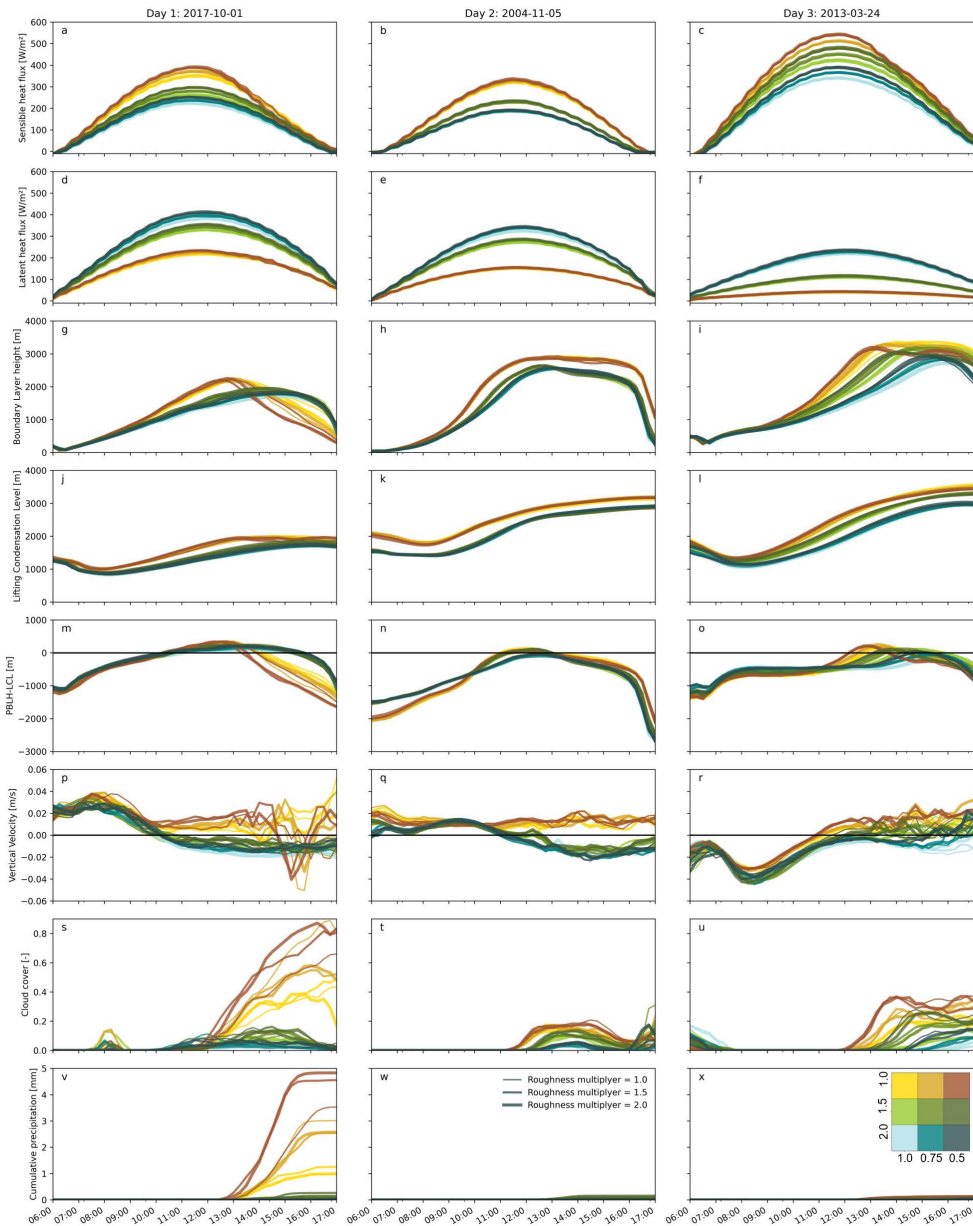
Supplementary Figure 5.4 | Validation of model results. Thermodynamic diagram simulated (WRF) and measured (sounding) temperature (T), dew point temperature (Td), parcel profile, lifting condensation level (LCL) and wind speed and direction (barbs, simulated is black, measured is gray) at Niamey on Day 1 (a), Day 2 (b) and Day 3 (c). Simulated temperature, dew point temperature and pressure are obtained from Domain 4 at the location of Abidjan.



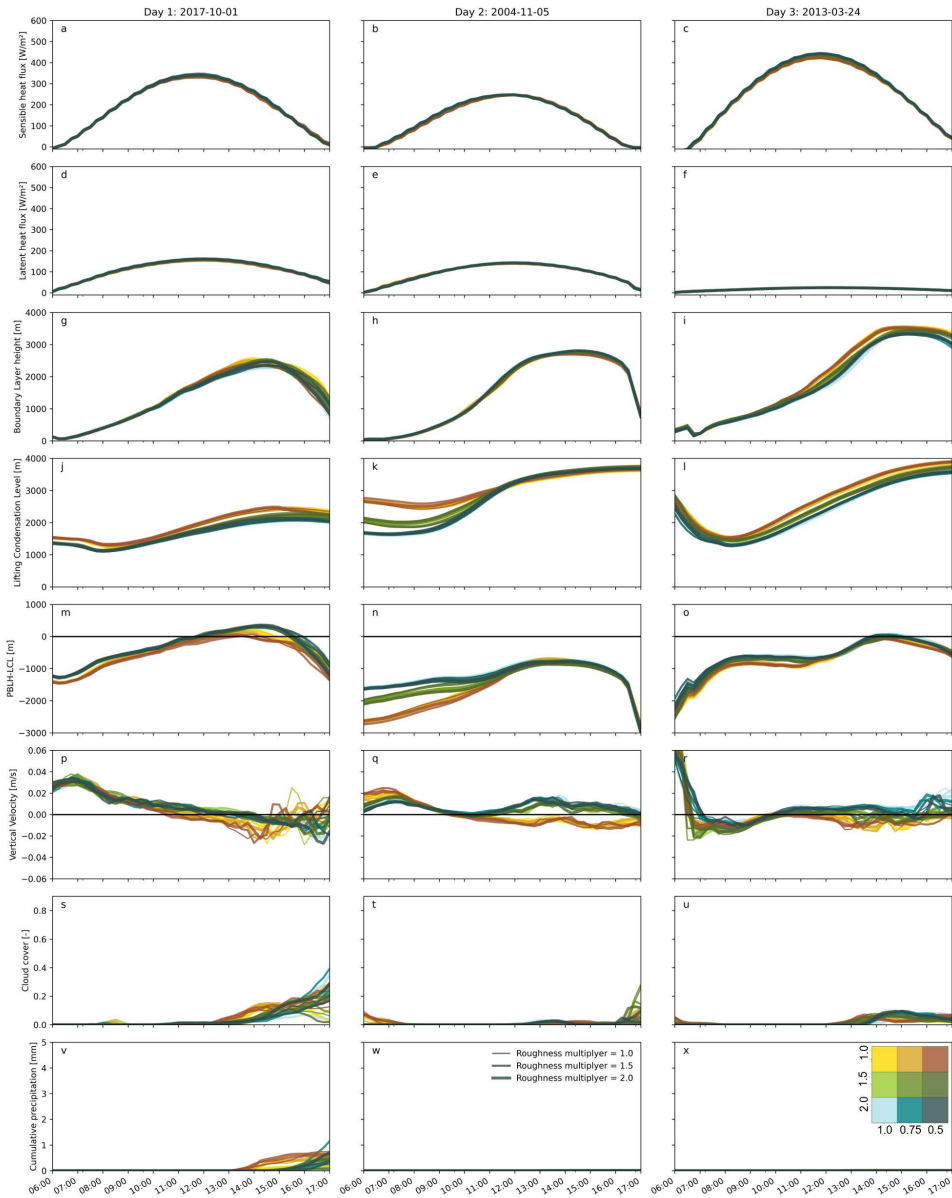
Supplementary Figure 5.5 | Cloud cover (white) under different parameter combinations on Day 2 (2004/11/05) at 14:00 UTC in Domain 4 (a). Cloud cover is defined as having a liquid water path (LWP) higher than 0.001 m. The parameter combination is indicated at the top (roughness multiplier), side (soil moisture multiplier) and bottom (albedo multiplier). The background image is obtained from Google Earth (Map data: Google, NASA). As a reference, the image on the left shows an Aqua MODIS reflectance image at 2004/11/05 12:43 UTC in Domain 4 (Vermote, 2015)(b). The parameters are only changed in the forested areas (c)



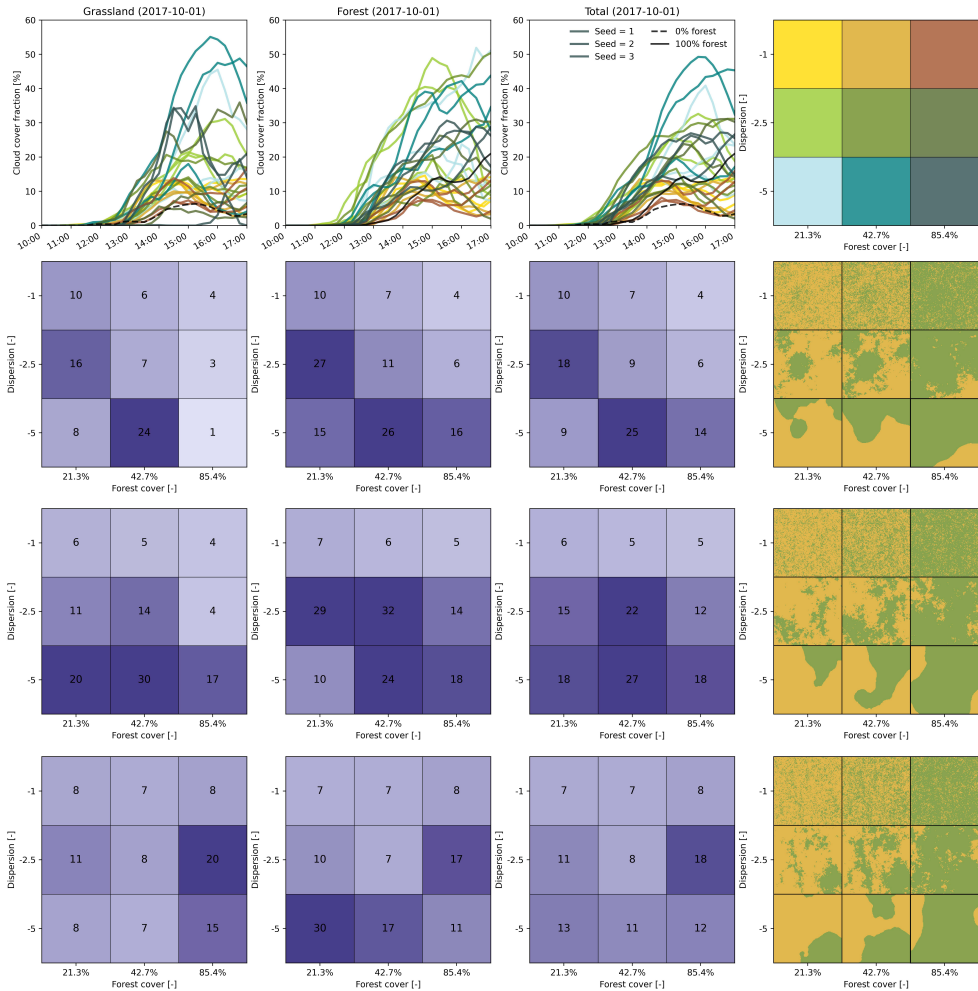
Supplementary Figure 5.6 | Cloud cover (white) under different parameter combinations on Day 3 (2013/03/24) at 14:00 UTC in Domain 4 (a). Cloud cover is defined as having a liquid water path (LWP) higher than 0.001 m. The parameter combination is indicated at the top (roughness multiplier), side (soil moisture multiplier) and bottom (albedo multiplier). The background image is obtained from Google Earth (Map data: Google, NASA). As a reference, the image on the left shows an Aqua MODIS reflectance image at 2013/03/24 13:03 UTC in Domain 4 (Vermote, 2015) (b). The parameters are only changed in the forested areas (c).



Supplementary Figure 5.7 | Effect of surface properties on surface fluxes, boundary layer growth and precipitation in the forest area. (a-c) Sensible heat flux, (d-f) latent heat flux, (g-i) boundary layer height, (j-l) lifting condensation level, (m-o) difference between boundary layer height and lifting condensation level, (p-r) vertical velocity, (s-u) cloud cover fraction and (v-x) cumulative precipitation in the forest area over the course of Day 1, Day 2 and Day 3 (06:00-17:00 UTC). The colours are similar to Figure 5.5. The inset in (x) shows the colour legend with albedo (horizontal) and soil moisture (vertical) multipliers. The colours are similar to Figure 5. Clouds are defined as areas with an LWP higher than 0.001 m.



Supplementary Figure 5.8 | Effect of surface properties on surface fluxes, boundary layer growth and precipitation in the grassland area. (a-c) Sensible heat flux, (d-f) latent heat flux, (g-i) boundary layer height, (j-l) lifting condensation level, (m-o) difference between boundary layer height and lifting condensation level, (p-r) vertical velocity, (s-u) cloud cover fraction and (v-x) cumulative precipitation in the grassland area over the course of Day 1, Day 2 and Day 3 (06:00-17:00 UTC). The colours are similar to Figure 5.5. The inset in (x) shows the colour legend with albedo (horizontal) and soil moisture (vertical) multipliers. Positive values indicate the value is higher in the forest area. Clouds are defined as areas with a LWP higher than 0.001 m.



Supplementary Figure 5.9 | Effect of restoration design on cloud development. Cloud cover fraction over the course of the day (a) over the grassland, (b) over the forest and (c) over the total domain. The line colours indicate different restoration scenarios with varying forest cover and spatial dispersion, as shown in (d) (and similar to the box outlined in Figure 5.8). Afternoon (12:00-17:00) average cloud cover fraction (%) (e) over the grassland, (f) over the forest and (g) inside the total domains for the separate random variations.

Code and Data Availability

Chapter 2

View the Google Earth Engine scripts: <https://code.earthengine.google.com/2ca1cef5d2c1c81de776624aa8388b86>. Explore data in the GEE application: <https://jessicaruijsch-wur.users.earthengine.app/view/landscape-restoration-and-greening-in-africa>. Download the local greening map: <https://figshare.com/s/0f5ea3889c62d8173132>

Chapter 3

MODIS NDVI (MOD13Q1.061), LST (MOD11A1.061), WSA (MCD43A3.006) and Land Cover (MCD12Q1) data are directly available through Google Earth Engine (<https://developers.google.com/earth-engine/datasets>), or can be downloaded from the NASA Earth Observing System Data and Information System (<https://earthdata.nasa.gov/>). Eddy covariance measurements are obtained from FLUXNET and are available through (<https://fluxnet.org/data/fluxnet2015-dataset/>). WOCAT data is available through (<https://www.wocat.net/en/>). Data created in this study is available at <https://doi.org/10.6084/m9.figshare.24072723>. Google Earth Engine scripts are available at: <https://code.earthengine.google.com/5deb2d58430918d3b6d14a1ed6481891>. Other (Python) scripts and tiff are available at files: <https://doi.org/10.6084/m9.figshare.24072723>.

Chapter 4

MODIS NDVI (MOD13Q1.061) and SRTM Elevation can be directly accessed through Google Earth Engine (<https://developers.google.com/earth-engine/datasets>) or can be downloaded from the NASA Earth Observing System Data and Information System (<https://earthdata.nasa.gov/>). Also the CALIPSO Vertical Feature Mask is available here. WDPA regions can be accessed at Protected Planet (<https://www.protectedplanet.net/>). MSG HRV and MSG cloud mask data can be accessed through the EUMETSAT Data Catalogue (<https://user.eumetsat.int/catalogue/>). Satellite-derived products of sensible and latent heat flux are obtained from the Satellite Application Facility on Land Surface Analysis (LSA SAF) from EUMETSAT (<https://lsa-saf.eumetsat.int/en/>). Python scripts containing the HRV cloud detection algorithm and the additional data analysis are available at <http://doi.org/10.6084/m9.figshare.26484841>.

Chapter 5

The WRF model is available at <https://github.com/wrf-model/WRF.git>. Radiosonde data is obtained from https://weather.uwyo.edu/upperair/sounding_legacy.html. The WRF namelist.input and namelist.wps files and the scripts to run the sensitivity analysis and restoration scenarios with the WRF model area available at <https://figshare.com/s/444b19d12bc157543599f>. Also the used validation data and average cloud cover fraction data are included here.

Statement of Author Contribution

Initials

J.R.	Jessica Ruijsch	Wageningen University & Research (ESC)
R.W.A.H.	Ronald W.A. Hutjes	Wageningen University & Research (ESC)
A.J.R	Adriaan J. Teuling	Wageningen University & Research (HWM)
J.V.	Jan Verbesselt	Wageningen University & Research (GRS)
G.D.	Gregory Duveiller	Max Planck Institute for Biogeochemistry
C.M.T.	Christopher M. Taylor	UK Centre for Ecology and Hydrology
G.J.S.	Gert-Jan Steeneveld	Wageningen University & Research (MAQ)

Chapter 2

J.R., A.J.T., J.V. and R.W.A.H. designed research; J.R. performed research; J.R. and J.V. contributed new reagents/analytic tools; J.R., A.J.T., J.V. and R.W.A.H. analysed data; J.R., A.J.T., J.V. and R.W.A.H. wrote the paper.

Chapter 3

J.R. designed the research, performed the research, contributed new analytic tools, analysed the data, and wrote the paper. A.J.T. designed the research, analysed the data and wrote the paper. G.D. analysed the data and wrote the paper. R.W.A.H. designed the research, analysed the data and wrote the paper.

Chapter 4

J.R. designed the research, performed the research, contributed new analytic tools, analysed the data, and wrote the paper. C.M.T analysed the data, contributed new analytic tools, and wrote the paper. R.W.A.H. designed the research, analysed the data and wrote the paper. A.J.T. designed the research, analysed the data and wrote the paper.

Chapter 5

J.R. designed the research, performed the research, analysed the data, and wrote the paper. A.J.T. designed the research, analysed the data and wrote the paper. C.M.T analysed the data and wrote the paper. G.J.S. analysed the data and wrote the paper. R.W.A.H. designed the research, analysed the data and wrote the paper.

List of Publications

Peer-reviewed publications (this thesis)

Ruijsch, J., Teuling, A. J., Verbesselt, J., & Hutjes, R. W. A. (2023). Landscape restoration and greening in Africa. *Environmental Research Letters*, *18*(6), 064020.

<https://doi.org/10.1088/1748-9326/acd395>

Ruijsch, J., Teuling, A. J., Duveiller, G., & Hutjes, R. W. A. (2024). The local cooling potential of land restoration in Africa. *Communications Earth & Environment*, *5*, 495.

<https://doi.org/10.1038/s43247-024-01650-x>

Ruijsch, J., Taylor C. M., Hutjes, R. W. A. & Teuling, A. J. (2025). Scale-dependent cloud cover changes due to land restoration in West African drylands. *Communications Earth & Environment*. *6*, 174.

<https://doi.org/10.1038/s43247-025-02154-y>

Peer-reviewed publications (other)

Ruijsch, J., Versteegen, J. A., Sutanudjaja, E. H., & Karssenberg, D. (2021). Systemic change in the Rhine-Meuse basin: Quantifying and explaining parameters trends in the PCR-GLOBWB global hydrological model. *Advances in Water Resources*, *155*, 104013.

<https://doi.org/10.1016/j.advwatres.2021.104013>

Shen, Y., **Ruijsch, J.**, Lu, M., Sutanudjaja, E. H., & Karssenberg, D. (2022). Random forests-based error-correction of streamflow from a large-scale hydrological model: Using model state variables to estimate error terms. *Computers & Geosciences*, *159*, 105019.

<https://doi.org/10.1016/j.cageo.2021.105019>

van Hateren, T. C., Jongen, H. J., Al-Zawaidah, H., Beemster, J. G. W., Boekee, J., Bogerd, L., Gao, S., Kannen, C., van Meerveld, I., de Lange, S. I., Linke, F., Pinto, R. B., Remmers, J. O. E., **Ruijsch, J.**, Rusli, S. R., van de Vijzel, R. C., Aerts, J. P. M., Agoungbome, S. M. D., Anys, M., Blanco Ramírez, S., van Emmerik, T., Gallitelli, L., Chiquito Gesualdo, G., Gonzalez Otero, W., Hanus, S., He, Z., Hoffmeister, S., Imhoff, R. O., Kerlin, T., Meshram, S., Meyer, J., Meyer Oliveira, A., Müller, A. C. T., Nijzink, R., Scheller, M., Schreyers, L., Sehgal, D., Tasseron, P. F., Teuling, A. J., Trevisson, M., Waldschläger, K., Walraven, B., Wannasin, C., Wienhöfer, J., Zander, M. J., Zhang, S., Zhou, J., Zomer, J. Y. & Zwartendijk, B. W. (2023). Where should hydrology go? An early-career perspective on the next IAHS Scientific Decade: 2023–2032. *Hydrological Sciences Journal*, *68*(4), 529-541.

<https://doi.org/10.1080/02626667.2023.2170754>

In preparation

Ruijsch, J., Teuling, A.J. , Steeneveld, G.J., Taylor C.M., & Hutjes, R.W.A. (2025). Clustered land restoration projects increase cloud formation in West African drylands [*Preprint*].

<https://doi.org/10.22541/essoar.174898798.80926616/v1>

Professional reports

Ruijsch, J., Hutjes, R. W., & Teuling, A. J. (2023). Heeft landgebruik effect op ons weer?: Literatuuronderzoek relatie landgebruik en klimaat op regionale en lokale schaal: De Kleine Waterkringloop. *Wageningen University & Research*.
<https://doi.org/10.18174/640643>

Science communication

Ruijsch, J., Teuling, A. J., Hutjes, R. W. A., de Redelijkheid M. & Adams, H. (2023, November 7). Regen zaaien of regen oogsten? De rol van de kleine waterkringloop in het klimaatbestendig maken van Nederland. *H2O*.
<https://www.h2owaternetwerk.nl/h2o-podium/uitgelicht/regen-zaaien-of-regen-oogsten-de-rol-van-de-kleine-waterkringloop-in-het-klimaatbestendig-maken-van-nederland>

Ruijsch, J. (2023, December 8). Kun je met een ander landgebruik het weer beïnvloeden? *Kennisportaal Klimaatadaptatie*.
<https://klimaatadaptatienederland.nl/actueel/actueel/nieuws/2023/interview-jesscia-ruijsch/>

Soil restoration in Africa has a warming and cooling effect. *Resource*.
<https://www.resource-online.nl/index.php/2023/10/10/soil-restoration-in-africa-has-a-warming-and-cooling-effect/?lang=en>

Africa not always made cooler by more greenery. *Wageningen World*.
https://issuu.com/wageningenur/docs/ww_02_en2023?fr=sMWNmNjY5MDEyOTA

Acknowledgement

I would like to end this thesis with the quote I used at the start: *"In this great chain of causes and effects, no single fact can be considered in isolation"*. This quote not only captures the interconnectedness of the land and atmosphere, but also reflects the process of completing a PhD, a journey I could never have undertaken alone. Completing a PhD is often seen as stressful and challenging, and I cannot deny having experienced difficult moments myself. However, I can also say that I have genuinely enjoyed (most of) this process over the past years, and that is largely thanks to the people who have supported me, both intellectually and emotionally.

Thank you, Ronald and Ryan, for being my supervisors and promoters. Over the past years, you have not only guided me, but also encouraged me to challenge myself. You make a fantastic supervision team, without whom this thesis would not be in front of you today. Ryan, your expertise at the intersection of hydrology and meteorology, your great eye for detail, and your instinct for identifying opportunities have been invaluable to me. Ronald, you have always ensured that I never lost sight of the bigger picture while giving me the freedom to make my own decisions and find my own way. Thank you for contributing so much to my personal and academic development.

I also want to express my gratitude to the enthusiastic and knowledgeable co-authors of the different chapters. Most of you I had not met before, and your willingness to collaborate after just an email or a brief conference meeting has been amazing. Jan, thank you for your help with the BFAST algorithm, especially within Google Earth Engine. Greg, thank you for your insights into remote sensing of biophysical variables. Chris, thank you for sharing your knowledge of cloud processes in the Sahel region. And Gert-Jan, thank you for helping me with WRF and sharing your meteorological expertise (which does not always come naturally to me).

A special thanks to Vivian, who has shown me the value of land restoration from a completely different perspective. It has been great to collaborate with you. I also want to thank you and your family for your hospitality, both in Rome and in Washington, over these past years. Thank you, Ishani, Tijmen, Johanna, Maud, Noëlle, and Nika, for your enthusiasm during your master theses. The insights you developed in such a short time have truly helped me. Thank you also to all the anonymous reviewers (yes, even reviewer #2) and opponents for reading and commenting on my papers in your free time and for considerably improving my research. Even though the review process is, in my opinion, the most frustrating and humbling part of being a researcher, peer review is an essential part of the scientific process.

Thank you to Caroline and Eric from Stichting SUBACA, not only for making this project possible, but also for your encouragements and continuous interest in this work.

To all my WSG/ESC colleagues, thank you for creating a comfortable environment where I could be myself and have some fun during stressful periods. Thank you to my officemates Ilaria, Mirjam, Paul, Kim, Dianneke, Aslihan, Cengiz, Anna, and Mohammed. Without your emotional support, laughter, and (sometimes a bit too long) chats, this experience would have been much less enjoyable. Thank you, Sony, for the dinners, talks, and advice. Mirjam and Paul, thank you for being my paranymphs and supporting me during this exciting day. Thank you, Hugo, Wouter, Ilaria, Meijun, and Nancy, for organizing the PhD trip to Bologna with me. Thank you, Sarra and Wout for your support when our trip to South Africa did not go as planned. Thank you to all the organizers of the ECS and HWM trips throughout Europe. Thank you, Anne, Jolanda, Agnes, Sarah, and Imme, for the limited in number but highly valuable discussions on vegetation and moisture recycling. I would also like to thank all the institutes I have visited over the years, especially CMCC in Lecce, for their hospitality and interest in my work during the short visits.

I am very grateful to all my friends. Aan Amanda, Anne-Jaël, Guusje, Klaske en Lonit, jullie vriendschap betekent ontzettend veel voor mij. Ik vind het zo bijzonder dat we elkaar op de eerste dag van de middelbare school (of zelfs daarvoor) hebben leren kennen, en nu al deze verschillende momenten in het leven samen kunnen vieren (en de meesten van ons zelfs een PhD doen!). Aan mijn oude huisgenoten en vrienden van de Warande, dank jullie wel voor alle gesprekken en discussies tijdens de diners en vakanties.

And of course, I am forever grateful to my family. Bedankt papa, mama, Kevin en Denise voor jullie onvoorwaardelijke steun. Bedankt oma, opa en oma voor jullie eindeloze interesse. Ook de familie van Francesco bedankt voor jullie aanmoedigen (Grazie!). En natuurlijk, bedankt Francesco voor jouw onvoorwaardelijke liefde. Ik kijk ernaar uit om alle volgende stappen in mijn leven (en carrière) samen met jou te zetten.

Curriculum Vitae

- 14/11/1996 **Born in Wageningen, the Netherlands**
- 2015 – 2018 **BSc Earth Sciences (*cum laude*)**
Utrecht University, the Netherlands
- 2018 – 2020 **MSc Earth Surface and Water (*cum laude*)**
Utrecht University, the Netherlands
- 2020 – 2025 **PhD Candidate**
Wageningen University, the Netherlands





*Netherlands Research School for the
Socio-Economic and Natural Sciences of the Environment*

D I P L O M A

for specialised PhD training

The Netherlands research school for the
Socio-Economic and Natural Sciences of the Environment
(SENSE) declares that

Jessica Ruijsch

born on 14 November 1996 in Wageningen, The Netherlands

has successfully fulfilled all requirements of the
educational PhD programme of SENSE.

Wageningen, 25 September 2025

SENSE coordinator PhD education

Dr Ir Peter Vermeulen

The SENSE Director

Dr Jampel Dell'Angelo



The SENSE Research School declares that **Jessica Ruijsch** has successfully fulfilled all requirements of the educational PhD programme of SENSE with a work load of 60.4 EC, including the following activities:

SENSE PhD Courses

- o Environmental research in context (2021)
- o Research in context activity: 'Organizing a seminar called: "The Value of Water: at the crossroads between climate change, scarcity and political ecology" at Bologna University, Department of Geography' (2022)

Selection of Other PhD and Advanced MSc Courses

- o Boundary-layer processes, Wageningen University (2021)
- o Atmospheric modelling, Wageningen University (2022)
- o Systematic approaches to reviewing literature, Wageningen Graduate Schools (2021)
- o Presenting with impact, Wageningen Graduate Schools (2023)
- o Teaching and supervising thesis students, Wageningen University (2023)
- o Land dynamics in an era of change, PE&RC and University of Free State (2023)
- o Writing grant proposals, Wageningen Graduate Schools (2025)

External training at a foreign research institute

- o Tour de PhD with HWM group to LIST, Karlsruhe, Freiburg and Zurich (2022)

Management and Didactic Skills Training

- o Organize PhD trip for WSG group to University of Bologna and CMCC (2022)
- o Supervising four MSc and two BSc students with thesis (2022-2025)
- o Creating and coordinating the BSc course 'Assessment of Marine Nature Based Solutions' (2023-2024)
- o Coaching in MSc thesis ring (2023)
- o Supervising in the MSc course 'Climate Change Studies Topics and Approaches' (2021-2023)
- o Supervising in the MSc course 'Academic Consultancy Training' (2021)

Oral Presentations

- o *Detecting greening effects of land restoration in semi-arid Africa using a spatial-context approach in Google Earth Engine.* EGU General assembly, 23- 27 May 2022, Vienna, Austria
- o *Assessing the Cooling Potential of Land Restoration in Africa with Google Earth Engine.*, EGU General assembly, 24-28 April 2023, Vienna, Austria
- o *The effect of land restoration on cloud cover in West Africa.* EGU General assembly, 15 - 19 April 2024, Vienna, Austria
- o *Scale-dependent Cloud Enhancement from Land Restoration in West African Drylands.* AGU Annual meeting, 09- 13 December 2024, Washington D.C., United States

Colofon

The research described in this thesis was financially supported by Stichting SUBACA. Financial support from Wageningen University for printing this thesis is gratefully acknowledged.

Cover design by Jessica Ruijsch. The cover shows a true colour satellite image from the MODIS sensor on 2 November 2014 13:30 UTC. The image shows part of West Africa, with regions within Cote d'Ivoire, Ghana, Togo, Benin, Nigeria, Niger, Burkina Faso and Mali.

Printed by Proefschriftmaken.

This thesis has been printed on FSC-certified paper.

